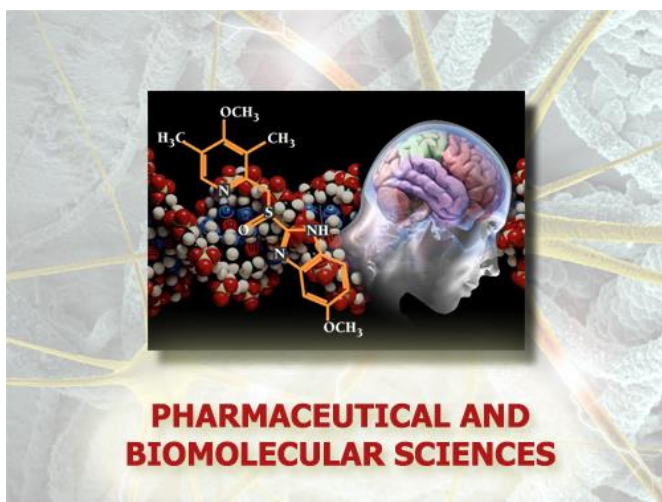**Università degli Studi di Torino**

Scuola di Dottorato in
Scienze della Natura e Tecnologie Innovative

Dottorato in
Scienze Farmaceutiche e Biomolecolari
(XXX ciclo)

Interfacial molecular recognition in complex systems: chemical investigation of the interaction between silica surfaces and biomembranes

Candidato: Riccardo Leinardi   **Tutors: Prof. Gianmario Martra**
                                                                          Dr. Francesco Turci

Università degli Studi di Torino

Dottorato in
Scienze Farmaceutiche e Biomolecolari

Tesi svolta presso il
Dipartimento di Chimica

CICLO:XXX

TITOLO DELLA TESI: Interfacial molecular recognition in complex systems: chemical investigation of the interaction between silica surfaces and biomembranes

TESI PRESENTATA DA: Riccardo Leinardi

TUTORS: Prof. Gianmario Martra, Dr. Francesco Turci

COORDINATORE DEL DOTTORATO: Prof. Gianmario Martra

ANNI ACCADEMICI: 2014/2015, 2015/2016, 2016/2017

SETTORE SCIENTIFICO-DISCIPLINARE DI AFFERENZA: Chim/03 (Chimica generale ed inorganica)

"A model must be wrong, in some respects, else it would be the thing itself. The trick is to see where it is right."

Henry Bent

Table of Contents

Chapter 1: Introduction

Chapter 2: Synthesis and characterization of crystalline silica particles with tailored physico-chemical properties as natural quartz surface model

Chapter 3: The pathogenetic activity of quartz: the role of crystallinity and surface features

Chapter 4: Amorphous silica & membrane perturbative activity: interaction of surface-controlled silica nanoparticles with natural and synthetic membrane models

Chapter 5: Evaluation of the interaction of respirable quartz crystals with macrophage cell lines

Chapter 6: General discussion and conclusion

Acknowledgments

Abbreviations

AFM Atomic force microscopy
AM Alveolar macrophages
AOP Adverse outcome pathway
BET Brunauer Emmet Teller
BSA Bovine serum albumin
DCS Differential centrifugal sedimentation
DLS Dynamic light scattering
DMEM Dulbecco's modified Eagle's medium
DMPO 5,5-Dimethyl-L-pyrroline-N-oxide
DOPC 1,2-Dioleoyl-sn-glycero-3-phosphocholine
DOPG 1,2-Dioleoyl-*sn*-glycero-3-phospho-*rac*-(1-glycerol)
DPBS Dulbecco's phosphate buffered saline
DSN Dense silica nanoparticle
EDS Energy dispersive X-ray spectrometry
ELISA Enzyme-linked immunosorbent assay
ELS Electrophoretic light scattering
EPR Electron paramagnetic resonance
FBS Fetal bovine serum
FPIA Flow particle image analysis
FRAP Fluorescence recovery after photobleaching
FTIR Fourier transform infrared spectroscopy
GUV giant unilamellar vesicles
HCA High content analysis
J774 Mouse monocyte macrophage cell line
KE Key events
LDH Lactate dehydrogenase
LMP Lysosomal membrane permeabilization
LPS Lipopolysaccharide
LUV Large unilamellar vesicles
MIE Molecular initiating event
MSN Mesoporous silica nanoparticle
Na-MTS Sodium metasilicate pentahydrate
NP Nanoparticle
PBS Phosphate buffered saline
MSN Mesoporous silica nanoparticles
PC Phosphatidylcholine
PTFE Polytetrafluoroethylene
QCM Quartz crystal microbalance

QD Quantum dot

QNAR Quantitative nanostructure-activity relationship

QSAR Quantitative structure–activity relationship

RBC Red blood cell

RPMI Roswell Park Memorial Institute *medium*

SEM Scanning electron microscopy

SLB Supported lipid bilayer

SPE Surface plasmon resonance

SSA Specific surface area

SUV Small unilamellar vesicles

TEM Transmission electron microscopy

XRF X-ray fluorescence

XRPD X-ray powder diffraction

ZPC Zero point charge

Chapter 1

Introduction

1.1 Silica

The occurrence of silica-related diseases, including autoimmune diseases, silicosis, and lung cancer, rose awareness about the occupational risk of some kind of silica. The mechanism of toxicity of silica, especially the crystalline forms such as quartz and cristobalite, have been intensively investigated in the last 50 years by the industrial and scientific community. Especially, the researchers' interest was devoted to the physical-chemical properties of silica that are related to its toxicity. The toxicological investigations of crystalline silica pathogenicity, particularly quartz, has been carried out so far on quartz dusts obtained through the grinding of natural crystals. Mechanical fracturing produced on one hand a suitable size distribution to correctly represent respirable crystals but on the other hand yielded to crystals with irregular distribution of crystallographic surfaces, exposure of conchoidal fractures (Margolis & Krinsley, 1974; Murashov, Harper, & Demchuk, 2006), incorporation of trace metals – especially iron from mill, and the occurrence of an amorphous layer covering crystal faces (Fubini, 1998; Li, Bandara, & Shultz, 2004; Nagelschmidt, Gordon & Griffin, 1952; Steinike, Hennig, Richter-Mendau & Kretzschmar, 1982). If those samples could correctly be representative of industrial and occupational exposure, the investigation of the molecular determinants could not be properly designed on the altered surfaces of grinded crystals. In view of that, the synthesis of highly-pure crystalline silica specimen, in respirable size, represents a breakthrough in the possibility to design a scientifically sound evaluation of the quartz toxicity in in-vitro and in-vivo studies.

Silicion (Si) is one of Earth's most abundant elements, making up 27.7% of the crust. Nevertheless, it can be found very rarely as pure element, but it is mostly distributed in dust and sand as several forms of silicon dioxide (SiO_2, silica), combined with oxygen in a 1:2 stoichiometric ratio. Indeed, over 90% of the Earth's crust is composed of silicate minerals, which share with silica the tetrahedron $[SiO_4]^{4-}$ chain structure (Deer, Howie and Zussman, Introduction to the Rock-Forming Minerals, Mineralogical Society). Silica exists naturally in many different forms (*polymorphs*), that can be crystalline and non-crystalline (amorphous). In the majority of silicates, the Si atom show tetrahedron coordination with four O atoms, which surrounds a central silicon atom (SiO_4): the quartzite polymorph represents a very appropriate example of such structure. SiO_4 units are linked one to each other through oxygen atoms, which act as bridges between two Si atoms. Thus, the general formula for silicon dioxide is $(SiO_2)_n$ (Fig. 1.1).
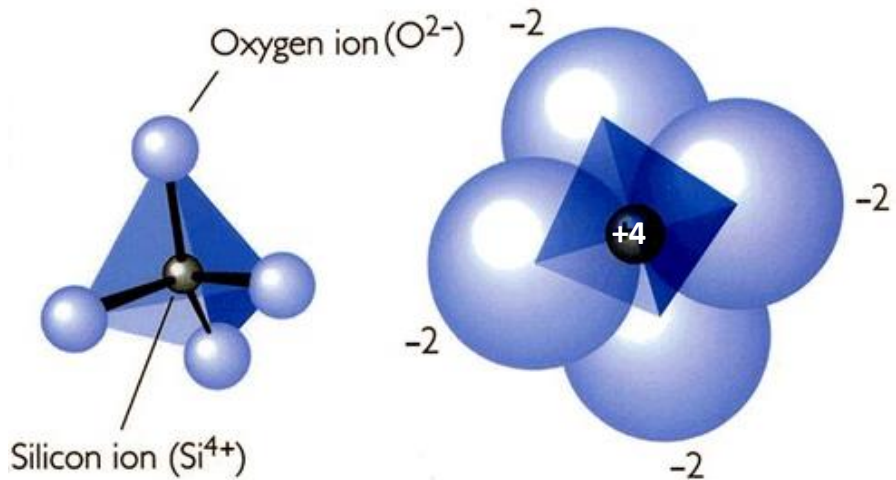
Fig. 1.1 The building block of silica, Si-O tetrahedron (Egger, 2006)

The [SiO_4] unit is rigid. On the contrary, the Si-O-Si angle that connects two different tetrahedrons can change, depending on temperature, pressure or geometrical constraints. Due to this flexibility, a large number of silica-based materials exist in nature, moving from dense crystalline to amorphous structures (quartz, glasses) to porous systems (aerogels, sponges, mesoporous materials) (Rimola, Costa, Sodupe, Lambert, & Ugliengo, 2013).
The following table (Table 1.1) sums up a list of the most common forms of natural silicas, classified as amorphous and crystalline.

Table 1.1 most common forms of natural silicas and their origin

Silica form	Origin	
	Mineral	**Biogenic**
Crystalline	α-quartz cristobalite tridymite	
Amorphous	Vitreous silica Hydrous silica (opal)	Diatomaceous earth Plants (sugar cane, rice, grain, wheat)

Amorphous structures are characterized by random networks of [SiO$_4$] units, which lack of periodicity in bond orientation and result in the formation of disordered systems. On the contrary, the tetrahedrons in crystalline silica are regularly arranged and their orientation and relative position are characteristics for each crystalline polymorph.

Concerning biogenic silica, which is silica originating in living matter, the two main examples are represented by diatomaceous earth, formed upon the deposition of siliceous frustules of diatoms at the ground, and silica from crop plants (sugar cane, rice and millet), which accumulate silica in their tissues in order to ensure structural integrity and give protection against pathogens and insects.

1.2 Crystalline Silica

A crystalline solid is a material in which constituents (atoms, molecules, and ions) are arranged in a highly ordered microscopic structure, forming a crystal lattice, which extends in all directions. Moreover, macroscopic single crystals are usually identifiable by their geometrical shape, consisting of flat faces, with specific characteristic orientations. In particular, crystalline silica is able to originate different ordered structures, all sharing the same chemical formula, called polymorphs. Most common natural crystalline forms of silica are: quartz, cristobalite, tridymite, coesite and stishovite: they differ one from each other in terms of length and angle of the Si-O-Si. For each polymorph, more crystallographic forms exist, depending on the arrangements of the SiO$_4$ tetrahedron.

Of all silica polymorphs, quartz is the only stable form at normal environmental conditions, and all other polymorphs will, in a sufficient time, eventually transform into quartz. The other polymorphs are stable at different and very particular conditions (high temperatures and pressures), but some of them can also form at lower temperature and pressure, conditions at which quartz is stable (Tab. 1.2). At low pressures, there are actually three groups of silica polymorphs, each of which has two closely related members: one low-temperature member given a α-prefix (low), and one high-temperature member of the same name, but with a β-prefix (high).

Table 1.2 During the transition from a α- to a β-variant the atoms in the crystal lattice only get slightly displaced relative to each other, but they don't change places inside the crystal lattice. α-β-transitions are only based on alterations of the angles and the lengths of the chemical bonds. Thus, they occur instantaneously. Such a phase transition is generally called displacive, as it only requires relative displacements of the atoms without the need to break chemical bonds. Because the angular Si-O-Si bonds get straightened out, the high-

temperature silica polymorphs all possess a higher symmetry than their low-temperature counterparts (hexagonal > trigonal > triclinic; cubic > tetragonal) (*www.thequartzpage.de*).

Low Pressure Silica Polymorphs						
high- or β-polymorph	**β-Quartz**		**β-Tridymite**		**β-Cristobalite**	
stable at metastable at	573°C - 870°C -		870°C - 1470°C 117°C - 870°C		> 1470°C 270°C - 1470°C	
crystal system	hexagonal		hexagonal		cubic	
Si-O-Si angle	153°		180°		151°	
low- or α-polymorph	**α-Quartz**		**α-Tridymite**		**α-Cristobalite**	
stable at metastable at	< 573°C -		- < 117°C		- < 270°C	
crystal system	trigonal		triclinic		tetragonal	
Si-O-Si angle	144°		140°		147°	

During the transition from a α- to a β- phase, the atoms in the crystal lattice get moderately displaced relative to each other, without changing their position inside the crystal lattice (preservation of the topology). Due the fact that these α-β transitions are based exclusively on alterations of the angles and the lengths of the chemical bonds, they take place instantaneously. The following table (Table 1.3) lists angles and distances for a set of crystalline silica polymorphs.

Table 1.3 List of most common silica polymorphs, with the indication of Si-O-Si angle and Si-O distance (*Rykart, 1995; [@]Holleman & Wiberg, 1995)

Polymorph	Si-O-Si Angle (°)	Si-O distance (nm)
α-Quartz	144	0.16101*
β-Quartz	153	0.161[@] / 0.1609*
α-Cristobalite	147	0.160 – 0.161[@]
β- Cristobalite	151	0.158 – 0.169[@]
α-Tridymite	ca. 140	0.154 – 0.171[@]
β-Tridymite	180	0.153 – 0.155[@]

Such a phase transition is generally called displacive, as it only requires relative displacements of the atoms, without the need to break chemical bonds. Because the angular Si-O-Si bonds get straightened out, the high-temperature polymorphs are characterized by a higher symmetry, than their low-temperature counterparts.

Fig. 1.2 shows the temperature and pressure conditions where silica polymorphs are stable (phase diagram of silica). It does not contain all natural polymorphs, but only those that are formed starting from pure SiO_2, at certain temperatures and pressures. Moreover, also metastable polymorphs are absent.
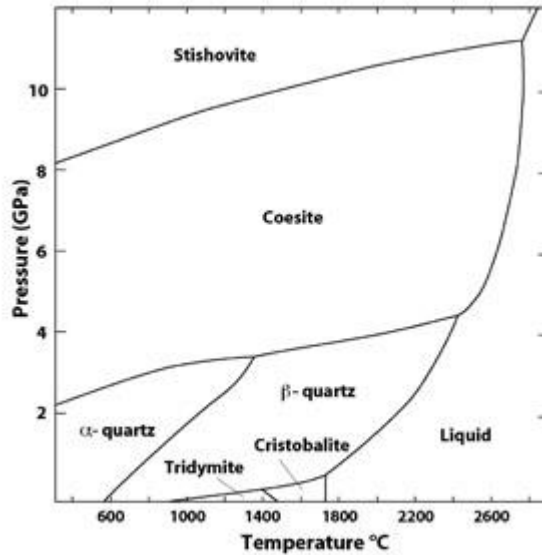
Figure 1.2 Phase diagram of crystalline silica (Koike et al., 2013)

Most of the phase boundaries are inclined to the right. Quartz, for example, will transform into β-quartz at 573°C at normal pressures, but the transition temperature increases quickly with pressure. At a pressure of ca. 2 GPa, β-quartz forms at about 1000°C. The higher temperature increases the vibrations of the atoms, which occupy more space, but the external pressure compresses the crystal lattice and counteracts the effect of temperature. As shows, α-quartz, β-quartz, β-tridymite and β-cristobalite are low pressure polymorphs, while coesite and stishovite are high pressure polymorphs, unstable at normal pressure.

1.2.1 Quartz
Historically, the different quartz varieties were considered as mineral species of their own and were not systematically grouped together before the 19th century. The Swedish chemist Tobern Bergman, at the end of the 18th century, discovered their common chemical nature, and for decades, until 1823, "silica" was considered a chemical element. For a long time, the classification of quartz was mostly based on the visual appearance and the possibility to resolve structural elements in an optical microscope. The classification scheme used today differentiates among crystalline forms, called "macrocrystalline" quartz, and dense and compact forms, "cryptocrystalline" or "microcrystalline" quartz. Macro- and cryptocrystalline quartz forms differ in the growth pathway: macrocrystalline quartz grows by the addition of molecules to the crystal

surface, layer by layer. Cryptocrystalline quartz forms starting from a colloidal watery solution of silica.

Quartz crystals typically grow in hydrothermal reactions, at temperature between 100 and 450°C, and high pressure. In such hydrothermal syntheses, there are no free silica molecules, and quartz crystals grow by the addition of dissolved orthosilicic acid (H_4SiO_4) at their surface, releasing water, layer by layer. The reactive general formula is:

$$[Si_nO_m]\text{-}OH + H_4SiO_4 \rightarrow [Si_{n+1}O_{m+2}]\text{-}OH + 2\ H_2O$$
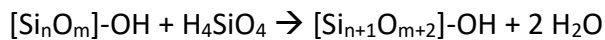
The dissolution of quartz in water is the opposite chemical process, which leads to the formation of orthosilicic acid:

$$SiO_2 + 2H_2O \rightarrow H_4SiO_4$$
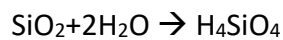
Quartz formation and growth in nature

a. Growth in water solution: in the following figure (Fig. 1.3), the growth process in a water solution is summarized.
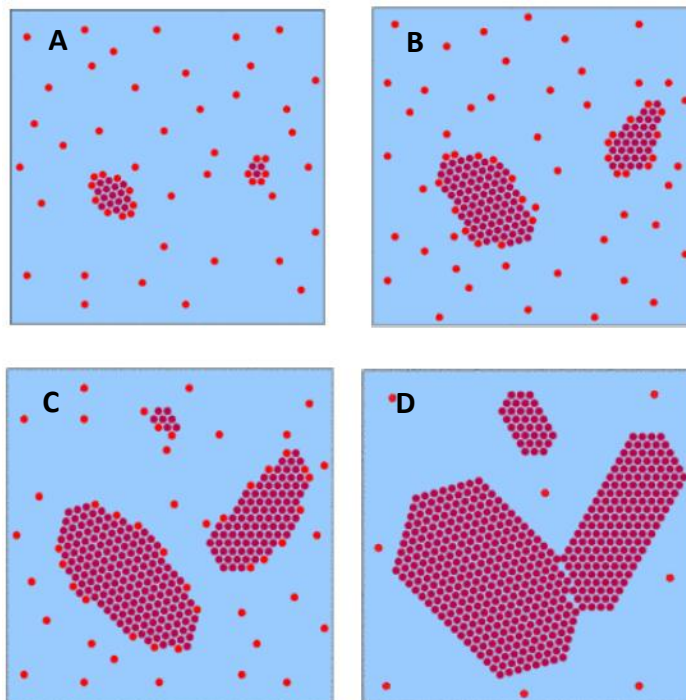
Fig. 1.3 Growth process of quartz crystals in water solution (www.quartzpage.de)

In panel A, individual orthosilicic acid molecules (red dots) in water were dissolved from surrounding rocks. Whether the temperature or the pressure fall, the solubility of silica decreases and the solution will get saturated with respect to quartz. If quartz grains are present in adjacent rocks, the H_4SiO_4 molecules will be added to them and the crystal will grow into the solution. On the contrary, the H_4SiO_4 molecules will aggregate and form floating crystals that will bind other H_4SiO_4 molecules. The spontaneous growth of crystals is only possible in an oversaturated solution. SiO_4 tetrahedrons fully incorporated into the quartz crystal are represented by dark red dots (panel A). In the case of slow temperature and pressure changes, the formation of small crystals does not occur, and only the already present crystals will keep growing, by the addition of SiO_4 tetrahedron sheet by sheet (panel B). In conditions of slow growth, larger crystals are favoured, because the growth is not only the result of the addition of molecules to a crystal, but also the result of both addition and removal of molecules. Molecules are removed from the edges of the crystals, and the relation of the number of edges to the overall volume of the crystal, is not favourable to small crystals. Thus, small crystals growth will be particularly slow, and they may get dissolved again. Nevertheless (panel C), in an unsteady environment, the temperature (or pressure) might fall particularly quickly, and the solution becomes highly oversaturated. Hence, new crystals will form and continue to grow. Then, upon the fall of the temperature, the solubility of silica and the mobility of orthosilicic acid and, consequently, the supply of new molecules, will decrease further and the growth of the crystals could stop (panel D). Because crystals enclose droplets of the surrounding water solution during growth, it is possible to reconstruct the changing environmental conditions.

Fall of temperature/pressure are essential condition for growth of quartz crystals: for example, if hot brines from deeper rocks quickly enters rocks at the surface via cracks, they will cool rapidly. The result is a quick precipitation of silica in the cracks and the formation of massive white vein or gangue quartz. If, however, the water solutions are enclosed in a cavity inside the rocks, the solution will cool just as fast or slow as the host rock. For example, hot magma that intrudes in a rock will heat up its vicinity. Depending on the size of the magmatic body, the cooling of the body and the adjacent rocks, can take hundreds or hundred thousands of years.

Quartz crystals usually do not growth in a continue way, but in short phases (pulsating growth). This kind of growth is sometimes explained with tectonic activity, causing a sudden uplift of the host rock and a relatively fast drop in pressure.

b. Growth in igneous rocks

In magmatic igneous rocks, the mechanism of crystal growth is comparable to that in water solutions. Magmatic rocks are a mixture of metal cations (potassium, K^+, calcium, Ca^{2+}), water, and anions (PO_4^{3-}, SiO_4^{4-}, usually present as chains of SiO_4 tetrahedron).

Depending on the water amount, two different conditions may occur:

```
     O⁻    O⁻    O⁻    OH    O⁻    O⁻    O⁻
     |     |     |     |     |     |     |
...-O-Si-O-Si-O-Si-O-Si-O-Si-O-Si-O-Si-O...
     |     |     |     |     |     |     |
     O⁻    O⁻    OH    O⁻    O⁻    O⁻    O⁻
```

i) low water content

```
     O⁻    OH    O⁻    OH    O⁻    OH    OH
     |     |     |     |     |     |     |
...-O-Si-O-Si-O-Si-O-Si-O-Si-O-Si-O-Si-O...
     |     |     |     |     |     |     |
     OH    OH    OH    O⁻    O⁻    OH    O⁻
```
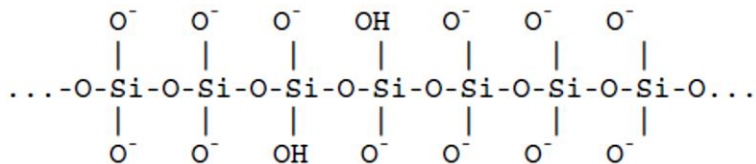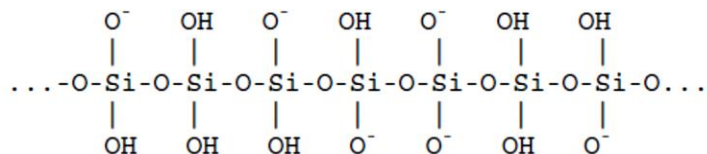
ii) high water content

These flexible species are the cause for the high viscosity of lava, and the more silica a rock contains, the more viscous is its melt. They carry negative charges and hydrogen atoms in hydroxyl groups (-OH), but the relation of [O^-] to [OH] depends on the amount of water dissolved in the magma. When magma cools rapidly (typically after a volcanic eruption), the rupture of the bonds in the SiO_4 and the generation of new bonds in ordered structures of crystallized silicates is prevented. This reaction results in the generation of volcanic glass (e.g. obsidian). On the contrary, when the magma, in certain conditions, cools slowly, crystals of different mineral begin to appear in the melt, in an order determined by the chemical composition of the magma. In granite magma, for example, mica crystals are the first to form, followed by feldspars, and finally quartz. Quartz crystals in igneous rock may show an onion-like internal structure: this indicate a pulsating addition of outer layers to the crystals.

The cryptocrystalline variety of quartz, called chalcedony, is composed of intergrown aggregates of microscopic or sub-microscopic quartz crystals. Such materials, like agate, onyx, and many others, are commonly translucent to opaque.

The following table lists factors that promote or inhibit the formation of macrocrystalline or cryptocrystalline quartz.

Macrocrystalline quartz:

Promoting Factors	Inhibiting Factors
Temperature > 150°C	Temperature < 100°
Low silica concentration in water solution	High silica concentration in water solution
Presence of electrolytes (NaCl, etc.) in water solution	

Cryptocrystalline quartz:

Promoting Factors	Inhibiting Factors
Temperature < 150°C	Temperature > 200°C
High silica concentration in water solution	Presence of electrolytes (NaCl, etc.) in water solution
	Absence of water

However, there is no a clear separation on the conditions that guide crypto- rather than macrocrystalline quartz formation, and, obviously, there is not a single determining factor. Other several factors, like pressure, may also play a key role.

1.3 Amorphous Silica

Amorphous silica differs from crystalline because of the heterogeneous and irregular arrangement of SiO_4 tetrahedrons. Among the different forms of amorphous silica, the most common are vitreous silica, precipitated silica and pyrogenic silica, which have a synthetic origin, and diatomaceous earth, which, on the contrary, has a biogenic nature.

Vitreous silica can be obtained through the rapid solidification of melted quartz. During the heating phase, tetrahedrons move randomly one respect each other. During the cooling phase, which is extremely rapid, tetrahedrons result blocked in random positions, building a disordered and non-crystalline lattice, characterized by the absence of the long-range order typical of crystals. On the contrary, can be found a short-range order (three of four tetrahedrons).

Biogenic silica is a form of silica synthesized by living organisms through a process called "bio-silicification", in which isolated particles, skeletal structures and surface elements are generated.

1.4 Synthesis of silica: state of art

The synthesis of α-quartz crystals in respirable size is not a trivial issue, especially for what concern the systematic control of the particle size and morphology. The understanding of the mechanisms of reactivity of the crystal surfaces of quartz, and how they interact with biological matter, is of great importance in toxicology and occupational safety fields. Unfortunately, due to extreme variability of natural silica, models of particle are needed to unveil these mechanisms.

Currently, several examples of synthetic pathways have been developed, in which physico-chemical properties of synthetic silica depend on the followed procedure. Thus, several methodologies have been developed several to grow silicas with different and tuneable properties, including porosity, crystallinity and size. A general scheme of silica synthesis routes is shown in fig.1.4.
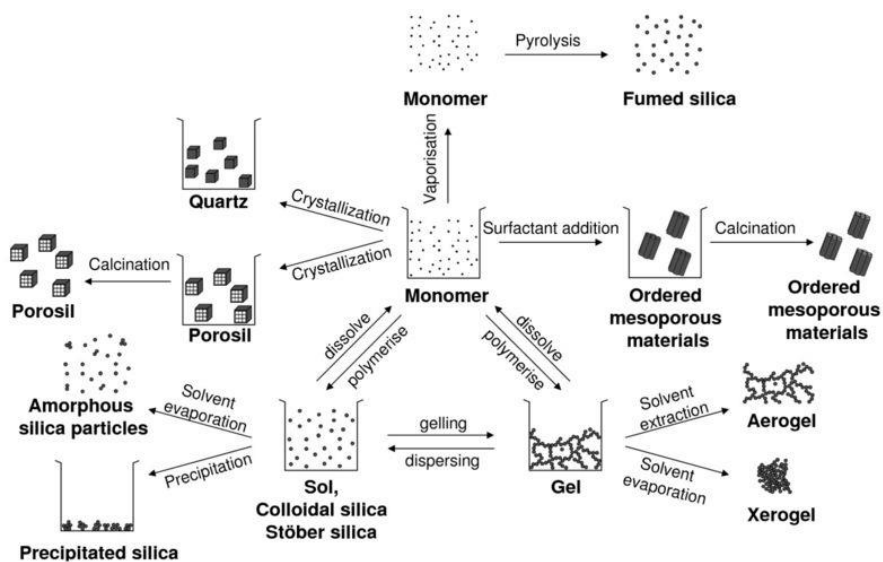
Fig. 1.4 Synthetic methodologies to grow silica particles and gels (Napierska, Thomassen, Lison, Martens, & Hoet, 2010)

Specifically, the synthesis of highly-pure α-quartz crystals, well dispersed and in respirable size has been a very complex subject, on which several works, in different research fields, including toxicology, have been carried out (Brinker,

1988; Carretero-Genevrier et al., 2013; Jiang et al., 2012). Synthesis in solution is not trivial because of the high temperature required and, as a consequence, the subsequent poor chemical stability of templating surfactants. In this context, several synthetic routes, with different advantages and drawbacks, were developed.

One of the most common and popular methodology for the synthesis of micron-sized quartz crystals is represented by the hydrothermal synthetic method. Some decades ago, Hosaka and coworkers developed several techniques based on the hydrothermal growth of crystals in pure water, KCl and NaCl solutions, and through a hot-press method (Hosaka, 1991). Following these methodologies, they were able to synthesize α-quartz microcrystals at high temperature, characterized by defects due to a non-proportional growth of crystal faces, which largely affected the quality of crystals. To date, synthesis in solution continue to be the most convenient available technique, because dry or solvent-free synthetic pathways tend to result in the generation of macro-sized crystals (Sochalski-Kolbus et al., 2015).

The main advantage of sol-gel and hydrothermal synthesis is the possibility to overcome the need of high temperatures, providing the alternative to develop synthetic approach under mild conditions. Through the exploitation of these improvements, De Angelis and colleagues were able to grow highly-pure iron-silicate single crystals (fayalite), developing a synthetic method in which the supersaturation of a mixed solution produces a precursor gel, upon the addition of a crystallizing reagent in a soluble state supersaturates a solution (DeAngelis, Rondinone, Pawel, Labotka, & Anovitz, 2012) In hydrothermal synthesis, it is very common the use of a mineralizer, which affects the size and morphology of resulting crystals (Lee, Seo, Yu & Mok, 1996). Unfortunately, in this case the synthesis is extremely complicated, due to the tendency of the material to form cristobalite or keatite, and not pure quartz.

Recently, several hydrothermal synthetic methods have been developed. The main challenge is speeding up nucleation rates but, at the same time, reducing crystals growth. This would allow to tune size distribution and modulate crystal morphology. However, these conditions are extremely difficult to reach for quartz synthesis, because of the naturally high rate of crystal growth.

In this sense, Brinker and coworkers (Jiang, Jiang, & Brinker, 2011), developed a method for the synthesis of nanospheres of α-quartz, using Stober silica colloids as precursor, and using NaCl and alkaline hydroxides as mineralizators. Through this technique, which uses lower temperature and pressure, they tried to overcome the issue of the crystal size and shape control, typical for hydrothermal synthesis.

1.5 Surface chemistry, crystallinity and variability of quartz hazard

Prolonged and continuative exposure to silica dusts may induce severe diseases, including autoimmune diseases, silicosis and lung cancer. Lung cancer is associated with occupational exposure to crystalline silica, but not all forms of crystalline silica are equally suspected to act as carcinogen. IARC (International Agency for Research on Cancer) stated that carcinogenicity may be dependent on inherent characteristics of the crystalline silica, or on external factors that affect its biological activity (IARC, 2012; Fubini, 1998). These characteristics, regarding the state of the external surface, are determined by the origin of the sample, while external factors indicate the contact, association or contamination by impurities that might activate silica carcinogenicity. What is common among the occurrence of diseases associated to crystalline silica exposure is that crystals were ground and fractured. Recently, new cases of silica-related malignancies were highlighted, and all of them presented scenarios in which workers were exposed to fractured silica dusts, e.g. denim sandblasting, artificial stone processing, and hydraulic fracturing.

Several studies showed that crystalline silica particles have a strong pathogenic potential toward cells (Kawasaki, 2015). Nevertheless, it has been evidenced an extreme variability in the biological responses among different sources of particulate silica (Pavan & Fubini, 2017). Such variability, however, is the consequence of the intrinsic variability of silica as a solid, which in turn is related to the particular nature of the Si-O-Si bond. The Si-O bond is covalent, with a polar character: this effect results in two possible cleavages (Fubini, 1998): a homolytic fracture, which results in the generation of two highly reactive radical species (dangling bonds, $\equiv Si^\bullet$ and $\equiv Si\text{-}O^\bullet$), or a heterolytic fracture, which generates a positive charge on Si and a negative one on oxygen (Si^+ and $Si\text{-}O^-$). All these species promptly react with atmospheric water during post-fracturing surface reconstruction and yield surface silanol ($\equiv Si\text{-}OH$) groups. Ideal silica surface present also arrays of polar Si-O-Si bonds (siloxane bridges) that, in the presence of water, tend to react and form two silanols ($\equiv Si\text{-}OH$) (Fubini et al., 1993). The opposite reaction might occur upon heating (Bolis et al., 1991) (Fig. 1.5): the condensation process can also result in the generation of siloxane rings $(SiO)_n$.
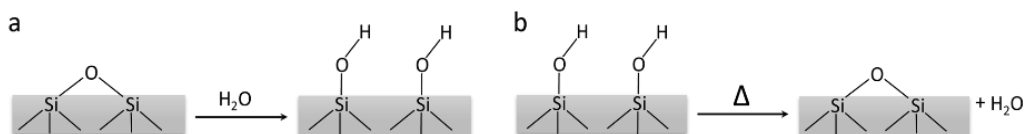
Fig. 1.5 Formation of Si-OH groups upon siloxane ring opening (panel a) and the opposite reaction (panel b), condensation of silanols into siloxanes upon heating. (Pavan & Fubini, 2017)

Silica surfaces are characterized by several coexisting families of ≡SiOH groups, which, in some cases, are able to mutually interact through H-bond (Rimola et al., 2012). The various families are classified for the inter-distance between two silanols: in isolated silanols, the distance between two SiOH groups is too large to let them establish mutual interactions (> ca. 3.3 Å). In geminal silanols, two - OH groups are linked to the same Si atom, that cannot be involved in mutual H-bonding because of the –OH orientations. Vicinal silanols, which are separated by less than 3 Å, are usually not able to interact by H-bonding, or, as consequence of local geometrical constrains, are able to experiment weakly H-bonding.

The isolated and geminal groups are thus free to establish H-bond interactions with external molecules, acting as H-bond donor or acceptor, but only if placed in the right position, because of the strong directional nature of H-bonding. Two silanols that do not belong to directly connected tetrahedron (as the vicinal ones) or the same tetrahedron (as the germinal ones), but nonetheless are closer than 3.3 Å will estabilish H-bonding, are called interacting or H-bonded (Pavan & Fubini, 2017) (Fig. 1.6).
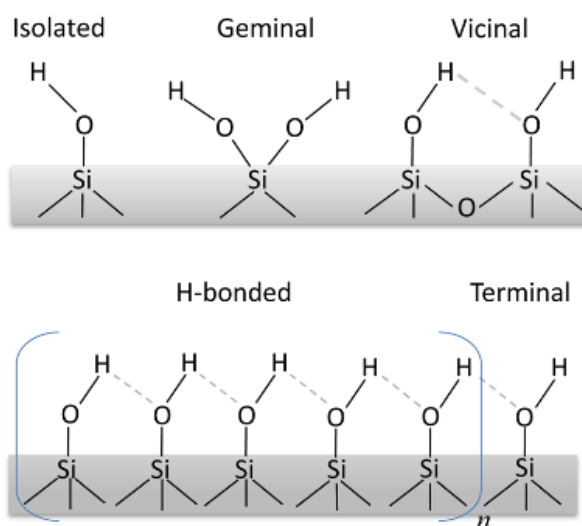
Fig. 1.6 Different silanol families (high) and H-bonding patterns (low) on a silica surface (Pavan & Fubini, 2017)

Surface distribution of silanols and siloxanes varies among different sources of silica particles. Silanol patterns on a silica surface give rise to specific FTIR spectra. A typical spectrum of a pyrolytic sample is shown in Fig. 1.7 (Pavan & Fubini, 2017): the peak at 3747 cm^{-1} belongs to isolated or geminal silanols,

which through this technique cannot be distinguished. The intermediate band (3720-3600 cm^{-1}) is associated to weak H-bonding -SiOH, while the broad band at 3600-3000 cm^{-1} is ascribable to SiOH interacting through strong H-bonding (Catalano et al., 2015).
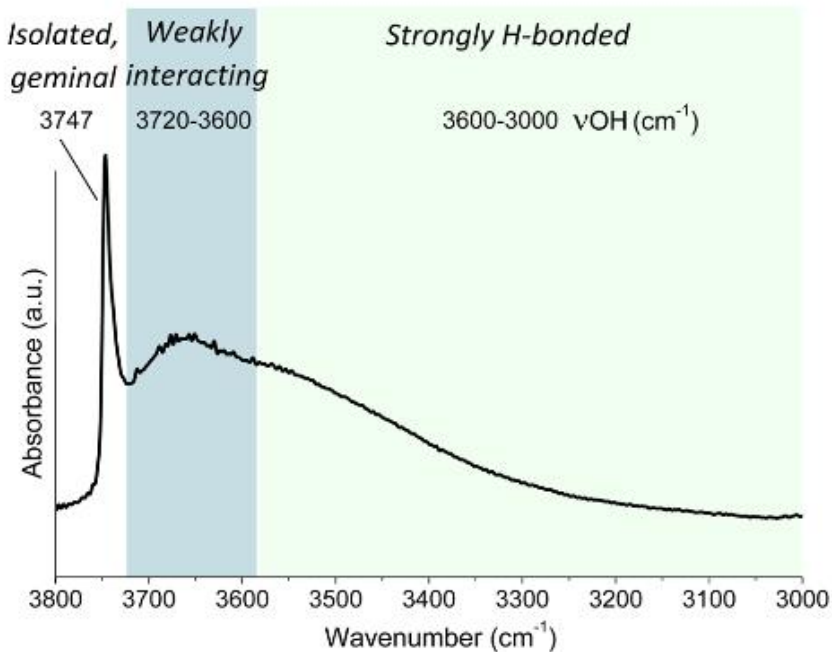
Fig 1.7 FTIR pattern in the hydroxyl spectral region (3800-3000 cm-1) of a pyrolytic silica, where it is appreciable the distinction of isolated or geminal silanols, silanols interacting via Van der Waals or weak H-bonding, and silanols interacting via strong H-bonding. (Pavan & Fubini, 2017)

Siloxanes and isolated silanols impart hydrophobic character to the surface, while other families impart hydrophobicity (Bolis et al., 1991). Any silica surface shows hydrophilic and hydrophobic patches, whose distribution is characteristic of that specific sample and its thermal history. This aspect must be taken in particular account in the interaction with biomatter, including peptides and proteins.

1.6 Physico-chemical properties imparting variability to silica toxicity

Notwithstanding, more than 50 years ago, it was already clear that several cells and mediators were involved in the damage of the lung tissue in silica-related pathologies, including silicosis and bronchogenic carcinoma, the physico-chemical features of crystalline silica responsible for those adverse outcomes were unknown. Pioneering studies (King et al., 1953; Vigliani et al., 1948) indicated a possible role of silica chemistry as main factor of toxicity, focusing the attention on the definition of one single key-property. Later, not just one, but a series of physico-chemical properties (listed below), with a particular attention devoted to the surface properties, were indicated as crucial in the determination of the toxic activity of silica.

1.6.1 Bulk features:

- *Crystal structure*, specifically the difference between ordered (crystalline silica) or irregular (amorphous silica) arrangement of the SiO_4 tetrahedron, which give also rise to the different crystalline polymorphs.

- *Size and morphology*, strictly dependent on particle origin. Pathogenic fractured dusts show irregular surfaces, kinks and edges. Their crystals are characterized by a polydisperded size, from micron-sized particles to nanometric fragments (B. Fubini, 1998). On the contrary, amorphous particles usually show smooth surfaces and spherical morphologies (Napierska et al., 2010).

1.6.2 Surface features:

- *ROS and surface radicals*, generated during mechanical fracturing of macro-sized crystals to obtain a crystalline silica dust. In the process, the homolytic or heterolytic cleavage of Si-O bonds results in the generation of highly-reactive surface radicals with an unpaired electron in a p orbital (Si$^{\bullet}$ and SiO$^{\bullet}$) and surface charges (Si$^+$ and SiO$^-$) (Fubini, Bolis, Cavenago, & Volante, 1995; Fubini, Giamello, Volante, & Bolis, 1990). Upon Si-O bond breaking, surface reconstruction occurs and dangling bonds tend to recombine in order to form strained reactive Si-O rings (Rimola et al., 2013), or to react with atmospheric components, generating reactive oxygen species (ROS), including hydroxyl radicals, superoxide anion and peroxides. These species are known to be extremely reactive and, thus, responsible for some steps of the pathogenic activity of silica (Donaldson & Borm, 1998; Shi et al., 2001; Shi, Dalai, Hu, & Vallyathan, 1989).

- *Silanol and siloxane groups,* associated to the degree of surface hydrophylicity, as above mentioned (Bolis, Fubini, Marchese, Martra, & Costa, 1991). The hydrophobic/hydrophilic behaviour of the surface is one of the main determinant in silica toxicity (Hemenway et al., 1994; Marucco et al., 2014; Pandurangi, Seehra, Razzaboni, & Bolsaitis, 1990).

- *Surface charge*, originated as the consequence of heterolytic rupture of Si-O bonds or through the deprotonation of surface silanols when silica particles are dispersed in an aqueous medium (Kosmulski & Matijević, 1992). Surface silanols can be treated as weak monoprotic Brönsted acids, following the equilibrium:

$$\equiv SiOH + H_2O \rightleftarrows \equiv Si\text{-}O^- + H_3O^+$$

Consequently, in an alkaline environment (pH > 7), most of the silanols will be dissociated (Si-O$^-$, silanolate), imparting to silica surface a net negative charge. As the pH become more acid, the protonated form will be favored, thus the overall net charge increases. At strong acidic pH, all silanols will be in the protonated form, and the quartz ZPC (zero point charge) will be reached. The surface charge received a particular attention only upon the increased utilization of nanomaterials, due their eventual interaction with biomolecules (Luyts, Napierska, Nemery, & Hoet, 2013). It is known that the protein layer adsorbed on particle surface, the so-called *protein corona*, may indeed alter particle recognition, uptake, and cytotoxicity (Ge et al., 2015; Lesniak et al., 2012; Liu, Wu, Chen, Chou, & Chen, 2015; Lundqvist et al., 2008; A. E. Nel et al., 2009; Walczyk, Bombelli, Monopoli, Lynch, & Dawson, 2010; Wang et al., 2013).

- *Metal ions and contaminants*, as substituting for Si in the [SiO$_4$] framework, such as Al^{3+} or Fe^{3+}, or impurities adsorbed on silica surface, including Al^{3+}, Fe^{2+}, Fe^{3+}, Cu^{2+}, are often present in mineral silica dusts (IARC, 1997). Overall, Al and Fe are the most present, because their particular charge/radius ratio, and the geometrical features of the surface oxygen groups (Nolan, Langer, Harington, Oster, & Selikoff, 1981). They also can substitute for Si in the tetrahedron framework. Of course, the reactivity of silica is strongly modified in presence of contaminants: reduction of membranolysis and in-vivo toxicity (Le Bouffant, Daniel, & Martin, 1975; Kriegseis et al., 1987) was evidenced for Al-doped quartz, while Fe-doped specimen are able to trigger ROS generation, enhancing DNA damage, cancerogenesis and pulmonary reactions (Castranova et al., 1997). In some cases, quartz crystals with Fe deposited on their surface showed a decrease in cytotoxicity and inflammatory responses in AM (Ghiazza et al., 2011).

1.7 Overview of silica pathogenicity: state of the art

Pioneering studies, carried out in the '50s, suggested the possible role of surface chemistry as crucial parameters in determining the toxicity of silica (King et al., 1953a; King et al., 1953b; Vigliani & Mottura, 1948). Crystallinity was believed to be responsible, because absent in amorphous silica, considered less harmful than quartz. Later, because of its role in the direct contact with cells and tissue, a central role in the silica pathogenicity was recognized to the particle surface. Several methodologies developed to decrease and modulate cellular responses, consisted in the modification or covering the particle surface in many different ways, including etching with HF, aluminium lactate, and polymer deposition (Daniel et al., 1995; Duffin et al., 2001; Fubini et al., 2004). More recently, it became clear that a cluster of properties, including particle shape and size (I Fenoglio, Fubini, Tiozzo, & Di Renzo, 2000; Wiessner, Mandel, Sohnle, & Mandel, 1989), free radical release (Dalal, Shi, & Vallyathan, 1990; Schins et al., 2002; Vallyathan, Shi, Dalal, Irr, & Castranova, 1988), the degree of hydrophilicity (Hemenway et al., 1994), were contemporarily involved in in-vitro and in-vivo adverse effects of silica. Thanks to the investigation of several cellular endpoints carried out on different sets of crystalline silica samples, characterized by a large range of toxic activity, researches clarified that the mechanism of toxicity is not only complicated by the occurrence of several biochemical events contributing to pathogenicity, but also by the various silica features, associated with each one of those events (Bruch et al., 2004; Cakmak et al., 2004).

Taken together, data allowed to propose a model of silica pathogenicity, summarized in Fig. 1.5.
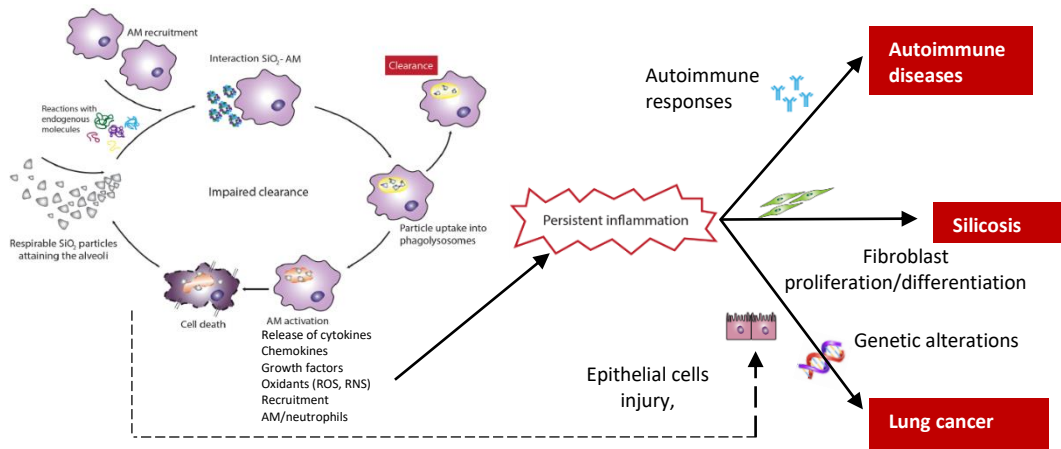
Fig. 1.5 Proposed mechanism of toxicity of silica particles attaining the alveolar space. Particles may directly stress the epithelium or engulf alveolar macrophages. Phagocytosis may result in particle clearance or macrophage activation, followed by the prolonged recruitment of AMs and a condition of persistent inflammation, which might degenerate into the development of autoimmune diseases, silicosis or lung cancer. (Pavan & Fubini, 2017; IARC Monograph Vol. 100, 2012)

In the proposed model, the inhaled silica particles attaining the alveolar space, upon reaction and coverage with endogenous molecules (proteins and surfactants), are recognized and phagocytated by alveolar macrophages (AMs) into a phagosome. Phagosome fuses with lysosome to form a phagolysosome and particle clearance by AM should occur. The clearance is unimpaired while the silica burden remains below a critical level, or can be successful only with few silica samples. This is a crucial point, where the responsible molecular mechanisms, also related to silica properties, are still not well defined. Once the critical level is reached further, clearance becomes impaired, and an inflammatory reaction take place, through the activation of AM. Eventually, the direct interaction of particles with the phagolysosomal membrane will result in AM stress, with consequent induction of pro-inflammatory and cell death pathways. The deposition of non-cleared particles onto the alveolar epithelium will cause the recruitment and the activation of new macrophages and neutrophils, in a circular detrimental process which gives rise to a persistent inflammation as long as the particles remain in the alveolar space. The sustained

inflammation, in turn, might result in fibroblast stimulation and growth, fibrosis and abnormal collagen synthesis. The following cascade of events may induce the development of several diseases, including bronchogenic carcinoma. A direct damage of particles to the epithelium, which of course may induce further damage, was also hypothesized (Donaldson & Borm, 1998; Fubini, 1998; Fubini & Hubbard, 2003; Hamilton, Thakur, & Holian, 2008; Knaapen, Borm, Albrecht, & Schins, 2004; Sayan & Mossman, 2016; Schins, 2002; Wynn, 2011).

In the present mechanism, each step is ruled by specific features of (crystalline) silica particles. To date, the goal to associate a given physico-chemical property with a specific toxic/inflammatory step, is far to be accomplished. Considering the recent physico-chemical and biochemical results (Ankley et al., 2010), a model for silica inflammogenicity was proposed (Fig. 1.6).
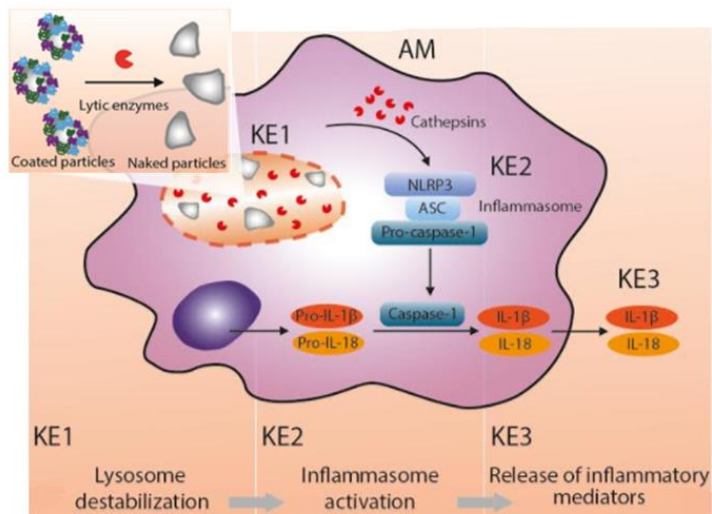
Fig. 1.6 proposed model for silica induced inflammogenicity. The destabilization of the phagolysosomal membrane due to direct interaction with silica particles (KE1) results in the release of the phagolysosomal content into the cytosol and the consequent activation of the inflammasome machinery (KE2). This event triggers the activation of the proteolytic enzyme Caspase-1 and release of active pro-inflammatory cytokines. (Pavan & Fubini, 2017)

In this model, the particular event recognized to be as crucial towards the development of an inflammatory response, is the destabilization of the phagolysosomal membrane of alveolar macrophages and the consequent release of the phagolysosome content into the cytosol. The latter event triggers the activation of the inflammasome machinery through an extremely complex process. When endocytosed, nano- and micrometric particles can induce

lysosomal modifications and interfere with autophagy/mitophagy (selective degradation of mitochondria by autophagy), resulting in the release of ROS, cathepsins or calcium in the cytosol (Rabolli, Lison, & Huaux, 2015). These events promote the assembly of inflammasome components and subsequent IL-1β and IL-18 release, resulting in a sustained inflammatory response in the lungs. In this view, while the *in vivo* interaction with the plasma membrane is known to be mediated by the protein corona adsorbed on the particle surface (Mortensen et al., 2013), which is then digested upon internalization in the phagolysosome (Wang et al., 2013), a still unanswered question is how the naked silica surface can interact, and possibly disrupt, the inner surface of the phagolysosome membrane. Several hypotheses have been presented (Fubini, 1998), but a unique answer is yet to be found.

1.8 Membrane models as useful tool to understand particles-cell membrane interaction

Over the past two decades, the need to fill the gap concerning the understanding of particles and nanoparticles behavior upon contact with biological media and cell membrane, led to the strong development of the synthesis of biomimetic membrane models, which represent a very interesting tool to move towards the comprehension of the mechanisms that guide the interactions between (nano)particles and cells. Nanomaterial scale confers particular physico-chemical properties (optical, magnetic, catalytic, thermal, *etc.*) to materials: the surface to volume ratio is extremely high, and this results in a higher surface reactivity (Oberdorster et al., 2005). Such properties, together with surface features (see paragraph 1.6), govern the biological responses and toxic effects of the particles. The main toxic effects of (nano)particles are linked to their interactions with cellular components, such as the plasma membrane, cytoplasmic organelles, or macromolecules (nucleic acids, proteins, *etc.*) (Lewinski, Colvin, & Drezek, 2008). In this context, membrane models provide the right answer to overcome the extreme complexity of biological systems (Beddoes, Case, & Briscoe, 2015). Membrane models are simplified systems, in which almost all physical and chemical parameters may be tuned. Their main purpose is the systematic evaluation and characterization of the relationship between (nano)particles and membrane and their eventual disruption upon the interaction (Chen & Bothun, 2014). To date, three main types of membrane models are relevant to interaction studies: lipid vesicles (liposomes), planar lipid models and, more recently, computational models (Rascol, Devoisselle, & Chopineau, 2016). Each of these different models provides several and complementary data, contributing to the comprehension of the relationship between particle physico-chemical properties, and toxic effects (Fig. 1.7).
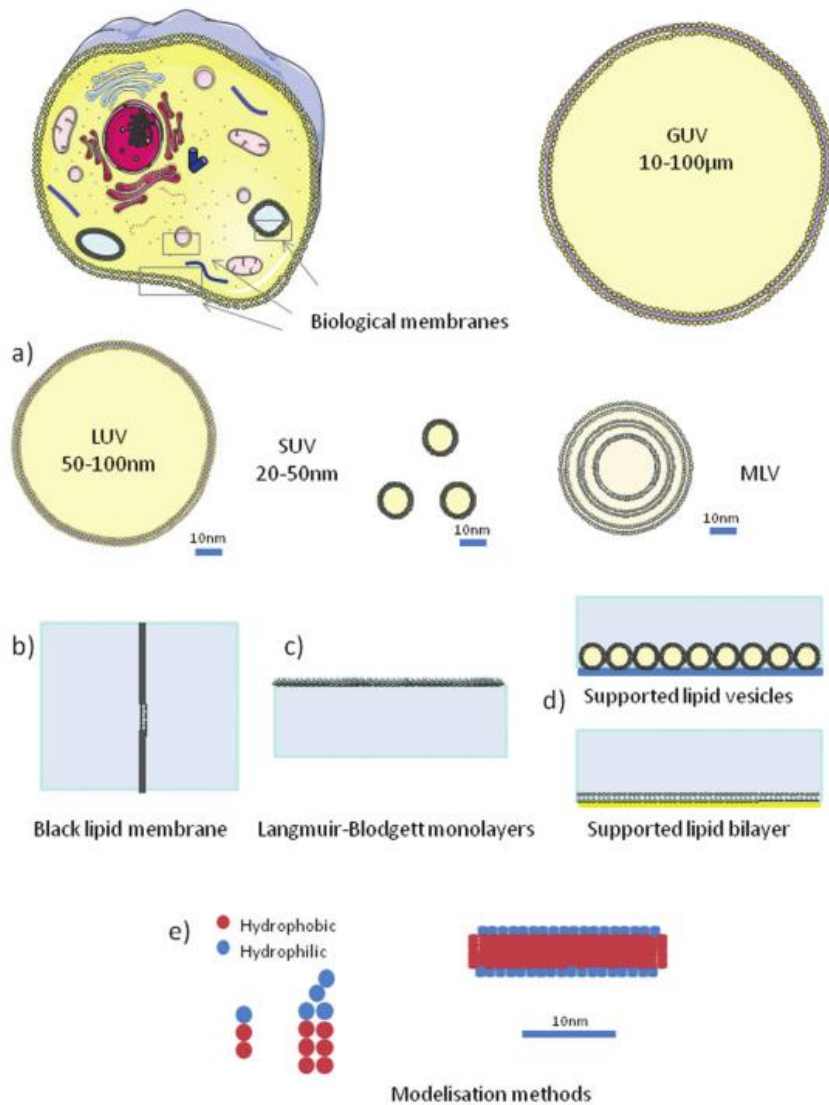
Fig. 1.7 Most used artificial membrane models to evaluate the particle-biomembrane interaction. It is evident the strong evolution of models, from vesicles at extreme low complexity (a), to supported bilayers (b, c, d), which can exist in several forms, concluding with more recent computational models (e). (Rascol, Devoisselle, & Chopineau, 2016)

Liposomes, which are spherical lipid vesicles composed of a bilayer separating two aqueous compartments, represent the most famous biomembrane model. Its particular structure gives the possibility to load hydrophilic compounds inside the aqueous pocket, or hydrophobic molecules into the lipid bilayer. Liposomes can be unilamellar (one bilayer) or multilamellar (multiple bilayers), small (Small Unilamellar Vesicles, SUV, 50 nm), large (Large Unilamellar Vesicles, LUV, 50-100 nm) and giant (Giant Unilamellar Vesicles, GUV, 10-100 µm) (Roiter et al., 2009). Since they are particular easy to handle, and suitable for different techniques (microscopy, fluorescence, surface-sensitive techniques, *etc.*), liposomes are convenient tool to investigate the role of membrane lipids upon the interaction of particles with biological membrane. Visualization of the interaction is possible to be observed, through the use of a particular electron microscopy techniques (cryoTEM), which allows the real-time monitoring of changes in the vesicle morphology in response to pressure changes, due to the attachment of particles to the surface (Le Bihan et al., 2009; Strobl et al., 2014). A simpler method to evaluate liposome-particle interaction, is the dye-leakage assay (Weinstein, Yoshikami, Henkart, Blumenthal, & Hagins, 1977): in this method, a hydrophilic molecular probe (e.g. calcein, a self-quenching fluorescent dye) is encapsulated inside the internal aqueous pocket. After the interaction with particles, perturbations on the membrane can occur, resulting in the leakage of the probe from the liposome. This assay was used for the first time in 2004, to evaluate the interaction between biomembrane and gold nanoparticles (Goodman, McCusker, Yilmaz, & Rotello, 2004). Similar assays are based on the fluorescent recovery after photobleaching (FRAP), which are techniques that exploit the bleaching of fluorescent molecules when exposed to white light (Deschout, Raemdonck, Demeester, De Smedt, & Braeckmans, 2014), often associated to confocal microscopy. This technique allows the determination of lateral mobility of lipids and their diffusion coefficients that represent fundamental parameters of biomembrane stability. Confocal studies are very promising for investigating the fate of particles upon interaction: Laurencin and coworkers (Laurencin, Georgelin, Malezieux, Siaugue, & Ménager, 2010), varying the membrane composition, evaluated the interaction with differently charged lipids, obtaining crucial information on particle localization, binding or internalization in vesicles. Same technique was followed by Zhang et al (S. Zhang, Nelson, & Beales, 2012), to understand the impact of particle size in the interaction. They concluded that small nanoparticles (< 20 nm) are able to absorb on the vesicle surface, inducing leakage and generation of pores in the bilayer, while the interaction with bigger particles (> 150 nm) resulted in membrane wrapping.
Moreover, using liposomes, Pera and colleagues (Pera, Nolte, Leermakers, & Kleijn, 2014a) were able to evaluate of the role of electrostatic attraction

between particles and biomembrane, through the contact of silica and titanium oxide nanoparticles with various charged DOPC/DOPG liposomes.

More recently, other biomembrane models have been developed. An example, as above mentioned, is represented by supported lipid bilayers (SLB), which are planar membranes synthesized on the top of a solid support (gold, silver, quartz, glass, silicon, *etc.*), whose nature depends on the analytical method used to measure the particle-membrane interaction (Rossi & Chopineau, 2007). SLBs are often used to evaluate the direct interaction with particles, which can be measured through several techniques, including SPE (surface plasmon resonance), QCM (quartz crystal microbalance) and AFM (Atomic force microscopy). SPR is associated to the plasmonic properties of a noble metal. This technique is often used to investigate specific and direct interactions between particle and membrane (Giess, Friedrich, Heberle, Naumann, & Knoll, 2004), while structural/morphological changes of the lipid bilayer (i.e. wrapping, pores generation, membrane thinning and disruption) upon the contact with particles are well evidenced through AFM and QCM. These methodologies can also be combined in order to investigate the passive insertion of particles inside the membrane (Frost, Jönsson, Chakarov, Svedhem, & Kasemo, 2012; Leroueil et al., 2008). A particular type of lipid bilayer was developed to perform electrical measurements and registration of ionic fluxes, which can be carried out through the use of Black Lipid Membrane models (BLM). The BLM setup (Mueller, Rudin, Ti Tien, & Wescott, 1962) consists of a lipid bilayer which separates two compartments, containing an electrolytic solution in which electrodes are plunged. This methodology, developed by Ramachandran and coworkers (Ramachandran, Merrill, Blick, & Van Der Weide, 2005), is suitable to detect nanoparticles-membrane interactions, and then translate into electrical events. Authors evaluated the interaction of biomembranes with CdSe quantum dots (QD) and concluded that aggregation of QD and their attachment to the membrane resulted in the generation of nanopores, allowing a flow of ionic and zwitterionic molecular species. The extreme advantage of BLM model is the strong correlation of the results with *in cellulo* assays (Tao, Toms, Goodisman, & Asefa, 2009), evidencing the possibility to use this method as a predictive assay to test toxicity of particles on cells.

Last but not least, in the last few years, a strong development of computational modeling of the interaction occurred. The method provides an efficient confirmation of experimental results. Particular assays, i.e. those concerning the dynamic rearrangement of ligands on the surface of (nano)particles (Van Lehn & Alexander-Katz, 2011) or the obtainment of mechanistic data regarding NPs-biomembrane interaction, can be performed from simulation experiments, in which each parameter of the system (including lipid charge, composition, particle size, surface chemistry, *etc.*) is controlled (Nangia & Sureshkumar, 2012).

However, it is advisable, and also interesting, to combine computational methods with experimental assays, using the same nano-bio interface system. Biomembrane models are particularly useful when the physico-chemical features of particles are not directly related to a pathogenic process, because of the extreme complexity not only of cellular models, but also of the surface state of the solid material (silica, in our case). Thus, the adoption of a reproducible model of interaction is crucial. Due to the fact that the cell membrane is the first site of the interaction of particles with cells, the role of plasma membrane and phagolysosome membrane damage in toxicity mechanism of silica has been considered since a long time (Allison, 1966; Nash, Allison, & Harington, 1966). Red blood cells (RBC) represent a well-assessed and robust model to specifically test membranolytic activity of a particle, because RBCs are not able to actively phagocytize external matter. RBC lysis, although is not directly involved in the pathogenesis of silicosis or lung cancer induced by silica, can be considered as a robust proxy for the cytotoxicity of mineral particles (Nolan, Langer, Harington, Oster & Selikoff, 1981; Summerton & Hoenig, 1977; Depasse, 1980) and, in some specific cases, the evaluation of hemolytic activity can be considered a very efficient predictive test of the inflammatory response induced by silica and inorganic particulates in general. Thus, red blood cell and artificial biomimetic membrane models, characterized by a different chemical-physical and structural complexity, represent particularly suitable methodologies to fill the existing knowledge gap between the interaction with plasmamembrane and the biological responses (Alkhammash, Li, Berthier, & de Planque, 2015; Kettiger, Québatte, Perrone, & Huwyler, 2016; Murray, Harrison, & Wallace, 2005). Moreover, focusing the attention on the surface features which impart to silica particles the potential to disrupts membranes. Biomembrane models can represent a convenient and helpful tool to clarify the association between particle surface features and cell inflammation.

1.9 Aim of the work

Occupational exposure to crystalline silica dust in respirable size, particular in the form of α-quartz, is associated to the development of severe diseases, including lung cancer. In the last 20 years, researchers demonstrated the specific role of silica surface in triggering several adverse biological outcomes, modulated by an extremely high physico-chemical variability.

Such a variability reflects in the biological response to silica: strong differences in pathogenic activity among different silica sources and polymorphs. Moreover, the multiple cellular mechanisms involved in silica pathogenicity make the system particularly intricate and difficult to be fully understood. In view of that, because of the intrinsic complexity of the interaction between inorganic silica and biological systems, particle and cell membrane simple models are required to achieve fundamental insights into the molecular mechanisms involved.

The main aim of this work is to provide advances in the understanding of the molecular mechanisms involved in the silica-membrane interaction. To achieve this ambitious goal, robust and reliable models are needed to simplify the complexity. Since silica dusts used in toxicology investigations derive from the mechanical fracturing of natural larger crystals and are always characterized by particularly variable surface chemistry, the first objective of this PhD project was the development of an efficient synthetic method for obtaining a model for crystalline silica, specifically α-quartz crystals in respirable size, with tuneable and controlled bulk and surface properties.

A second objective was aimed at the development of protocols for obtaining biomembrane models at increasing complexity. Specifically, we focussed on artificial lipid vesicles (liposomes) and human red blood cells (RBC). Liposomes represent a well-known membrane models used to understand particle-cell membrane interaction. Liposomes are particularly easy to handle and suitable for different techniques, allowing the obtainment of good qualitative data. Red blood cells, which represent a more complex system, have been typically employed as a model to investigate the membranolytic activity of particulates, due to its specific role in triggering adverse effects of silica.

The third objective was the translation of membrano-perturbative data obtained with membrane models to cellular toxicity, through the investigation of several toxicity endpoints elicited by our tailored quartz samples on macrophage cell lines.

Summarizing, the aim of this thesis was the **chemical investigation of the molecular determinants that modulate the interaction between silica surfaces and biomembranes**. In this view, the work was divided in three sub-objectives:

1. The development of a **synthetic protocol** for the obtainment of surface-tailored quartz crystals

2. The development of protocols for investigating **biomembrane models** at increasing complexity, in order to evaluate:

    i) the role of **crystallinity** in the pathogenicity of silica particles
    ii) the role of **surface features** and **geometry** in defining the interaction

3. The investigation of whether, and how, differences in surface chemical properties among several quartz models affect eventual **cellular toxicity**

Bibliography

Alkhammash, H. I., Li, N., Berthier, R., & de Pla2nque, M. R. R. (2015). Native silica nanoparticles are powerful membrane disruptors. *Physical Chemistry Chemical Physics : PCCP*, *17*(24), 15547–60. https://doi.org/10.1039/c4cp05882h

Allison, A. C. (1966). An examination of the cytotoxic effects of silica on macrophages. *Journal of Experimental Medicine*, *124*(2), 141–154. https://doi.org/10.1084/jem.124.2.141

Ankley, G. T., Bennett, R. S., Erickson, R. J., Hoff, D. J., Hornung, M. W., Johnson, R. D., … Villeneuve, D. L. (2010). Adverse outcome pathways: A conceptual framework to support ecotoxicology research and risk assessment. *Environmental Toxicology and Chemistry*. https://doi.org/10.1002/etc.34

Beddoes, C. M., Case, C. P., & Briscoe, W. H. (2015). Understanding nanoparticle cellular entry: A physicochemical perspective. *Advances in Colloid and Interface Science*. https://doi.org/10.1016/j.cis.2015.01.007

Bolis, V., Fubini, B., Marchese, L., Martra, G., & Costa, D. (1991). Hydrophilic and hydrophobic sites on dehydrated crystalline and amorphous silicas. *Journal of the Chemical Society, Faraday Transactions*, *87*(3), 497. https://doi.org/10.1039/ft9918700497

Brinker, C. J. (1988). Hydrolysis and condensation of silicates: Effects on structure. *Journal of Non-Crystalline Solids*, *100*(1–3), 31–50. https://doi.org/10.1016/0022-3093(88)90005-1

Bruch, J., Rehn, S., Rehn, B., Borm, P.J.A., & Fubini, B. (2004). Variation of biological responses to different respirable quartz flours determined by a vector model. *International Journal of Hygiene and Environmental Health* 207, 203-216

Cakmak, G.D., Schins, R.P., Shi, T., Fenoglio, I., Fubini, B., & Borm, P.J. (2004). In vitro genotoxicity assessment of commercial quartz flours in comparison to standard DQ12 quartz. *International Journal of Hygiene and Environmental Health 207*, 105-113

Carretero-Genevrier, A., Gich, M., Picas, L., Gazquez, J., Drisko, G. L., Boissiere, C., Sanchez, C. (2013). Soft-Chemistry-Based Routes to Epitaxial α-Quartz Thin Films with Tunable Textures. *Science*, *340*(6134), 827–831. https://doi.org/10.1126/science.1232968

Castranova, V., Vallyathan, V., Ramsey, D. M., McLaurin, J. L., Pack, D., Leonard, S., Teass, A. (1997). Augmentation of pulmonary reactions to quartz inhalation by trace amounts of iron-containing particles. *Environmental Health Perspectives*, *105 Suppl 5*, 1319–1324. https://doi.org/10.2307/3433554

Catalano, F., Alberto, G., Ivanchenko, P., Dovbeshko, G., and Martra, G. (2015) Effect of silica surface properties on the formation of multilayer or submonolayer protein hard corona: Albumin adsorption on pyrolytic and colloidal SiO$_2$ nanoparticles. *J. Phys.Chem. C* 119, 26493-26505). https://doi.org/10.1021/acs.jpcc.5b07764

Chen, K. L., & Bothun, G. D. (2014). Nanoparticles meet cell membranes: Probing nonspecific interactions using model membranes. *Environmental Science and Technology*, *48*(2), 873–880. https://doi.org/10.1021/es403864v

Dalal, N. S., Shi, X. L., & Vallyathan, V. (1990). ESR spin trapping and cytotoxicity investigations of freshly fractured quartz: mechanism of acute silicosis. *Free Radic Res Commun*, *9*(3–6), 259–266. https://doi.org/10.3109/10715769009145684

Daniel, L. N., Mao, Y., Wang, T. C., Markey, C. J., Markey, S. P., Shi, X., & Saffiotti, U. (1995). DNA strand breakage, thymine glycol production, and hydroxyl radical generation induced by different samples of crystalline silica in vitro. *Environ Res*, *71*(196357199), 60–73. https://doi.org/10.1006/enrs.1995.1068

DeAngelis, M. T., Rondinone, A. J., Pawel, M. D., Labotka, T. C., & Anovitz, L. M. (2012). Sol-gel synthesis of nanocrystalline fayalite (Fe 2SiO 4). *American Mineralogist*, *97*(4), 653–656. https://doi.org/10.2138/am.2012.3899

Deschout, H., Raemdonck, K., Demeester, J., De Smedt, S. C., & Braeckmans, K. (2014). FRAP in pharmaceutical research: Practical guidelines and applications in drug delivery. *Pharmaceutical Research*. https://doi.org/10.1007/s11095-013-1146-9

Donaldson, K., & Borm, P. J. A. (1998). The quartz hazard: A variable entity. *Annals of Occupational Hygiene*, *42*(5), 287–294. https://doi.org/10.1016/S0003-4878(98)00044-1

Duffin, R., Gilmour, P. S., Schins, R. P., Clouter, a, Guy, K., Brown, D. M., Stone, V. (2001). Aluminium lactate treatment of DQ12 quartz inhibits its ability to cause inflammation, chemokine expression, and nuclear factor-kappaB activation. *Toxicology and Applied Pharmacology*, *176*(1), 10–7.

https://doi.org/10.1006/taap.2001.9268

Fenoglio, I., Fubini, B., Tiozzo, R., & Di Renzo, F. (2000). Effect of micromorphology and surface reactivity of several unusual forms of crystalline silica on the toxicity to a monocyte-macrophage tumor cell line. *Inhalation Toxicology*, *12*(3), 81–89. https://doi.org/10.1080/08958370050164914

Frost, R., Jönsson, G. E., Chakarov, D., Svedhem, S., & Kasemo, B. (2012). Graphene oxide and lipid membranes: Interactions and nanocomposite structures. *Nano Letters*, *12*(7), 3356–3362. https://doi.org/10.1021/nl203107k

Fubini, B. (1998). Surface chemistry and quartz hazard. *Annals of Occupational Hygiene*. https://doi.org/10.1016/S0003-4878(98)00066-0

Fubini, B., Bolis, V., Cavenago, A., Garrone, E., & Ugliengo, B. (1993) Structural and induced heterogeneity at the surface of some SiO_2 polymorphs from the enthalpy of adsorption of various molecules. *Langmuir*, 9, 2712-2720

Fubini, B., Bolis, V., Cavenago, A., & Volante, M. (1995). Physicochemical properties of crystalline silica dusts and their possible implication in various biological responses. *Scandinavian Journal of Work Environment Health*, *21*, 9–14. Retrieved from lw0816.pdf

Fubini, B., Giamello, E., Volante, M., & Bolis, V. (1990). Chemical Functionalities At the Silica Surface Determining Its Reactivity When Inhaled - Formation and Reactivity of Surface Radicals. *Toxicology and Industrial Health*, *6*(6), 571–598.

Fubini, B., & Hubbard, A. (2003). Reactive oxygen species (ROS) and reactive nitrogen species (RNS) generation by silica in inflammation and fibrosis. *Free Radical Biology and Medicine*. https://doi.org/10.1016/S0891-5849(03)00149-7

Ge, C., Tian, J., Zhao, Y., Chen, C., Zhou, R., & Chai, Z. (2015). Towards understanding of nanoparticle–protein corona. *Archives of Toxicology*. https://doi.org/10.1007/s00204-015-1458-0

Ghiazza, M., Scherbart, A. M., Fenoglio, I., Grendene, F., Turci, F., Martra, G., Fubini, B. (2011). Surface iron inhibits quartz-induced cytotoxic and inflammatory responses in alveolar macrophages. *Chemical Research in Toxicology*, *24*(1), 99–110. https://doi.org/10.1021/tx1003003

Giess, F., Friedrich, M. G., Heberle, J., Naumann, R. L., & Knoll, W. (2004). The Protein-Tethered Lipid Bilayer: A Novel Mimic of the Biological Membrane. *Biophysical Journal*, *87*(5), 3213–3220. https://doi.org/10.1529/biophysj.104.046169

Goodman, C. M., McCusker, C. D., Yilmaz, T., & Rotello, V. M. (2004). Toxicity of gold nanoparticles functionalized with cationic and anionic side chains. *Bioconjugate Chemistry*, *15*(4), 897–900. https://doi.org/10.1021/bc049951i

Hamilton, R. F., Thakur, S. A., & Holian, A. (2008). Silica binding and toxicity in alveolar macrophages. *Free Radical Biology and Medicine*. https://doi.org/10.1016/j.freeradbiomed.2007.12.027

Hemenway, D., Absher, A., Fubini, B., Trombley, L., Vacek, P., Volante, M., & Cavenago, A. (1994). Surface functionalities are related to biological response and transport of crystalline silica. *Annals of Occupational Hygiene*, *38*(inhaled_particles_VII), 447–454. https://doi.org/10.1093/annhyg/38.inhaled_particles_VII.447

Holleman, A., & Wiberg, E. (1995). *Lehrbuch der Anorganischen Chemie*. *Journal of Chemical Information and Modeling* (Vol. 53). https://doi.org/10.1017/CBO9781107415324.004

Hosaka, M. (1991). Synthesis of micro α-quartz crystals by hydrothermal hot-press method. *Journal of Crystal Growth*. https://doi.org/10.1016/0022-0248(91)90931-T

Jiang, X., Bao, L., Cheng, Y.-S., Dunphy, D. R., Li, X., & Brinker, C. J. (2012). Aerosol-assisted synthesis of monodisperse single-crystalline α-cristobalite nanospheres. *Chem. Commun.*, *48*(9), 1293–1295. https://doi.org/10.1039/C1CC15713B

Jiang, X., Jiang, Y.-B., & Brinker, C. J. (2011). Hydrothermal synthesis of monodisperse single-crystalline alpha-quartz nanospheres. *Chemical Communications*, *47*(26), 7524. https://doi.org/10.1039/c1cc11115a

Kawasaki, H. (2015). A mechanistic review of silica-induced inhalation toxicity. *Inhalation Toxicology*, *27*(8), 363–377. https://doi.org/10.3109/08958378.2015.1066905

Kettiger, H., Québatte, G., Perrone, B., & Huwyler, J. (2016). Interactions between silica nanoparticles and phospholipid membranes. *Biochimica et Biophysica Acta - Biomembranes*, *1858*(9), 2163–2170. https://doi.org/10.1016/j.bbamem.2016.06.023

King, E.J., Mohanty, G.P., Harrison, C.V., Nagelschmidt, G., (1953), The action of different forms of pure silicates on the lungs of rats, *British Journal of Industrial Medicine*, 10(1):9-17

King, E.J., Mohanty, G.P., Harrison, C.V., Nagelschmidt, G., (1953), The action of flint of variable size injected at constant weight and constant surface into the lungs of rats, *British Journal of Industrial Medicine*, 10(2):76-92

Knaapen, A. M., Borm, P. J. A., Albrecht, C., & Schins, R. P. F. (2004). Inhaled particles and lung cancer. Part A: Mechanisms. *International Journal of Cancer*. https://doi.org/10.1002/ijc.11708

Koike, C., Noguchi, R., Chihara, H., Suto, H., Ohtaka, O., Imai, Y., … Tsuchiyama, A. (2013). Infrared spectra of silica polymorphs. In *Proceedings of Science*. https://doi.org/10.1088/0004-637X/778/1/60

Kosmulski, M., & Matijević, E. (1992). Formation of the surface charge on silica in mixed solvents. *Colloid & Polymer Science*, *270*(10), 1046–1048. https://doi.org/10.1007/BF00655975

Kriegseis, W., Scharmann, A., Serafin, J. (1987) Investigations of surface properties of silica dust with regard to their cytotoxicity. The Annals of occupational hygiene, 31(4A):417-427

Laurencin, M., Georgelin, T., Malezieux, B., Siaugue, J. M., & Ménager, C. (2010). Interactions between giant unilamellar vesicles and charged core-shell magnetic nanoparticles. *Langmuir*, *26*(20), 16025–16030. https://doi.org/10.1021/la1023746

Le Bihan, O., Bonnafous, P., Marak, L., Bickel, T., Trépout, S., Mornet, S., … Lambert, O. (2009). Cryo-electron tomography of nanoparticle transmigration into liposome. *Journal of Structural Biology*, *168*(3), 419–425. https://doi.org/10.1016/j.jsb.2009.07.006

Le Bouffant, L., Daniel, H., & Martin, J. C. (1975). The therapeutic action of aluminium compounds on the development of experimental lesions produced by pure quartz or mixed dust. *Inhaled Particles*, *4 Pt 1*, 389–401.

Leroueil, P. R., Berry, S. A., Duthie, K., Han, G., Rotello, V. M., McNerny, D. Q., Holl, M. M. B. (2008). Wide varieties of cationic nanoparticles induce defects in supported lipid bilayers. *Nano Letters*, *8*(2), 420–424. https://doi.org/10.1021/nl0722929

Lesniak, A., Fenaroli, F., Monopoli, M. P., Åberg, C., Dawson, K. A., & Salvati, A. (2012). Effects of the presence or absence of a protein corona on silica

nanoparticle uptake and impact on cells. *ACS Nano*, *6*(7), 5845–5857. https://doi.org/10.1021/nn300223w

Lewinski, N., Colvin, V., & Drezek, R. (2008). Cytotoxicity of nanoparticles. *Small (Weinheim an Der Bergstrasse, Germany)*, *4*(1), 26–49. https://doi.org/10.1002/smll.200700595

Li, I., Bandara, J., & Shultz, M. J. (2004). Time Evolution Studies of the H 2 O/Quartz Interface Using Sum Frequency Generation, Atomic Force Microscopy, and Molecular Dynamics. *Langmuir*, *20*(24), 10474–10480. https://doi.org/10.1021/la048639u

Liu, T.-P., Wu, S.-H., Chen, Y.-P., Chou, C.-M., & Chen, C.-T. (2015). Biosafety evaluations of well-dispersed mesoporous silica nanoparticles: towards in vivo-relevant conditions. *Nanoscale*, *7*(15), 6471–6480. https://doi.org/10.1039/C4NR07421A

Lundqvist, M., Stigler, J., Elia, G., Lynch, I., Cedervall, T., & Dawson, K. A. (2008). Nanoparticle size and surface properties determine the protein corona with possible implications for biological impacts. *Proceedings of the National Academy of Sciences of the United States of America*, *105*(38), 14265–70. https://doi.org/10.1073/pnas.0805135105

Luyts, K., Napierska, D., Nemery, B., & Hoet, P. H. M. (2013). How physico-chemical characteristics of nanoparticles cause their toxicity: complex and unresolved interrelations. *Environ. Sci.: Processes Impacts*, *15*(1), 23–38. https://doi.org/10.1039/C2EM30237C

Margolis, S. V, & Krinsley, D. H. (1974). Processes of formation and environmental occurrence of microfeatures on detrital quartz grains. *American Journal of Science*, *274*(5), 449–464. https://doi.org/10.2475/ajs.274.5.449

Marucco, A., Turci, F., O'Neill, L., Byrne, H. J., Fubini, B., & Fenoglio, I. (2014). Hydroxyl density affects the interaction of fibrinogen with silica nanoparticles at physiological concentration. *Journal of Colloid and Interface Science*, *419*, 86–94. https://doi.org/10.1016/j.jcis.2013.12.025

Mortensen, N. P., Hurst, G. B., Wang, W., Foster, C. M., Nallathamby, P. D., & Retterer, S. T. (2013). Dynamic development of the protein corona on silica nanoparticles: composition and role in toxicity. *Nanoscale*, *5*(14), 6372. https://doi.org/10.1039/c3nr33280b

Mueller, P., Rudin, D. O., Ti Tien, H., & Wescott, W. C. (1962). Reconstitution of cell membrane structure in vitro and its transformation into an excitable

system. *Nature*, *194*(4832), 979–980. https://doi.org/10.1038/194979a0

Murashov, V., Harper, M., & Demchuk, E. (2006). Impact of Silanol Surface Density on the Toxicity of Silica Aerosols Measured by Erythrocyte Haemolysis. *Journal of Occupational and Environmental Hygiene*, *3*(12), 718–723. https://doi.org/10.1080/15459620601015950

Murray, D. K., Harrison, J. C., & Wallace, W. E. (2005). A 13C CP/MAS and 31P NMR study of the interactions of dipalmitoylphosphatidylcholine with respirable silica and kaolin. *Journal of Colloid and Interface Science*, *288*(1), 166–170. https://doi.org/10.1016/j.jcis.2005.02.065

Nangia, S., & Sureshkumar, R. (2012). Effects of nanoparticle charge and shape anisotropy on translocation through cell membranes. *Langmuir*, *28*(51), 17666–17671. https://doi.org/10.1021/la303449d

Napierska, D., Thomassen, L. C., Lison, D., Martens, J. A., & Hoet, P. H. (2010). The nanosilica hazard: another variable entity. *Particle and Fibre Toxicology*, *7*(1), 39. https://doi.org/10.1186/1743-8977-7-39

Nash, T., Allison, A. C., & Harington, J. S. (1966). Physico-chemical properties of silica in relation to its toxicity. *Nature*, *210*(5033), 259–261. https://doi.org/10.1038/210259a0

Nel, A. E., Mädler, L., Velegol, D., Xia, T., Hoek, E. M. V., Somasundaran, P., … Thompson, M. (2009). Understanding biophysicochemical interactions at the nano-bio interface. *Nature Materials*. https://doi.org/10.1038/nmat2442

Nolan, R. P., Langer, A. M., Harington, J. S., Oster, G., & Selikoff, I. J. (1981). Quartz hemolysis as related to its surface functionalities. *Environmental Research*, *26*(2), 503–520. https://doi.org/10.1016/0013-9351(81)90226-7

Oberdorster, G., Maynard, A., Donaldson, K., Castranova, V., Fitzpatrick, J., Ausman, K. (2005). A report from the ILSI Research Foundation/Risk Science Institute Nanomaterial Toxicity Screening Working Group. Principles for characterizing the potential human health effects from exposure to nanomaterials: elements of a screening strategy. *Particle and Fibre Toxicology*, *2*(1), 8. https://doi.org/10.1186/1743-8977-2-8

Pandurangi, R. S., Seehra, M. S., Razzaboni, B. L., & Bolsaitis, P. (1990). Surface and bulk infrared modes of crystalline and amorphous silica particles: A study of the relation of surface structure to cytotoxicity of respirable silica. *Environmental Health Perspectives*, *86*, 327–336. https://doi.org/10.1289/ehp.9086327

Pavan, C., & Fubini, B. (2017). Unveiling the Variability of "Quartz Hazard" in Light of Recent Toxicological Findings. *Chemical Research in Toxicology*, *30*(1), 469–485. https://doi.org/10.1021/acs.chemrestox.6b00409

Pera, H., Nolte, T. M., Leermakers, F. A. M., & Kleijn, J. M. (2014). Coverage and disruption of phospholipid membranes by oxide nanoparticles. *Langmuir*, *30*(48), 14581–14590. https://doi.org/10.1021/la503413w

Rabolli, V., Lison, D., & Huaux, F. (2016). The complex cascade of cellular events governing inflammasome activation and IL-1β processing in response to inhaled particles. Particle and Fibre Toxicology, 13:40. https://doi.org/10.1186/s12989-016-0150-8

Ramachandran, S., Merrill, N. E., Blick, R. H., & Van Der Weide, D. W. (2005). Colloidal quantum dots initiating current bursts in lipid bilayers. In *Biosensors and Bioelectronics* (Vol. 20, pp. 2173–2176). https://doi.org/10.1016/j.bios.2004.08.042

Rascol, E., Devoisselle, J.-M., & Chopineau, J. (2016). The relevance of membrane models to understand nanoparticles–cell membrane interactions. *Nanoscale*, *8*(9), 4780–4798. https://doi.org/10.1039/C5NR07954C

Rimola, A., Costa, D., Sodupe, M., Lambert, J. F., & Ugliengo, P. (2013). Silica surface features and their role in the adsorption of biomolecules: Computational modeling and experiments. *Chemical Reviews*. https://doi.org/10.1021/cr3003054

Roiter, Y., Ornatska, M., Rammohan, A. R., Balakrishnan, J., Heine, D. R., & Minko, S. (2009). Interaction of lipid membrane with nanostructured surfaces. *Langmuir*, *25*(11), 6287–6299. https://doi.org/10.1021/la900119a

Rossi, C., & Chopineau, J. (2007). Biomimetic tethered lipid membranes designed for membrane-protein interaction studies. *European Biophysics Journal*. https://doi.org/10.1007/s00249-007-0202-y

Sayan, M., & Mossman, B. T. (2016). The NLRP3 inflammasome in pathogenic particle and fibre-associated lung inflammation and diseases. *Particle and Fibre Toxicology*, *13*(1), 51. https://doi.org/10.1186/s12989-016-0162-4

Schins, R. P. F. (2002). Mechanisms of genotoxicity of particles and fibers. *Inhalation Toxicology*, *14*(1), 57–78. https://doi.org/10.1080/089583701753338631

Schins, R. P. F., Duffin, R., Höhr, D., Knaapen, A. M., Shi, T., Weishaupt, C., & Borm, P. J. A. (2002). Surface modification of quartz inhibits toxicity, particle

uptake, and oxidative DNA damage in human lung epithelial cells. *Chemical Research in Toxicology*, *15*(9), 1166–1173. https://doi.org/10.1021/tx025558u

Shi, X., Ding, M., Chen, F., Wang, L., Rojanasakul, Y., Vallyathan, V., & Castranova, V. (2001). Reactive oxygen species and molecular mechanism of silica-induced lung injury. *J Environ Pathol Toxicol Oncol*, *20 Suppl 1*, 85–93. Retrieved from http://www.ncbi.nlm.nih.gov/pubmed/11570677

Shi, Dalai, N. S., Hu, X. N., & Vallyathan, V. (1989). The chemical properties of silica particle surface in relation to silica-cell interactions. *Journal of Toxicology and Environmental Health*, *27*(4), 435–454. https://doi.org/10.1080/15287398909531314

Sochalski-Kolbus, L. M., Wang, H.-W., Rondinone, A. J., Anovitz, L. M., Wesolowski, D. J., & Whitfield, P. S. (2015). Solvothermal Synthesis and Surface Chemistry To Control the Size and Morphology of Nanoquartz. *Crystal Growth & Design*, *15*(11), 5327–5331. https://doi.org/10.1021/acs.cgd.5b00882

Strobl, F. G., Seitz, F., Westerhausen, C., Reller, A., Torrano, A. A., Bräuchle, C., Schneider, M. F. (2014). Intake of silica nanoparticles by giant lipid vesicles: Influence of particle size and thermodynamic membrane state. *Beilstein Journal of Nanotechnology*, *5*(1), 2468–2478. https://doi.org/10.3762/bjnano.5.256

Tao, Z., Toms, B. B., Goodisman, J., & Asefa, T. (2009). Mesoporosity and functional group dependent endocytosis and cytotoxicity of silica nanomaterials. *Chemical Research in Toxicology*, *22*(11), 1869–1880. https://doi.org/10.1021/tx900276u

Vallyathan, V., Shi, X. L., Dalal, N. S., Irr, W., & Castranova, V. (1988). Generation of free radicals from freshly fractured silica dust. Potential role in acute silica-induced lung injury. *The American Review Of Respiratory Disease*, *138*(5), 1213–1219. https://doi.org/10.1164/ajrccm/138.5.1213

Van Lehn, R. C., & Alexander-Katz, A. (2011). Penetration of lipid bilayers by nanoparticles with environmentally-responsive surfaces: simulations and theory. *Soft Matter*, *7*(24), 11392. https://doi.org/10.1039/c1sm06405c

Vigliani, E.C., & Mottura, G., 1948, Diatomaceous earth silicosis, British Journal of Industrial Medicine, 5(3):148-60

Walczyk, D., Bombelli, F. B., Monopoli, M. P., Lynch, I., & Dawson, K. A. (2010). What the cell "sees" in bionanoscience. *Journal of the American Chemical*

Society, *132*(16), 5761–5768. https://doi.org/10.1021/ja910675v

Wang, F., Yu, L., Monopoli, M. P., Sandin, P., Mahon, E., Salvati, A., & Dawson, K. A. (2013). The biomolecular corona is retained during nanoparticle uptake and protects the cells from the damage induced by cationic nanoparticles until degraded in the lysosomes. *Nanomedicine: Nanotechnology, Biology, and Medicine*, *9*(8), 1159–1168. https://doi.org/10.1016/j.nano.2013.04.010

Weinstein, J. N., Yoshikami, S., Henkart, P., Blumenthal, R., & Hagins, W. a. (1977). Liposome-cell interaction: transfer and intracellular release of a trapped fluorescent marker. *Science*, *195*(4277), 489–492. https://doi.org/10.1126/science.835007

Wiessner, J. H., Mandel, N. S., Sohnle, P. G., & Mandel, G. S. (1989). Effect of Particle Size on Quartz-Induced Hemolysis and on Lung Inflammation and Fibrosis. *Experimental Lung Research*, *15*(6), 801–812.

Wynn, T. A. (2011). Integrating mechanisms of pulmonary fibrosis. *The Journal of Experimental Medicine*, *208*(7), 1339–1350. https://doi.org/10.1084/jem.20110551

Zhang, S., Nelson, A., & Beales, P.A. (2012). Freezing or Wrapping the Role of Particle Size in the Mechanism of Nanoparticle-Biomembrane Interaction. Langmuir, 28(35), 12831-12837. https://doi.org/10.1021/la301771b

Synthesis and characterization of crystalline silica particles with tailored physico-chemical properties, as natural quartz surface model

2.1 Background

Occupational exposure to fine and ultrafine crystalline silica dust, particularly quartz, is known to induce severe diseases, including lung cancer. An impressive body of experimental work in the past 20 years, reported in recent reviews and books (Donaldson & Seaton, 2012; Fubini, 1998; Pavan & Fubini, 2017; Rimola, Costa, Sodupe, Lambert, & Ugliengo, 2013; Verma & Stellacci, 2010; IARC, 1997), has evidenced two key aspects in the interaction between crystalline silica and cells: i) the crucial role played by the particle surface in triggering the adverse biological response, and ii) the extreme variability in the pathogenic potential among different sources of particulate silica (Donaldson & Borm, 1998; B. Fubini, 1998). Such variability is the consequence of differences in silica bulk and surface chemistry, including the occurrence of free radical generation centers ($Si^\bullet$ and $SiO^\bullet$ as well as redox-reactive metal impurities) and the nature, abundance and spatial disposition of silanol (–Si-OH) families. Silanols are acidic moieties with a potential for H-bonding, and have a key role in defining silica interaction with cells. Silica surface is characterized by different families of –Si-OH groups, including isolated (the most common), geminal, and vicinal silanols. Isolated silanols impart hydrophobicity to the surface, while all other types render surface more hydrophilic. Thus, long-range order and distribution of silanol patches on silica surface, impart specific characteristics to different silica specimen. Quartz dusts used so far in particle toxicology assays have been obtained by grinding rock containing natural quartz, a process that affects crystallinity and yields samples with extreme variable and complex surface states. To overcome the variability of mineral quartz dusts, we have developed an innovative method to grow highly-pure quartz crystals in respirable size with controlled surfaces. Such crystals allow us to investigate, at the molecular level, the mechanisms related to quartz toxicity.

2.2 Experimental section and discussion

The method employs an amorphous silica gel, obtained from 25% Na-metasilicate solution (Na-MTS), polymerized through the use of mineral acids (HNO_3 and H_2CO_3) chosen to reduce the chemical complexity of the gel as starting phase. A full characterization of the synthetic α-quartz crystals obtained was carried out: the crystal structure (XRPD), surface area (Kr-BET), surface charge (ELS), crystal morphology (SEM) and particle size (DCS) were evaluated and compared to a natural quartz dust (reference sample), previously used in several toxicological studies. These physico-chemical properties determine the particle dispersion state in biological solutions, and the biophysico-chemical interactions that occur at the solid-bio interface.

Results showed that, despite the use of two different polymerizing agents (HNO_3 and CO_2), both synthetic routes allowed to grow highly-pure α-quartz crystals after an optimized growth run of 168 h. Shorter time periods (i.e. 24 h) affected crystalline quality of the product. The use of different polymerizing agents resulted in non-negligible chemical-physical differences among NG- (HNO_3 as polymerizing agent) and CG- (H_2CO_3 as polymerizing agent) crystals. Through a thorough characterization, we were able to observe strong differences in the inner structure of the quartz-forming gels (NG- and CG- polymerized gels), which affected the growth mechanisms (see paragraph 4.1 and 4.2 in Pastero et al., 2016).

Main differences can to be ascribed to i) different transport efficiency of the NG- and CG- silica sponges, and ii) the presence of impurities. At room temperature, in fact, only diffusion as matter transport process was present in both gels. Upon heating, an increase in the convective component of transport was observed. In CG-gel, the convective regime was demonstrated to be stronger than in the NG case (see paragraph 4 in Pastero et al., 2016), hence resulting in a more functional medium for crystal growth. In addition, in the case of H_2CO_3 as polymerizing agent, the presence of large bubbles, due to CO_2 bubbling inside the Na-MTS solution, moved the process from nucleation to growth. Furthermore, in CG-case, bubbles worked as heterogeneous nucleation sites, showing a double crystallization direction. On the other hand, in NG- synthetic route, the smaller size of bubbles resulted in a more performing gel, in which nucleation was favoured than growth. For this reason, CG-grown samples were characterized by a bimodal size distribution (see fig. 4 in Pastero et al.). Moreover, in the CG-case, quartz growth took advantage from good epitaxy conditions *(epitaxial growth)* between quartz and the guest phase in the growing medium (mainly trona, ($Na_3H(CO_3)_2 \bullet H_2O$). Theoretical epitaxies were calculated to confirm this effect, and very good epitaxy conditions between quartz and some Na-carbonate-phases were found (see Table 3, Pastero et al., 2016). No epitaxy was found in the NG-case. These results validate a model of cooperation between phases during the quartz growth.

2.3 Main achievements

During the last 150 years, a growing interest, in several research fields, has been devoted towards the synthesis of α-quartz crystals. In particular, in nanotoxicology, the synthesis of crystalline silica particles with controlled and tuneable surface properties is of the outmost importance, to avoid the extreme variability that characterises mineral silica dusts. The possibility to tune some of the key physico-chemical features relevant in quartz toxicity makes this approach a basic tool in the increasing of the knowledge concerning the relationship between quartz surface functionalities and its toxic potential.

2.4 Publication 1: Synthesis of α-Quartz with Controlled Properties for the Investigation of the Molecular Determinants in Silica Toxicology

(Pastero, L., Turci, F., Leinardi, R., Pavan, C., & Monopoli, M., *Crystal Growth & Design, 2016*)

Author's contribution: RL performed the synthesis and part of the physical-chemical characterization, including XRPD structural analysis of synthetic quartz crystals, BET surface analysis and FT-IR spectroscopy. In addition, he conducted part of the data analysis, under the supervision of FT and LP.

Appendix: Introduction of aluminium oxide as source of bulk properties variability of quartz crystals

As previously reported (see Introduction), one of the main aspects that affect silica toxicology is due to the extreme variability in bulk and surface properties, among quartz dusts arising from different sources. This peculiarity can be explained considering the huge contrast, in terms of surface chemistry, among the crystalline phases which characterize each different polymorph. One of the mainly proposed source of chemical variability, which can alter the reactivity of silica surface, comes from the presence of metal impurities such as, for example, aluminium ions, which are able to substitute for silicon in the tetrahedron framework of silica.

In this context, to obtain crystalline silica crystals at higher complexity (in respect to the highly-pure crystals, synthesized following the approach described in the work of Pastero and coworkers) (Pastero, Turci, Leinardi, Pavan, & Monopoli, 2016) and evaluate the physical-chemical features mainly involved in quartz toxicity, we grown and fully characterized α-quartz crystals in respirable size, containing aluminium ions in the crystal bulk, at different percentage Al/Si ratio.

a.1 Synthetic Route

Crystalline silica samples have been synthesized following the hydrothermal synthetic pathway above described, with minimum modifications. Briefly, in a 12.2% w/w Na-MTS aqueous stock solution, we added aluminium hydroxide ($Al(OH)_3$) as aluminium source. A 1M HNO_3 solution was used as polymerizing agent. The addition of $Al(OH)_3$ was stoichiometrically calculated, in order to have three increasing Al/Si ratios, respectively of:

  i)   0.15%
  ii)   0.4%
  iii) 0.75%

Growth runs of 168 h were performed at 210°C in PTFE reactors sealed into steel autoclaves.

All samples were then characterized for physical-chemical properties mainly involved in quartz pathogenicity, and compared to highly-pure synthetic quartz crystals.

a.2 Structural evaluation: XRPD and Raman techniques

To evaluate possible variations of bulk and surface properties of the crystals due to the presence of impurities, we tried to increase the complexity of the crystalline system, adding aluminium ions during the synthetic pathway. Trivalent aluminium can substitute for Si_4^+ in the crystal lattice of quartz. Thus, due to the subsequent disequilibrium in the electric charge balance, a positive charge (counterion) is needed to compensate for the presence of a negative one. This role can be only played by a Na^+ cation or a proton (H^+).

Through the developed approach, we were able to obtain a set (summarized in table a.2.1) of α-quartz submicron-sized crystals, characterized by a variable theoretical Al/Si ratio.

Table a.2.1 List of synthetic AlQz samples with the indication of the calculated stoichiometric Al/Si ratio

Sample name	Na-MTS %	Al(OH₃), mg	Theoretical % Al/Si
AlQz 11	12.2	1.56	0.15
AlQz 12	12.2	7.8	0.75
AlQz 15	12.2	4	0.4
AlQz 16	12.2	1.56	0.15
AlQz 20	12.2	1.56	0.15
AlQz 23	12.2	4	0.4

Structural analysis, carried out through a PANalytical PW3040/60 X'Pert PRO MPD X-ray powder diffractometer, in a 2θ range between 20 and 80, did not evidence foreign or amorphous phases, but α-quartz was the only crystalline phase detected (fig. a.2.1)
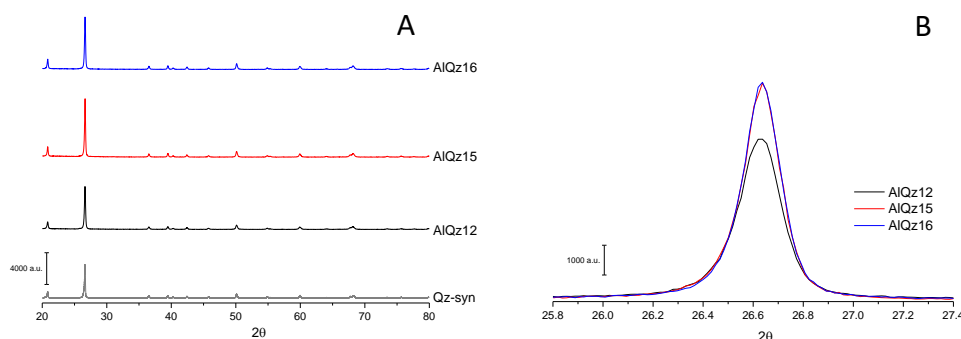
Fig. a.2.1 (Panel A) Perfect correspondence of diffraction peaks among AlQz crystals and a highly pure synthetic quartz dust (Qz-syn) is shown through comparison of XRPD patterns. No foreign phases are observed. Magnification of the principal diffraction peak (2θ=26.6) of AlQz samples (panel B) does not evidence amorphous phases.

Analysis of the phases and evaluation of the presence of eventual polymorphs was also performed by Raman spectroscopy, through an integrated micro / macro "JobinYvon" Raman spectrometer, Mod. Labram HRVIS (Horiba Scientific, Japan). Main Raman bands of α-quartz are summarized in the following table (table a.2.2)

Table a.2.2 Raman-active phonon frequencies of α-quartz (Gillet, Le Cléac'h, & Madon, 1990)

Raman shift (cm^{-1})	Mode symmetry
128	$E_{(LO+TO)}$
206	A_1
265	$E_{(LO+TO)}$
355	A_1
394	$E_{(TO)}$
401	$E_{(LO)}$
< 400 cm-1: torsional vibrations and bending modes O-Si-O	
450	$E_{(TO)}$
464	A_1
511	$E_{(LO)}$
400-530 cm-1: O movements in bending-stretching symmetrical in O-Si-O	
696	$E_{(LO+TO)}$
796	$E_{(TO)}$
808	$E_{(LO)}$
1069	$E_{(TO)}$
1085	A_1
1162	$E_{(LO+TO)}$
1230	$E_{(LO)}$
>600 cm-1: stretching modes Si-O	

Raman spectroscopy was performed only for samples AlQz 12, AlQz 15 and AlQz 16, because of the different Al/Si ratio in the considered synthetic approach. As showed in Fig. a.2.1, in which Raman spectra of the analysed samples are compared, it is possible to note, along with the typical vibrational bands of α-quartz, a shoulder centered at 502 cm^{-1}. This peak can be associated to moganite, a polymorph of quartz. Moganite, a crypto-crystalline phase, consists in a 4-membered ring of SiO_4, in a tetrahedron configuration.
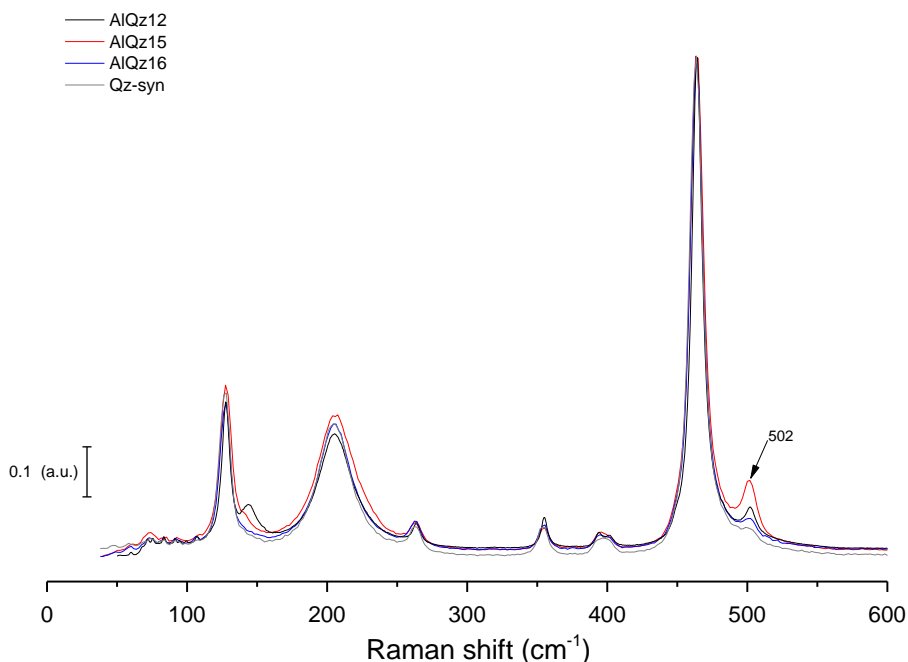
Fig. a.2.1 Comparison of Raman spectrum of AlQz crystals: the pattern is comparable to that of mineral quartz. Peak at 502 cm^{-1} was tentatively assigned to moganite, a quartz polymorph.

It has been shown (Kingma & Hemley, 1994) that tetrahedral SiO$_4$ structures are characterized by vibrational modes v_s(T-O-T) centered at around 500 cm^{-1}, while same vibrational modes of six-membered ring structures, such as quartz, are centered between 380 and 480 cm^{-1}. It is conceivable that the presence of moganite as accessory phase can be due to the setting up, during the synthesis, of epitaxial conditions. Epitaxy, in mineralogy, refers to the deposition of a crystalline overlayer on a crystalline substrate. In this case, the particular orientation taken by the growing crystal, is determined by the underlying crystal. Thus, we may suppose that moganite, working as a "chemical stabiliser" of the growing system, assists and makes the growth of quartz crystals easier to take place.

Sample AlQz12, obtained by the addition of the highest concentration of aluminium, was also characterized by the presence of fibrous crystals (SEM imaging). Through a Raman spectroscopy investigation (fig. a.2.2), such crystals, were assigned, according to RRUFF Project database, to an accessory phase generated during the synthesis belonging to zeolites (aluminosilicate minerals), supposedly to a particular zeolite known as clinoptolite-Na (Na,K,Ca)$_2$-

$3Al_3(Al,Si)_2Si_{13}O_{36}12 \cdot H2O$). However, the elongated shape of the accessory phase, and the absence of K and Ca, as evidenced through the ELS investigation (see paragraph a.5), suggest the correspondence with a fibrous zeolite, known as Na-mazzite ($Na_8Al_8Si_{28}O_{72} \cdot 30H_2O$).
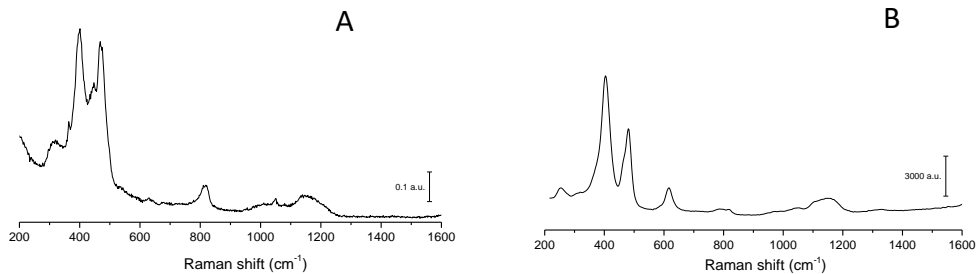
Fig. a.2.2 Comparison between Raman spectra of accessory fibrous phase generated during growth of sample AlQz samples (panel A) and spectra of clinoptolite-Na (panel B, from RRUFF Project database).

The presence of these unusual structures, whose occurrence was particularly limited (as confirmed by SEM-EDS analysis), can be explained as the result of an excess of aluminium in the growth system that, instead of coordinating in substitution of Si atoms in α-quartz structure, led to the generation of aluminosilicate minerals, crystallized in the form of fibrous zeolite. These particular structures seem to be present, to a lesser extent, also in samples AlQz15 and AlQz16, as evidenced through SEM imaging.

a.3 Size and specific surface area evaluation

To obtain an exhaustive dimensional characterization, the size of synthetic quartz crystals (hydrodynamic radius) was estimated by means of DLS (dynamic light scattering) and FPIA (flow particle image analyser), to complementarily evaluate nanometric and micrometric sizes. DLS analysis showed for all samples a range between 300 and 450 nm, characterized by a high polydispersion index (PDI > 0.3). However, the value does not represent the real size of single crystals, because of the strong particle aggregation that can occur in water. Through FPIA analysis, we evidenced that bigger particles/aggregates range at around 1.5 μm, indicating that the whole set of crystals were grown in a fully respirable size (< 4 μm). In the following table (table a.2.3) the size distribution and specific surface area of synthetic quartz crystals are summarized, and compared to samples synthesized in the work of Turci and colleagues (Turci et al., 2016). Min-U-Sil 5, a commercial quartz dust, is also added. Analysis of SSA was carried out

by means of the BET method, based on Kr adsorption. Quartz samples were degassed for hours prior to analysis, which was carried out at -196°C (ASAP 2020 Micromeritics, Norcross, USA).

Table a.2.3 Particle size, evaluated by means of FPIA and DLS. Specific surface area was measured through BET. Size comparison between AlQz crystals and a typical quartz dust (Min-U-Sil 5) shows a notable agreement.

Sample	# Analysed particles	∅1 (10%)[§], μm	∅2 (50%)[§], μm	∅3 (90%)[§], μm	DLS Zeta-Average[@], nm (PDI)	SSA Kr-BET m²/g
AlQz12	28641	0.358	0.594	1.053	369±15 (0.41)	1.9
AlQz15	3344	0.361	0.613	1.132	427±4 (0.42)	1.7
AlQz16	17993	0.359	0.598	1.047	337±8 (0.38)	4.1
Min-U-Sil 5	62690	0.437	0.817	1.487	>1000	5.2

[§]measured through FPIA
[@]measured through DLS

The comparison of dimensional characterization between the two methods, showed a very good mutual correspondence among Al-doped and commercial α-quartz crystals. High PdI values, common for the whole set of samples, indicate a substantial variability in size range, consequent to the strong crystals aggregation in water. It is also important to consider, particularly with a view to eventual cytotoxicity assessment, that size ranges of synthetic samples were extremely comparable to those of the commercial dust. SSA evaluation showed low values for AlQz samples, especially AlQz12 and AlQz15, compared to commercial quartz (Min-U-Sil 5).

In addition to size, FPIA analysis is also able to detect a further morphological parameter, which represents the shape of the particles, determined through the evaluation of their circularity, defined as the ratio between the circumference of a circle of equivalent area to the particle and the perimeter of the particle itself. The more spherical the particle, the closer its circularity is to 1. The more elongated the particle, the lower its circularity. Data concerning circularity are summarized in table a.2.4.

Table a.2.4 Particle circularity evaluated through FPIA analysis shows good correspondence of AlQz particles with synthetic pure quartz particles (Qz-syn).

Sample	# Analysed particles	⌀1 (10%), μm	⌀2 (50%), μm	⌀3 (90%), μm
AlQz12	28641	0.630	0.817	0.942
AlQz15	3344	0.640	0.812	0.937
AlQz16	17993	0.622	0.808	0.936
Qz-syn	11259	0.626	0.802	0.935

Data indicated an increasing in circularity, which ranged from 0.6 to 0.95, together with particle size. This phenomenon resulted from the aggregation of crystals in water, to form spherical aggregates (*spherulites*). A more efficient evaluation of size and morphology of the particles was carried out through SEM microscopy (see below).

a.4 Evaluation of surface charge

The surface charge of inorganic particles is considered as one of the main physico-chemical properties involved in the mechanism of particle toxicity (Pavan & Fubini, 2017). Evaluation of the ζ-potential was mainly carried out to investigate the homogeneity of surface acidic moieties (silanols) of the synthetic samples. As a matter of fact, in an aqueous media, silanols acts like Brönsted acidic sites, and the equilibrium can be described by the following equation:

$$\equiv SiOH + H_2O \leftrightharpoons \equiv Si\text{-}O^- + H_3O^+$$
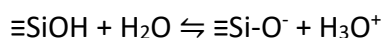
Regarding the distribution of acidic sites, silica surface is particularly heterogeneous, hosting several silanol families, all of them characterized by different acidity constants. According to the literature (Leung, Nielsen, & Criscenti, 2009; Ong, Zhao, & Eisenthal, 1992), nevertheless the assignment of the different acidity constants to the multiple silanol populations is still a much-debated issue, silanols acidity ranges from pK_a 4.5 to 8.5 (due to the chemical surroundings of each silanol), giving to the silica surface a negative net charge. The extreme variability of acidic behaviour of silica is a mark of the heterogeneity of the complex array of silanol families on the surface, and can be described investigating the variation of the zeta potential in aqueous medium as a function of pH, by way of a titration curve (ζ-plot). Titration curve trend of silica surface

can be comparable to that of weak acidic species, in the ideal case, obviously, of a surface that exhibits a chemically-homogeneous silanol family, i.e. expressing a unique pK_a. In the case of a more heterogeneous surface, the trend will be less regular, and the comparability will be lost. It should be pointed out that $SiOH_2^+$ species exist only at extremely acidic pH values (<2) (Duval, Mielczarski, Pokrovsky, Mielczarski, & Ehrhardt, 2002) while, at pH values from 2 to 14, the presence of $SiOH_2^+$ represents just a minor fraction of the overall chemical surface moieties.

Surface silanol titration was evaluated by means of electrophoretic light scattering (ELS) (Zetasizer Nano-ZS). In this technique, the velocity of a particle in an oscillating electric field, proportional to its zeta potential, is measured by light scattering. The ζ-potential was measured suspending quartz particles in ultrapure water (0.6 mg/ml), and the pH of the dispersion was adjusted with 0.1 M HCl or 0.1 M NaOH. The dispersion was finally probe-sonicated for 3 minutes at 25% amplitude. ζ-plots of Al-quartz samples, compared to that of a highly pure synthetic quartz dust, are shown below (Fig. a.2.2)
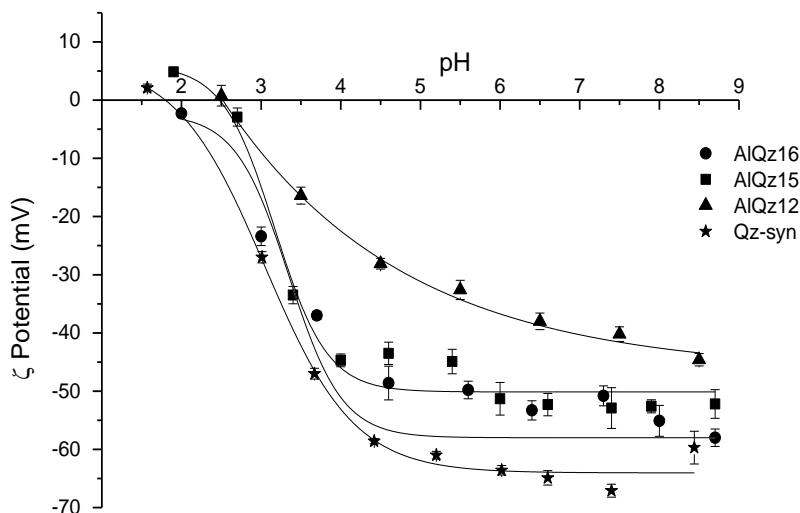
Fig. a.2.2 Z-plot (ζ potential vs pH) of AlQz (12, 15, 16) and highly pure (Qz-syn) synthetic quartz crystals. Experimental points acquired with at least three measurements are fitted with a non-linear curve to help the reader's eye. The slope of the tangent line at the inflection point is a convenient estimate of the heterogeneity of surface silanol acidity. The steeper the slope of the tangent line, the more homogeneous the acidic nature of the silanols at the surface

In a recent research carried out by our group (Turci et al., 2016), the surface distribution of silanols/silanolates was considered as crucial to explain the membrano-perturbative activity of quartz particles towards liposomes and red blood cells, used as biomembrane models at increasing complexity. According to the literature (Chen & Bothun, 2014; Ivana Fenoglio, Fubini, Ghibaudi, & Turci, 2011; Sun et al., 2016), the evaluation of the damage to the RBC membrane can have a huge predictive value towards particle-induced inflammation. Thus, same approach will be in future followed for AlQz samples, in order to describe possible difference in chemical surface features, supposed to be crucial in the pathogenic activity of crystalline silica.

Results in Fig. a.2.2 suggested that, in an alkaline environment (pH > 7), for the whole set of samples, surface silanols appear to be dissociated, resulting in a strong negative net surface charge. As the pH became more acidic, their protonation was promoted and, consequently, the net charge moved towards less negative values, until reaching the ZPC at pH ca. 2 (except sample AlQz16, whose zeta potential was always < 0, in the applied measurement conditions). This is a common behaviour for silica, as evidenced by highly pure synthetic quartz crystals (Qz-syn): generally, at pH < 2, all surface silanols are supposed to be in the protonated form (Si-OH). Hence, the overall charge is essentially zero. More specifically, sample AlQz12 showed a tighter curve than other samples, with the lowest zeta potential value set at ca. –40 mV at pH ~ 8. The trend of the curve, with a gently slope, could be correlated to a larger heterogeneity of the surface, in term of distribution of silanol families. On the contrary, sample AlQz15 was characterized by a quasi-constant zeta potential value from pH 8 up to ca. 6, a slight increase from pH 6 to 4, and a conclusive, very strong upsurge towards positive values. ZPC was reached at pH ca. 2.5. AlQz16 showed a very similar tendency, although having origin at lower ζ-Potential values, too.

Taken together, data indicated that overall surface charge in the considered range of pH was mostly negative, confirming the theoretical weak acidic behaviour of Si-OH groups, which was, surprisingly, not affected by the presence of aluminium ions into the crystals bulk. At a physiological pH (7.4), all samples showed a strong net negative charge. This suggest that silanol groups, as expected, virtually have the tendency to act as a proton donor expressing, at specific pH values, Si-O$^-$ functionalities able to interact with the polar groups of biomembrane and, thus, driving quartz-membrane adsorption processes.

However, it should be clarified that the evaluation of the zeta potential above reported does not differentiate between two different species simultaneously present in the same dust (quartz spherulites and fibrous zeolites, in our case), but represents an average description of the sample. Thus, especially for sample AlQz12, the considerable presence of the accessory phase in the analysed dust, which clearly affect the titration curve, should be certainly considered.

a.5 Evaluation of morphology and elemental analysis

Though scanning electron microscopy (SEM), we were able to investigate size and morphology of synthetic quartz particles. As above mentioned (see Introduction chapter), particle size and morphological features (like irregular surfaces, spikes and edges) represent two of the main several physico-chemical characteristics involved in the variability of quartz toxicity (Fenoglio, Fubini, Tiozzo, & Di Renzo, 2000; Fubini, Fenoglio, Elias, & Poirot, 2001).

To investigate these specific features, quartz samples were analysed through an EVO 50XVP SEM microscope (Zeiss, Oberkochen, Germany), dropping off quartz samples on graphite tapes, thus allowing the investigation of elemental composition of crystals by means of Energy Dispersive X-ray Spectrometry (EDS). Finally, particles were coated with gold, in order to prevent the electron beam from charging the sample.

Images showing morphological features of synthetic Al-quartz crystals are reported in figure a.2.3.
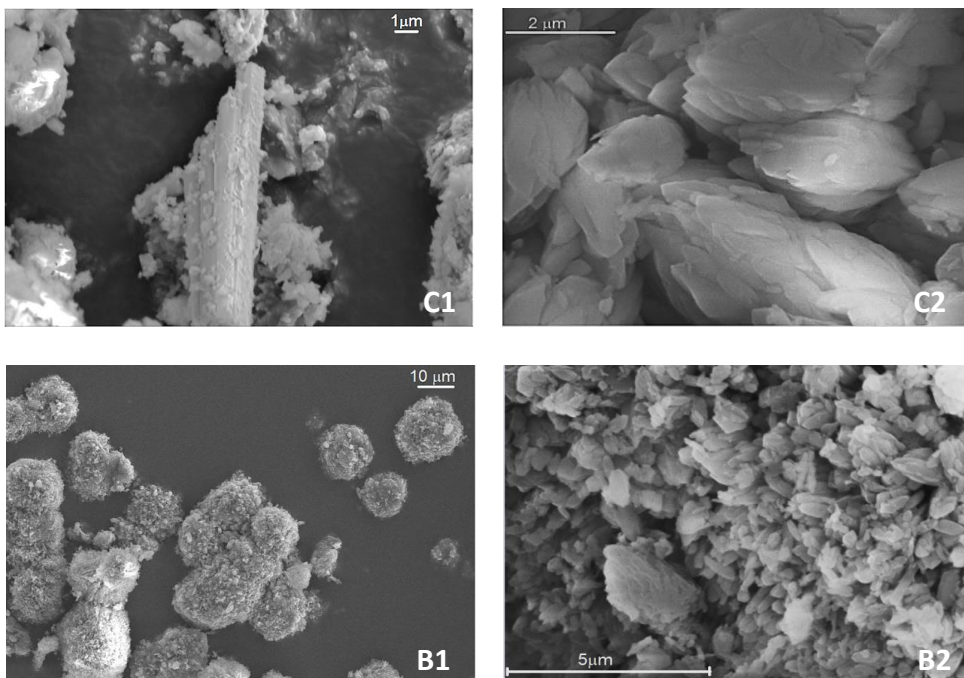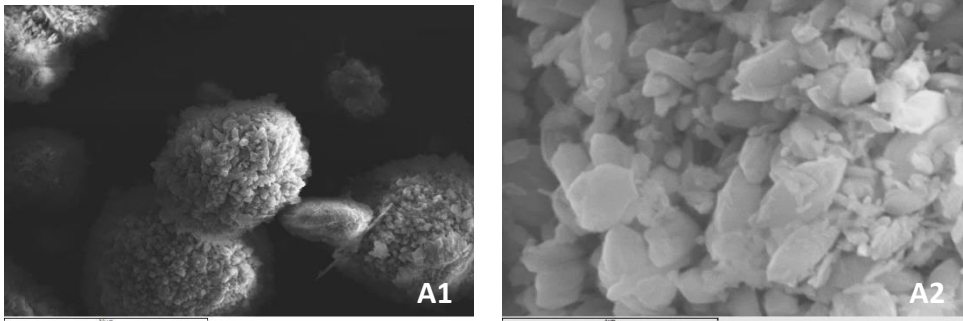
Fig. a.2.3 SEM Images of as-grown aggregates of AlQz synthetic quartz crystals (A: AlQz12; B: AlQz15; C: AlQz16). All samples share the same typical morphology, with the presence of spherulitic aggregates. Pictures at higher magnification (A2, B2, C2) confirm the presence of edges and spikes.

Imaging characterization of sample AlQz12 (A1, A2) showed aggregates of single crystals, which formed spherical structures with a diameter of ca. 20 μm. Moreover, it could be noted that these particular structures, known as spherulites, consisted of a radial arrangement of crystals. At a larger magnification, smooth surfaces were observed, and a particular morphology of crystals, characterized by elongated shapes with irregular ends, probably without any kind of fractures, was evidenced. Single crystals reached the size of ca. 2-3 μm. Sample AlQz15 (B1, B2) presented a morphology extremely comparable to that of previously discussed sample. Interestingly, SEM imaging highlighted the presence of foreign elongated fibrous structures, whose elemental composition was evaluated through EDS spectrometry (Fig. a.2.4).
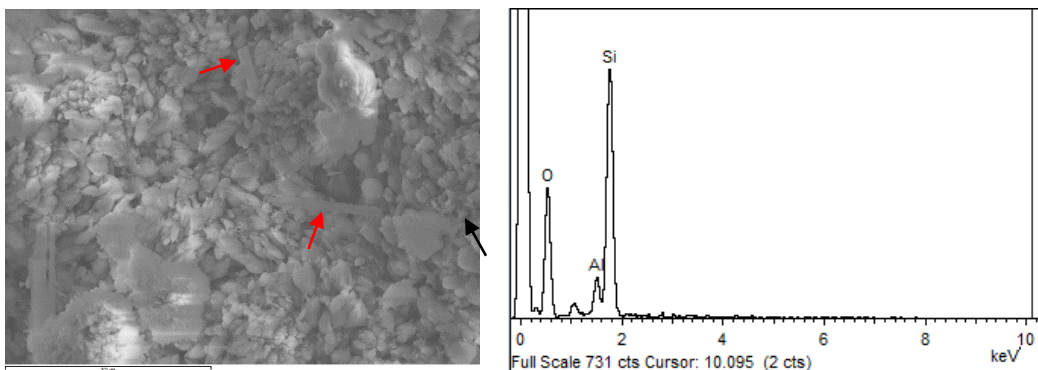
Fig. a.2.4 Elemental analysis of AlQz15 sample shows the presence of Al in the bulk of crystals. Fibrous elongated structures are clearly evidenced (red arrows).

Sample AlQz16 also showed spherulitic aggregates and, in accordance with other synthesis, the presence of single fibrous crystals, resulting in an elongated pattern along the *c* growth axis. Here again, quartz crystals morphology was characterized by spikes and edges, and no fractures were detected on the surface. Regarding particle size, it was possible to presume a sub-micrometric range. Elemental analysis indicated that fibrous structures contained silicon, oxygen and, at a lesser percentage, sodium and aluminium, at a comparable atomic % among the three synthesis (tab. a.2.5), suggesting that the byproduct phase was the same for different synthetic routes.

Table a.2.5 EDS analysis of fibrous structures grown during the AlQz synthetic routes.

	Element	Atomic %
Byproduct of AlQz12 Synthetic route	O	76.67±0.94
	Na	2.42±0.57
	Al	2.91±0.70
	Si	18.03±1.58
Byproduct of AlQz15 Synthetic route	O	71.71±0.13
	Na	3.21±0.28
	Al	3.64±0.32
	Si	22.47±0.16
Byproduct of AlQz16 Synthetic route	O	68.37±3.83
	Na	2.23±0.42
	Al	3.14±1.77
	Si	26.32±2.87

Same analysis, carried out on AlQz crystals, showed an atomic % of bulk sodium and aluminium lower than 0.5%, for the whole set of samples. Interestingly, atomic % of aluminium inside the quartz spherulites was found to follow a "periphery-to-center" gradient distribution. The highest Al concentration was in fact detected in the peripheral regions of particles (ca. 0.2 atomic % for sample AlQz12, slightly lower for AlQz15 and 16), and gradually lower moving towards the central region, where no aluminium was observed.

a.6 XRF quantification of aluminium in crystal bulk

A quantitative evaluation of the presence of aluminium in the crystal structure was carried out by X-Ray Fluorescence technique (XRF), through an Eagle-III µProbe X-ray spectrometer (EDAX Inc., USA). XRF technique is non-destructive analytical methodology used to determine the elemental composition of materials, by measuring the fluorescent (or secondary) X-ray emitted from a sample when it is excited by a primary X-ray source. Each of the elements present in a sample generates a set of characteristic fluorescent X-rays (a "fingerprint") that is unique for that specific element.

In our case, peak intensities of the spectrum fall at energy values which correspond at the allowed transitions (*k, l, m*) due to the interaction between x-ray and the considered sample. Thus, we made a comparison between XRF spectra of AlQz samples and the spectra of a highly-pure synthetic α-quartz dust (Fig. a.2.5)
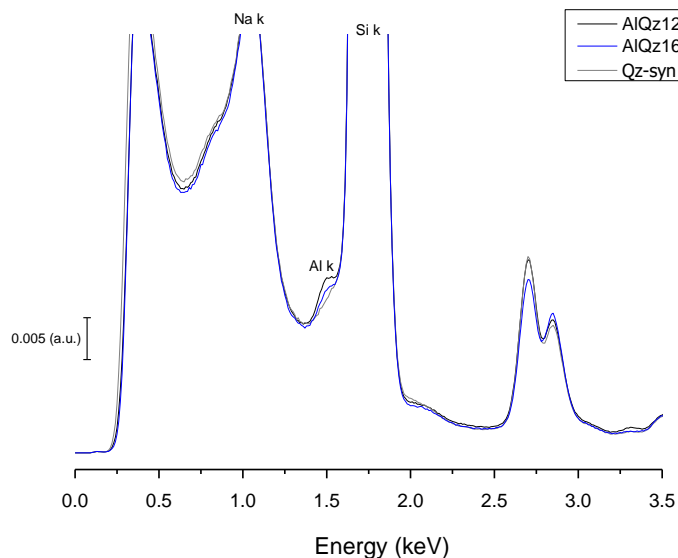
Fig. a.2.5 X-ray fluorescence spectrum of AlQz samples, compared to that of a pure synthetic quartz dust (Qz-syn). Presence of aluminium is evidenced by a shoulder centered at around 1.5 keV.

As shown in Fig. a.2.5, XRF spectra of AlQz crystals 12 and 16 were characterized by a weak peak centered at around 1.5 keV, which indicated the presence of bulk aluminium ions. As expected, the peak was totally absent in the spectrum of pure α-quartz crystals. The presence of silicon was well highlighted. However, due to the low intensity of the peak, it was not possible to assess properly the exact concentration of Al in the bulk, but it can only be approximated to a

concentration, expressed in atomic %, lower than 2% (expressed in atomic %). However, it was possible to estimate the Si/Al ratio, expressed in atomic %. (Tab. a.2.6).

Tab a.2.6 Determination of the Al/Si ratio of synthetic AlQz crystals (AlQz12 and AlQz16), calculated through XRF spectrometry investigation

Sample	Al/Si ratio (At%)
Qz-syn	0
AlQz12	2.31
AlQz16	2.67

The present values do not match the theoretical stoichiometric ratio of the precursors in the synthesis (see Tab. a.2.1). We can hypothesize that this is due to the significant amount of Si atoms observed into the byproduct phase, thus excluded from quartz growth. On the contrary, the evaluation suggests that aluminium atoms can get into the quartz crystals bulk up to a specific concentration. The remaining surplus is redistributed as constituent of a foreign phase.

a.7 Discussion

Through the full characterization of the key physico-chemical features of synthetic quartz samples, we were able to investigate the main crystallographic features and evaluate possible differences among highly-pure and Al-doped quartz crystals. XRD analysis evidenced the full crystallinity of all samples, and the absence of any amorphous phase. Crystal morphology, evaluated by means of SEM microscopy, highlighted the presence of micron-sized spherical aggregates (spherulites), due to very small bubbles entrapped inside the gel, which act as nucleation centers for the crystal growth (Pastero et al., 2016). Crystal surfaces appeared to be smooth and lacking of structural fractures. The addition of aluminium ions in the system, in the form of aluminium hydroxide, did not implicate the loss of the crystalline structure of quartz. Moreover, we also observed (through EDS and XRF) the possibility to insert aluminium ions within the crystal lattice, in place of silicon ions. However, due to the extreme low concentration of bulk Al (< 0.2%, as atomic%), it was not possible to observe significant variations of the crystal structure (XRD, Raman spectroscopy). The increasing of Al concentration in the growth medium did not result in a significant enrichment of bulk aluminium in quartz crystals, but led to the generation of foreign crystalline phases with a particular fibrous morphology,

although in limited amounts, composed of silicon, aluminium and sodium oxides (EDS). In this context, XRF and EDS evaluations, which observed aluminium preferentially in the peripheral regions of quartz spherulites, suggested that the incorporation of Al atoms in the crystal lattice of quartz is not favoured, but, on the contrary, the process starts to take place as the Si/Al atomic ratio in the system decreases. Thus, the growth of mixed phases (e.g. aluminosilicates), it should not come as a surprise.

This aspect has been also confirmed by Raman analysis. Through this investigation, we assigned elongated structures to the mineral family of fibrous zeolites, supposedly a Na, Si and Al-containing zeolite known a Na-mazzite, characterized by a fibrous structure. All these elements were present into the Na-MTS solution. In view of that, it is reasonable to assume that a relatively high concentration of aluminium in the gel led towards the separation of secondary crystal phases, rather than the inclusion of Al ions into the quartz bulk (thus, confirming previous speculations). In this view, further modifications of the synthetic approach will be needed to efficiently increase the concentration of Al ions inside the crystal lattice, in order to observe the desired structural alterations.

Furthermore, Raman analysis suggested, especially for AlQz samples, the presence of moganite, a meta-stable crystalline silica polymorph, which might act as a quartz precursor. The intensity of moganite Raman peak, centered at ca. 502 cm^{-1}, appears to be not proportionally related with the amount of aluminium into the system, but just associated to its presence.

Moganite may act as a precursor of quartz. Hence, during the synthetic pathway, it can be assumed that the direct crystallization of quartz occurs only in the event that the process is stabilized by an accessory phase. Differently, the presence of precursors is needed, to grow quartz crystals. This specific case of crystal growth is denominated *heterogeneous nucleation (Pastero et al., 2016)*

Surface area of AlQz crystals was considerably lower in respect to that of synthetic pure quartz crystals (2-4 m^2/g versus 6.2 m^2/g). Such low values were not imputable to huge differences in crystal size among doped and pure dusts, but to the growth of micrometric spherulites, often intimately connected one to each other. Moreover, it is reasonable hypothesize that the introduction of Al ions, although not substantially affecting the average size of the unit cell of quartz, led to a different morphology in respect to pure crystals, resulting in variations of the particle surface area. This scheme may be due to a less defective and complex crystal surface. Furthermore, surface modification of Al-quartz crystals was also confirmed by the investigation of the acidity of surface silanols, performed through acid-base titration, by means of evaluation of the zeta potential vs pH. ζ-potential of quartz crystals doped with aluminium is strongly negative at physiological pH, becoming more positive only at acidic values, with

a trend similar to that of pure silica crystals. Nevertheless, comparing the ζ-plot, a non-negligible difference in the pattern of each single curve can be underlined among the Al-samples, in particular at pH < 5. This aspect corroborates the hypothesis of a substantial surface variability due not only to aluminium ions into the crystal bulk, but also to the increasing concentration of ions (depending on the quantity of $Al(OH)_3$ added during the synthetic route), which affect the surface distribution of silanol families. Sample AlQz12 was characterized by a gentler slope of the zeta-potential curve in respect to samples 15-16, thus reflecting a larger heterogeneity of silanols at the surface of particles (Turci et al., 2016). On the other hand, the dust contained a not negligible presence of accessory phase, grown due the introduction of $Al(OH)_3$ as aluminium precursor: this phase may strongly contribute to the variation of the titration curve. Furthermore, the higher amount of aluminium, could also result in higher concentration of surface species more acidic than silanols on the surface of quartz crystals, such as Al-OH or Si-OH interacting with vicinal Al^{3+}. Incorporation of aluminium into the crystal bulk could also result in a partial loss of crystallinity because of eventual distortions of the crystal lettuce. However, eventual crystallinity loss, was not detected through XRPD investigation, in any synthetic sample.

Obviously, a further chemical-physical characterization is required to investigate the key features of the unit cell in greater detail, in order to evaluate differences among synthetic quartz crystals with and without bulk impurities, and for a better understanding of changes in distribution and displacement of surface moieties, which can strongly affect the pathogenic potential of dusts, through more direct techniques (i.e. FTIR spectroscopy and TEM imaging).

Bibliography

Chen, K. L., & Bothun, G. D. (2014). Nanoparticles meet cell membranes: Probing nonspecific interactions using model membranes. *Environmental Science and Technology*, *48*(2), 873–880. https://doi.org/10.1021/es403864v

Donaldson, K., & Borm, P. J. A. (1998). The quartz hazard: A variable entity. *Annals of Occupational Hygiene*, *42*(5), 287–294. https://doi.org/10.1016/S0003-4878(98)00044-1

Donaldson, K., & Seaton, A. (2012). A short history of the toxicology of inhaled particles. *Particle and Fibre Toxicology*, *9*(1), 13. https://doi.org/10.1186/1743-8977-9-13

Duval, Y., Mielczarski, J. A., Pokrovsky, O. S., Mielczarski, E., & Ehrhardt, J. J. (2002). Evidence of the existence of three types of species at the quartz-aqueous solution interface at pH 0-10: XPS surface group quantification and surface complexation modeling. *Journal of Physical Chemistry B*, *106*(11), 2937–2945. https://doi.org/10.1021/jp012818s

Fenoglio, I., Fubini, B., Ghibaudi, E. M., & Turci, F. (2011). Multiple aspects of the interaction of biomacromolecules with inorganic surfaces. *Advanced Drug Delivery Reviews*. https://doi.org/10.1016/j.addr.2011.08.001

Fenoglio, I., Fubini, B., Tiozzo, R., & Di Renzo, F. (2000). Effect of micromorphology and surface reactivity of several unusual forms of crystalline silica on the toxicity to a monocyte-macrophage tumor cell line. *Inhalation Toxicology*, *12*(3), 81–89. https://doi.org/10.1080/08958370050164914

Fubini, B. (1998). Surface chemistry and quartz hazard. *Annals of Occupational Hygiene*. https://doi.org/10.1016/S0003-4878(98)00066-0

Fubini, B., Fenoglio, I., Elias, Z., & Poirot, O. (2001). Variability of biological responses to silicas: effect of origin, crystallinity, and state of surface on generation of reactive oxygen species and morphological transformation of mammalian cells. *J.Environ.Pathol.Toxicol.Oncol.*, *20 Suppl 1*, 95–108. https://doi.org/10.1615/JEnvironPatholToxicolOncol.v20.iSuppl.1.90

Gillet, P., Le Cléac 'h, A., & Madon, M. (1990). High-temperature Raman spectroscopy of s io2 and geo2 polymorphs: anharmonicity and

thermodynamic properties at high-temperatures. *Journal of Geophysical Research, 95655*(10), 635–21. https://doi.org/10.1029/JB095iB13p21635

International Agency for Research on Cancer (IARC, 1997) Working Group on the Evaluation of Carcinogenic Risks to Humans. Silica, some silicates, coal dust and para-aramid fibrils. Lyon, 15-22 October 1996. Monogr. Eval. Carcinog. Risks Hum. 68:1 – 475

Kingma, K. J., & Hemley, R. J. (1994). Raman spectroscopic study of microcrystalline silica. *American Mineralogist*.

Leung, K., Nielsen, I., & Criscenti, L. (2009). Elucidating the bimodal acid– base behavior of the water– silica interface from first principles. *Journal of the American Chemical Society*, *131*(51), 18358–18365. https://doi.org/10.1021/ja906190t

Ong, S., Zhao, X., & Eisenthal, K. B. (1992). Polarization of water molecules at a charged interface: second harmonic studies of the silica/water interface. *Chemical Physics Letters*, *191*(3–4), 327–335. https://doi.org/10.1016/0009-2614(92)85309-X

Pastero, L., Turci, F., Leinardi, R., Pavan, C., & Monopoli, M. (2016). Synthesis of α-Quartz with Controlled Properties for the Investigation of the Molecular Determinants in Silica Toxicology. *Crystal Growth and Design*, *16*(4), 2394–2403. https://doi.org/10.1021/acs.cgd.6b00183

Pavan, C., & Fubini, B. (2017). Unveiling the Variability of "Quartz Hazard" in Light of Recent Toxicological Findings. *Chemical Research in Toxicology*, *30*(1), 469–485. https://doi.org/10.1021/acs.chemrestox.6b00409

Rimola, A., Costa, D., Sodupe, M., Lambert, J. F., & Ugliengo, P. (2013). Silica surface features and their role in the adsorption of biomolecules: Computational modeling and experiments. *Chemical Reviews*. https://doi.org/10.1021/cr3003054

Sun, B., Wang, X., Liao, Y. P., Ji, Z., Chang, C. H., Pokhrel, S., Xia, T. (2016). Repetitive Dosing of Fumed Silica Leads to Profibrogenic Effects through Unique Structure-Activity Relationships and Biopersistence in the Lung. *ACS Nano*, *10*(8), 8054–8066. https://doi.org/10.1021/acsnano.6b04143

Turci, F., Pavan, C., Leinardi, R., Tomatis, M., Pastero, L., Garry, D., Fubini, B. (2016). Revisiting the paradigm of silica pathogenicity with synthetic quartz crystals: the role of crystallinity and surface disorder. *Particle and Fibre Toxicology*, *13*(1), 32. Retrieved from http://www.ncbi.nlm.nih.gov/pubmed/27286702%5Cnhttp://www.pubm edcentral.nih.gov/articlerender.fcgi?artid=PMC4902968

Verma, A., & Stellacci, F. (2010). Effect of surface properties on nanoparticle-cell interactions. *Small*. https://doi.org/10.1002/smll.200901158

The pathogenetic paradigm of quartz: the role of crystallinity and surface features

3.1 Background

Since ancient times, crystallinity is traditionally considered as the key feature for silica pathogenicity. Nevertheless, according to IARC (*IARC monograph, volume 68*), which classified, in 1997, crystalline silica as a Group 1 carcinogen, not all forms of crystalline silica dusts are equally pathogenic. In its monography, IARC stated that "…*the Working Group noted that carcinogenicity in humans was not detected in all industrial circumstances studied. Carcinogenicity may be dependent on inherent characteristics of the crystalline silica or on external factors affecting its biological activity or distribution of its polymorphs…*". Furthermore, it has been recently demonstrated (Costantini, Gilberti, & Knecht, 2011; Kim, Joachim, Choi, & Kim, 2015; Yu et al., 2009) that several amorphous silicas have the potential to cause adverse cellular effects, often linked to the development of silica-related pathologies. Moreover, vitreous silica particles, which show the same biological responses of quartz in vitro, share with quartz all the physico-chemical properties, except crystallinity (Ghiazza et al., 2010; Fubini, 1998). Thus, the classical paradigm of crystalline silica toxicity, specifically based on its crystalline character, comes under discussion. To date, even though several studies have been carried out, the specific role of each physico-chemical feature of quartz in triggering a specific biological effect remains unclear, due to, not only the extreme variability of silica sources analysed, but also the variability introduced during industrial processing, which hugely alters several key surface features.

In view of that, in order to shed light on these aspects, we have investigated, at a molecular level, the role of crystallinity in quartz pathogenicity, through synthetic crystals with tuneable properties, grown under controlled conditions. Crystals were synthesized in submicrometric (n-Qz-syn) and micrometric (μ-Qz-syn) size. Both fractions were full respirable. A portion of the micrometric fractions was mechanically fractured, in order to introduce surface structural and morphological alterations (μ-Qz-syn-f). Results of the in-vitro assays were compared to that of a mineral quartz dust, well known for its toxicity.

3.2 Experimental section and discussion

As-grown and fractured quartz crystals with tuneable properties, synthesized *ad-hoc* (see Pastero et al., 2016), were tested, and compared to mineral quartz dusts, in several cellular and acellular assays relevant for the pathogenicity of silica particles, including:

  i)   membrano-perturbative activity towards artificial (phosphatidylcholine unilamellar liposomes) and biological (red blood cells, RBCs) membranes, at different complexity (see fig.3 of appended paper "Revisiting the paradigm of silica pathogenicity with

synthetic quartz crystals: the role of crystallinity and surface disorder", by Turci et al., *Part. Fibre Tox.*, 2016)

ii)   cell viability and stress-related endpoints in murine macrophages, through a high content analysis (High Content Assay) (see fig. 2 of Turci et al., 2016)

iii)   particle uptake/internalization (bio-TEM) (see fig. S2 of Turci et al., 2016, supporting materials).

Independently from size, intact crystals with regular faces did not show cellular toxicity and lysosomal stress, and were inert towards membrane models. Upon fracturing, synthetic quartz particles attained the typical morphology of natural dusts, and induced cellular toxicity and strong membrane perturbative activity. Furthermore, fracturing imparted a higher heterogeneity of silanol acidic sites (fig. 4, Turci et al., 2016) and radical species (fig. 5) at the quartz surface.

Data allowed us to hypothesize that the biological reactivity of quartz was actually related to chemical disorder in the crystal lattice, and not purely and simply to crystallinity, thus contradicting the classical paradigm for quartz toxicity. The progressive surface reconstruction, occurring upon mechanical fracturing, can in fact leave hydrophilic and hydrophobic patches and disordered silanol arrays, similar to the surface of some amorphous silicas, reported as highly haemolytic (Zhang et al., 2012).

3.3 Main achievements

Data of the work in question are consistent with the notion that most of the biological reactivity of quartz dusts is originated via fragmentation, when cell membranes and tissues interact with conchoidal fractures and not with regular as-grown crystal faces. This indicates that a regular and homogeneous distribution of the silanols at the particle surface was shown to occur in synthetic as-grown quartz crystals. Then, mechanical fracturing led to a disorganization of these surface moieties, causing a loss of the long-range spatial order and probably creating reactive surface silanol patches. The increasing in surface silanols heterogeneity degree in acidity was assessed by ζ potential evaluation, before and after mechanical fracturing, and it was evidenced by the lower steepness of the ζ plot (ζ potential *vs.* pH). Thus, biological reactivity, and possibly toxicity, appears related with disordered surface functionalities following crystal structure.

3.4 Publication 2: Revisiting the paradigm of silica pathogenicity with synthetic quartz crystals: the role of crystallinity and surface disorder

(Turci, Pavan, Leinardi, Tomatis, Pastero, Garry, Anguissola, Lison, & Fubini; Particle and Fibre Toxicology, 2016)

Author's contribution: RL performed synthesis and part of physical-chemical characterization of quartz crystals, including surface area determination (BET), solid state electron paramagnetic resonance (EPR) spectroscopy, carbon-centered free radical detection (EPR) coupled with the spin trapping technique, and ζ Potential evaluation (ELS). Moreover, he carried out the preparation and leakage assay of phosphatidylcholine vesicles, and part of data analysis, under the supervision of FT.

Bibliography

Costantini, L. M., Gilberti, R. M., & Knecht, D. A. (2011). The phagocytosis and toxicity of amorphous silica. *PLoS ONE*, *6*(2). https://doi.org/10.1371/journal.pone.0014647

Ghiazza, M., Polimeni, M., Fenoglio, I., Gazzano, E., Ghigo, D., & Fubini, B. (2010). Does vitreous silica contradict the toxicity of the crystalline silica paradigm? *Chemical Research in Toxicology*, *23*(3), 620–629. https://doi.org/10.1021/tx900369x

International Agency for Research on Cancer (IARC, 1997) IARC Monographs on the Evaluation of Carcinogenic Risks to Humans. Lyon: IARC; Silica, Some Silicates, Coal Dust and Para-Aramid Fibrils. [

Kim, I. Y., Joachim, E., Choi, H., & Kim, K. (2015). Toxicity of silica nanoparticles depends on size, dose, and cell type. *Nanomedicine: Nanotechnology, Biology, and Medicine*, *11*(6), 1407–1416. https://doi.org/10.1016/j.nano.2015.03.004

Turci, F., Pavan, C., Leinardi, R., Tomatis, M., Pastero, L., Garry, D., Fubini, B. (2016). Revisiting the paradigm of silica pathogenicity with synthetic quartz crystals: the role of crystallinity and surface disorder. *Particle and Fibre Toxicology*, *13*(1), 32. Retrieved from http://www.ncbi.nlm.nih.gov/pubmed/27286702%5Cnhttp://www.pubmedcentral.nih.gov/articlerender.fcgi?artid=PMC4902968

Yu, K. O., Grabinski, C. M., Schrand, A. M., Murdock, R. C., Wang, W., Gu, B., … Hussain, S. M. (2009). Toxicity of amorphous silica nanoparticles in mouse keratinocytes. *Journal of Nanoparticle Research*, *11*(1), 15–24. https://doi.org/10.1007/s11051-008-9417-9

Zhang, H.Y., Dunphy, D.R., Jiang, X.M., Meng, H., Sun, B.B., Tam, D., Xue, M., Wang, X., Lin, S.J., Ji, Z.X., et al. (2012). Processing pathway dependence of amorphous silica nanoparticle toxicity: colloidal vs pyrolytic. *Journal of American Chemical Societ*y, 134:15790-804

Chapter 3

Amorphous silica & membrane-perturbative activity: interaction of surface-controlled silica nanoparticles with natural and synthetic membrane models

4.1 Background

In the last few years, the rapid growth of nanotechnology has brought a strong increase in the use of nanomaterials in several human activities. Although they represent a new frontier in material science, the unknown effects on human health and environment, are becoming a problematic issue (Borm et al., 2006; Handy & Shaw, 2007; Kuempel, Geraci, & Schulte, 2012; Ray, Yu, & Fu, 2009; Tetley, 2007). Nanoparticles (NPs) may enter an organism through different routes (inhalation, intravenous injection or skin absorption), each of which lead to different biological reactions. The eventual negative effects of nanoparticle interactions on cell membrane, organelles and macromolecules, can be represented by oxidative stress, lipid peroxidation, inflammatory response, or DNA damage (A. Nel, 2006). By contrast, cell-internalized nanoparticles could be used for benefit effects in cancer gene therapy, imaging and diagnostics. During these processes, the contact with biomembrane (e.g. cell membrane) is not avoidable (He et al., 2015): the direct contact of NPs with cell membrane, may cause membrane rupture and cytotoxic effects (De Planque, Aghdaei, Roose, & Morgan, 2011). Mesoporous silica nanoparticles (SNPs) were recently proposed as intravenous drug-delivery system and imaging agents, even if several authors reported about SNPs being hemolytic (Kettiger, Québatte, Perrone, & Huwyler, 2016). It is well known that when nanoparticles get in direct contact with blood constituents, interaction with plasma components, immune cells, and erythrocytes, occur. As confirmed by many works published during the last 50 years, silica amorphous particles are hemolytic towards mammalian red blood cells (Diociaiuti et al., 1999; Murashov et al., 2006; Nash et al., 1966; Razzaboni & Bolsaitis, 1990). Several explanations for hemolytic activity have been proposed: generation of ROS induced by surface of silica (Nash et al., 1966), denaturation of membrane proteins upon electrostatic interactions with silicate (Balduzzi, Diociaiuti, De Berardis, Paradisi, & Paoletti, 2004), interaction between silicates and tetra-alkyl-ammonium groups on RBCs membrane (Depasse & Warlus, 1976; Stodghill, Smith, & O'Haver, 2004; Yawata, 2003). The exact mechanism, however, is still a very active subject.

The surface chemistry of amorphous silica consists of several species, including geminal, vicinal (which increase the hydrophilic character of silicas) and isolated (typical in more hydrophobic surfaces) silanols, siloxane bridges (Si-O-Si) and ionic species (Si-O⁻). Generally, the relative density of these groups is related to the synthetic route (Patwardhan et al., 2012; Rimola et al., 2013). To date, many works carried out in the field indicate that silica hemolytic activity is related to the density of surface silanol groups (Murashov et al., 2006). Moreover, Slowing et al. (Slowing, Wu, Vivero-Escoto, & Lin, 2009), investigating the eventual differences in hemolysis between mesoporous and amorphous non-porous silica nanoparticles, reported that mesoporous particles showed low hemolytic

potential than amorphous. According to Lin and Haynes (Y.-S. Lin & Haynes, 2010), size-dependent hemolysis of mesoporous silica occurs only when the nanoparticles have a long-range ordered porous structure, but the hemolytic activity is still lower in respect to nonporous silica particles of similar size. Furthermore, they showed that nanoparticle-induced hemolysis can be eliminated through modifying the surface silanols with a poly(ethylene glycol) (PEG) coating (Y. S. Lin & Haynes, 2009), thus affecting the biocompatibility degree of particles. To clarify how silica amorphous nanoparticles may exert several and different biological effects, we have investigated the molecular mechanism that drive the interaction between silica surface and biological membrane, through the evaluation of perturbation events caused by dense and mesoporous amorphous silica nanoparticles on simplified (liposome) and complex (red blood cells) membrane models. Since the past, RBC plasma membrane was used as model for membrane characterization for its easy isolation and preservation (Cooper & Sunderland, 2000). The effects of interaction between nanoparticles and RBC are based on different parameters: hemolytic activity, deformation of morphological alterations of plasma membrane (Zhao et al., 2011). Concerning liposomes, a large collection of methods has been used to characterize nanoparticle interaction with liposome membranes (Rascol, Devoisselle, & Chopineau, 2016). One of the most common approach to assay the propensity of nanoparticles to perturb lipid membrane is the liposome leakage assay (Chen & Bothun, 2014; Leroueil et al., 2007, 2008), in which the amount of dye leakage is indicative of nanoparticle-induced membrane perturbation. To this aim, we have explored the effect of surface charge, surface geometry and surface silanol groups of two sets of surface-controlled amorphous silica nanoparticles, mesoporous and dense, contacted with membrane models, different in complexity. Results of each set were compared to a pyrolytic silica (P-SiO$_2$, namely Aerosil®50 by Evonik), well characterized and known for its membranolytic potential.

The experiments were conducted on mesoporous and nonporous (dense) silica nanoparticles, before and after surface functionalization with amino-propyl groups.

4.2 Experimental section

4.2.1 Silica samples

We have evaluated a set of silica nanoparticles (see Tab. 4.1), divided into two main groups:

i) Mesoporous silica nanoparticles (MSN), in native form (MSN-OH), and surface-functionalized with aminopropyl groups (MSN-NH$_2$), were synthesized by the group of Dr. Gloria Berlier (dept. of Chemistry, University of Turin, Italy). Synthetic route, physico-chemical characterization and functionalization technique are reported in the work of Musso and coworkers (Musso, Bottinelli, Celi, Magnacca, & Berlier, 2015).

ii) Dense silica nanoparticles (DSN), in native form (DSN-OH), and surface functionalized with aminopropyl groups, were synthesized and supplied by the group of Prof. Gianmario Martra (dept. of Chemistry, University of Turin, Italy). Chemical functionalization was carried out via one-pot (DSN-HD, *high-density* of surface NH$_2$-groups) route (Catalano et al., 2015)

iii) P-SiO$_2$, namely Aerosil OX 50, a non-porous pyrolytic silica, from Evonik Industries (Essen, Germany), with primary particle size of 40 nm and specific surface area of 50 m^2/g.

Size, evaluated through electron microscopy, specific surface area (excluding pores, for mesoporous particles), evaluated by BET (Branauer-Emmett-Teller) method, surface charge, by means of ζ-Potential through ELS (Electronic Light Scattering) technique and dispersion state in aqueous media, assessed via DLS (Dynamic Light Scattering), are summarized in the table below (Table 4.1).

Table 4.1: Physico-chemical characterization of investigated silica nanoparticles.

Sample	Surface state	External SSA BET (m²/g)	DLS Size (nm) [£]	ζ-Potential @ pH 7.4 (mV)[£]	Silanol density (OH/nm²)	DLS Dispersion State[£]
MSN-OH	pristine	290	275±11	-18.4±1.42	3.3*	Agglomerate
MSN-NH$_2$	-NH$_2$	290	> 1000	+4.74±0.41	-	Agglomerate
DSN-OH	pristine	95	111±10	-22.1±1.30	3-4[#]	Monodisperse
DSN-HD	-NH$_2$	80	>1000	+11.3±0.94	-	Agglomerate
P-SiO$_2$	pristine	ca. 50	450±10	-35±2.50	1.6[#]	Agglomerate

[*] Musso et al., PCCP, 2015 – Valentina Ricci, Master degree thesis, University of Torino, 2016

[#] Catalano et al., JPCC, 2015

[£] evaluated by means of DLS and ELS technique, in 0.01 M PBS (pH 7.4)

4.2.2 Analysis of particle size and dispersion state (DLS)

DLS technique was used to evaluate particle dispersion state in 0.01 M phosphate buffer (PBS), pH 7.4.

- MSN-OH were suspended at a concentration of 100 µg/ml in 0.01 M PBS, pH 7.4. Suspension was probe-sonicated for 60 sec., power 25 W. 80 µl of the suspension were dispersed in 1 ml of 0.01 M PBS. The same dispersion protocol was maintained for MSN-NH$_2$.
- An aliquot of 80 µl of a parent suspension of DSN-OH particles was transferred in 1 ml of ultrapure water (milliQ, Millipore). No sonication passage was necessary for particle dispersion. The same dispersion protocol was used for DSN-HD.
- P-SiO$_2$ particles were dispersed at a concentration of 0.5 mg/ml in 0.01 M PBS, pH 7.4. Dispersion was probe-sonicated 3 minutes, at 25% amplitude.

4.2.3 Evaluation of the surface charge in the analysis medium

Silica nanoparticles surface charge, in 0.01 M PBS, pH 7.4, was evaluated by means of electrophoretic light scattering (ELS) (Zetasizer Nano-ZS). In this technique, the velocity of a particle in an oscillating electric field, which is proportional to its ζ-Potential, is measured by light scattering.

i) MSN: MSN-OH were suspended at a concentration of 100 μg/ml in 0.01 M PBS, pH 7.4. Suspension was probe-sonicated for 60 sec., power 25 W. 80 μl of the suspension were dispersed in 1 ml of 0.01 M PBS. The pH of the suspension was then adjusted with 0.1M HCl or 0.1M NaOH. The same dispersion protocol was maintained for MSN-NH$_2$.

ii) DSN: 80 μl of a parent DSN-OH suspension were transferred in 1 ml of 0.01 M PBS (milliQ, Millipore), to evaluate the ζ-Potential at pH 7.4, only. No sonication passage was performed. The same dispersion protocol was used for DSN-HD.

iii) P-SiO$_2$: 5 mg of particles were suspended in 10 ml of 0.01 M PBS, and the zeta potential was evaluated at a pH 7.4. Before the measurement, particle dispersion was probe sonicated for 3 minutes at 25% of amplitude.

4.2.4 Preparation of liposomes as biomembrane model

Calcein (a fluorescent dye with excitation and emission wavelengths of 495/515 nm, respectively, which self-quenches at concentrations above 70mM, commonly used as indicator of lipid vesicle leakage) was included inside unilamellar phosphatidylcholine vesicles, prepared through hydration of a dry lipid film and purified by size exclusion chromatography using a Sepharose CL-4B gel (GE Healthcare, UK). 10 mg of α-L-phosphatidylcholine (Sigma-Aldrich, MO, USA) were dissolved in a mixture of methanol-chloroform (1:2 V/V), which was then evaporated with a rotary evaporator (*Büchi Rotavapor R*-200*, Büchi,* Germany) and a stream of nitrogen gas. The lipid film was then hydrated with 5 ml of a 0.01M calcein solution in 0.01 M PBS, which had been adjusted to pH 7.4 with NaOH to ensure complete solubilization of the calcein crystals. To separate the calcein-loaded vesicles from the free calcein molecules, a gel filtration step was performed. Approximately, 1 ml of liposome dispersion was loaded in a syringe column filled with 10 ml of Sepharose CL-4B beads (GE Healthcare, UK), using 0.01 M PBS as eluent. The vesicles were then stored at +4°C and used within 1 week. Liposome dispersion was characterized by dynamic light scattering (DLS) and ζ-potential measurements (ZetaSizer Nano-ZS, Malvern

Instruments, Worcesterchire, UK) at pH 7.4, at 25°C. The ζ-Potential, evaluated at pH 7.4, was -12±0.9 mV.

4.2.5 Evaluation of the interaction between particles and artificial biomembrane: liposome leakage assay

The leakage test is a commonly used assay for probing membrane integrity in intensity. In our experiments, each silica sample was suspended in PBS 0.01M, pH 7.4, immediately before the incubation. The amount of silica was selected to have a final dose concentration of 100 µg/ml. The stock suspension was sonicated 60 seconds, in ice, at 30% amplitude, and then diluted to the final concentrations for experiments (100, 50, 25, 12.5, and 6.25 µg/ml) in 0.01 M PBS. The method refers to the works of Alkhammash & coworkers and Lodokhin & coworkers, with minor modifications given by Turci and colleagues (Alkhammash et al., 2015; Ladokhin, Wimley, & White, 1995; Turci et al., 2016). Liposomes were diluted (1:16) in 0.01 M PBS and then distributed (200 µl per well) in a 96-well microplate. Negative and positive controls consisted of 0.01 M PBS and 20% Triton X-100, which disrupts 100% of vesicles. With an excitation wavelength of 490 nm and an emission wavelength set at 520 nm, a baseline fluorescence signal was recorded. Subsequently, the appropriate amount of particles (20 µl) in 0.01 M PBS (in quadruplicate for each concentration) was added to each well and the same volume of 0.01 M PBS was added to wells containing only liposome dispersion, to consider fluorescence decrease due to dilution. Then, after 30 minutes of incubation, two fluorescence signals were measured (I_t (liposomes + silica particles) and I_{t0} (liposomes + PBS), respectively). Finally, 20 µl of a 20% solution of Triton X-100 were added to completely disrupt the vesicles and to determine the fluorescence intensity (I_{max}) for complete release of the self-quenching dye from the vesicles. The percentage of dye release from the vesicles, for each concentration, was calculated as:

$$\frac{I_t - I_{t0}}{I_{max} - I_{t0}} * 100$$

Fluorescent assay measurements were performed using a FLX 800 Fluorescence Reader (BioTek Instruments Inc., VT, USA). Released calcein did not adsorb on silica samples.

Samples were prepared as follows:

MSN: pristine and amino-functionalized mesoporous silica nanoparticles (1 mg) were suspended in 1 ml of 0.01 M PBS and sonicated in ice with an ultrasonic probe (60 seconds, 25 W, Sonoplus, Bandelin, Berlin, Germany). The initial suspension (1000 cm^2/ml) was diluted to the final concentrations for experiments (100-50-25-12.5-6.25 µg/ml for liposome leakage, 500-250-100-50-25-6.25 µg/ml for hemolysis) in 0.01 M PBS.

- *DSN*: pristine and amino-functionalized dense silica nanoparticles were dispersed in 0.01 M PBS to reach a final volume of 1 ml and sonicated with the same procedure used for MSN. The initial suspension (1000 cm^2/ml) was diluted to the final concentrations for experiments (100-50-25-12.5-6.25 µg/ml for liposome leakage, 500-250-100-50-25-6.25 µg/ml for hemolysis) in 0.01 M PBS.

- *P-SiO$_2$*: a well characterized pyrolytic silica, was used as positive control. 1 mg of powder was suspended in 1 ml of 0.01 M PBS and horn-sonicated with the same procedure as for the other silica particles. The initial suspension (1000 cm^2/ml) was diluted to the final concentrations for experiments, comparable to MSN and DSN doses, in 0.01 M PBS.

4.2.6 Calcein fluorescence curve characterization
To carried out a titration curve of calcein, 187 mg of calcein powder was suspended in 3 ml of 0.01 M PBS. The stock solution (100 mM) was then diluted to the final concentrations for the assay (10-1-0.1-0.01 and 0.001 mM), in 0.01 M PBS, pH 7.4. Each concentration was distributed (200 µl) in quadruplicate in a 96-well plate, and fluorescence emission was recordered at 520 nm. For each concentration, fluorescence intensity was expressed as mean±standard deviation (SD) and plotted as a function of calcein concentration (mM).
Stability of calcein was then evaluated. Calcein (3.12 mg) was suspended in 5 ml of 0.01 M PBS. The stock solution was then diluted, in 0.01 M PBS, at the final concentrations for the measurements (0.5-0.1-0.01 mM). 200 µl of each calcein concentration was distributed in quadruplicate in a 96-well plate, and fluorescence emission at 520 nm was recorded after 0-15-30-45-60 minutes of incubation, at room temperature, in the dark. For each concentration, fluorescence intensity was expressed as mean±standard deviation (SD) and plotted as a function of calcein concentration (mM).

Calcein adsorption on particles: 187 mg of calcein were suspended in 3 ml of 0.01 M PBS. The stock suspension (100 mM) was then diluted to a final concentration of 0.01 mM, in 0.01 M PBS. MSN-OH were suspended in 1 ml of 0.01 M PBS and

sonicated in probe (60 seconds, 25 W), then diluted to the final concentrations for experiments (100-10-10 μg/ml). 200 μl of calcein solution were distributed in quadruplicate in a 96-well plate, and fluorescence emission was recorded as a "I_0" signal. 20 μl/well of silica nanoparticle dispersions were then distributed in quadruplicate, for each concentration. 200 μl of calcein solution were also distributed in quadruplicate as negative control (fluorescence "I_{neg}"). Fluorescence emission was evaluated at 0-15-30-60 minutes, and, for each well, calcein adsorption onto nanoparticles was calculated through the equation:

$$\% \, Adsorption: \frac{I_0}{I_{neg}} * 100$$

For each concentration, adsorption was expressed as the mean value ± standard deviation (SD).

4.2.7 Evaluation of the interaction between particles and natural biomembrane: hemolysis of human RBCs

In order to evaluate hemocompatibility of silica nanoparticles, and evidence possible difference among porous and dense ones, hemolysis assay was performed incubating erythrocytes with nanoparticles at increasing concentrations, expressed as surface dose area. The method (for assessing the hemolytic activity induced by particles refers to Lu et al. (Lu et al., 2009) with minor modifications given by Pavan and coworkers (Pavan et al., 2013). RBCs were separated from fresh human blood of healthy volunteer donors not receiving any pharmacological treatment by centrifugation (10 minutes, 1200 g) and purified with four washing in 0.9% NaCl (Eurospital, Trieste, Italy). Final red blood cells suspension contained 5% of RBCs in 0.01 M PBS. First, each particle concentration (150 μl/well) was distributed in quadruplicate in a 96 well-plate. Positive (6% Triton X 100) and negative (0.01 M PBS) controls were also added in quadruplets. Then, RBCs suspension (75 μl/well) was distributed in each well. The plate was incubated in agitation at room temperature for 60 minutes. After, it was centrifuged for 5 minutes at 1200 rcf and 24°C (Heraeus Megafuge 1.0R, Hereaus, Germany). From each well, 75 μl of supernatant were transferred in a new plate for UV/Vis measurement (Benchmark Plus Microplate Reader, BIO-RAD, CA, USA). The released hemoglobin was measured at 540 nm did not adsorbed on quartz samples (data not shown), and hemolysis percentage calculated according to Pavan and colleagues (Pavan et al., 2013).
A well-characterized commercial amorphous silica, P-SiO$_2$ (Aerosil OX 50, Evonik Industries, Germany), known for its strong hemolytic activity, well was used as reference sample.

The samples were prepared as follows:

- MSN: mesoporous silica nanoparticles (in pristine form and amino-functionalized) (2.4 mg) and P-SiO$_2$ were suspended in 1.6 ml of 0.01 M PBS and probe-sonicated in ice through an ultrasonic probe (Sonoplus, Bandelin, Germany) for 60 seconds, 25 W. The initial suspension (1000 µg/ml) was diluted to the final concentrations of 500-100-50-25-6.25 µg/ml, in 0.01 M PBS.

- DSN: stock suspensions of pristine and amino-functionalized nanoparticles (at a concentration of 1000 µg/ml) were diluted to the final concentrations of 500-100-50-25-6.25 µg/ml, in 0.01 M PBS., and probe-sonicated in ice for 60 seconds at 25 W.

The same protocol was followed for P-SiO$_2$ nanoparticles.

Hemoglobin adsorption on particles: adsorption of hemoglobin onto silica particles was evaluated through a methodology developed by Ferenc et al. Briefly, hemoglobin obtained from RBCs rupture, was purified (5% in 0.01 M PBS) and frozen at -80°C overnight. The suspension of red blood cells was centrifuged (1200 g, 10 minutes) to obtain a solution containing hemoglobin only. 150 µl of particles were distributed in a 96-well plate, for each concentration, and 150 µl/well of negative control were added in quadruplets. Then, hemoglobin was distributed (75 µl/well), and incubated with particles (60 minutes); the protocol follows the same used for the hemolysis assay. For each well, adsorption was calculated from the following equation:

$$\% \, Absorbance = \frac{Abs_{sample}}{Abs_{negative \, control}} * 100$$

For each concentration, adsorption was expressed as the mean value ± standard deviation (SD).

4.2.8 Statistical analysis of data

Data are expressed as the mean ± standard deviation (SD). The statistical significance of the differences among each sample was analysed using one-way analysis of variance (ANOVA) with Tukey's post-hoc test. Differences with p value < 0.005 were considered statistically significant.

4.3 Results

4.3.1 Calcein calibration curve

The calibration curve of calcein solution (concentration vs. fluorescence intensity, in 0.01 M PBS) was evaluated in the 10^{-3} - 100 mM range. Data (Fig. 4.1) evidenced a strong self-quenching above the concentration of 1 mM, and an almost negligible fluorescence at molar concentrations > 70 mM (according to the literature, see Alkhammash et al., 2015). In the 10^{-3}-1 mM range, the fluorescence intensity of calcein quickly increased with the dye concentration, until a maximum value, at ca. 1 mM. The increase was linear for 0-0.01 mM. This concentration range represents the linear detection regime for calcein. The last part of the curve showed a strong self-quenching activity of the probe, starting from 1 mM, at which the fluorescence intensity began to decrease.
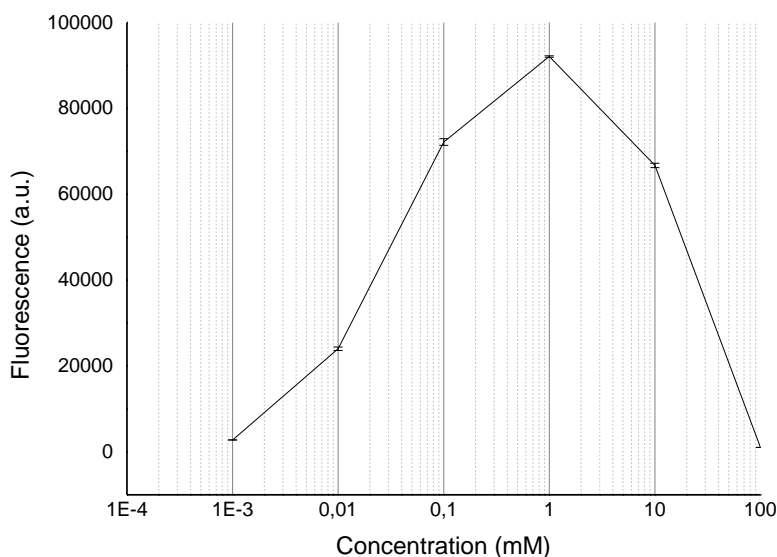
Fig. 4.1 Diagram of calcein calibration curve. Fluorescence intensity as a function of the calcein concentration was evaluated in 0.01M PBS, pH 7.4. Self-quenching of the fluorescence starts to prevail at a probe concentration of 1 mM.

4.3.2 Calcein stability

Fluorescence emission intensity was monitored over time (Fig. 4.2) for specific concentrations (0.01-0.1-0.5-1 mM), to exclude excessive degradation of the probe during the leakage assay and, thus, ensure reliable results.
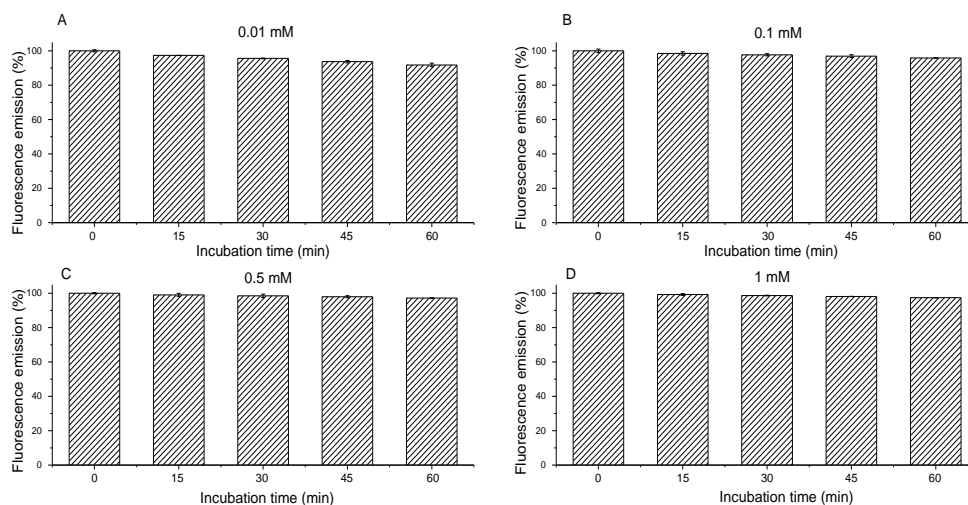
Fig. 4.2 Calcein stability evaluated by time-monitored fluorescence emission measurement, plotted as incubation time vs. % of fluorescence emission. A slight decay in fluorescence intensity is evidenced.

Results showed a fluorescence intensity decay of ca. 10% after 60 minutes, for the highest calcein concentration (0.01 mM, panel A). This effect may be due to a photo-induced damage of the fluorophore, due to light exposure during the incubation. Thus, during the assay, the probe needs to be carefully protected from light exposure.

4.3.3 Evaluation of calcein adsorption on particles

To exclude any undesired adsorption event of calcein onto surface of silica nanoparticles, the direct interaction between as-synthesized mesoporous particles (MSN-OH) and calcein, at a concentration of 100 mM, was evaluated (Fig. 4.3). In the case of adsorption phenomena occurred at the silica surface, the fluorescence emission should decrease as particle concentration increases.
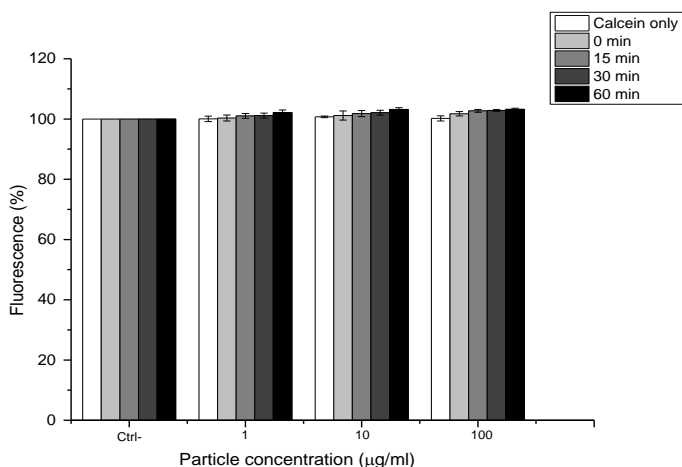
Fig. 4.3 Investigation of the calcein adsorption on MSN-OH. % of fluorescence related to the negative control (no particles) as a function of particle concentration.

Fluorescence data showed that intensity decay percentage at the presence of nanoparticles at each concentration investigated, did not differ from negative control (calcein without particles).

4.3.4 Liposomes characterization (size and surface charge)

Surface charge: liposome surface charge was evaluated by means of the ζ-Potential vs. pH, in 0.01 M PBS. Results indicated a negative charge predominance (-12±0.9 mV) at physiologic pH (7.4). This may due to the methyl group surrounding amine in the phosphatidylcholine head group, which reduce the positive charge contribution to electrophoretic mobility, thus resulting in negative phosphate charge prevalence in the measurement conditions.

Size distribution: vesicle size (Fig. 4.4) was evaluated through DLS technique. Results showed a bimodal size distribution profile, with the contemporary presence of micrometric and nanometric fractions. A rough estimate of the respective volumes of the nanometric and micrometric populations, could be obtained through the analysis of DLS data. Assuming that all liposomes had a spherical shape, the volume of the nanometric and micrometric fractions accounted for ca. 25 and 75% of the total liposome volume, respectively.

Z-Average: 166.7 nm
PdI: 0.309
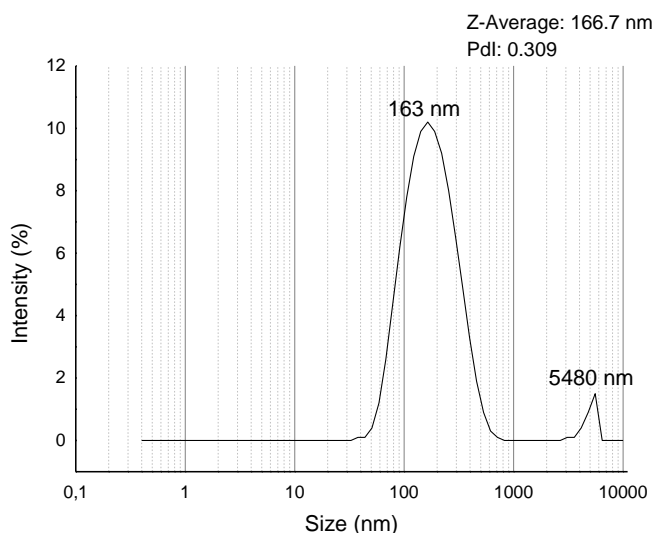
Fig. 4.4 Size distribution profile (nm) vs. % intensity of non-extruded lipid vesicles. It is possible to note a bimodal size distribution, with the peaks centred at ca. 160 and 5500 nm, respectively.

4.3.5 Investigation of the interaction between nanoparticles and membrane models at increasing complexity

Interaction between silica nanoparticles, in pristine and modified forms, and liposomes and red blood cells as biomembrane models was assessed through calcein liposome leakage assay and hemolysis assay, respectively (Ladokhin et al., 1995; Michel & Gradzielski, 2012; Moghadam, Hou, Corredor, Westerhoff, & Posner, 2012; Pera, Nolte, Leermakers, & Kleijn, 2014b; Sani, Gagne, Gehman, Whitwell, & Separovic, 2014; Wei et al., 2015). The method of leakage of fluorescent probe is based on the fluorescence quenching. The key principle of this assay is that the fluorescence of the dye is quenched in the vesicles, due to the high concentration, but upon leakage into the large volume of measurement buffer in the well, the dye becomes diluted and will fluoresce. Hence, the fluorescence intensity is directly proportional to the amount of dye that leaked out of the liposomes. Particle-liposome interaction can be therefore evaluated in terms of the extend of dye release, with substantial amount of leaked dye corresponding to significant particle-induced bilayer perturbation.

Hemolytic activity is assessed through the exposition of human red blood cells to the nanoparticles. Upon the incubation, the supernatant and intact cells are separated by centrifugation. At this stage, oxyhemoglobin present in the supernatant can be detected via UV-Vis spectrophotometry.

4.3.5.1 Part i) Membrane-perturbative activity of dense silica nanoparticles (DSN) vs pyrolytic silica

The interaction between dense silica nanoparticles, in pristine form and upon functionalization with aminopropyl groups, with artificial phosphatidylcholine liposomes and red blood cells, both negatively charged, was evaluated via liposome leakage assay and hemolysis, respectively (Fig. 4.5).
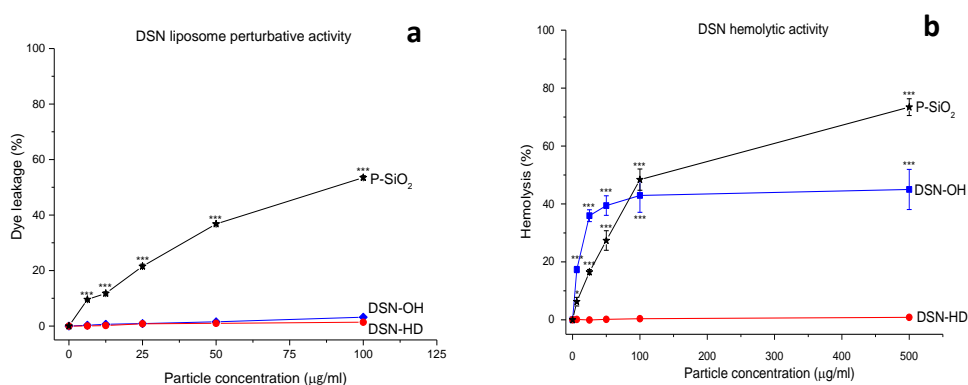
Figure 4.5 Liposome leakage (a) and hemolysis (b) induced by pristine and amino-functionalized dense silica nanoparticles. Particles were incubated ad increasing concentration (expressed in μg/ml) with phosphatidylcholine vesicles or purified human red blood cells (RBCs). Naked DSN (DSN-OH) showed a weak perturbative activity versus liposomes and a moderate hemolysis. Upon surface functionalization, haemolytic activity dramatically decreased.
P-SiO$_2$ was used as positive control, both for dye leakage and hemolysis. Values are mean ± SD from at least X independent experiments. *p < 0.05, **p < 0.01 and ***p < 0.001 *vs* control not exposed to silica particles.

The incubation of pristine dense silica nanoparticles, characterized by a substantial net negative charge, with artificial lipid vesicles, induced a negligible perturbative activity with a constant dose-response trend. On the other hand, a noticeable hemolytic activity was detected, with a burst phase at lowest particle concentration (≤ 50 μg/ml), which ends with a plateau at highest concentration. As expected, pyrolytic silica particles, showed a considerable perturbative activity towards liposomes in which a full set of silanol families is represented (isolated, weakly interacting and strongly interacting by H-bonds) (Catalano et al., 2015) and strong membranolysis.
To determine if the chemical functionalization of the surface with amynopropyl groups, which lead to a strong decrease in the silanol density, affects the degree

of interaction, dye leakage and hemolytic activity induced upon the incubation of membrane models with amino-functionalized DSN (DSN-HD) was carried out. Pristine and functionalized DSN are different for surface charge (pristine: negative; amino-functionalized: positive) and agglomeration state, at pH 7.4.

As showed in Fig. 4.5, consequently to the surface functionalization, the formerly weak perturbative activity towards liposomes of native DSN was totally quenched. Same quenching effect, was evidenced towards red blood cells. Taken together, data indicate that the alteration in surface Si-OH amount due to chemical masking with aminogroups, results in a substantial decrease in the interaction degree.

No significant adsorption of hemoglobin or calcein occurred on the particles.

4.3.5.2 Part ii) Membrane-perturbative activity of mesoporous silica nanoparticles (MSN) vs pyrolytic silica
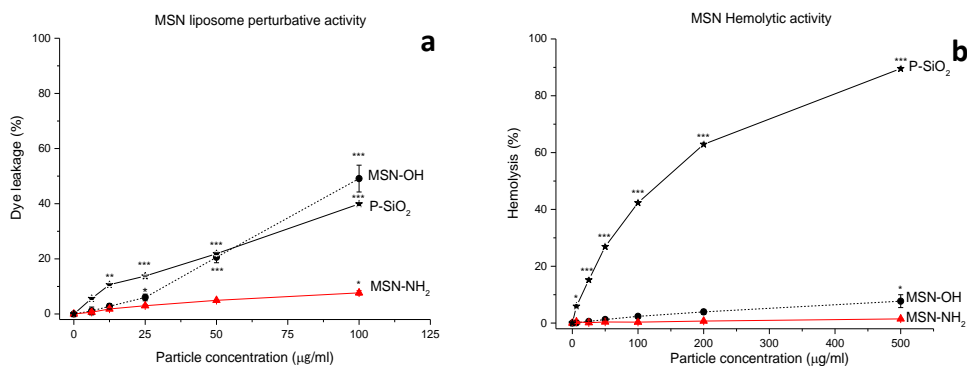
Figure 4.6 Liposome dye-leakage (a) and hemolysis (b,) induced by pristine and NH$_2$-functionalized mesoporous silica nanoparticles. Different perturbative behaviour clearly appears between the two membrane models. In both cases, surface chemical modification led to a reduction in perturbative activity (extreme, toward liposomes). Values are mean ± SD from at least X independent experiments. *p < 0.05, **p < 0.01 and ***p < 0.001 *vs* control not exposed to silica particles.

The membrano-perturbative activity of mesoporous nanoparticles towards biomembranes was investigated, and compared to that of a pyrolytic silica. In this context, the incubation of nanoparticles with nanometric liposomes and RBCs, before and after the amino-functionalization of the surface, in order to decrease the amount of silanols, was evaluated through liposome leakage assay and hemolysis, respectively (Fig. 4.6).

Mesoporous nanoparticles, which were characterized by a net negative charge (in the experimental conditions) comparable to that of pyrolytic silica particles, showed a dual and opposite behavior during the interaction with the two membrane models: towards liposomes, the reactivity was even larger than the reference sample. On the contrary, unlike P-SiO$_2$, switching to a more complex model (the red blood cell membrane), perturbative activity greatly decreased, even at higher concentrations (200-500 µg/ml). P-SiO$_2$, as expected, kept showing a strong reactivity, comparable among the two bilayer models.

Surface amino functionalization, commonly for dense nanoparticles (see above), resulted in the masking of silanols, leading to a strong decrease in the perturbation.

No significant adsorption of hemoglobin or calcein occurred on the particles.

4.4 Discussion

4.4.1 Part i: dense silica nanoparticles (DSN) vs pyrolytic silica

In their work, Catalano et al. (Catalano et al., 2015) evaluated the adsorption of bovine serum albumin (BSA) on two types of silica nanoparticles, one pyrolytic (P-SiO$_2$, namely commercial AOX 50, by Evonik Industries), the other colloidal, synthesized ad-hoc (DSN-OH), different in size, surface area, ζ-potential, dispersion state in different media, amount and distribution of silanols. They evidenced that the protein absorption on particles was driven by each component of the system (silica and proteins). The distribution of surface silanols on the two silicas, and, thus, the surface hydrophobicity/hydrophilicity, was found to play a significant role in the amount of the adsorbed proteins. In this context, they ascribed the lack of isolated silanols (Si-OH) as the factors limiting the irreversible absorption of BSA on DSN-OH surface in respect to P-SiO$_2$

In our experiment, we have evaluated and compared the interaction of the same two silicas samples with two different membrane models, at different complexity. First, through a dye leakage assay, the principle of which is the leakage of a self-quenching fluorescent dye (calcein) from liposomes upon the contact with nanoparticles, interaction of SiO$_2$ particles with nanometric phosphatidylcholine liposomes was investigated. Then, we switched towards a model more reflecting real biomembranes, the red blood cell.

Due to their incapacity to phagocyte, RBCs may be severely damaged and disrupted upon the contact with silica nanoparticles (hemolysis). Although

several researches focused on the evaluation of the molecular mechanism behind this activity have been carried out, many questions are still unanswered. The two membrane models were different for size (liposomes diameter was ca. 160 nm, red blood cells ranges around 7-10 μm), shape and curvature (liposomes are spherical, RBCs have a round biconcave shape), surface charge (both negative, but red blood cells show patches of positive charge, not present in liposomes, represented by phospholipids containing tetra-alkyl-ammonium groups) and, last but not least, composition of the double layer (only phosphatidylcholine in liposomes, cholesterol, several lipids and proteins in the red blood cell).

As expected, pyrolytic nanoparticles were found to be extremely reactive towards both membrane models. On the contrary, DSN-OH particles showed a substantial perturbative activity only versus red blood cells, while totally inert against liposomes.

Not negligible contrast in reactivity towards red blood cells can be ascribed to the different distribution of surface silanol groups. Recently, it was demonstrated (*Pavan, Ph.D. Thesis, 2016*), that a significant decrease in hemolytic activity of P-SiO$_2$ occurred upon heating the particles at 700°C. While at room temperature (25°C), FTIR profiles of pristine pyrolytic silica nanoparticles were characterized by the contemporary presence of isolated, weakly interacting and strongly H-bonded silanols. Upon heating at 700°C, the broad bands of strongly interacting silanols (3100-3600 cm^{-1}) disappeared, while the band assigned to weakly interacting silanols was strongly decreased, in favor of the isolated silanols band. In other words, this process resulted in a strong skimming of Si-OH populations, leading to an increase in the surface chemical order compared to pristine P-SiO$_2$ particles. Hemolytic activity of heated samples was extremely lower than untreated ones. Hence, supposedly, the surface disorder in silanol distribution, characterized by a huge portion of weakly interacting silanols, allows pristine P-SiO$_2$ to energetically interact with biomembranes.

DSN-OH particle surface presented scarcity of isolated Si-OH groups (that also results in the poor coverage by BSA, in respect to P-SiO$_2$), and was consequently characterized by a lower chemical heterogeneity. As a consequence, this aspect resulted in a weaker interaction with red blood cell membrane, even at higher doses. Towards liposomes, extremely different behavior might be due to the different nature of artificial vesicles, both physical (size and shape, which affect phospholipid packing and stability) and chemical (due to different composition, and consequently complexity, of the membrane models). Pyrolytic nanoparticles, because of their particular surface chemistry and a more negative zeta potential (-35 *vs* -22 mV), kept experimenting strong interactions, especially with positively charged phosphatidylcholine heads. DSN-OH, notwithstanding

they also had a net negative surface charge, did not show any perturbative activity. We can thus hypothesize that this behavior was also due, commonly for red blood cells, to the higher chemical disorder on the surface, imparted by the heterogeneous distribution of surface functionalities, as observed by FTIR spectroscopy (Fig. 4.7), carried out by Catalano and coworkers (Catalano et al., 2015).
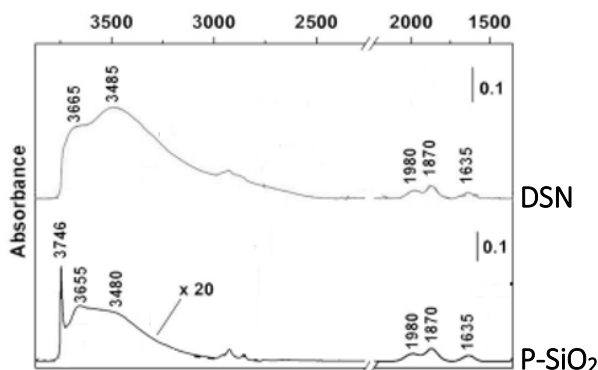
Fig. 4.7. Comparison of IR spectra of DSN and P-SiO$_2$ particles outgassed at r.t. A more disorganized and heterogeneous pattern is shown for P-SiO$_2$. (Catalano et al., 2015).

A further proof of the crucial role of surface silanols in driving the interaction, was given through the surface functionalization with aminopropyl groups, which changed surface properties of particles, resulting in a higher agglomeration (similar to P-SiO$_2$) and a positive zeta potential value. Actually, zeta potential of DSN-HD (aminopropyl-functionalization performed through a one-pot route), was positive (see table 4.1), but the membrano-perturbative activity of DSN-HD towards liposomes, was absolutely comparable to that of naked DSN. In view of that, we can probably exclude surface charge and dispersion state having a key role in the interaction, and focusing the attention only on surface silanols.

4.4.2 Part ii: mesoporous silica nanoparticles (MSN) vs pyrolytic silica

The interaction of MCM-41-like mesoporous silica nanoparticles (MSN), in pristine form and upon surface functionalization with amino groups, with nanometric liposomes and micrometric red blood cells, was evaluated by means of dye leakage assay and hemolysis assay. Results of the two assays were then compared to that a hemolytic amorphous pyrolytic silica dust (P-SiO$_2$).

Although the FTIR patterns of the two samples were quite similar, both rich in isolated and interacting silanols, thus imparting a surface chemical disorder, such similarity did not reflect in a comparable reactivity behavior, especially towards red blood cells.

It is well known that amorphous silica surface exhibits different distribution and density of silanol groups (Zhuravlev, 2000). Surface charge is affected to the dissociation of silanol groups ($\equiv$Si-OH) in silanolates ($\equiv$Si-O-) in particular condition of ionic strength and pH (Iler, 1979). In our specific case, the two tested samples showed a different silanol density: for MSN, it was estimated a silanol density of 3.3 OH per nm^2 (Musso et al, 2015), while 1.6 OH/nm^2 was calculated for pyrolytic SiO_2 particles (Catalano et al., 2015). Thus, we could suppose that, considering the fact that the hemolytic amorphous silica, actually contained a number of Si-OH groups lower than the inert, perturbative properties were not proportional to the amount of silanol groups. This assumption seems to contradict what evidenced by Murashov and coworkers., who reported that the divergent, and known, difference in hemolytic activity between amorphous silica and mesoporous particles was due to different amount of surface silanols (Murashov et al., 2006). Interestingly, the zeta potential, evaluated by means of electrophoretic light scattering in 0.01 M PBS of mesoporous silica (ca. -18 mV) was moderately lower to that of P-SiO2 (-35 mV), even if the silanol density of the latter is 2-fold lower. This result suggests that, even if MSNs have, overall, more silanol groups than amorphous silica, most of them are located inside the pores, in the interior of the particles, and, consequently, that the external surface of pyrolytic silica is more abundant in negatively charged groups (Si-O-) than that of MSN-OH. Hence, this "hidden" groups, not able to contribute to the electrophoretic mobility of the particles, were, a fortiori, excluded to experiment any kind of interaction with biomatter.

Moreover, assuming that silanol groups were uniformly distributed throughout the entire surface area of the particles (ca. 1100 m^2/g), this might indicate that only a small fraction of silanols were accessible. This structural effect, ensured by the high porosity of the material, may explain the low hemolysis of MSNs. This suggest that, even if mesoporous nanoparticles had a larger number of Si-OH groups than pyrolytic silica, most of them are inaccessible for a direct interaction with the cell membrane. Furthermore, Roiter et al. (Roiter et al., 2008, 2009) recently calculated that a stable interaction, driven by electrostatic forces, between a convex silica surface and a lipid bilayer, can occurs only if the silica surface is continuous for more than 22 nm. In that case, the stress generated by the deformation of the lipid bilayer, can be overcome by considerable attractive interactions between surface Si-OH groups and the phospholipid heads. Hence, for MSNs, considering morphology and size, diameter of pores (ca. 30 Å) and TEM imaging of particles (Musso et al., 2015)

this condition can be discarded. On the contrary, for amorphous silica, due to the surface long-range continuity, strong and continuous interactions can be more easily established between nonporous particles and membrane lipids.

Concerning the direct interaction with liposomes, presumably, the extremely small size of our lipid vesicles, commensurate to that of particles (and particularly smaller than particle aggregates), entails that the interaction with mesoporous nanoparticles occurred regardless of the pores, in an extent comparable to amorphous P-SiO$_2$, due to i) not dramatically different surface charge, ii) comparable size of the aggregates, iii) similar FTIR pattern. These aspects suggest that, in all likelihood, small-sized liposomes might not be the most suitable model to mime the interaction of MSN particles with red blood cells. In this context, for mesoporous nanoparticles, we can exclude the evaluation of dye leakage activity of nanosized liposomes as a predictive assay for hemolysis, even considering the strong physico-chemical differences between the two membrane models

Commonly for what evidenced for dense nanoparticles, surface amino functionalization of MSN resulted in a suppression of the perturbative activity towards both models. Addition of aminogroups led indeed to a strong variation of the FTIR pattern, that evidenced a strong loss in surface silanols. Actually, peaks relative to Si-OH groups decreased, and bands due to v_{as}/v_{sym} NH$_2$ modes appeared (Musso et al., 2015), as a fingerprint of the amino-functionalization. Fall in silanol density was also evidenced by zeta potential investigation: value changed from -18 to +4 mV. Nevertheless, the negative value, proper of naked MSNs (MSN-OH), is not far to that of pristine dense silica nanoparticles (DSN-OH, 4.3.5, part i), which, as previously described, showed a substantial hemolytic activity towards red blood cells. Taken together, data indicate the absence of a direct connection between ζ-potential value of silica particles and the hemolytic activity, but, accordingly to recent literature (Slowing et al., 2009; H. Zhang et al., 2012) what accounts for the interaction is i) the density of accessible surface silanols and ii) the fact to have, or not, a surface free of structural discontinuity (Fig. 4.8).

Surface continuity
(P-SiO$_2$)

Surface discontinuity
(MSN)
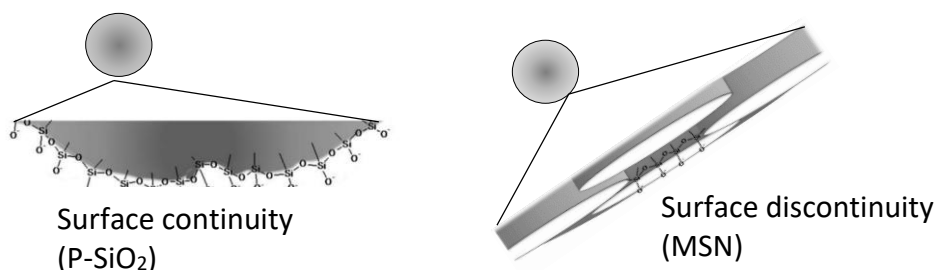
Fig. 4.8. Continuity *vs* discontinuity: continuous geometry allows particles to establish strong and cumulative interactions with biomembrane, which result in membrane disruption. On the contrary, discontinuous geometry, even when associated to a comparable surface Si-OH density and surface charge to that of a continue surface, can only allow to experiment a weak interaction with the phospholipid double layer. Chemical masking of Si-OH groups results in a large decrease in membrane perturbative activity.

4.5 Conclusions

The investigation of molecular mechanisms that drive the interaction of surface-controlled silica particles having different surface features and morphology with biomembrane, allowed to observe the key role played by surface silanols and, in particular, the distribution of silanol families onto the silica particle surface. In this context, a lower heterogeneity in the distribution, appears to result in the absence, or, in a particularly weak interaction, slightly perturbative only towards red blood cells. On the other hand, in silica particles characterized by a comparable surface chemical heterogeneity (pyrolytic silica and mesoporous silica nanoparticles, in our case) the source of a contrasting behavior, in particular towards RBCs, is attributable to the morphological difference between the two silica models. Porosity, as expected, prevents particles to experiment long-range interactions with the natural membrane model, thus showing a good compatibility. The opposite reactivity towards liposomes, leaves the door open for future investigations, involving the testing of liposomes differing in size and membrane rigidity (i.e. through the addiction of cholesterol), trying to reach a better compatibility with RBC. In addition, an efficient and interesting tool to investigate molecular details of the interaction may be represented by theoretical modeling (Mu et al., 2014). Theoretical modeling allows to obtain complex information, under well-defined conditions of size, shape, surface geometry and chemistry. Recently, Fourches et al. (Fourches at al., 2004) developed the so-called Quantitative Nanostructure-Activity Relationship (QNAR), an application of the more classic quantitative structure-activity

relationship (QSAR) modeling to nanomaterials. Aim of QNAR modeling is the investigations of biological effects of particles in relation to their key physico-chemical properties (i.e. surface chemistry, charge and size).

Appendix: Size matters? Investigation of the liposome size effect on the interaction with silica particles

a.1 Experimental section

To investigate the effect of liposome size on membrane stability and resistance to deformation/rupture induced by the interaction with silica samples, we incubated a set two well characterized particles, the already described amorphous pyrolytic silica (P-SiO$_2$), and the commercial quartz Min-U-Sil 5, previously tested in several toxicological investigations, with non-extruded and extruded artificial lipid vesicles.

The liposomes were synthesized and purified following the procedure reported in chapter 4, paragraph 2.4. To control and uniform the size, a portion of the liposome dispersion was extruded two times through 0.22 μm pores polycarbonate filters (Nucleopore, Milan, Italy), by a gas extruder (Lipex, Vancouver, Canada).

a.1.1 Sample preparation

P-SiO$_2$ and Min-U-Sil 5 (1 mg each) were suspended in 1 ml of 0.01M PBS and probe-sonicated following the same procedure as for the other silica samples (60 seconds, 25 W). The stock suspension (1000 μg/ml) was diluted to the final concentrations for experiment (200, 100 and 12.5 μg/ml), which was carried out in 0.01M PBS. Non-extruded liposomes (NEL) were diluted 1:16, while extruded vesicles (EL) 1:32 in 0.01 M PBS, pH 7.4.

a.1.2 Liposome leakage assay

The interaction with liposomes as membrane model was entirely carried out following the procedure above described (4.2.5).

a.2 Results

The effect of vesicle size on the interaction with silica particles has been performed incubating phosphatidylcholine liposomes at different size with two silica samples, an amorphous ultra-fine commercial dust (P-SiO2) and a crystalline powder (Min-U-Sil 5), both well known for their membrane-perturbative activity.

The non-extruded liposomes (NEL) showed a broader size distribution, ranging from 50 nm to 5 μm, while the extruded ones (EL), almost monodispersed (polydispersion index ca. 0.1), were characterized by a DLS average size of 180 nm. Results of the interaction with silica dusts is summarized in fig a.4.1.
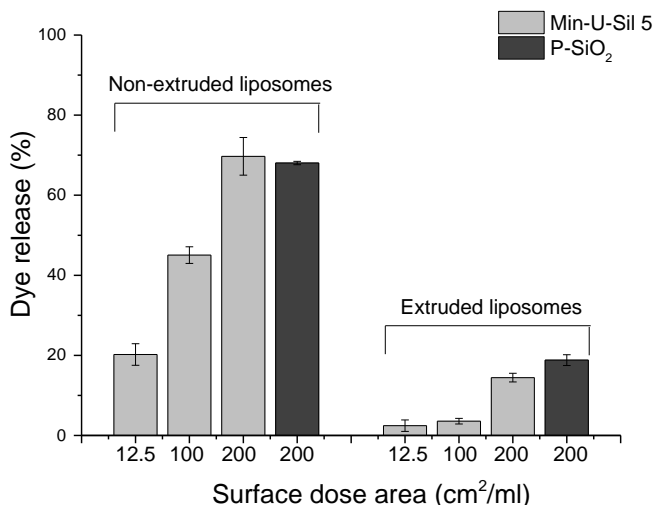
Fig. a.4.1 NEL and EL dye leakage vs. particle concentration (calculated from specific surface area). Three concentrations for Min-U-Sil 5 and one for P-SiO$_2$ were chosen. Different membrane perturbation behaviour of two types of liposome size can be observed.

The dose-dependent trend was still present in extruded liposomes but, as evidenced by the graph, they induced a lower perturbation of membrane, than NELs. Dye leakage induced by Min-U-Sil 5 quartz dust at a concentration of 200 cm^2/ml on NEL, was ca. 70%, while, for 220 nm EL, it was particularly lower (ca. 20%).
A single high-dose of P-SiO$_2$ (200 cm^2/ml), confirmed the stronger membrane integrity of extruded liposomes (ca. 20% of leakage) with respect to non-extruded ones (dye leakage around 75%).

a.3 Discussion
The behavior observed for the two population of liposomes (NEL and EL), characterized by a different size distribution, is of course crucial in the understanding of the mechanism of liposome-particle interaction, from a "morphological" point of view, considering the liposome size variation.

We can ascribe the observed behavior to:

i)   the extreme difference in the volume/surface area of the two liposome families

or

    ii)   the large discrepancy in membrane curvature, and the consequent contact-surface with silica

Since small liposomes are characterized by a significant area/volume ratio, the interaction of particles with extruded liposomes (diameter: 180 nm) could be weakened by the large amount of lipid patches released in the incubation medium upon membrane disruption. We hypothesize that such patches could adsorb on the silica surface, thus preventing any further interaction with the remaining liposomes, and, consequently, resulting in a low dye leakage. On the other hand, non-extruded vesicles (NEL) size distribution showed micrometric liposomes (ca. 5 μm) (GUVs, giant unilamellar vesicles), characterized by a relatively low area/volume ratio. To confirm the direct role of liposome size in determining the outcome of the interaction, some assumptions must be done: first and foremost, we considered the NEL population as the combination of a bi-modal population with average diameters of 163 and 5480 nm. The relative volume of these two populations was calculated from the DLS data, and reported as 25 and 75%, respectively. On the contrary, the size distribution of the EL population was considered to be mono-modal, with an average diameter of 166 nm. Therefore, considering this approximation, we were free to calculate the theoretical volume of a single vesicle, that represented the whole liposome population subjected to membrane disruption and dye leakage. Thus, postulating that all the liposomes were spherical and supposing that calcein release resulted just upon complete membrane disruption, on the basis of the % of dye release, we were able to calculate the theoretical number of liposome/well that were damaged, and, also, the total surface area of lipid bilayer disarranged after the interaction with silica. The values reported in the following table (Table a.4.1) refer to the disrupted liposomes after adding of Triton X-100 to the medium, hence account for the complete lysis (100% dye leakage) of all liposomes available in each well.

Table a.4.1 NEL and EL surface area of disrupted liposomes, calculated for each silica concentration and after exposure to Triton X-100 (Total).

Liposome	Relative volume (%)	Hydrodynamic diameter (nm)	Disrupted liposome volume (µl)	Disrupted liposome number per well	Total surface area (cm²)
NEL					
MIN 12.5	75	5480	5.26	6.10E+07	5.76E-03
	25	163	1.75	7.73E+11	6.45E-02
MIN 100	75	5480	11.71	1.36E+08	1.28E-02
	25	163	3.90	1.72E+12	1.44E-01
MIN 200	75	5480	18.13	2.10E+08	1.99E-02
	25	163	6.04	2.67E+12	2.22E-01
P-SiO$_2$	75	5480	17.70	2.05E+08	1.94E-02
	25	163	5.90	2.60E+12	2.17E-01
TOTAL	75	5480	26.01	3.02E+08	2.85E-02
	25	163	8.67	3.82E+12	3.19E-01
EL					
MIN 12.5	100	166	0.69	2.89E+11	2.50E-02
MIN 100	100	166	1.01	4.21E+11	3.64E-02
MIN 200	100	166	4.09	1.71E+12	1.48E-01
P-SiO$_2$	100	166	5.33	2.23E+12	1.93E-01
TOTAL	100	166	28.32	1.18E+13	1.02E+00

The total surface of disrupted liposomes was then compared to the silica surface available for the adsorption, in each well (Table a.4.2). In this regard, we supposed that the membrane patches resulting from all disrupted liposomes, adsorb themselves on silica surface, thus impairing further interactions with liposomes. Accordingly, the amount of free silica surface (S_{free}) after each experiment, calculated as the relative difference between the silica surface available in each well (S_a) and the total surface area of disrupted liposomes (S_l), is reported for NEL and EL, as:

$$S_{free} = \frac{S_a - S_l}{S_a} * 100$$

Table a.4.2 Free silica surface area available after each experiment

Silica dose (cm²/ml)	Well volume (µL)	Silica surface area in each well (cm²)	Silica surface still available at equilibrium (NEL)	Silica surface still available at equilibrium (EL)
12.5	240	3.00E+00	98%	99%
100	240	2.40E+01	99%	100%
200	240	4.80E+01	99%	100%

Taken together, data indicates that the approximation allows us to quantitatively appreciate the large excess of inorganic (e.g. silica) surface available for the interaction with vesicles in each experiment, even at the lowest silica concentration evaluated. Indeed, the free silica surface after the experiment at 12.5 cm²/ml, was 98 and 99% for NEL and EL, respectively. Such data implies that the model is not affected by not specific lipid adsorption. Therefore, analyzing the effects on membrane integrity determined by the different liposome size (Fig. a.4.1), it is possible to consider the size as an *influencer* of membrane integrity, through the modulation of the curvature of the liposomes. Considering the morphology, larger micrometric liposomes have a quasi-flat surface, with respect to the highly-convex membrane of the extruded ones. This aspect determines a larger amount of area available for the interaction with silica. Extrusion, certainly, can also result in smaller liposomes with strong lipid packing (Maherani, Arab-Tehrany, Kheirolomoom, Geny, & Linder, 2013), and increased resistance to the nanoparticle-induced membrane perturbation. By contrast, the membrane of micrometric liposomes might be more subjected to interaction with particles, due to a weaker lipid packing between the hydrocarbon chains. Although the dimensional characterization carried out is not able to explain all possible correlations between vesicle size and membranolytic activity, some indications achieved could be helpful for future investigations. These will include non-extruded liposomes separation to be performed through FFF technique (Flow-Field Fractionation), in order to obtain a more accurate size distribution, and try to build a theoretical model that could help the comprehension of different dye leakage behavior.

Bibliography

Alkhammash, H. I., Li, N., Berthier, R., & de Planque, M. R. R. (2015). Native silica nanoparticles are powerful membrane disruptors. *Physical Chemistry Chemical Physics : PCCP*, *17*(24), 15547–60. https://doi.org/10.1039/c4cp05882h

Balduzzi, M., Diociaiuti, M., De Berardis, B., Paradisi, S., & Paoletti, L. (2004). In vitro effects on macrophages induced by noncytotoxic doses of silica particles possibly relevant to ambient exposure. *Environmental Research*, *96*(1), 62–71. https://doi.org/10.1016/j.envres.2003.11.004

Borm, P. J. A., Robbins, D., Haubold, S., Kuhlbusch, T., Fissan, H., Donaldson, K., … Oberdorster, E. (2006). *The potential risks of nanomaterials: a review carried out for ECETOC. Particle and fibre toxicology* (Vol. 3). https://doi.org/10.1186/1743-8977-3-11

Catalano, F., Alberto, G., Ivanchenko, P., Dovbeshko, G., & Martra, G. (2015). Effect of silica surface properties on the formation of multilayer or submonolayer protein hard corona: albumin adsorption on pyrolytic and colloidal SiO_2 nanoparticles. *The Journal of Physical Chemistry C,* 119(47), 26493-26505. https://doi.org/10.1021/acs.jppc.5b07764

Chen, K. L., & Bothun, G. D. (2014). Nanoparticles meet cell membranes: Probing nonspecific interactions using model membranes. *Environmental Science and Technology*, *48*(2), 873–880. https://doi.org/10.1021/es403864v

Cooper, G., & Sunderland, M. (2000). Structure of the Plasma Membrane. *The Cell: A Molecular Approach*, 1–6. https://doi.org/10.1007/978-1-4615-6484-3_4

De Planque, M. R. R., Aghdaei, S., Roose, T., & Morgan, H. (2011). Electrophysiological characterization of membrane disruption by nanoparticles. *ACS Nano*, *5*(5), 3599–3606. https://doi.org/10.1021/nn103320j

Depasse, J., & Warlus, J. (1976). Relation between the toxicity of silica and its affinity for tetraalkylammonium groups. Comparison between Si02 and Ti02. *Journal of Colloid And Interface Science*, *56*(3), 618–621.

https://doi.org/10.1016/0021-9797(76)90129-6

Diociaiuti, M., Bordi, F., Gataleta, L., Baldo, G., Crateri, P., & Paoletti, L. (1999). Morphological and functional alterations of human erythrocytes induced by SiO2 particles: An electron microscopy and dielectric spectroscopy study. *Environmental Research*, *80*(3), 197–207. https://doi.org/10.1006/enrs.1998.3892

Fourches, D., Pu, D., Tassa, C., Waissleder, R., Shaw, S.Y., Mumper, R.J., & Tropsha, A. (2010), Quantitative Nanostructure-Activity Relationship (QNAR) Modeling, *ACS Nano*, 4(10): 5703-5721 https://doi.org/10.1021/nn1013484

Handy, R. D., & Shaw, B. J. (2007). Toxic effects of nanoparticles and nanomaterials: Implications for public health, risk assessment and the public perception of nanotechnology. *Health, Risk & Society*, *9*(2), 125–144. https://doi.org/10.1080/13698570701306807

He, X. C., Lin, M., Li, F., Sha, B. Y., Xu, F., Qu, Z. G., & Wang, L. (2015). Advances in studies of nanoparticle-biomembrane interactions. *Nanomedicine (Lond)*, *10*(1), 121–141. https://doi.org/10.2217/nnm.14.167

Iler, R. K. (1979). The chemistry of silica: solubility, polymerization, colloid and surface properties, and biochemistry. *Lavoisierfr*, 892 pp. https://doi.org/10.1002/ange.19800920433

Kettiger, H., Québatte, G., Perrone, B., & Huwyler, J. (2016). Interactions between silica nanoparticles and phospholipid membranes. *Biochimica et Biophysica Acta - Biomembranes*, *1858*(9), 2163–2170. https://doi.org/10.1016/j.bbamem.2016.06.023

Kuempel, E. D., Geraci, C. L., & Schulte, P. A. (2012). Risk assessment and risk management of nanomaterials in the workplace: Translating research to practice. In *Annals of Occupational Hygiene* (Vol. 56, pp. 491–505). https://doi.org/10.1093/annhyg/mes040

Ladokhin, A. S., Wimley, W. C., & White, S. H. (1995). Leakage of membrane vesicle contents: determination of mechanism using fluorescence requenching. *Biophysical Journal*, *69*(5), 1964–71. https://doi.org/10.1016/S0006-3495(95)80066-4

Leroueil, P. R., Berry, S. A., Duthie, K., Han, G., Rotello, V. M., McNerny, D. Q., … Holl, M. M. B. (2008). Wide varieties of cationic nanoparticles induce defects in supported lipid bilayers. *Nano Letters*, *8*(2), 420–424. https://doi.org/10.1021/nl0722929

Leroueil, P. R., Hong, S., Mecke, A., Baker, J. R., Orr, B. G., & Holl, M. M. B. (2007). Nanoparticle interaction with biological membranes: Does nanotechnology present a janus face? *Accounts of Chemical Research*, *40*(5), 335–342. https://doi.org/10.1021/ar600012y

Lin, Y.-S., & Haynes, C. L. (2010). Impacts of Mesoporous Silica Nanoparticle Size, Pore Ordering,and Pore Integrity on Hemolytic Activity. *J Am Chem Soc*, *132*(16), 4834–4842. https://doi.org/10.1021/ja910846q

Lin, Y. S., & Haynes, C. L. (2009). Synthesis and characterization of biocompatible and size-tunable multifunctional porous silica nanoparticles. *Chemistry of Materials*, *21*(17), 3979–3986. https://doi.org/10.1021/cm901259n

Lu, S., Duffin, R., Poland, C., Daly, P., Murphy, F., Drost, E., … Donaldson, K. (2009). Efficacy of simple short-term in vitro assays for predicting the potential of metal oxide nanoparticles to cause pulmonary inflammation. *Environmental Health Perspectives*, *117*(2), 241–247. https://doi.org/10.1289/ehp.11811

Maherani, B., Arab-Tehrany, E., Kheirolomoom, A., Geny, D., & Linder, M. (2013). Calcein release behavior from liposomal bilayer; Influence of physicochemical/mechanical/structural properties of lipids. *Biochimie*, *95*(11), 2018–2033. https://doi.org/10.1016/j.biochi.2013.07.006

Michel, R., & Gradzielski, M. (2012). Experimental Aspects of Colloidal Interactions in Mixed systems of liposome and inorganic nanoparticle and their applications. *International Journal of Molecular Sciences*. https://doi.org/10.3390/ijms130911610

Moghadam, B. Y., Hou, W. C., Corredor, C., Westerhoff, P., & Posner, J. D. (2012). Role of nanoparticle surface functionality in the disruption of model cell membranes. *Langmuir*, *28*(47), 16318–16326. https://doi.org/10.1021/la302654s

Mu, Q.,. Jiang, G., Chen, L., Zhou, H., Fourches, D., Tropsha, A., & Bing, Y., (2014) Chemical basis of interactions between engineered nanoparticles and biological systems. *Chemical reviews*, 114(15), 7740-7781

https://doi.org/10.1021/cr400295a

Murashov, V., Harper, M., & Demchuk, E. (2006). Impact of Silanol Surface Density on the Toxicity of Silica Aerosols Measured by Erythrocyte Haemolysis. *Journal of Occupational and Environmental Hygiene*, *3*(12), 718–723. https://doi.org/10.1080/15459620601015950

Musso, G. E., Bottinelli, E., Celi, L., Magnacca, G., & Berlier, G. (2015). Influence of surface functionalization on the hydrophilic character of mesoporous silica nanoparticles. *Phys. Chem. Chem. Phys.*, *17*(21), 13882–13894. https://doi.org/10.1039/C5CP00552C

Nash, T., Allison, A. C., & Harington, J. S. (1966). Physico-chemical properties of silica in relation to its toxicity. *Nature*, *210*(5033), 259–261. https://doi.org/10.1038/210259a0

Nel, A. (2006). Toxic Potential of Materials at the Nanolevel. *Science*, *311*(5761), 622–627. https://doi.org/10.1126/science.1114397

Patwardhan, S. V., Emami, F. S., Berry, R. J., Jones, S. E., Naik, R. R., Deschaume, O., Perry, C. C. (2012). Chemistry of aqueous silica nanoparticle surfaces and the mechanism of selective peptide adsorption. *Journal of the American Chemical Society*, *134*(14), 6244–6256. https://doi.org/10.1021/ja211307u

Pavan, C.*,* On the Variability of silica toxicity: role of surface reactivity in membranolysis and in the activation of inflammatory pathways*, Ph.D Thesis, University of Turin, 2016*

Pavan, C., Tomatis, M., Ghiazza, M., Rabolli, V., Bolis, V., Lison, D., & Fubini, B. (2013). In search of the chemical basis of the hemolytic potential of silicas. *Chemical Research in Toxicology*, *26*(8), 1188–1198. https://doi.org/10.1021/tx400105f

Pera, H., Nolte, T. M., Leermakers, F. A. M., & Kleijn, J. M. (2014). Coverage and disruption of phospholipid membranes by oxide nanoparticles. *Langmuir*, *30*(48), 14581–14590. https://doi.org/10.1021/la503413w

Rascol, E., Devoisselle, J.-M., & chopineau, joel c. (2016). The relevance of membrane models to understand nanoparticles-cell membrane interactions. *Nanoscale*, *8*, 4780–4798. https://doi.org/10.1039/C5NR07954C

Ray, P. C., Yu, H., & Fu, P. P. (2009). Toxicity and environmental risks of nanomaterials: Challenges and future needs. *Journal of Environmental Science and Health - Part C Environmental Carcinogenesis and Ecotoxicology Reviews*. https://doi.org/10.1080/10590500802708267

Razzaboni, B. L., & Bolsaitis, P. (1990). Evidence of an oxidative mechanism for the hemolytic activity of silica particles. *Environmental Health Perspectives*, *87*, 337–341. https://doi.org/10.1289/ehp.9087337

Rimola, A., Costa, D., Sodupe, M., Lambert, J. F., & Ugliengo, P. (2013). Silica surface features and their role in the adsorption of biomolecules: Computational modeling and experiments. *Chemical Reviews*. https://doi.org/10.1021/cr3003054

Roiter, Y., Ornatska, M., Rammohan, A. R., Balakrishnan, J., Heine, D. R., & Minko, S. (2008). Interaction of nanoparticles with lipid membrane. *Nano Letters*, *8*(3), 941–944. https://doi.org/10.1021/nl080080l

Roiter, Y., Ornatska, M., Rammohan, A. R., Balakrishnan, J., Heine, D. R., & Minko, S. (2009). Interaction of lipid membrane with nanostructured surfaces. *Langmuir*, *25*(11), 6287–6299. https://doi.org/10.1021/la900119a

Sani, M. A., Gagne, E., Gehman, J. D., Whitwell, T. C., & Separovic, F. (2014). Dye-release assay for investigation of antimicrobial peptide activity in a competitive lipid environment. *European Biophysics Journal*, *43*(8–9), 445–450. https://doi.org/10.1007/s00249-014-0970-0

Slowing, I. I., Wu, C.-W., Vivero-Escoto, J. L., & Lin, V. S. Y. (2009). Mesoporous silica nanoparticles for reducing hemolytic activity towards mammalian red blood cells. *Small*, *5*(1), 57–62. https://doi.org/10.1002/smll.200800926

Stodghill, S. P., Smith, A. E., & O'Haver, J. H. (2004). Thermodynamics of micellization and adsorption of three alkyltrimethylammonium bromides using isothermal titration calorimetry. *Langmuir*, *20*(26), 11387–11392. https://doi.org/10.1021/la047954d

Tetley, T. D. (2007). Health effects of nanomaterials. *Biochemical Society Transactions*, *35*(Pt 3), 527–531. https://doi.org/10.1042/BST0350527

Turci, F., Pavan, C., Leinardi, R., Tomatis, M., Pastero, L., Garry, D., Fubini, B. (2016). Revisiting the paradigm of silica pathogenicity with synthetic quartz

crystals: the role of crystallinity and surface disorder. *Particle and Fibre Toxicology*, *13*(1), 32. Retrieved from http://www.ncbi.nlm.nih.gov/pubmed/27286702%5Cnhttp://www.pubmedcentral.nih.gov/articlerender.fcgi?artid=PMC4902968

Wei, X., Jiang, W., Yu, J., Ding, L., Hu, J., & Jiang, G. (2015). Effects of SiO2 nanoparticles on phospholipid membrane integrity and fluidity. *Journal of Hazardous Materials*, *287*, 217–224. https://doi.org/10.1016/j.jhazmat.2015.01.063

Yawata, Y. (2003). *Cell Membrane: The Red Blood Cell as a Model*. *Book*. https://doi.org/10.1002/3527601538

Zhang, H., Dunphy, D. R., Jiang, X., Meng, H., Sun, B., Tarn, D., Brinker, C. J. (2012). Processing pathway dependence of amorphous silica nanoparticle toxicity: Colloidal vs pyrolytic. *Journal of the American Chemical Society*, *134*(38), 15790–15804. https://doi.org/10.1021/ja304907c

Zhao, Y., Sun, X., Zhang, G., Trewyn, B. G., Slowing II, & Lin, V. S. (2011). Interaction of mesoporous silica nanoparticles with human red blood cell membranes: size and surface effects. *ACS Nano*, *5*(2), 1366–1375. https://doi.org/10.1021/nn103077k

Zhuravlev, L. T. (2000). The surface chemistry of amorphous silica. Zhuravlev model. *Colloids and Surfaces A: Physicochemical and Engineering Aspects*. https://doi.org/10.1016/S0927-7757(00)00556-2

Evaluation of the interaction of respirable quartz crystals with macrophage cell lines

5.1 Surface-controlled synthetic crystalline silica: effect of quartz internalization on macrophage viability and intracellular alterations

5.1.1 Background

As previously mentioned (Introduction chapter), several studies have clarified that the cellular exposure to crystalline silica dusts is correlated to detrimental and severe biological effects (W. Lin, Huang, Zhou, & Ma, 2006; Ye, Liu, Xu, et al., 2010; Ye, Liu, Chen, Sun, & Lan, 2010). Among the various effects reported, some are related to particle-membrane interactions (such as the response observed in hemolysis assay), and others to the activation of lung cells (e.g. alveolar macrophages, AM). It is known that inhaled quartz particles are recognized in the lungs by AM, which, because of their specific role, can be considered as the first cell of the body to get significantly in contact with the inhaled particles. Thus, the outer plasma membrane can be the very first possible target of silica particles, and the interaction may result in several detrimental effects (Kawasaki, 2015). The contact triggers a specific response, which starts with the uptake of particles through phagocytosis. The following interactions of the particles with the inner membrane of the phagolysosome may then induce destabilization, membrane damage and lysis. Therefore, lysosomal enzymes and particles may be released into the cytoplasm, leading to macrophage death or activation of inflammatory pathways (Pavan, Rabolli, Tomatis, Fubini, & Lison, 2014). This hypothesis requires further confirmation, especially regarding the molecular mechanisms and chemical moieties that rule the interaction between silica particles and cells.

Previous described detrimental effects, however, may be decreased upon surface modification by a range of substances that affects the quartz surface. Various external coating agents, such as lipid surfactants, proteins, organosilanes, and the polymer polyvinyl-pyridine-n-oxide (PVPNO), were used to reduce silica toxicity (Donaldson & Borm, 1998), thus suggesting a crucial role of particle surface in evoking toxic effects.

A second still unanswered question is how the surface characteristics of the silica particle can affect the uptake from extracellular fluids, and at which extent the internalization may be modulated by adsorbed proteins. A stable protein layer, the so-called protein corona, could affect particle recognition and, at a second stage, the internalization by cells, altering the bare surface properties. It was demonstrated (Lesniak et al., 2010) that the intracellular concentration of polystyrene nanoparticles is strongly affected by the amount of adsorbed proteins. Concerning silica, the eventual modulation of quartz particles uptake by the protein layer adsorbed on the surface, is still a question to be answered. Although the first site of interaction of the particle with cells is the cell membrane, one of the key targets of silica particulate is the phagolysosomal

membrane, whose rupture results in the leakage of the phagolysosomal content into the cytosol, such as the proteases cathepsins B and S. This event triggers the activation of the inflammasome machinery (Hughes et al., 2016), which in turn cause the activation of the proteolytic enzyme caspase-1 and release of active pro-inflammatory cytokines (i.e. IL-1β and IL-18). Extracellular cathepsin S and intracellular caspase 1 activation are surrogate biomarkers of particulate-induced lysosomal disruption in macrophages (Cassel et al., 2008; Hornung et al., 2008).

To fill the gap in the association between particle surface features, the interaction with phagolysosomal membrane and its disruption, which then results in silica pathogenicity, we have translated the knowledge acquired evaluating the interaction with simple biomembrane models (liposome and red blood cell), towards a more complex model, specifically the phagolysosomal membrane of murine and human macrophage cell lines. To this, we have investigated several cytotoxicity endpoints upon the evaluation of the incubation of cells with a set of quartz particles. By comparing the effect of ad-hoc synthesized crystals, with intact and fractured faces, with the usual quartz particles obtained by grinding, exhibiting different surface features, we have evaluated eventual perturbation on intracellular organelles, especially the lysosomes, as effects of quartz internalization, focusing the attention on the nature and spatial displacement of surface silanols, chemical species supposed to play a key role in defining silica interaction with cells.

5.2 Experimental section

5.2.1 Crystalline silica samples

The set of quartz crystals selected and analysed, is described in table 5.1. In detail, two as-grown synthetic samples (n-Qz-syn and μ-Qz-syn), with intact faces, produced through the approach previously described (Chapter 2.4), were tested and for their cytotoxicity, and compared to a mineral α-quartz dust, Min-U-Sil 5 quartz (US Silica Co., Berkeley Springs, WV, lot number 15062696), largely used in studies of experimental silicosis and lung cancer.

A portion (75 mg) of the micrometric quartz (μ-Qz-syn) was mechanically fractured by milling in a mixer mill (Retsch MM200) in agate jars (27 Hz, two spheres) to induce structural morphology and surface alterations (μ-Qz-syn-f), including radicals and a new silanol distribution, in freshly formed surfaces.

Table 5.1 Main physico-chemical properties of selected samples

Sample name	Origin	Surface state	DLS Size[a] (H$_2$O), nm	DLS Size[a] (in RPMI), nm	SSA[b] (Kr-BET), m^2/g	ζ-pot @[c] pH 7.4 (RPMI), mV
n-Qz-syn	synth	intact	310±2	313±40	6.2	-10.4±0.8
μ-Qz-syn	synth	intact	440±46	706±62	0.3	-11±1
μ-Qz-syn-f	synth	fractured	255±5	999±431	9.5	-10.4±0.3
Min-U-Sil 5	natural	fractured	1004±12	1320±305	6.2	-10± 0.8

[a]Particle size was determined by DLS (Dynamic Light Scattering) technique, using a Zetasizer Nano ZS device (Malvern Instruments Ltd, Malvern, UK). A sample dispersion of 0.5 mg/ml in MilliQ water (or RPMI medium) was prepared and probe sonicated for 3 minutes at 25% amplitude

[b]Specific surface area (SSA) was evaluated using the BET (Brunauer-Emmett-Teller) method, based on Kr adsorption. Quartz samples was firstly degassed for several hours. The analysis was performed at -196°C (ASAP 2020 Micromeritics, Norcross, USA).

[c]The ζ potential for the set of as-grown and fractured crystals was evaluated by means of electrophoretic light scattering (ELS) (Zetasizer Nano–ZS). In this technique, the velocity of a particle in an oscillating electric field, which is proportional to its ζ potential, is measured by light scattering. The ζ potential was measured suspending quartz (0.6 mg/ml) in RPMI medium + 10% FBS.

5.2.2 Chemical reagents and cell culture

RPMI 1640, FBS and DPBS were purchased by Gibco (Thermo Fischer Scientific, Waltham, MA, USA). Experiments have been performed on murine (MH-S, ATCC#CRL-2019) and human (THP-1, monocyte-like cell line derived from leukaemia from a one year old boy, ATCC#TIB-202) (Tsuchiya et al., 1980)]. Floating cells were cultured in RPMI 1640 + 10% FBS, at 37°C and 5% CO$_2$. Just before the seeding, a proper fraction of cells was differentiated into macrophages through a treatment, in the culture medium, with 100 nM PMA (phorbol 12-myristate 13-acetate), using a concentration of 0.5 μl PMA/1 ml cell culture. Cells were then allowed to differentiate for at least 24 hours.

The MH-S cell line was obtained from a 7 week-old male BALB/cJ mouse by bronchoalveolar lavage followed by SV-40 transformation of an adherent cell enriched population of alveolar macrophages. Adherent cells were cultured in

RPMI 1640 medium, enriched with 10% FBS + penicillin/streptomycin (100 μg/ml), at 37°C in a 5% CO_2 atmosphere.

5.2.3 Particle exposure and evaluation of cytotoxicity

Recent relevant studies (Rabolli et al., 2014; Schremmer et al., 2016; Sellamuthu et al., 2017) showed that silica exposure is linked to the development of biological signals (i.e. release of cytokines, chemokines and growth factors), which can lead to cellular death. Notwithstanding the interaction between silica and cells have been extensively studied in the last 20 years, molecular mechanism at the base of cellular toxicity remains still unclear (Gilberti, Joshi, & Knecht, 2008; Hamilton et al., 2008). Among several cell-lines, the most relevant to evaluate the cytotoxic potential of quartz particles are alveolar macrophages (AM): because of their specific role in the lungs, they can be considered as the first cell of the body to get significantly in contact with the inhaled particles (Hamilton et al., 2008).

To assess the cytotoxic potential of synthetic quartz crystals, we have evaluated several cytotoxicity endpoints:

i) permeability of the plasma membrane was investigated by monitoring the release of lactate dehydrogenase (LDH) in the culture medium (Decker & Lohmann-Matthes, 1988), followed by the evaluation of the ability of the samples to stimulate the generation of nitric oxide species (NO). Lactate dehydrogenase is an enzyme characteristic of almost all animal cells. Its presence into the supernatant is an indication of cell membrane damage. The LDH leakage assay is in fact a common assay for the detection of cytotoxicity or cell viability following exposure to toxic substances. LDH activity was measured spectrophotometrically into culture supernatant (LDH_{ext}) and in cell lysates (LDH_{int}), obtained through the probe-sonication of detached cells. Cell viability was calculated according to the formula:

$$\% \; cell \; viability = \left(\frac{LDH_{int}}{LDH_{int} + LDH_{ext}} \right) * 100$$

LDH reagent set was purchased from Sigma-Aldrich.

ii) the indirect determination of NO (nitric oxide) levels, through the spectrophotometric measurement of its stable decomposition products NO_3^- and NO_2^-, requires that NO_3^- first be reduced by reductase enzyme to NO_2^- and then NO_2^- determined by the Griess reaction. Briefly, in the Griess reaction, the NO-derived nitrosating agent (dinitrogen trioxide, N_2O_3) generated from the acid-catalyzed formation of nitrous acid from nitrite (or

auto-oxidation of NO) reacts with sulfanilamide to produce a diazonium ion, which is then coupled to N-(1-napthyl)ethylenediamine to form a chromophoric azo products, that absorbs strongly at 540 nm (Grisham, Johnson, Gautreaux, & Berg, 1995).

The assay was performed in a 96-well plate. 150 µl of cellular supernatant were mixed with 150 µl of Griess reagent (1% sulfanilamide, 0.1% naphthylethylenediamine dihydrochloride), at 37°C. After 10 minutes, optical density was evaluated and then expressed in nmol/mg.

The assays above were carried out on murine MH-S macrophages.

iii) cell metabolic activity was assessed through a MTT (3-(4,5-dimethylthiazol-2-yl)-2,5-diphenyltetrazolium bromide)) assay (Gerlier & Thomasset, 1986). The MTT assay is a colorimetric assay for assessing cell metabolic activity. NAD(P)H-dependent cellular oxidoreductase enzymes may, under defined conditions, reflect the number of viable cells present. These enzymes are capable of reducing the tetrazolium dye MTT 3-(4,5-dimethylthiazol-2-yl)-2,5-diphenyltetrazolium bromide to its insoluble formazan, which has a purple colour. During the reaction, MTT, a yellow tetrazole, is reduced to purple formazan in living cells. A solvent (usually dimethyl sulfoxide, DMSO) is added to dissolve the insoluble purple formazan product in to a coloured solution. The absorbance of this coloured solution can be quantified by measuring at a certain wavelenght (550 nm) with a spectrophotometer. THP-1 differentiated cells were plated at a density of 50,000 cells/well in 96-well dishes and treated, after 48 h, with quartz particles at increasing final concentrations (10-50-100-250-500-1000 µg/ml), in complete medium (RPMI medium + 10% FBS), and then incubated at 37°C and 5% CO_2 for 4 or 24 hours. 25 µg/ml 50nm NH_2-polystyrene nanoparticles was used as assay positive control (Xia et al., 2007) (data not shown). Cell viability after 4 h of incubation was only evaluated at a particle concentration of 100 µg/ml. At the indicated times, each well was washed with PBS and then treated with 0.5 mg/ml MTT for 20 minutes at 37°C. Then, MTT reagent was discarded and 200 µl of DMSO was added to each well, to solubilise formazan crystals. Each well was pipetted again to mix, and plates were read at 550 nm to measure change in absorbance. All values were normalized to control wells (untreated cells), which were calculated to represent 100% viability.

- *THP-1 cells differentiation protocol*: THP-1 monocytes were differentiated into macrophages using PMA (Phorbol 12-myristate

13-acetate) (Smith et al., 2015). Briefly, the calculated amount of monocyte cells was centrifuged 5 minutes at 2000 rpm, and resuspended in fresh cRPMI media. Then, PMA was added, to a final concentration of 100 nM. Cells were incubated at 37°C and 5% CO_2, and allowed to differentiate for 24 hours.

iv) evaluation of effect of protein corona on quartz crystals impact on cell viability. This was carried out by investigation of cell membrane permeabilization, through propidium iodide staining by flow cytometry (Dengler, Schulte, Berger, Mertelsmann, & Fiebig, 1995). Propidium iodide (PI) is a popular red-fluorescent nuclear and chromosome counterstain. Since propidium iodide is not permeant to live cells, it is also commonly used to detect dead cells in a population. PI binds to DNA by intercalating between the bases with little or no sequence preference. In aqueous solution, the dye has excitation/emission maxima of 493/636 nm. Once the dye is bound, its fluorescence is enhanced 20- to 30-fold, the fluorescence excitation maximum is shifted ~30–40 nm to the red and the fluorescence emission maximum is shifted ~15 nm to the blue, resulting in an excitation maximum at 535 nm and fluorescence emission maximum at 617 nm.

In this assay, THP-1 differentiated cells were grown on a 24-well plate, seeded at a number of 100,000 cells/well (70-80% confluence). 48 hours after seeding, cells were exposed to the particle dispersions prepared by dilution of the quartz stock into serum free and complete RPMI, for 1 (Min-U-Sil only, at several concentrations), 4 and 24 h (complete medium only). Then, to assess eventual effects on cell membrane permeability, due to the direct interaction between cells and (bare and corona coated) particles, harvested cells were stained with 5 µg/ml PI at room temperature. After incubation with the dye, samples were measured using a CytoFlex flow cytometer (Beckman Coulter). Forward and side scattering dot plots were used to discriminate cellular debris. Data were analysed using the FlowJo software (FlowJo, LLC, USA).

Same assay was performed on aminomodified polystyrene nanoparticles, at a concentration of 25 µg/ml, after 4 and 24 hours of incubation.

5.2.4 Evaluation of intracellular effects due to particle internalization

i) investigation of lysosome stress upon cellular uptake:

For the evaluation of lysosomal stress after interaction and internalization of particles, THP-1 cells differentiated into macrophages were exposed to the particle dispersions (100 μg/ml) prepared by dilution of the stock into complete RPMI. Cells were grown on transparent 24-well plates (100,000 cells/well) and, 48 h after seeding, were exposed to quartz particles. Two incubation time points, 6 and 24 hours, were evaluated. After the incubation, cells were washed with PBS and harvested with trypsin. PS-NH_2 nanoparticles, known for their ability to induce lysosomal stress, were added as a further positive control, at a concentration of 25 μg/ml. For LysoTracker staining, harvested cells were stained with 100 nM LysoTracker Red (Life Technologies, CA, USA) in PBS at 37°C per 15 min. After incubation with the dye, samples were measured using a CytoFlex flow cytometer (Beckman-Coulter). LysoTracker Red fluorescence intensity was analysed in FL3 channel

ii) investigation of intracellular ROS generation upon particle internalization

For the measurement of intracellular ROS levels, cells were stained with 2.5 μM CM-H_2DCFDA (2',7'-dichlorodihydrofluorescein diacetate), which becomes fluorescent when oxidized by intracellular ROS (Eruslanov & Kusmartsev, 2010). The emission of the excite dye was collected using a 530±40 nm band pass filter (green channel, FL1). To this aim, 10^5 THP-1 cells, differentiated into macrophages, were seed to 70-80% confluency, and exposed to 100 μg/ml quartz particles in cRPMI (RPMI + 10% FBS) for 24 h. To expose cells to particles, 100,000 cells were seeded into a 24-well plate, and 48 h after seeding, all wells were washed with 500 μl of RPMI. Then, the medium was replaced by 300 μl freshly prepared 100 μg/ml quartz dispersion in cRPMI. After 4 hours of incubation with particles, cells were harvested with trypsin and stained with 2.5 μM CM-H_2DCFDA.

iii) screening of intracellular caspase activity:

The Caspase-Glo® 3/7 Assay (Promega, WI, USA) is a luminescent assay that measures caspase-3 and -7 activities in purified cultures of adherent or suspension cells. The assay provides a proluminescent caspase-3/7 substrate, which contains the tetrapeptide sequence DEVD. This substrate is cleaved to release aminoluciferin, a substrate of luciferase used in the production of light. THP-1 differentiated cells were plated at 50,000 cells per well in 96-well dishes and treated, after 48 h, with quartz at a concentration of 100 μg/ml, in complete

medium (RPMI+ 10% FBS). Cells with particles were then incubated at 37°C for 24h. 25 µg/ml 50nm NH_2-polystyrene nanoparticles were used as positive control (Bexiga et al., 2011). At the desired endpoint time (24 h), the supernatant from each well was removed and cells were treated with 70 µl of Caspase-Glo 3/ reagent. Plate with cells was then incubated for 1h at room temperature, trying to avoid fluctuations of temperature. The luminescence of each sample was then measured at an interval of 1 sec/well in a plate-reading luminometer.

5.3 Results

The cytotoxic potential of a set of α-quartz crystals, with intact and fractured surfaces, was evaluated by the investigation of several endpoints of cellular toxicity, upon the incubation of crystals with macrophages. Macrophages have been chosen due to their specific biological role in the lungs.

Cytotoxic assessment was carried out on the following samples:

- n-Qz-syn: synthetic highly-pure quartz dust with as-grown faces, in sub-micrometric size, synthesized with nitric acid as polymerizing agent, not membranolytic towards red blood cells;
- μ-Qz-syn: synthetic highly-pure quartz dust with as-grown faces, in micrometric size (< 4 μm), synthesized with carbonic as polymerizing agent, not membranolytic towards red blood cells;
- μ-Qz-syn-f: synthetic highly-pure quartz dust with fractured faces, obtained from μ-Qz-syn sample after mechanical crushing. The dust showed a strong membranolytic activity towards red blood cells.

In each experiment, a mineral quartz dust (Min-U-Sil 5) was used as positive control (Ctrl+), due to its ability to induce cytotoxicity. Test have been conducted on two different cell lines, murine (MH-S) and human (THP-1) macrophages.

5.3.1 Evaluation of cell membrane permeability as endpoint of cytotoxicity of as-grown and fractured quartz crystals towards murine MH-S alveolar macrophages

The first evaluated endpoint of cytotoxicity was the loss of membrane integrity resulting from the 24 h incubation, in RPMI +10%FBS (cRPMI) culture medium, with increasing concentration of as-grown and fractured crystals (50-100-200-400 μg/ml), by means of the investigation of the cellular release of LDH enzyme in the extracellular matrix (LDH assay). The results of the assay (Fig. 5.1) are expressed as extracellular LDH/total LDH ratio, which represent the enzymatic activity, expressed as μmol of oxidized NADH per minute.
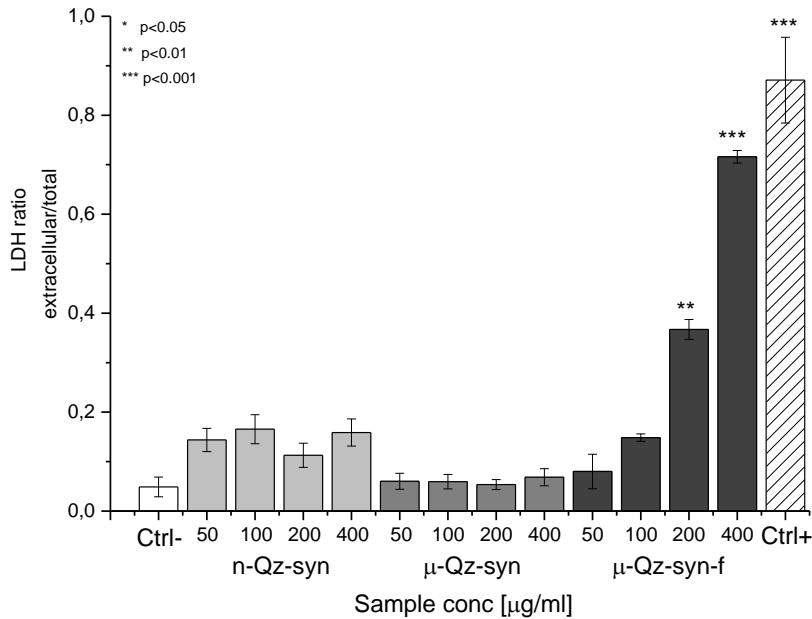
Fig. 5.1 Lactate dehydrogenase (LDH) assay for cellular viability. Values of 100% indicate total cellular toxicity. As-grown crystals did not evidence significant effect on viability, which was affected by fractured samples. Differences among groups have been evaluated through a 1-way ANOVA, followed by Tukey's post-hoc analysis. p-values > 0.05 have been considered statistically significant.

The results clearly showed absence of cytotoxicity for as-grown samples (n-Qz-syn and μ-Qz-syn), not highlighting any significant difference in membrane permeability compared to the negative control (untreated cells). On the contrary, upon fracturing (μ-Qz-syn-f), crystals acquired a substantial and dose/response trend cytotoxicity, comparable to the positive control (mineral quartz dust). Combined with LDH assay, membrane permeability related to cell viability was also evaluated through the investigation of the accumulation of nitrite (NO_2^-) in cell culture supernatant, by means of the Griess assay (Fig 5.2).
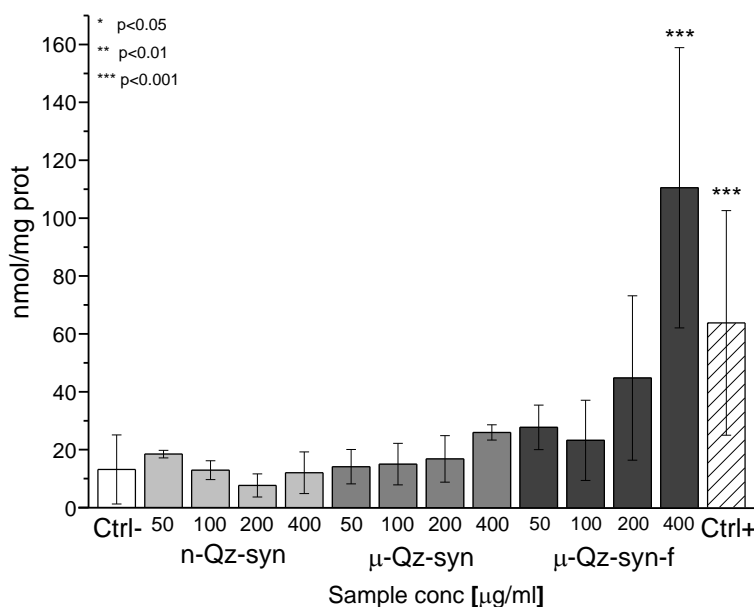
Fig. 5.2 Cellular nitric oxide generation upon the incubation with synthetic quartz crystals at increasing concentrations. Min-U-Sil 5 was used as positive control (400 μg/ml). Data are expressed as mean±SD of at least three independent experiments, each using 4 replicate wells per concentration. Differences among groups have been evaluated through a 1-way ANOVA, followed by Tukey's post-hoc analysis. p-values > 0.05 have been considered statistically significant.

In agreement with the previous results, as-grown crystals did not evidence the generation of nitric oxides, showing values comparable to negative control. As expected, on the contrary, for fractured crystals the increase in reactivity is clear, which translates in a larger biological response.

5.3.2 Assessment of cell metabolic activity upon incubation of quartz crystals with human THP-1 macrophages

The metabolic competence of the cells was evaluated through a MTT assay, which allows for the quantitative measurement of cell metabolic activity upon exposure to particles. The results of the MTT assay, after 4h (at a single particle dose of 100 μg/ml) and 24h (several doses: 10-50-100-250-μg/ml) treatments with the different quartz preparations, are shown in the following figures.
The incubation has been carried out in complete-medium (RPMI+10% FBS).
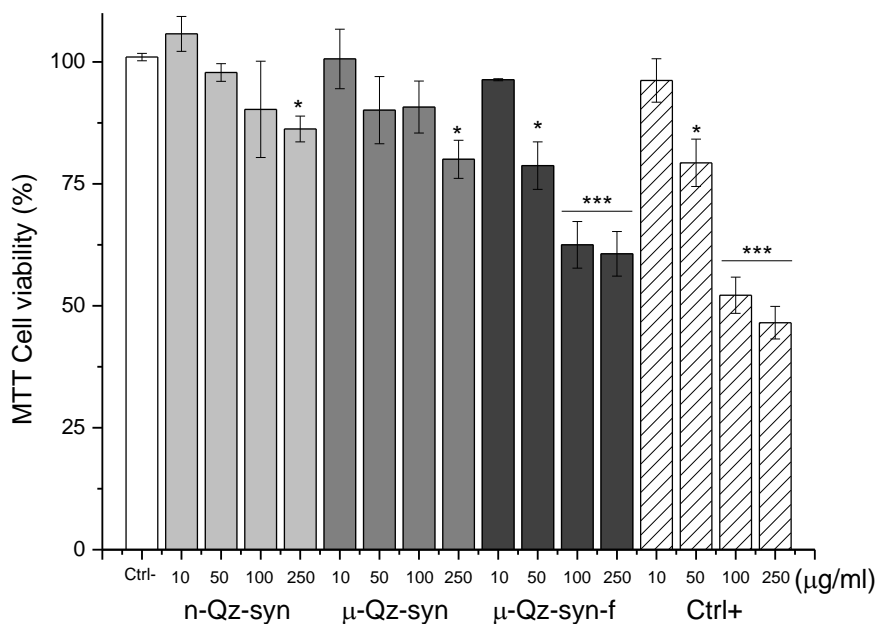
Fig. 5.3 *In vitro* MTT cytotoxicity of the different quartz dusts in THP-1 differentiated human alveolar macrophages. Cells were exposed for 24 h to quartz particles at increasing concentrations, in culture medium with fetal bovine serum. Cytotoxicity was evaluated using the MTT assay as a measure of metabolic competence of the cells. The cell viability is expressed as a percentage of negative control values. Data relative to 10-50 μg/ml and 100-250 μg/ml exposure result from two independent experiments, each using 4 replicate wells per concentration. Data are expressed as mean±SD. Differences among groups have been evaluated through a 1-way ANOVA, followed by Tukey's post-hoc analysis. p-values > 0.05 have been considered statistically significant.

While as-grown crystals with intact surfaces did not show any reduction in MTT levels, except at the highest concentration (250 μg/ml), the fractured synthetic sample, on the contrary, showed a considerable toxicity already at low particle dosage , with a clear dose-response trend. As expected, the positive control (Min-U-Sil 5), known for its cytotoxic potential, evidenced a significant toxicity even after only 4 hours of incubation (Fig 5.3). At the lowest concentrations (10 μg/ml), cytotoxic effects were well comparable among the entire set of samples. At 50 μg/ml, such effects began to differentiate from as-grown to fractured crystals.

Investigation of toxicity at a shorter time (4 hours, 100 µg/ml only, Fig. 5.4) showed a pattern of cytotoxicity very similar to that of 24 hours of exposure. No difference in metabolic activity was detected among the negative control and as-grown crystals, while, after fracturing, a substantial cytotoxicity was shown.
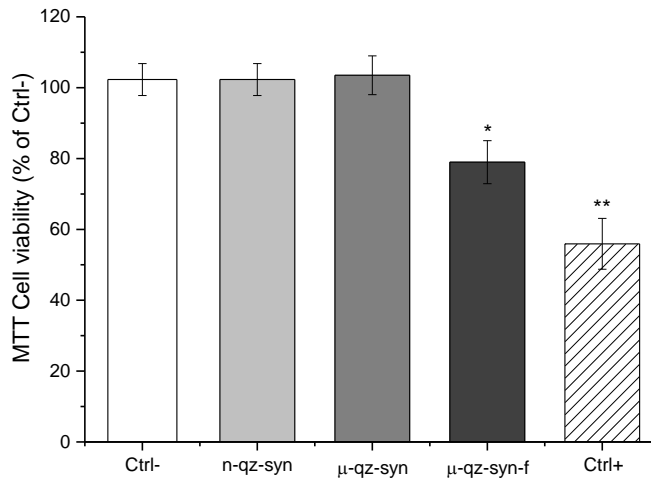
Fig. 5.4 Evaluation of cell death upon 4h exposure to quartz particles complete medium condition at a particle concentration of 100 µg/ml. Differences among groups have been evaluated through a 1-way ANOVA, followed by Tukey's post-hoc analysis. p-values > 0.05 have been considered statistically significant.

Result of the MTT assay carried out at extreme particle concentration (500-1000 µg/ml) were discarded because of the strong agglomeration of particles and the possibility of a direct and non-excludable physical damage on cells, as evidenced by the image of wells in which cells were exposed to 1000 µg/ml (Fig. 5.5)
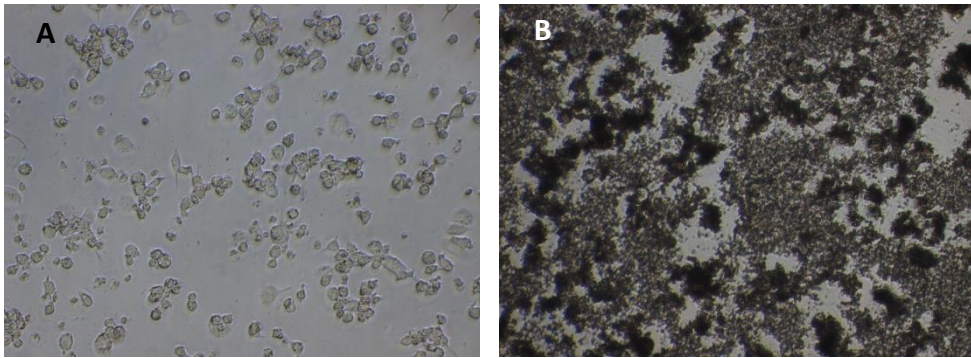
Fig. 5.5 Comparison of wells containing untreated cells (panel A) and cells exposed to 1000 µg/ml of sample µ-Qz-syn-f (B). The particle overloading and the presence of large aggregates of crystals, which might result in physical disruption of cells, were clearly visible.

5.3.3 Investigation of lysosome stress upon particle internalization

One possible explanation for macrophage stress after the interaction with quartz crystals might be the perturbation of the acidic compartments in the cells, intended as the increase in the volume of phagolysosomes upon the internalization of particles. In view of that, we have evaluated this effect, after 6 and 24 hours of incubation, by the use of the acidotropic dye LysoTracker Red, through flow cytometry.

As shown in figure 5.6, a slight increase in LysoTracker Red fluorescence was only evidenced after 24 h exposure, upon the incubation of macrophages with fractured crystals.
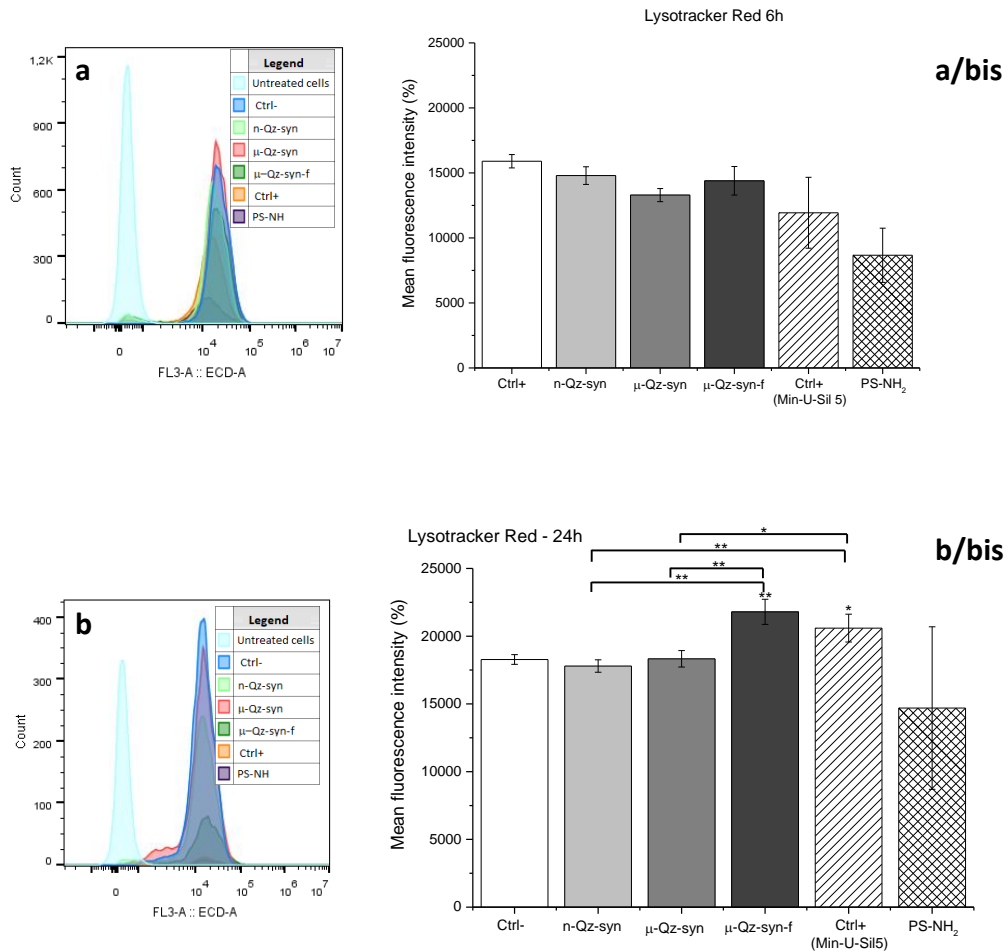
Fig.5.6 Distribution of LysoTracker Red fluorescence intensity after 6 (panel a) and 24 (panel b) hours of incubation, showing that upon treatment with particles, a strong cell death occurs, as evidenced by the decrease in peak count (y axes). Cells in late stages of cell death (FL3-A peak centered at zero fluorescence) are not stained by the dye. A slight right shift of the main cell population to higher fluorescence intensities was observed only at the 24 h time-point (panel b). Cells with lower LysoTracker Red intensity may suggest loss of lysosomal integrity. A general increase in fluorescence, between the two evaluated exposure times points, is evidenced.

Differences among negative control and samples, and among groups, were evaluated through a 1-way ANOVA, followed by Tukey's post-hoc analysis. p-values > 0.05 were considered statistically significant.

Shift in the fluorescence intensity, evaluated by means of the MFI calculated in the FL3 channel (Fig. 5.6, panels a/bis and b/bis), indicated absence of lysosomal perturbation at a six-hours incubation. On the contrary, at 24 hour exposure, a minor significant difference in behaviour between fractured and as-grown crystals arose. Cells treated with probe only were used as negative control. Surprisingly, in this cell line the incubation with 25 µg/ml positively charged polystyrene nanoparticles (PS-NH$_2$) did not evidence lysosomal stress, as observed instead in other cell types (Anguissola et al., 2014).

Taken together, the result suggested that synthetic fractured crystals seemed to perturbate lysosomes in a comparable way in respect to mineral crystalline fractured particles (Min-U-Sil 5). However, the effect was very small and results were complicated by the strong cell death observed in these cells. Furthermore, the absence of lysosomal stress upon the interaction with amino-modified polystyrene nanoparticles (PS-NH$_2$), which are usually used as positive control due to their ability to induce lysosome stress (pH acidification and increasing in lysosomal volume, including a strong increase in LysoTracker fluorescence) made the interpretation of the assay not trivial and, hence, further investigations are needed.

5.3.4 Generation of intracellular reactive oxygen species (ROS) upon quartz internalization

It is well known from the literature (Abdal Dayem et al., 2017; Bice Fubini & Hubbard, 2003; Manke, Wang, & Rojanasakul, 2013) that silica exposure, especially in the crystalline form, might result in a persistent inflammation due to prolonged activation of macrophages. This may lead to the release of intracellular oxidant species in the alveolar space. Specifically, reactive oxygen species (ROS) including hydroxyl radical, superoxide anion, hydrogen peroxide and singlet oxygen are generated by phagocytic cells, which attempt to digest the silica particles.

In this context, we have evaluated whether silica-induced ROS on THP-1 macrophages, upon 4 hours of exposure, to 100 µg/ml of synthetic and mineral quartz particles, through DCFH assay. ROS levels were measured by flow cytometry, in complete medium, in which cells were stained with 2.5 µM CM-H$_2$DCFDA (Life Technologies).

Results (Fig. 5.7) are reported as mean fluorescence intensity of the oxidized probe % ± SD, calculate from triplicate measurements of each condition.
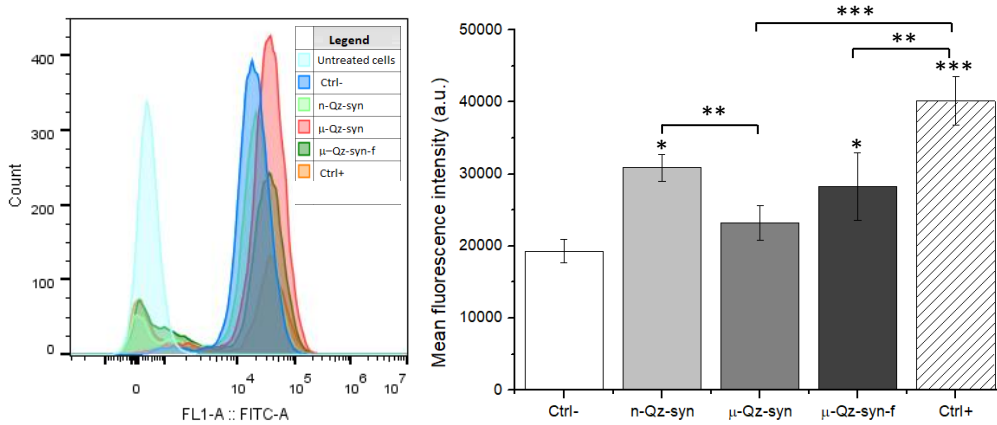
Fig. 5.7 Distributions of CM-H$_2$DCFDA fluorescence intensity (A, Logarithmic scale) and median fluorescence intensity (B) show modest increase in intracellular ROS generation in the main cell population. No distinction was detected among as-grown and fractured crystals. Min-U-Sil only (Ctrl+) show a significant increase, after 4h of incubation. Differences among negative control and samples, and among groups, have been evaluated through a 1-way ANOVA, followed by Tukey's post-hoc analysis. p-values < 0.05 have been considered statistically significant.

Lysosomal damage and several other forms of cellular damage can ultimately result in increase of intracellular ROS, thus creating a loop-cycle which can further amplify the cellular damage (Guicciardi, Leist, & Gores, 2004). After 4 hours of exposure, the population of cells exposed to quartz crystals (both as-grown and fractured), showed a modest increase in ROS generation, not distinguishable among samples. ROS generation can be directly related to the ability of particles to generate ROS or can be a response to other forms of damage induced by particles. Since the surface of crystals is covered by the protein corona until accumulation in the lysosomes, the ROS generation is probably a consequence of the damage induced by the particles, rather than a direct production on the crystal surface. As evidenced by flow cytometry measurement, the population with lower FS, characterized by an extremely low CM-H$_2$DCFDA intensity, consisted of cells in late stage cell death, which probably are not stained by the fluorescent dye. The incubation with the positive control, as expected, led to a further ROS generation, probably due to the presence of bulk impurities, especially iron and aluminium.

5.3.5 Cell death occurring upon particle exposure and internalization does not follow apoptotic pathways

In a recent review, Rabolli et al. (Rabolli et al., 2015) summarized the cascade of intracellular events which governs inflammasome machinery activation and Il-1β processing, upon the internalization of silica particles, in THP-1 cells. It has been seen that cell death occurs through a necrotic inflammatory pathway termed "pyroptosis" (Vince & Silke, 2016), in which cell swelling and plasma membrane rupture are induced, together with the release of mature IL-1β (a crucial mediator of the inflammatory response) and intracellular content, resulting into an inflammatory reaction. In this specific pathway, it is particularly involved the caspase-1 enzyme, whose activation begins the inflammatory cascade.

In view of that, we have tested the activation of other caspases, specifically 3 and 7, mainly involved in apoptotic pathways, to test whether the cell death occurs through apoptosis. The assay has been performed by the Caspase-Glo® 3/7 Assay, upon a 24-hours exposure with quartz samples, at a concentration of 100 μg/ml, using 50 nm NH_2-polystyrene nanoparticles (25 μg/ml) as positive control of apoptosis (Ctrl+).
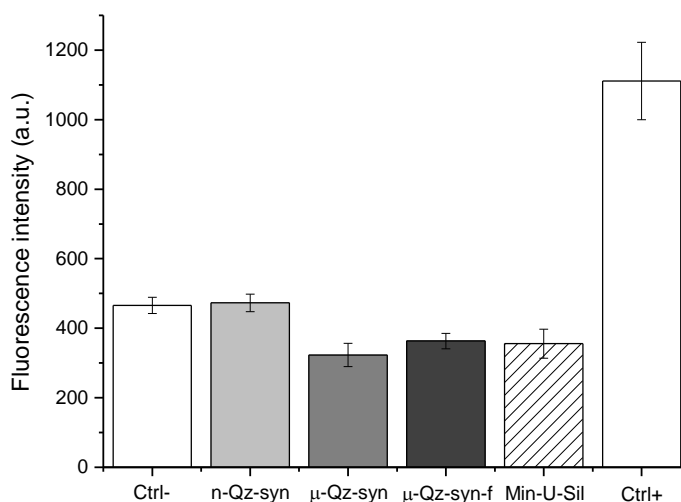
Fig. 5.8 Caspase 3/7 activity levels were used to assess the level of apoptosis. No evidence of caspase 3/7 activity among quartz samples was detected.

The result of the assay (Fig. 5.8) excluded the activation of caspase 3/7 related pathways among all the quartz tested samples (synthetic or mineral, as-grown or fractured), thus indicating these enzymes are not involved in the cell death

mechanism observed in our model. Thus, cell death did not follow the apoptotic pathway.

5.3.6 Evaluation of protein corona effect on quartz impact on cell viability

The effect of protein corona on crystals impact on the macrophages was evaluated by exposing the THP-1 macrophages to the same dust, before and after the addition of 10% fetal bovine serum (FBS) as source of proteins. Cell membrane permeability, upon interaction with quartz crystals in the two conditions (with (+) and without (-) protein corona), was assessed by propidium iodide (PI) assay. In view of that, cells were prepared for flow cytometry as previously described. After particles addition and wash, the cells were re-suspended in PBS and stained with 5 μg/ml PI. Then, after a short incubation (5 minutes) at room temperature, samples were run on the flow cytometer. Any cell exhibiting a strong fluorescence signal on the FL-2 channel was considered dead, as PI only enters dead cells. Results of the assays are reported as mean % of PI positive cells ± SD, calculate from triplicate measurements of each condition.

To build a comparative model, the impact of the protein corona was initially evaluated on aminomodified polystyrene nanoparticles. Due to the net positive surface charge, these particles strongly interact with plasmamembrane, through the establishing of electrostatic interactions with lipid heads, thus leading to fast PI permeability. When coated by corona, the early effect on cell membrane permeability is instead lost (Wang et al., 2013) Effects were evaluated at two different time-points, 4 and 24 hours. PS-NH$_2$ nanoparticles were tested at a concentration of 25 μg/ml (fig. 5.9), while quartz crystals (the full set of samples, Fig 5.9, panel A and B) at a concentration of 100 μg/ml.
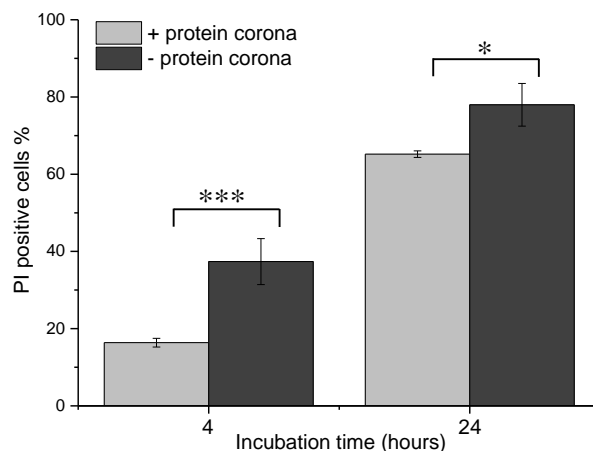
Fig. 5.9 Impact of protein corona on PS-NH$_2$ cytotoxicity towards differentiated THP-1 macrophages after 4 and 24 hours of exposure, evaluated by means of the variation in membrane permeability, calculated as propidium iodide positive cells. Data show different behaviour comparing the two conditions, especially at the short exposure time.

Cationic nanoparticles, such as the amino modified polystyrene nanoparticles used in this assay, are known to induce cell death via apoptosis when coated by corona. As shown in figure 5.9, positively charged polystyrene nanoparticles dispersed in the presence of FBS proteins (light grey bars) had a particularly low cytotoxic potential if compared to naked particles, while in serum-free conditions (no proteins in the incubation media, dark-grey bars), stronger effects might be detected on membrane permabilization, at an incubation of 4 hours only. Thus, particles were toxic also with protein corona, but mainly at long time and, presumably, via apoptosis. On the other hand, incubation with serum free particles resulted in fast necrosis and fast cell membrane permeabilization.
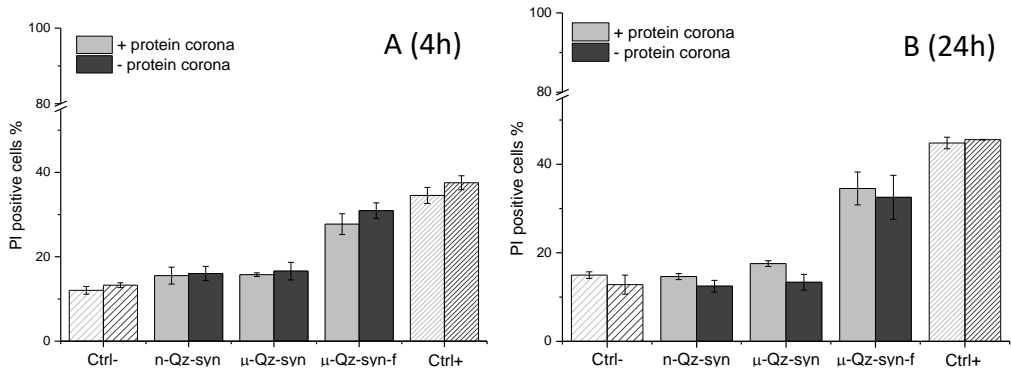
Fig. 5.10 Impact of protein corona on quartz cytotoxicity after 4 (panel A) and 24 (panel B) hours of exposure, evaluated by means of the variation in membrane permeability. Data show no different behaviour comparing the two conditions for the same sample. On the contrary, an increasing cytotoxicity can be noticed between as-grown and fractured crystals.

The same experiment was carried out, in the same conditions, incubating cells with as-grown and fractured quartz crystals. Differently from what evidenced for PS-NH$_2$, no difference in membrane permeability degree was noticed among the specific quartz crystals dust dispersed with or without the presence of serum proteins, at both short and long exposure times (Fig 5.10). The overall membrane permeability, as expected, increased upon the incubation of cells with fractured crystals, thus supporting the results obtained in the previous assays: a very low reactivity, comparable to that found for untreated cells, was evidenced for as-grown samples (n-Qz-syn, μ-Qz-syn). On the contrary, fractured synthetic samples, showed higher cell toxicity.

5.4 Discussion and Conclusions

The evaluation of the interaction between a set of quartz crystals synthesized ad hoc, with regular and fractured faces, and membrane models at increasing complexity (liposome and red blood cell, respectively), showed strong membrano-perturbative potential only for fractured crystals, while as-grown intact particles did not evidence any sign of reactivity. This particular behaviour has been explained considering the strong difference in surface chemistry, induced upon mechanical fracturing (Turci et al., 2016)*:* regular surfaces, characterized by the organized and homogeneous distribution of silanols array, might become strongly disorganized and heterogeneous, with the concomitant presence of hydrophilic and hydrophobic patches (Fig. 5.11). This particular surface, imparted strong reactivity to the surface. Thus, crystallinity seems to be not directly related to cytotoxicity.
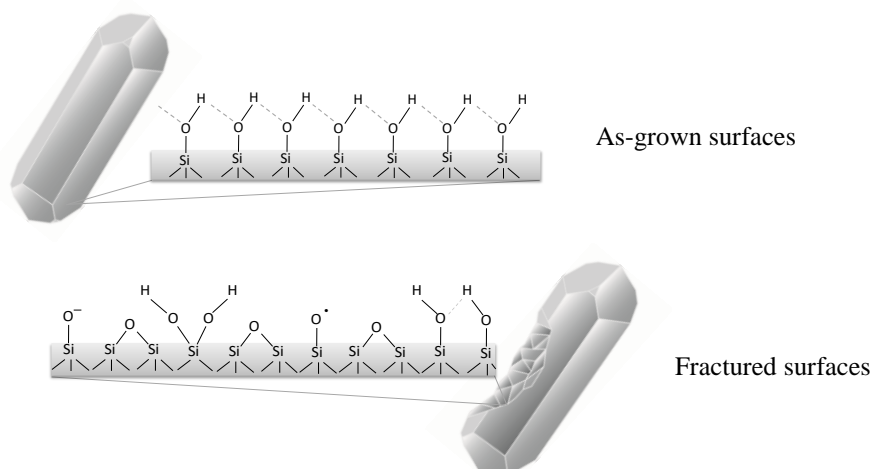
Fig. 5.11 As-grown surfaces are characterized by mutually H-bonded silanols, highly hydroxylated surfaces and a strong chemical ordered are non membranolytic. Fractured faces (highly membranolytic), on the other hand, might be characterized by silanols available for H-bonding with external molecules, heterogeneous and disorganized silanol patterns containing geminal, isolated, and weakly interacting silanols. (Pavan et al., 2013)

According to the literature, RBC lysis may be considered as a suitable model of phagolysosomal membrane damage, and hemolysis assay predictive of labilization of the phagolysosome, a process that lead to inflammasome activation and release of pro-inflammatory mediators (IL-1α, IL-1β) (Latz, Xiao, & Stutz, 2013; Mossman & Churg, 1998; Pavan et al., 2013; Rabolli et al., 2015; Sharma & Kanneganti, 2016). Through the evaluation of several cytotoxicity

endpoints, upon the incubation of murine and human macrophages with synthetic quartz crystals, we have investigated whether, and how, different surface properties affect cellular viability, by referring, in particular, to the phagolysosomal membrane as biomembrane model at extreme complexity, in order to obtain new insights on the first steps of crystals internalization.

Interestingly, a common pattern of cytotoxicity, in which only fractured crystals were found to strongly affect cellular viability, was evidenced through different endpoints (membrane permeability and metabolic activity), carried out in two distinct macrophage cell lines, murine and human. Since as-grown and fractured crystals were equally internalized by Raw 264.7 murine macrophages, as ascertained by bio-TEM imaging (Turci et al., 2016), macrophage stress was probably ascribable not to difference in uptake among intact and fractured crystals, but to different phagolysosome activation and perturbation upon phagocytosis. In this context, the small increase of LysoTracker fluorescence, which could be a sign of potential lysosomal alteration upon particle internalization, might represents a further proof of the different reactivity of regular and irregular surfaces, regardless their crystallinity. This may lead to generation of different levels of intracellular radical species (ROS), due to phagolysosomal damage (Driscoll, 1995) as the result of the strong interaction with fractured particles. Furthermore, these latter considerations could sustain the *in-vivo* proposed model of inflammogenicity (see Introduction chapter): according to this hypothesis, the enzymatic digestion of surfactants and proteins adherent to the particle surface, will allow the bare surface interact with the inner side of the phagolysosomal membrane. In the event that the interaction is so strong to result in the disruption of the membrane, this may lead to a heavy lysosome destabilization which might cause a condition of persistent inflammation, due to the activation of multiple macrophages. However, because of the small signal detected and the absence of lysosomal stress upon the interaction of TPH-1 macrophages with NH_2-polystyrene nanoparticles, which are known to induce extreme increase in volume and phagolysosomal membrane disruption in other cell lines, we cannot fully confirm a direct damage of quartz crystal towards lysosomes and, furthermore, a specific difference in lysosomal stress activity among as-grown and fractured samples. Same contradictory indications can be deduced from the evaluation of intracellular ROS generation. No difference between synthetic as-grown and fractured crystals has been evidenced.

ROS generation, however, it is not directly related to cell death. In our case, cell death occurred as evidenced by the investigation of the plasmamembrane permeability, through LDH and PI assays, via a non-apoptotic pathway, as deduced by the caspase assay. According to the literature (Hari et al., 2014; Rabolli et al., 2015) this latter result was expected. Macrophage death is known

to follow a particular pathway named "pyroptosis", a particular necrotic cell death that induces cell swelling and plasma membrane rupture, with release of mature IL-1β and cytoplasmic content leading to an inflammatory reaction.

The evaluation of the impact of protein corona on cytotoxicity allowed us to speculate about the direct interaction occurring with the phagolysosomal membrane upon the internalization of crystals. According to Wang (Wang et al., 2013), on human brain astrocytoma cells, the protein layer masks the positive charges on the surface of polystyrene nanoparticles, thus resulting in the phagocytosis of particles and consequent lysosomal membrane permeabilization, due to the direct interaction of particle surface, after degradation of the protein corona, limiting early stage of cell damage. On the contrary, in serum-free conditions, nanoparticles without protein coverage damage directly the plasmamembrane, leading to quick cell membrane disruption. Yan et al. (Yan et al., 2013) showed that the adsorption of serum proteins (especially albumin) onto the net negative surface of disulfide-stabilized poly-(methacrylic acid) nanoporous polymer particles (PMA_{SH} NPs) reduced the particle-membrane adhesion on monocytic THP-1 cells, hence resulting in a lower internalization efficiency, in contrast to bare nanoparticles. On the contrary, in macrophage-like THP-1 cells, the expression of SR-A receptors on the cell surface, due the TPA-induced differentiation, activated a unique recognition mechanism, particularly specific for protein-PMA_{SH} nanoparticle complexes. This event triggered the activation of SR-A-mediated phagocytosis by which protein-coated particles are more effectively internalized compared to pristine ones.

In our case, we have evidenced that the protein coverage did not show a dramatic impact on the internalization and the toxic potential of particles Such a particular behaviour might be explained considering the extremely low surface area of quartz crystals available for protein coverage, in respect to that of nanometric particles. We can hypothesize that, in our model, the amount of hard adsorbed serum proteins is negligible and, consequently, engulfed particles in the phagolysosome might be rapidly cleaned after fast digestion of the protein layer by lytic enzymes. Thus, at this stage, a bare crystal surface could be able to establish a direct interaction with the phagolysosomal membrane. However, this aspect should be further investigated, reducing the incubation time (i.e. 1 hour), in order to evaluate the eventual protein corona modulation from a kinetic point of view.

Considering all the results, what seems to be clear is that the interaction with fractured crystals results in stronger macrophage stress. Furthermore, the absence of modulation in toxicity given by the protein corona, is also of particular interest, and should be developed further.

Nevertheless, due to the fast biological answers and the extreme toxicity observed in the investigated cell line, emerges a substantial difficulty to reach clear and definitive conclusions, also considering the particular and unexpected responses given by particles (PS-NH$_2$) known for evoking specific effects towards other cell lines.

Bibliography

Abdal Dayem, A., Hossain, M., Lee, S., Kim, K., Saha, S., Yang, G.-M., Cho, S.-G. (2017). The Role of Reactive Oxygen Species (ROS) in the Biological Activities of Metallic Nanoparticles. *International Journal of Molecular Sciences*, *18*(1), 120. https://doi.org/10.3390/ijms18010120

Anguissola, S., Garry, D., Salvati, A., O'Brien, P.J., & Dawson, K.A. (2014) High content analysis provides mechanistic insights on the pathways of toxicity induced by amine-modified polystyrene nanoparticles, PLoS One, 19;9(9):e108025. https://doi.org/10.1371/journal.pone.0108025

Bexiga, M.G., Varela., J.A., Wang, F., Fenaroli, F., Salvati, A., Lynch, I., Simpson, J.C., Dawson, K.A. (2011). Cationic nanoparticles induce caspase 3-, 7- and 9-mediated cytotoxicity in a human astrocytoma cell line. Nanotoxicology, 5(4): 557-67. https://doi.org/10.3109/17435390.2010.539713,

Cassel, S. L., Eisenbarth, S. C., Iyer, S. S., Sadler, J. J., Colegio, O. R., Tephly, L. A., Sutterwala, F. S. (2008). The Nalp3 inflammasome is essential for the development of silicosis. *Proceedings of the National Academy of Sciences*, *105*(26), 9035–9040. https://doi.org/10.1073/pnas.0803933105

Decker, T., & Lohmann-Matthes, M. (1988). A quick and simple method for the quantitation of LDH release in measurements of cellular cytotoxicity and TNF activity. *J Immunol Methods*, *115*(1), 61–69.

Dengler, W. a, Schulte, J., Berger, D. P., Mertelsmann, R., & Fiebig, H. H. (1995). Development of a propidium iodide fluorescence assay for proliferation and cytotoxicity assays. *Anti-Cancer Drugs*. https://doi.org/10.1097/00001813-199508000-00005

Donaldson, K., Borm, P.J.A. (1998). The quartz hazard: a variable entity. *Ann. Occup. Hyg.*, 42:521-30

Driscoll, K. E. (1995). The toxicology of crystalline silica studied in vitro. *Applied Occupational and Environmental Hygiene*, *10*(12), 1118–1125. https://doi.org/10.1080/1047322X.1995.10389105

Eruslanov, E., & Kusmartsev, S. (2010). Identification of ROS using oxidized DCFDA and flow-cytometry. *Methods in Molecular Biology (Clifton, N.J.),*

594, 57–72. https://doi.org/10.1007/978-1-60761-411-1_4

Fubini, B., & Hubbard, A. (2003). Reactive oxygen species (ROS) and reactive nitrogen species (RNS) generation by silica in inflammation and fibrosis. *Free Radical Biology and Medicine*. https://doi.org/10.1016/S0891-5849(03)00149-7

Gerlier, D., & Thomasset, N. (1986). Use of MTT colorimetric assay to measure cell activation. *Journal of Immunological Methods*, *94*(1–2), 57–63. https://doi.org/10.1016/0022-1759(86)90215-2

Gilberti, R. M., Joshi, G. N., & Knecht, D. A. (2008). The phagocytosis of crystalline silica particles by macrophages. *American Journal of Respiratory Cell and Molecular Biology*, *39*(5), 619–627. https://doi.org/10.1165/rcmb.2008-0046OC

Grisham, M. B., Johnson, G. G., Gautreaux, M. D., & Berg, R. D. (1995). Measurement of Nitrate and Nitrite in Extracellular Fluids: A Window to Systemic Nitric Oxide Metabolism. *Methods*, *7*(1), 84–90. https://doi.org/10.1006/meth.1995.1012

Guicciardi, M. E., Leist, M., & Gores, G. J. (2004). Lysosomes in cell death. *Oncogene*. https://doi.org/10.1038/sj.onc.1207512

Hamilton, R. F., Thakur, S. A., & Holian, A. (2008). Silica binding and toxicity in alveolar macrophages. *Free Radical Biology and Medicine*. https://doi.org/10.1016/j.freeradbiomed.2007.12.027

Hari, A., Zhang, Y., Tu, Z., Detampel, P., Stenner, M., Ganguly, A., & Shi, Y. (2014). Activation of NLRP3 inflammasome by crystalline structures via cell surface contact. *Scientific Reports*, *4*. https://doi.org/10.1038/srep07281

Hornung, V., Bauernfeind, F., Halle, A., Samstad, E. O., Kono, H., Rock, K. L., … Latz, E. (2008). Silica crystals and aluminum salts activate the NALP3 inflammasome through phagosomal destabilization. *Nature Immunology*, *9*(8), 847–856. https://doi.org/10.1038/ni.1631

Hughes, C. S., Colhoun, L. M., Bains, B. K., Kilgour, J. D., Burden, R. E., Burrows, J. F., Scott, C. J. (2016). Extracellular cathepsin S and intracellular caspase 1 activation are surrogate biomarkers of particulate-induced lysosomal disruption in macrophages. *Particle and Fibre Toxicology*, *13*, 19.

https://doi.org/10.1186/s12989-016-0129-5

Kawasaki, H. (2015). A mechanistic review of silica-induced inhalation toxicity. Inhalation Toxicology, 27(8):363-377. https://doi.org/10.3109/08958.78.2015.1066905

Latz, E., Xiao, T. S., & Stutz, A. (2013). Activation and regulation of the inflammasomes. *Nature Reviews Immunology*. https://doi.org/10.1038/nri3452

Lesniak, A., Campbell, A., Monopoli, M., Lynch, I., Salvati, A., Dawson, K.A. (2010). Serum heat inactivation affects protein corona composition and nanoparticle uptake. *Biomaterials*, 31:9511-9518. https://doi.org/10.1016/j.biomaterials.2010.09.049

Lin, W., Huang, Y., Zhou, X.-D., & Ma, Y. (2006). In vitro toxicity of silica nanoparticles in human lung cancer cells. *Toxicology and Applied Pharmacology*, *217*(3), 252–259. https://doi.org/10.1016/j.taap.2006.10.004

Manke, A., Wang, L., & Rojanasakul, Y. (2013). Mechanisms of nanoparticle-induced oxidative stress and toxicity. *BioMed Research International*. https://doi.org/10.1155/2013/942916

Mossman, B. T., & Churg, A. (1998). Mechanisms in the pathogenesis of asbestosis and silicosis. *American Journal of Respiratory and Critical Care Medicine*, *157*(5 PART I), 1666–1680. https://doi.org/10.1164/ajrccm.157.5.9707141

Pavan, C., Rabolli, V., Tomatis, M., Fubini, B., & Lison, D. (2014). Why does the hemolytic activity of silica predict its pro-inflammatory activity? *Particle and Fibre Toxicology*, *11*(1), 76. https://doi.org/10.1186/s12989-014-0076-y

Pavan, C., Tomatis, M., Ghiazza, M., Rabolli, V., Bolis, V., Lison, D., & Fubini, B. (2013). In search of the chemical basis of the hemolytic potential of silicas. *Chemical Research in Toxicology*, *26*(8), 1188–1198. https://doi.org/10.1021/tx400105f

Rabolli, V., Badissi, A. A., Devosse, R., Uwambayinema, F., Yakoub, Y., Palmai-Pallag, M., Huaux, F. (2014). The alarmin IL-1α is a master cytokine in acute lung inflammation induced by silica micro- and nanoparticles. *Particle and Fibre Toxicology*, *11*(1), 69. https://doi.org/10.1186/s12989-014-0069-x

Rabolli, V., Lison, D., & Huaux, F. (2015). The complex cascade of cellular events governing inflammasome activation and IL-1β processing in response to inhaled particles. *Particle and Fibre Toxicology*, *13*(1), 40. https://doi.org/10.1186/s12989-016-0150-8

Schremmer, I., Brik, A., Weber, D. G., Rosenkranz, N., Rostek, A., Loza, K., Westphal, G. A. (2016). Kinetics of chemotaxis, cytokine, and chemokine release of NR8383 macrophages after exposure to inflammatory and inert granular insoluble particles. *Toxicology Letters*, *263*, 68–75. https://doi.org/10.1016/j.toxlet.2016.08.014

Sellamuthu, R., Umbright, C., Roberts, J. R., Young, S. H., Richardson, D., McKinney, W., Joseph, P. (2017). Molecular mechanisms of pulmonary response progression in crystalline silica exposed rats. *Inhalation Toxicology*, *29*(2), 53–64. https://doi.org/10.1080/08958378.2017.1282064

Sharma, D., & Kanneganti, T. D. (2016). The cell biology of inflammasomes: Mechanisms of inflammasome activation and regulation. *Journal of Cell Biology*. https://doi.org/10.1083/jcb.201602089

Tsuchiya, S., Yamabe, M., Yamaguchi, Y., Kobayashi, Y., Konno, T., & Tada, K. (1980) Establishment and characterization of a human acute monocytic leukemia cell line (THP- 1). *International Journal of Cancer* 26: 171-176, 1980

Turci, F., Pavan, C., Leinardi, R., Tomatis, M., Pastero, L., Garry, D., Fubini, B. (2016). Revisiting the paradigm of silica pathogenicity with synthetic quartz crystals: the role of crystallinity and surface disorder. *Particle and Fibre Toxicology*, *13*(1), 32.

Vince, J. E., & Silke, J. (2016). The intersection of cell death and inflammasome activation. *Cellular and Molecular Life Sciences*. https://doi.org/10.1007/s00018-016-2205-2

Wang, F., Yu, L., Monopoli, M. P., Sandin, P., Mahon, E., Salvati, A., & Dawson, K. A. (2013). The biomolecular corona is retained during nanoparticle uptake and protects the cells from the damage induced by cationic nanoparticles until degraded in the lysosomes. *Nanomedicine: Nanotechnology, Biology, and Medicine*, *9*(8), 1159–1168.

https://doi.org/10.1016/j.nano.2013.04.010

Yan, Y., Gause, K. T., Kamphuis, M. M. J., Ang, C. S., O'Brien-Simpson, N. M., Lenzo, J. C., … Caruso, F. (2013). Differential roles of the protein corona in the cellular uptake of nanoporous polymer particles by monocyte and macrophage cell lines. *ACS Nano*, *7*(12), 10960–10970. https://doi.org/10.1021/nn404481f

Xia, T., Kovochich, M., Liong, M., Zink, J.I., & Nel, A. (2008). Cationic polystyrene nanosphere toxicity depends on cell-specific endocytix and mitochondrial injury pathways, *ACS Nano*, 2(1), 85-96. https://doi.org/10.1021/nn700256c

Ye, Y., Liu, J., Chen, M., Sun, L., & Lan, M. (2010). In vitro toxicity of silica nanoparticles in myocardial cells. *Environmental Toxicology and Pharmacology*, *29*(2), 131–137. https://doi.org/10.1016/j.etap.2009.12.002

Ye, Y., Liu, J., Xu, J., Sun, L., Chen, M., & Lan, M. (2010). Nano-SiO2 induces apoptosis via activation of p53 and Bax mediated by oxidative stress in human hepatic cell line. *Toxicology in Vitro*, *24*(3), 751–758. https://doi.org/10.1016/j.tiv.2010.01.001

Chapter 6

General discussion and conclusion

6.1 Closing remarks

While the pathogenic potential of crystalline silica, and also its extreme variability, has long been recognized, the toxicity of amorphous silica is still under debate, in particular concerning the application of silica nanoparticles in nanomedicine (Pavan & Fubini, 2017). Despite crystalline and amorphous silica particles share the same chemical composition, while bulk and surface properties are extremely different. Accordingly, a strong distinction between the results obtained with crystalline and amorphous silicas is required, since they represent two specific and different entities.

However, a certain variability of outcomes in acellular assays showed by amorphous silica particles, reflects variability in the distribution of surface chemical functionalities, not so far from what discussed for crystalline silica (Pavan & Fubini, 2017). *In vivo* evaluations of toxicity, suggested that amorphous silica mostly causes transient effects (Napierska et al., 2010), likely due to its low biopersistence.

On the contrary, it is well known that the prolonged exposure to respirable crystalline silica dust, especially quartz, might result in the development of severe pathologies and malignancies, including autoimmune diseases, silicosis and lung cancer (IARC, 2012). Nevertheless, new outbreaks of silica-related diseases in occupational settings, in particular silicosis, were recently reported (Akgun et al., 2008; Perez-Alonso et al., 2014; Bang et al., 2015; Güngen, Aydemir, Çoban, Düzenli, & Tasdemir, 2016). All new cases were related to workers exposed to finely fractured or abraded quartz dusts or silica-containing minerals, confirming the high pathogenic activity of freshly fractured crystalline silica (Vallyathan et al., 1995). Quartz is indeed considered to be more toxic than amorphous silica because of its crystal structure that mainly affect particle solubility and consequently biopersistence in the lung (IARC, 1997 & 2012). However, not all silica polymorphs are considered to be equally pathogenic (Stratta, Canavese, Messuerotti, Fenoglio, & Fubini, 2001). Variability of crystalline silica pathogenicity is mainly linked to two different factors, namely the peculiar chemistry of the dust (B. Fubini, 1998) and to the several and complex interactions occurring *in vivo* between silica particles with biomolecules and cells. However, investigations carried out to understand the molecular mechanisms of action of crystalline silica, have been so far carried out on the same fractured mineral quartz dusts used in toxicological experiments. It is well-known that fracturing may affect particle crystallinity and yields samples with extreme variable and complex surface states. This has so far prevented researchers to attain a conclusive consensus on the molecular mechanisms of action of crystalline silica. Furthermore, a mechanistic understanding of the physico-chemical features of silica and their corresponding effects in biological and pathogenic response is not trivial, not only because of the variability of silica,

but also due to the complexity of cellular models. Thus, to fill this gap and learn more on which molecular mechanisms guide the interaction with plasma biomembrane, in particular phagolysosomal membrane, we have developed a simplified approach consisting of i) biomembrane models at increasing complexity, ii) ad-hoc prepared quarts respirable crystals, and iii) surface-controlled amorphous silica nanoparticles.

For the first time, to the best of our knowledge, models of silica crystals with intact and regular surfaces, synthesized *ad-hoc* to overcome the extreme variability of mechanically-fractured mineral quartz dusts and investigate the role of crystal structure, were grown in respirable size through a new synthetic approach. Such a model, with tunable characteristics, size and shape in particular, represents the perfect approach to evidence and investigate the interaction between a cell and a well-characterized quartz crystal. At the molecular level, the phenomenon involves the direct interaction between biomembranes and arrays of surface silanols allowing us to introduce the concept of "ordered" and "disordered" surfaces in the cytotoxic activity of quartz. On the other hand, to reduce the extreme complexity of living cell membranes, model of biomembranes allowed us to evidence, at a molecular level, the chemical nature of the interaction with quartz. *In-vivo* the first interaction between quartz crystals and cells upon inhalation of respirable quartz dusts occurs at the level of the cell membrane (Nash et al., 1966; Summerton, Hoenig, Butler, & Chvapil, 1977). Then, upon internalization, particles are engulfed inside phagolysosomes and phagolysosomal membrane might become another possible target of silica. In our work, the direct interaction with two different membrane models, at increasing complexity, have been evaluated: unilamellar liposomes, a very simple biomembrane model, and red blood cells, whose rupture can be considered an indication of particle cytotoxicity/inflammogenicity (Nolan et al., 1981). Finally, taking advantage of the knowledge acquired with model membranes, indications were translated towards a further complex model, namely two human and murine macrophage cell lines.

A crucial step of the present work, was the understanding of how such interaction occurs and whether, and at which extent, it is affected by differences in quartz crystals surface chemical features. Surface differences were induced through the mechanical milling of one of the synthetic crystal, in order to introduce defects and locally disordered conchoidal fractures, typical of natural dusts.

Results obtained through the investigation of crystalline silica and biomembrane models, have been confirmed upon the incubation with cell lines: low membrano-perturbative activity of crystals with intact surfaces, characterized by a homogeneous array of surface silanols towards biomembrane models,

indicated a negligible effect on cellular viability and likely toxicity. An opposite behavior was evidenced on quartz with fractured surfaces, in both cell-free and cellular tests. Overall, the results suggest that:

1. contrary to the classical paradigm for quartz toxicity, crystallinity *per se* seems not to be strictly related to pathogenicity;

2. among the several physico-chemical features that characterize silica particles, the *surface distribution of silanols* was found to play a key role in the interaction with bio-membranes. The crucial role of silanols, acidic moieties with a potential for H-bonding, in defining silica interaction with cells, has been thus confirmed experimentally for the first time;

3. in addition, the ζ–plot (zeta-potential *vs* pH) measured for as-grown quartz, suggested that silanols on regular surfaces have mostly the same acidity, indicating a *long-range silanol homogeneity*, that seems to be absent in irregular fractured surfaces, which were shown to strongly interact with membrane. Congruently, previous studies associated the hemolytic activity to some peculiar spatial arrangements of silanols and siloxanes (Murashov et al., 2006; Pavan et al., 2013; Pandurangi et al., 1990).

Hence, chemical and biological reactivity are probably related with the disordered surface moieties (silanols, silanolates, siloxanes) generated upon fracturing regular crystals, when conchoidal fractures are formed (Murashov & Demchuk, 2005) (see Fig. 1)
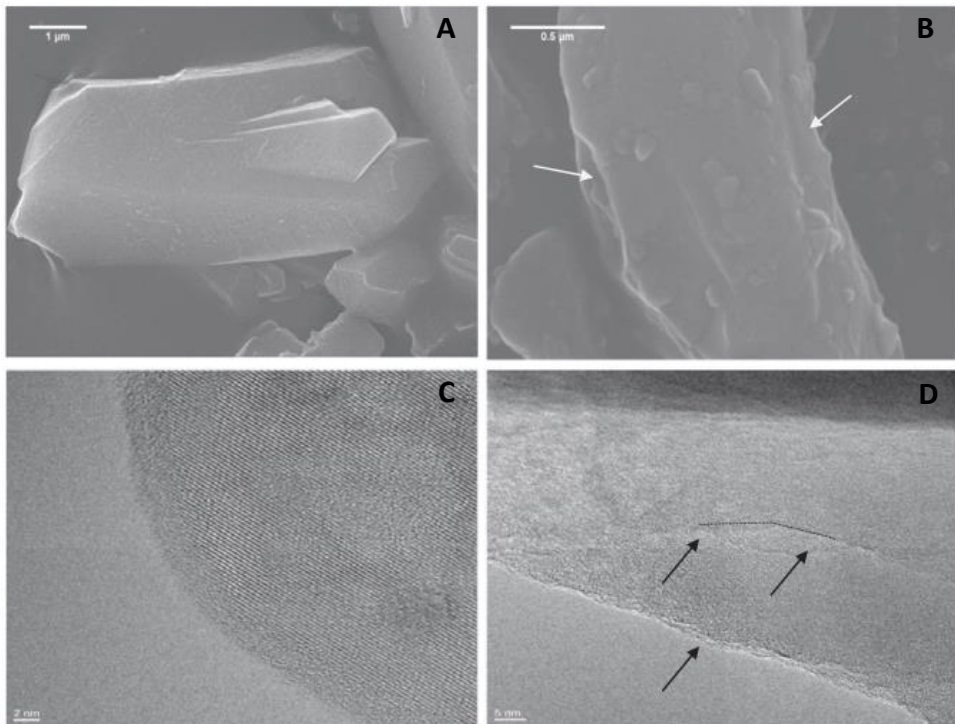
Fig. 1 FE-SEM imaging of synthetic quartz crystals, before (panel A) and after (panel B) mechanical fracturing. As-grown quartz shows regular, well-formed and smooth surfaces (A), while conchoidal fractures (white arrows) were visible on fractured particles (B and D). Crystal structure was preserved up to the very last atomic boundary of the synthetic crystal (C), while fracturing induced partial disorganization of crystal lattice (absence of diffraction fringes) and loss of long-range ordered crystalline planes (D, black arrows) (Turci et al., 2016)

An extreme interest was also devoted to gain a better understanding on how surface properties of crystalline silica can impact cell viability. We focused our attention on the evaluation of the phagolysosomal destabilization related to macrophage stress, with a particular attention to the chemical differences among ordered and disordered surfaces. Silica particles cannot be degraded by lysosomal lytic enzymes. This may lead to lysosomal membrane permeabilization (LMP), through a still unknown mechanism. In a very recent AOP (adverse outcome pathway) (Pavan & Fubini, 2017) proposed for silica-induced inflammogenicity, disruption of phagolysosome membrane results in the leakage of lytic enzymes, which trigger inflammasome machinery activation and, as a consequence, lung inflammation. Detrimental and cytotoxic effects of

particles can be modulated by the presence of proteins adsorbed from the surrounding environment on the particle surface were evaluated. Contrary to what expected or hypothesized, protein corona seems to be unable to modulate or modify the impact of quartz crystals on cell, probably due to the very low specific surface area available for the adsorption of serum proteins. This indication well correlates with the AOP model, supporting the hypothesis of a direct interaction with the inner side of the phagolysosomal membrane. Moreover, the results suggest that inside the phagolysosome, particles should act as naked, due to the quick enzymatic degradation of the protein layer. However, our study produced contrasting indications concerning the *in vitro* investigation of lysosome stress (increase in volume and acidification), probably due to the particular macrophage cell line chosen, and definitive conclusions, specifically regarding difference in internalization among the whole set of crystals, are still to be achieved.

The fundamental role of surface silanols distribution in driving the interaction was evidenced not only for crystalline silica samples, but also for amorphous particles. Heterogeneous surfaces were more perturbative towards liposomes and red blood cells, because of the simultaneous presence, on the same surface, of isolated, weakly interacting, and strongly H-bonded silanols. On the contrary, a different scenario was offered when the surface geometry of the particle is loss through the presence of structural pores. Porosity strongly demotes the interaction towards the red blood cell membrane, due to the inability of the particle to establish long-range interaction with RBC bilayer, even whether particle surface is particularly heterogeneous. Nanometric liposome, probably due to a) a smaller size and b) a simpler chemical composition, shows a contrasting behavior with respect to erythrocyte. Interestingly, the response among the two biomembrane model was comparable only when surface silanols of mesoporous and dense nanoparticles were masked by chemical functionalization with aminogroups. This is another powerful indication of the importance of Si-OH groups as the main molecular player in the definition of the silica-biomembrane interaction.

6.1 Prospects for future researches

The results achieved during this Ph.D. thesis allow several possible future research lines to be continued. Firstly, the identification of the active silanol sites could be carried out through an accurate surface physico-chemical characterization of silica synthetic models, both crystalline and amorphous. This knowledge might allow us to usefully predict the toxic activity of a given silica dust, before ethical and time-consuming animal tests are carried out. Furthermore, the characterization of silanol families of crystalline silica through FTIR spectroscopy, will allow to specifically assign to the observed differences in surface homogeneity showed by intact and fractured quartz crystals.

As above mentioned, several particle characteristics contribute to different extents to the overall pathogenicity of a specific source of silica. In this context, one could attempt to block one single step of the mechanism of toxicity, related by a specific particle feature. This methodology could offer at least two main advantages:

i) the *reduction* of the toxic potential of a definite silica with a safe-by-design approach;
ii) the opportunity to directly *relate* each step of the mechanism of toxicity with one, or more, specific particle feature.

This could also have a positive fall out for the evaluation of the occupational exposure to silica, fostering a safer and more conscious use of silica.

Such evaluation might also provide precious suggestion concerning the investigation of the internalization and engulfment of particles. Quartz uptake due to phagocytosis represents a key aspect of its *clearance* from the lungs, which is a crucial defense mechanism against foreign agents. To this, and also to clarify the *fate* of quartz particles after the uptake, a convenient approach could be the use of confocal microscopy coupled with particle light scattering, in order to avoid the surface functionalization of crystals with fluorescent probe, or cryo-TEM imaging. Such approaches might allow to monitor not only the intracellular localization of particles, but also the impact of the internalization on cytoplasmic organelles, especially the lysosomes. Furthermore, confocal microscopy could indicate whether different surface features of particles sharing the same chemical composition and bulk structure, reflects in a different uptake.

Different surface features could also be responsible of differences in the adsorption of specific serum proteins: in this view, a characterization of the protein corona might be useful to understand eventual effect of fracturing on

the interaction with biomolecules, and, moreover, clarify if proteins adsorption occurs on specific faces (regular or conchoidal-fractured ones), or, on the contrary, uniformly on the entire surface of the crystal. In this view, besides proteins, the interest could also be devoted to the investigation of the adsorption of membrane fragments, starting from simplified models (artificial bilayers and the so-called red blood cell *ghosts*), and then moving towards a more complex model (i.e. epithelial and macrophage cell lines). In this framework, a specific and detailed characterization of particle surface through ultra-resolved electron microscopies, could represent a suitable support to evidence eventual changes in surface morphology upon the interaction with protein/membrane fragments.

A strong innovation is also possible in the development of better artificial membrane models. The continuous evolution of synthetic bio-inspired membranes guarantees the possibility to obtain particularly accurate insights on the key mechanism of the interaction between particles and biomembrane, especially from a chemical point of view. New membranes, possibly enhanced with the use of probes, could clarify the specific or non-specific nature of the particle-membrane interactions. Slight modifications of the bilayer fluidity being possible could clarify the thermodynamic and kinetic aspects of the interaction. One of the main advantages of the approach, is the possibility to employ different techniques during the same experiment, which provide complementary data, in order to obtain a wider and more complete view of the system, avoiding to further increase its complexity.

In this sense, a specific attention has to be focused on the choice of lipid composition, which remains a critical point for the study of the interaction. Of course, it must be clear that, to date, membrane models do not provide a toxicity assessment, but only represent a suitable approach to investigate some specific toxic effects of inorganic particulates, associated with the disruptor of membrane and membranous lipids. In fact, membrane models can effectively provide precious information on the mechanical interaction and chemical reaction occurring between membranous lipids and particles, clarifying the process of the direct interaction.

Bibliography

Akgun, M., Araz, O., Akkurt, I., Eroglu, A., Alper, F., Saglam, L., Nemery, B. (2008). An epidemic of silicosis among former denim sandblasters. *European Respiratory Journal*, *32*(5), 1295–1303. https://doi.org/10.1183/09031936.00093507

Bang, K. M., Mazurek, J. M., Wood, J. M., White, G. E., Hendricks, S. A., & Weston, A. (2015). Silicosis, mortality trends and new exposures to respirable crystalline silica — United States, 2001-2010. *Morbidity and Mortality Weekly Report*, *64*(5), 117–133.

Fubini, B. (1998). Surface chemistry and quartz hazard. *Annals of Occupational Hygiene*. https://doi.org/10.1016/S0003-4878(98)00066-0

Güngen, A. C., Aydemir, Y., Çoban, H., Düzenli, H., & Tasdemir, C. (2016). Lung cancer in patients diagnosed with silicosis should be investigated. *Respiratory Medicine Case Reports*, *18*, 93–95. https://doi.org/10.1016/j.rmcr.2016.04.011

Murashov, V. V., & Demchuk, E. (2005). A comparative study of unrelaxed surfaces on quartz and kaolinite, using the periodic density functional theory. *Journal of Physical Chemistry B*, *109*(21), 10835–10841. https://doi.org/10.1021/jp050113a

Napierska, D., Thomassen, L.C.J., Lison, D., Martens, J.A., & Hoet, P.H. (2010). The nanosilica hazard: another variable entity. *Particle and Fibre Toxicology*, 7, 39. https://doi.org/10.1186/1743-8977-7-39

Nash, T., Allison, A. C., & Harington, J. S. (1966). Physico-chemical properties of silica in relation to its toxicity. *Nature*, *210*(5033), 259–261. https://doi.org/10.1038/210259a0

Nolan, R. P., Langer, A. M., Harington, J. S., Oster, G., & Selikoff, I. J. (1981). Quartz hemolysis as related to its surface functionalities. *Environmental Research*, *26*(2), 503–520. https://doi.org/10.1016/0013-9351(81)90226-7

Pandurangi, R.S., Seehra, M.S., Razzaboni, B.L., & Bolsaitis, P. (1990). Surface and bulk infrared modes of crystalline and amorphous silica particles: a study of the relation of surface structure to cytotoxicity of respirable silica. *Environmental Health Perspectives*, 86:327-336. https://doi.org

Pavan, C., & Fubini, B. (2017). Unveiling the Variability of "Quartz Hazard" in Light of Recent Toxicological Findings. *Chemical Research in Toxicology*, *30*(1), 469–485. https://doi.org/10.1021/acs.chemrestox.6b00409

Pavan, C., Tomatis, M., Ghiazza, M., Rabolli, V., Bolis, V., Lison, D., & Fubini, B. (2013). In search of the chemical basis of the hemolytic potential of silicas. *Chemical Research in Toxicology*, 26:1188-1198. https://doi.org/10.1021/tx400105f

Pérez-Alonso, A., Cordoba-Doña, J.A., Millares-Lorenzo, J.L., Figueroa-Murillo, E., Garcìa-Vadillo, C., & Romero-Morillos, J. (2014). utbreak of silicosis in Spanish quartz conglomerate workers. International Journal of Occupational and Environmental Health, 20(1):26-32

Stratta, P., Canavese, C., Messuerotti, A., Fenoglio, I., & Fubini, B. (2001). Silica and renal diseases: No longer a problem in the 21st century? *Journal of Nephrology*.

Summerton, J., Hoenig, S., Butler, C., & Chvapil, M. (1977). The mechanism of hemolysis by silica and its bearing on silicosis. *Experimental and Molecular Pathology*, *26*(1), 113–128. https://doi.org/10.1016/0014-4800(77)90071-5

Turci, F., Pavan, C., Leinardi, R., Tomatis, M., Pastero, L., Garry, D., Fubini, B. (2016). Revisiting the paradigm of silica pathogenicity with synthetic quartz crystals: the role of crystallinity and surface disorder. *Particle and Fibre Toxicology*, *13*(1), 32. Retrieved from http://www.ncbi.nlm.nih.gov/pubmed/27286702%5Cnhttp://www.pubmedcentral.nih.gov/articlerender.fcgi?artid=PMC4902968

Vallyathan, V., Castranova, V., Pack, D., Leonard, S., Shumaker, J., Hubbs, A.F., Shoemaker, D.A., Ramsey, D.M,. Pretty, J.R., & McLaurin, J.L. (1995). Freshly fractured quartz inhalation leads to enhanced lung injury and inflammation. Potential role of free radicals. *American Journal of Respiratory and Critical Care Medicine*, 152(3):1003-1009 https://doi.org/10.1164/ajrccm.152.3.7663775

1. Pastero, L., Turci, F., **Leinardi, R**., Pavan, C., & Monopoli, M. (2016). Synthesis of α-Quartz with Controlled Properties for the Investigation of the Molecular Determinants in Silica Toxicology. *Crystal Growth and Design*, *16*(4), 2394–2403. https://doi.org/10.1021/acs.cgd.6b00183

2. Turci, F., Pavan, C., **Leinardi, R**., Tomatis, M., Pastero, L., Garry, D., Fubini, B. (2016). Revisiting the paradigm of silica pathogenicity with synthetic quartz crystals: the role of crystallinity and surface disorder. *Particle and Fibre Toxicology*, *13*(1), 32. Retrieved from http://www.ncbi.nlm.nih.gov/pubmed/27286702%5Cn

3. **Leinardi, R**., Turci, F., Pavan, C., Berlier., G. Modulation of the interaction between amorphous silica nanoparticles and membrane models at increasing complexity: the case of particle geometry, *in prep*.

A. Synthesis of α-Quartz with Controlled Properties for the Investigation of the Molecular Determinants in Silica Toxicology. *Crystal Growth and Design*, 2016

B. Revisiting the paradigm of silica pathogenicity with synthetic quartz crystals: the role of crystallinity and surface disorder. *Particle and Fibre Toxicology,* 2016

Synthesis of α-Quartz with Controlled Properties for the Investigation of the Molecular Determinants in Silica Toxicology

Linda Pastero,[*,†,§,‖,⊥] Francesco Turci,[‡,§,‖] Riccardo Leinardi,[‡,‖] Cristina Pavan,[‡,‖] and Marco Monopoli[#,¶]

[†]Department of Earth Sciences, University of Torino, Via Valperga Caluso, 35, 10125 Torino, Italy [‡]Department of Chemistry, University of Torino, Via Pietro Giuria 7, 10125 Torino, Italy

[§]NIS Interdepartmental Center for Nanostructured Interfaces and Surfaces, University of Torino, Via Pietro Giuria 7, 10125 Torino, Italy

[‖]G. Scansetti Interdepartmental Centre for Studies on Asbestos and Other Toxic Particulates, University of Torino, Via Pietro Giuria 7, 10125 Torino, Italy

[⊥]CrisDi Interdepartmental Center for Crystallography, University of Torino, Via Pietro Giuria 7, 10125 Torino, Italy

[#]Centre for BioNano Interactions, School of Chemistry and Chemical Biology, University College Dublin, Dublin 4, Ireland

[¶]Department of Pharmaceutical and Medical Chemistry, Royal College of Surgeons in Ireland, 123 St. Stephen's Green, Dublin 2, Ireland

* Supporting Information

ABSTRACT: Many experimental studies about the harmful effects of crystalline silica on human health are present in the literature. However, the relationship between toxicological properties and surface functionalities of quartz is not yet fully explained because of the large intrinsic variability of natural samples. Specific surface properties are related to the surface structure: this implies that a reliable constraint on the crystal growth morphologies is necessary in order to control the behavior variability. With a view to understanding this relationship, a consistent, clean, and easy way to crystallize quartz is proposed. In this paper, α-quartz crystals with controlled morphology and properties were prepared by an unusual and accurate approach under mild hydrothermal conditions (200 °C, autogenic pressure) starting from silica gels prepared with different polymerizing agents. Gels and synthetic crystals were characterized using a wide range of experimental techniques: elemental analysis by ICP-OES, X-ray powder diffraction and Rietveld analysis, SEM and HR-TEM microscopies, BET surface analysis, differential centrifugal sedimentation, and FT-IR spectroscopy. Results are discussed in the light of the crystal growth mechanisms involved.
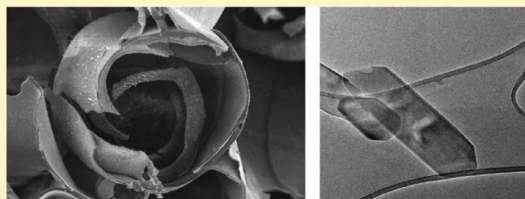
1. INTRODUCTION

During the past 150 years, the interest about the synthesis and crystal growth of α-quartz encompassed naturalistic, industrial, and toxicological researches. In these fields, an increasing attention has been devoted to tailoring quartz crystal size investigating surface properties, and understanding the interaction relation between crystal surface and biomolecules at the molecular level.[1−5]

In this context, the synthesis of amorphous silica and crystalline SiO_2, with controlled properties, has become a research frontier in the investigation of the molecular mechanism in silica toxicology.[6]

Crystalline silica is a well-known carcinogenic agent, and its inflammogenic potential has been often correlated to the occurrence of some specific surface properties.[7−10,4,6] A large body of scientific literature exits on the mechanisms that elicit quartz-induced detrimental effects on human health.[11,12] Nevertheless, previous attempts to draw a structure−activity

relationship (SAR) between quartz physico-chemical proper-ties, including size, surface charge, and surface functionality, have not yet provided a definitive picture, mainly because of the large intrinsic variability of natural quartz. A bottom-up synthetic approach has been largely exploited to systematically investigate the physico-chemical determinants of the interaction of amorphous silica with the biological environment, including protein, membrane, and cell.[13−16] Adapting this approach to crystalline silica, well-formed and surface-tailored synthetic crystals could be exploited to investigate the molecular nature of the interaction between quartz and living matter.

Many pioneering papers dealing with the hydrothermal synthesis of α-quartz from pure silica aqueous solutions or from amorphous silica in the presence of impurities (typically alkali

halides and alkali hydroxides) were published as from the second half of the 19th century. Inevitably, the negligible solubility of silica in water in standard conditions requires high pressure and temperature to completely dissolve the supply material and the quenching of the solution to induce nucleation of quartz commonly yields some amorphous unreacted material to remain at the end of the experiment.[17] Moreover, size and properties of the synthetic crystals are difficult to control.

Li and co-workers obtained spherulitic growth of quartz aggregates starting from a silica gel obtained by mixing a silica solution with hydrochloric acid until polymerization was reached.[18] Quartz crystals were characterized following the procedure proposed by Zhdanov, but neither control over crystallite size and surface properties was achieved nor explanations about the mechanism of crystal growth from gel were proposed.[19]

In the present work, a similar unconventional sol/gel approach which employs Na-metasilicate solution (Na-MTS) polymerized using mineral acids has been followed. To keep the chemical complexity of the gel as low as possible, HNO_3 and H_2CO_3 were used as polymerizing agents. The advantage of using a gel during the crystallization of large crystals of sparingly soluble salts mainly resides in the low supersaturation reached into the porous medium reaction even in the presence of high concentrated solutions. This limits the number of nuclei reaching the critical size and decreases the crystal growth rate, allowing controlling the surface reaction rate.[20,21] Some of us showed that the growth of large crystals from slightly soluble salts can be successfully carried out in gel under a pure diffusive regime.[22] Moreover, a gel minimizes the mechanical stress generated by the interactions among crystals, and between crystal and reactor wall coming to a suitable way to mimic microgravity conditions, allowing discriminating the effects of convection and diffusion during the crystal growth processes.[23]

Commonly, gel is assumed to be a chemically inert "glassy sponge", limiting the reaction rate and the effect of convection and gravity, disregarding the reactions between gel main constituents and counterions. However, during the growth of silicates, it may act as a semi-infinite reservoir[24−27] of highly reactive silica. Therefore, a systematic characterization of the gel properties was carried out by evaluating the gel structure and performance in fluid transport and substrate effectiveness (ICP-OES, SEM). The crystal structure (XRPD and TEM), surface area (Kr-BET), crystal morphology (SEM and TEM), particle size distribution (DCS), and chemical proximity of surface silanols (FT-IR spectroscopy) of the synthesized α-quartz crystals were evaluated and compared to a pure natural quartz, previously used in many toxicological studies. In this work, we succeeded in controlling, for the first time, some crystal properties (size, surface quality, defects) by modulating gel composition and reaction conditions. The mechanism for quartz formation supported by the proposed gel-induced crystal growth is also discussed.

2. EXPERIMENTAL SECTION

2.1. Materials and Reagents. Silica gel was prepared from 25% w/w Na-MTS solution (sodium metasilicate pentahydrate, Aldrich). The gel was polymerized using two mineral acids: (i) HNO_3, and (ii) H_2CO_3 obtained by bubbling CO_2 into the Na-MTS solution until gel formation. The two gels are hereafter referred to as NG and CG. Because of the weak acid dissociation constants of H_2CO_3 ($K_{a1} = 4.3 \cdot 10^{-7}$, $K_{a2} = 4.7 \cdot 10^{-11}$), the CG gel was stabilized at pH = ca. 8. A compatible pH range (between 7 and 8) was used with HNO_3 as polymerizing agent to ensure the highest consistency during growth.

Growth runs of 12−168 h were performed at 200 °C and autogenic pressure in PFTE liner sealed into steel autoclaves. Ultrapure water was employed for all solutions. All other reagents were of analytical purity grade and were supplied by Sigma.

A pure quartz specimen from Madagascar largely employed in several toxicological studies was used as comparison in some experiments.

2.2. Inductively Coupled Plasma Spectroscopy (ICP-OES). Elemental analysis of Na-MTS quartz-forming gels was carried out to investigate partition and properties of the CG and NG gels. Moving solution inside the gels was extracted by a spin dryer in order to evaluate their elemental compositions. Elemental analysis of free silicon and sodium inside these solutions was performed by ICP-OES (Thermo Jarrel Ash IRIS Advantage optical plasma spectrometer) under the following operating conditions: flush and analysis pump rate 2.22 mL/min, nebulizer pressure 23 psi, RF power 950 W.

Speciation into the sol/gel systems and saturation index calculations were performed using the PHREEQC program.[28]

2.3. XRPD and Rietveld Analysis. Structural analysis of synthetic quartz crystals was carried out by X-ray powder diffraction (XRPD) using a PANalytical PW3040/60 X'Pert PRO MPD X-ray powder diffractometer. Crystal phases and crystal quality were identified and evaluated by Rietveld data analysis (cell deformation with respect to the NIST SRM 1878a standard and crystallite size) using the MAUD program (Materials Analysis Using Diffraction), a diffraction analysis program mainly based on the Rietveld method.[29,30]

2.4. Electron Microscopies (SEM and HR-TEM). Sample morphology was investigated by scanning electron microscopy (SEM), Cambridge S-360 and Hitachi S-4300 field emission scanning electron microscope. Crystal samples were sonicated for 30 min in ultrapure water, dropped off on conductive stubs, and coated with gold in order to prevent the electron beam from charging the sample. The operating conditions were: EHT 15−25 kV, WD 1−6 mm, probe current 100 pA.

To give evidence of the local structural lattice order of the outer shells surrounding the crystals and to inspect the defectiveness of the quartz samples high-resolution transmission electron microscopy (JEOL 3010-UHR-TEM) equipped with a LaB_6 filament operated at 300 kV, beam current 114 μA, and equipped with a 2k × 2k pixels Gatan US1000 CCD camera was carried out. Elemental analysis was performed by an Oxford INCA X-ray energy-dispersive spectrometer (X-EDS) with a Pentafet Si(Li) detector. Quartz samples were dispersed in ultrapure water (Milli-Q system, Millipore) and sonicated for 20 min, and a droplet was deposited on lacey carbon Cu grids.

2.5. BET Surface Analysis. Surface area of the quartz crystals was measured by means of the BET method based on Kr adsorption at 77 K (ASAP 2020 Micrometrics, Norcross, GA).

2.6. DCS (Differential Centrifugal Sedimentation). The particle size distribution (PSD) of the synthetic and natural quartz samples has been determined by injecting ca. 100 μL of the sample suspended in phosphate buffer (PB, pH 7.4) in a CPS Disc Centrifuge (CPS Instruments, Europe) operated at 14k × g with a 6−24% sucrose gradient in PB. Each experiment has been repeated at least twice. Size distribution data are plotted by relative weight %.

2.7. FT-IR Spectroscopy. For the FTIR measurements (Bruker IFS28; resolution = 2 cm^{-1}; DTGS detector), the quartz samples, pressed into self-supporting pellets, were placed into a quartz IR cell equipped with KBr windows. Spectra were collected on pellets in air. Physisorbed molecular water was then removed at room temperature (RT) or at 400 °C by connecting the cell with the sample to a conventional vacuum line (residual pressure = 1 × 10^{-6} Torr, 1 Torr = 133.33 Pa) equipped with a liquid N_2 cold-trap.

3. RESULTS

3.1. Gel Characterization. In a sol/gel crystallization experiment, the gel can be considered as a wet sponge with a mobile solution flowing within interconnected cavities with variable pore size.

A thorough characterization was performed on both HNO_3 polymerized gel (NG) and CO_2 polymerized gel (CG). To characterize the volume and composition of the solution that flows through the cavities and to understand the growth mechanisms determining different crystal quality, NG and CG gels were prepared; then, they were aged at room temperature or heated at the crystallization temperature (200 °C) and autogenic pressure, so simulating a growth experiment, for 6 h. Such a short reaction time is not sufficient to obtain detectable quartz crystals, but when the temperature is raised, the convective regime is enhanced and the solution entrapped into the "glassy sponge" is forced to flow. Consequently, the gel structure changes and the transport regime moves from nearly pure diffusive to plainly convective: the gel role turns from sponge to nourishing reservoir. In order to evaluate the increase of the convective component of the flow, the aged/heated gels were centrifuged and the flowing solution was separated from the solid fraction. For each portion of gel, the percentage of extractable solution with respect to the total gel weight was measured. The Na and Si concentrations in the two flowing solutions were measured by ICP-OES and compared with those in the Na-MTS starting solutions.

In this way, the concentration of the circulating sodium and silica was evaluated for each gel to qualitatively estimate the transport and supersaturation conditions inside each reactor during quartz growth and to explain the quality of the crystals.

Elemental data are reported in Table 1.

Table 1. Percentages of Circulating Ions in Solution and of Total Flowing Solution in a Na-MTS Gel Polymerized with Nitric Acid (NG) or CO_2 Bubbling into the Metasilicate Solution (CG)[a]

	RT gel		200 °C gel	
	NG	CG	NG	CG
%Na$^+$	45	14	99	97
%Si^{4+}	5	1	5	13
pH	9.9	11.5	11.7	11.7
% w/w flowing solution	35	58	83	99

[a]Percentages are calculated with respect to the starting total concentration in the gels.

The percentage of extractable solution in CG reaches the striking value of 99% at 200 °C, with respect to the 83% in the NG case. This means that, in the CG case, the solution is free to flow supplying silica and mitigating supersaturation gradients during crystal growth. On the contrary, in the NG case, the volume of flowing solution is smaller and the supply of silica to the growing crystals is lower.

The high pH values in all cases fit with the presence of dissolved silica.

In the NG case, aging the sample at 200 °C entails an apparent increase in sodium availability and a constant free silicon percentage, but considering the dilution due to the increase of the moving solution from 35% to 83%, the free sodium percentage becomes constant and the free silicon decreases. On the contrary, in the CG case, heating the gel brings an increase for both sodium and silicon.

Speciation calculations performed using the PHREEQC software confirm the presence of host phases with concentration in solution lower than their saturation values both at room temperature and at the growth temperature of quartz:

nitratine ($NaNO_3$) in the NG gel and trona ($Na_3H(CO_3)_2 \cdot 2H_2O$), natron ($Na_2CO_3 \cdot 10H_2O$), and thermonatrite ($Na_2CO_3 \cdot H_2O$) in the CG case. The occurrence of some among these guest phases precipitated from the dehydrated gel was confirmed by XRPD, giving evidence of nitratine in NG and trona in CG.

The gel matrix before quartz crystallization has a sponge-like behavior, as shown in Figure 1a). The early stages of quartz crystallization are shown in Figure 1b−f. The presence of a substrate favoring the heterogeneous nucleation (the inner and outer walls of the bubbles) lowers the activation energy for nucleation of quartz that turns from 3D homogeneous nucleation in the volume to 2D heterogeneous nucleation on the substrate. This suggests that the gel works as substrate and hence induces the nucleation of quartz at lower supersaturation values than those required in growth from solution.

In the CG case, the formation of large gaseous bubbles inside the gel matrix brings to the development of huge cavities with respect to the crystal size, as shown in Figures 1 and 2.

To verify how the discontinuity induced by bubbles influences the sponge-like behavior of the gel, a growth run was carried out by bubbling N_2 into an NG forming gel. This brought to a clear morphological convergence in the matrix structures and, as a consequence, on a large scale crystallization behavior very similar to what was already observed for the CG system (Figure 3). On the contrary, the single crystal morphology and surface quality of the CG and NG + N_2 experiments largely differs. Discrepancies between surface behaviors are maintained because of (i) the chemical surroundings of the crystals, (ii) the presence of cooperative growth effects with host phases, and (iii) the transport regime imposed by the gel nature, as will be shown in the following section.

3.2. Bulk and Surface Characterization of the Synthetic Crystals. At the end of the crystallization, no foreign phases were detected by XRPD in both NG and CG experiments and α-quartz was the only crystalline phase to be synthesized.

XRPD data were analyzed by the Rietveld method. A comparison between crystal cells and crystallite sizes (see Figure S1) was done only on 168 h grown samples, having hypothesized that residual growth should be negligible and, obviously, no more nucleation did occur. Moreover, crystal cells were compared with the NIST SRM 1878a (respirable α-quartz) quartz standard in order to evaluate a cell deformation with respect to a recognized standard. Silicon NIST Standard (SRM 640c) was used to evaluate the instrumental function (Table 2).

The Rietveld refinement shows that the volume of the crystal cell of NG-grown quartz is about 0.2% smaller than that of the CG-grown quartz and very similar to that of the SRM 1878a certified cell (< 0.03%).

At the same time, the averaged crystallite size (evaluated from the refinement data) is 181 nm, for the GC-grown crystals, and 119 nm for the NG-grown crystals, suggesting, in the first case, a more performing circulation system and a stronger cooperative effect between host phases and quartz, during crystallization.

Particle size distribution (PSD) and specific surface area (BET-SSA) of the synthetic quartz crystals grown in CG and NG for 168 h were evaluated and compared with those of a natural, high-purity, well-characterized α-quartz specimen from Madagascar, milled according to the protocol employed in
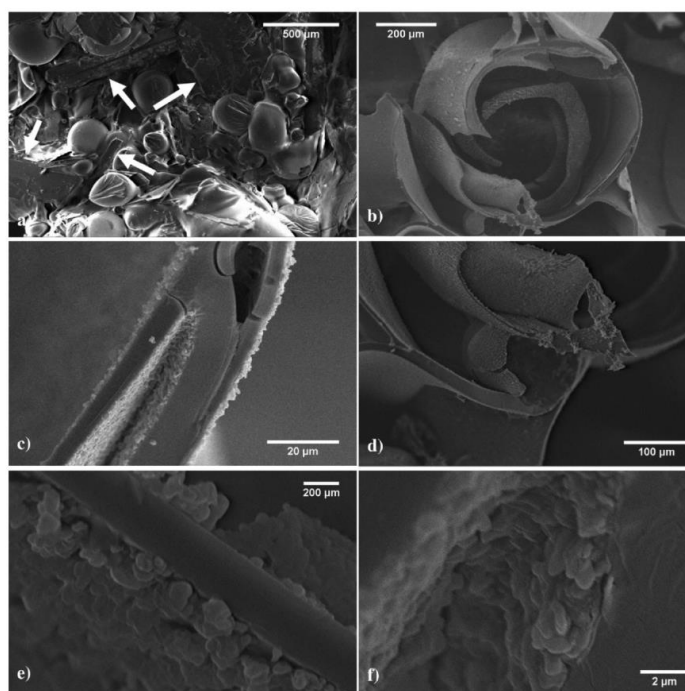
Figure 1. Sponge-like gel evolution with temperature: (a) bubbles and crystals of the guest phases (trona, white arrows) into the CG gel sponge; (b−f) early stages of heterogeneous quartz crystallization on the inner and outer walls of the bubbles.

previous toxicological studies on silica.[31,32] The particle size distribution of the three samples ranges from 100 nm to 2 μm in diameter (Figure 4). In the micrometric range, the size distributions of natural and CG quartz are almost super-imposable. Some smaller crystals with an average diameter of ca. 300 nm are clearly present in the CG-grown sample only, resulting in a peculiar bimodal distribution of particle size. The NG synthetic quartz exhibits a much smaller average particle size than CG and natural quartz, with the particle size distribution confined in the sub-micrometric range (100− 1000 nm). A reduced dispersion index (roughly, the fwhm of the distribution plot) is also observed for NG quartz with respect to CG and natural quartz, which show a more variable range of diameters. The specific surface area of GC and NC synthetic quartz is 1.1 and 6.2 m^2/g, respectively, measured with the Kr-BET method. It is worth noting that the natural quartz has a surface area of 6.1 m^2/g, very close to that of NG quartz.

A large body of scientific literature supports the key role of quartz surface chemistry in modulating quartz inflammogenic potential.[8,33−35] Quartz surfaces are stabilized by hydrogen bonds between vicinal silanol groups (interacting silanols), and networks of hydrogen-bonded silanols are found on all surfaces.[36] Surface silanols (> Si−OH), variously coordinated at the surface, may roughly be described in terms of proximity with other neighboring silanols. Amount and spatial arrange-ment of silanols affect surface charge and hydrophilic character of quartz, ultimately defining particle behavior toward cell membranes. To characterize the surface chemistry of silica, the chemical proximity of surface silanols is often evaluated by means of FTIR analysis. The bands in the region between 3800

and 3000 cm^{-1} correspond to the vibrational stretching modes of OH surface groups. A narrow peak at ca. 3750 cm^{-1}, related to the presence of isolated silanols, is commonly reported for both amorphous and crystalline silica[37] and can be observed when physisorbed, hydrogen-bonded, water molecules are removed from the surface. A broad band in the 3630−3260 cm^{-1} region, associated with different families of interacting silanols, is also observed. In Figure 5, the spectra collected on a quartz self-supporting pellet in air (a), after outgassing the pellet in vacuum at RT (b), and at 400 °C (c), are reported for NG- and CG-grown quartz, lower and upper series, respectively. When molecular water is removed from the surface (spectra b and b′), the narrow peak at 3740 cm^{-1} appears for the NG-grown, but not for the CG-grown quartz, signaling the occurrence of a family of isolated silanols only on the NG-quartz surface. Further removal of molecular water achieved by heating quartz in vacuum at 400 °C for 45 min (b → c, and b′ → c′) does not increase the amount of isolated silanols any further. When thermally outgassed, the CG- and NG-grown quartz show different behaviors. A virtually superimposable spectrum is recorded for NG-grown (spectra b and c), while a further loss of molecular water is observed for CG-grown quartz (spectra b′ and c′). This latter feature of the CG-grown quartz surface may signal a slightly more hydrophilic behavior with water being more strongly bound to surface silanols than NG quartz.

3.3. Effect of Gel Chemistry on the Crystal Morphology.
Concerning the growth morphology, some differences between CG- and NG-grown crystals may be outlined.

At variance with literature reports about crystallographic {hkil} forms obtained from hydrothermal quartz,[38,39] in all of
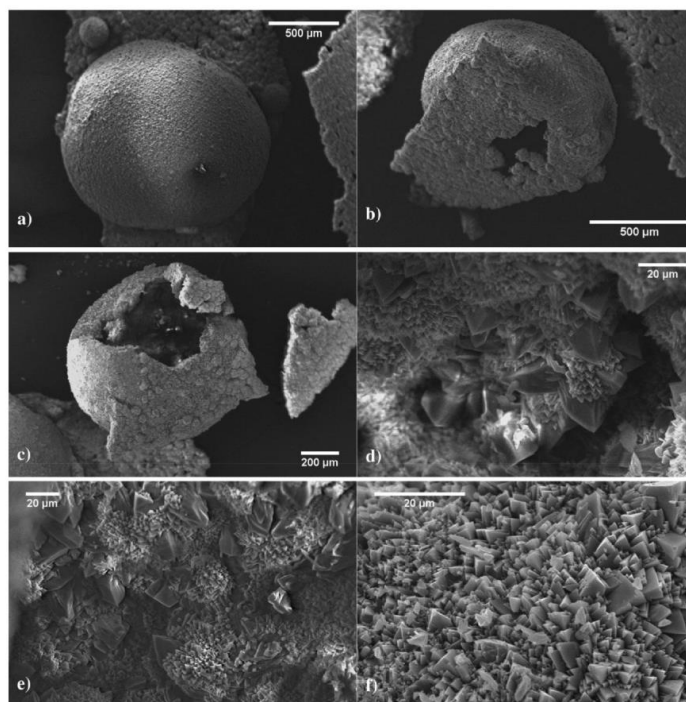
Figure 2. Polycrystalline quartz bubbles grown in CG (a), a polycrystalline quartz bubble detached from substrate (b), the same bubble shown in (b) cracked to highlight the different growth morphology of the inner and outer wall (c), with the inner wall showing a bimodal size distribution of polycrystalline quartz (d and e), and the outer wall showing a more homogeneous crystallization behavior (f).
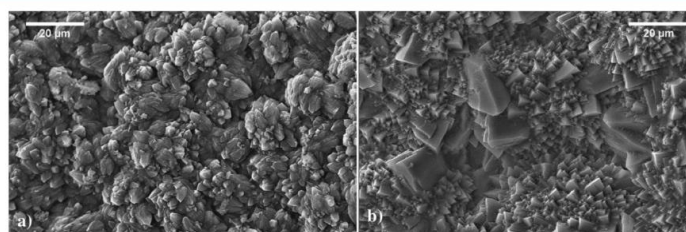

Figure 3. NG with bubbling N_2 during gel formation showing large quartz crystals emerging from the surface of the shell (a); CG gel grown quartz (b).

Table 2. Crystal Cell Parameters (a and c Axis Lengths, and Cell Volume) Calculated at Room Temperature for α-Quartz Crystals Grown in NG and CG Gel, Respectively. Cell Parameters of the NIST SRM 1878a Quartz Standard Are Reported for Comparison

	NG-grown quartz	SRM 1878a	CG-grown quartz
a (Å)	4.9133(3)	4.914	4.9167(4)
c (Å)	5.4050(2)	5.406	5.4083(8)
cell volume (Å^3)	112.9997(3)	113.037	113.2267(2)

our experiments, only one out the two rhombohedra (the direct $\{10\bar{1}1\}$ and the reverse $\{10\bar{1}\bar{1}\}$ one) is always present in the growth morphology, in association with the $\{1000\}$ prism. There was no evidence about which one of the two rhombohedra was experimentally obtained.

In CG experiments, both rhombohedron and prism forms grow by 3D nuclei juxtaposition. This growth mechanism results in a continuous coverage of a new crystal shell starting from the rhombohedron and overflowing on the prism surface, as shown in Figure 6b−f. In Figure 6d) white arrows evidence the nuclei disposition parallel to the prism striations acting as preferential nucleation sites. At the end of growth, the whole crystal will be encompassed by a growth shell which started from the rhombohedron surface. A similar growth mechanism was already observed by Pastero et al.,[40] when growing an anomalous mixed crystal of calcite in the presence of lithium carbonate. An early stage of this process is reported in Figure 6e,f (detail). Here, a macrostep on the cleavage rhombohedron surface is forming, but not yet overflowing onto the prism surface, the coverage being not perfectly uniform.
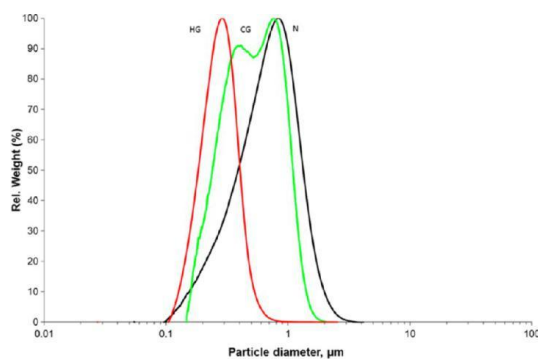
Figure 4. Particle size distribution of CG- and NG-grown samples (168 h), and natural quartz (N) measured by DCS. A bimodal size distribution can be observed for CG quartz.
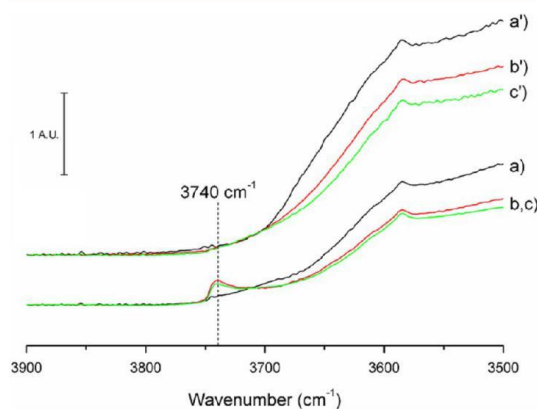

Figure 5. FTIR spectra of the −OH stretching region of NG- and CG-grown quartz collected on a self-supporting pellet in air, after outgassing the pellet in vacuum at RT, and at 400 °C (a, b, c, and a′, b′, c′, respectively). No isolated silanols are detected on CG-grown quartz.

In NG quartz growth, the crystals' surfaces are smooth and no surface structures are detectable, at low magnification (Figure 7 a−d). At higher magnification (Figure 7e) a uniformly distributed rough shell encompassing the whole crystal can be observed. HR-TEM observation (Figure 7f) suggests the occurrence of a few nanometer-thin layer with a lower order degree structure surrounding some well-formed, rounded crystals. In Figure 7c,d, representative TEM images show that no macrosteps spreading from the rhombohedron to the prism are detectable, as occurred in the CG case.

4. DISCUSSION

Keeping in mind that both NG- and GC-grown crystals were subjected to a common thermal treatment, the observed discrepancies in the two quartz samples, namely, the crystal morphology and surface behavior, the crystallite size and cell deformation, the specific surface area, and the occurrence of different families of silanols at the quartz surface, can be ascribed to the chemical and physical differences in the polymerizing agent. In fact, HNO_3 is a strong mineral acid and is supplied as solution, while H_2CO_3 is a relatively weak

diprotic acid and is supplied as CO_2 gas. This induces differences in the two quartz-forming gels that are specifically due to (i) different transport efficiency of the NG- and CG-silica sponges, and (ii) the presence of impurities. The supersaturation values locally reached in the two systems cannot be the same because of the different effectiveness in matter transport. At RT, only diffusion is virtually present in both gels. At higher temperature, a rise in the convective component of transport is observed, and this controls the mechanism for crystal nourishing. The gel role turns from "silica sponge" to silica source and nucleation substrate. In CG, as demonstrated with the gel characterization, the convective regime results to be stronger than in the NG case, resulting in a more functional medium for crystal growth. The mineral acids used as polymerizing agents during the gel preparation play a fundamental role in determining the chemical surroundings of the quartz crystals. Sodium, present in both CG and NG, is the counterion in many carbonate phases (also hydrated) and nitrates that could be present. It is well-known from the literature that the presence of guest phases into the growth environment, even if the solution is unsaturated with respect to the phase, could stabilize new surfaces and/or change their structure.

It is, therefore, convenient to discuss separately the growth mechanisms of the two quartz-forming gels.

4.1. The CG Case. CG polymerization promoted by bubbling CO_2 directly into the NaMTS solution yields a more concentrated gel with respect to NG, where NaMTS concentration is lowered by adding HNO_3 aqueous solution. Therefore, even if the absolute content of silica and sodium is the same in both CG and NG cases, the CG system reaches higher supersaturation values with respect to those reached by the NG gel. Furthermore, CO_2 bubbling generates bubbles into the forming gel and a high macroporosity of the gel is achieved. Raising the temperature during crystallization promotes migration and coalescence of CO_2 bubbles that form large cavities into the gel and act as communicating vessels. The walls of the cavities work as excellent substrates for the heterogeneous nucleation of quartz, lowering the nucleation energy with respect to that required for homogeneous nucleation in solution. The silica-rich solution can circulate into the gel cavities and a supersaturation value suitable to grow large and well-finished crystals can be preserved throughout the synthesis. When the temperature is raised, the gel surrounding the cavities becomes a moving SiO_2 reservoir, as suggested by the compositional data of the flowing solution. Additionally, the presence of free silica is guaranteed by the basic pH values. Bubbles work as heterogeneous nucleation sites and show a double crystallization direction:

(i). On the outer bubble wall, the almost constant supersaturation value due to the presence of a semi-infinite reservoir of silica feeding the moving solution determines the formation of a homogeneous small-sized population of quartz crystals.

(ii). On the inner wall, the fluid circulation is negligible, silica refilling from the surrounding reservoir being impaired. These conditions determine the quartz nucleation to occur under a decreasing supersaturation regime, and hence, fewer and larger crystals are grown.

The two complementary growth mechanisms are likely the cause of the bimodal size distribution of crystals evidenced by
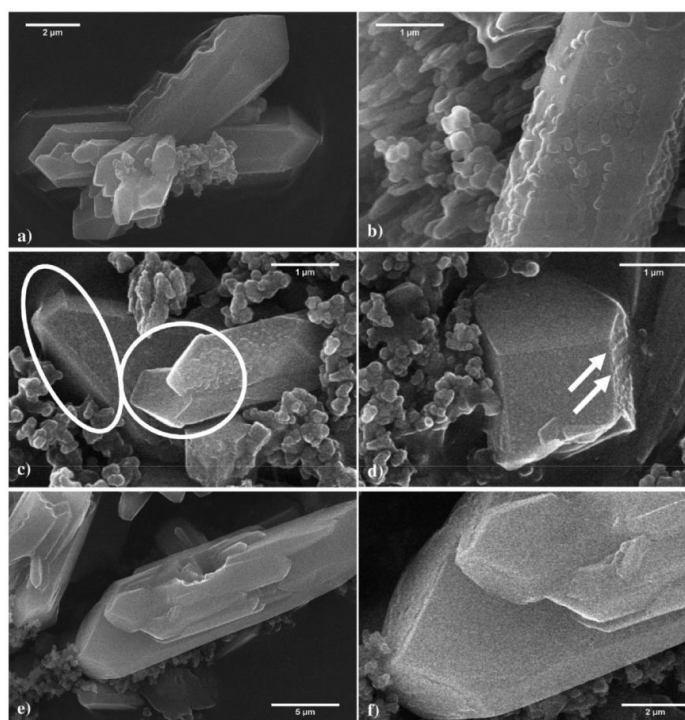
Figure 6. (a) CG-grown quartz aggregates (SEM pictures), (b) 3D nucleation of quartz on prism surfaces of an older crystal, (c) a continuous coverage of a new crystal shell starts from the rhombohedron and overflows on the prism surface, (d) nuclei disposition parallel to the prism striations are evidenced by arrows, (e) a CG aggregate, and (f) a detail of the rhombohedra surfaces.

the particle size distribution (PSD) analysis (Figure 4) for CG quartz only.

The higher supersaturation conditions of the CG case are pointed out not only by elemental analysis of the flowing solution (Table 1) but also by the presence of 3D nuclei on the quartz surfaces (Figure 6b−f). It is not surprising that, at the end of the experiment, when the temperature rapidly decreases, a shell of small 3D coalescent quartz crystals nucleates on the rhombohedron surfaces, forming macrosteps overflowing toward the surfaces of the prisms (Figure 6b−f).

Moreover, discussing the overlapping growth process (from the rhombohedron toward the prism) is not trivial. The structure of the crystal surfaces, already described in terms of periodic bond chains (PBC) profiles by Hartman,[41] should be put in relationship with the host phases present into the growth medium. From XRPD analysis, trona ($Na_3H(CO_3)_2 \cdot 2H_2O$) as crystalline impurity was detected in CG samples, but all the possible sodium and sodium hydrogen carbonates at different hydration degrees can be encountered during the experiment, depending on the local temperature, pH, and composition of the system. At the same time, a large amount of silica and sodium silicate phases at variable hydration levels can occur. Under these conditions, a cooperative effect during growth is expected. It is important to remember that a mechanism of silica gel ordering was already found by Bittarello and co-workers[42] during the growth of silica biomorphs in the presence of whiterite.

The detailed description of the cooperative effects on quartz growth in the presence of all the possible phases coming from the gel speciation is beyond our present purposes and will be discussed in a forthcoming paper.

It is well-known from the literature[17,43−46] that the best results on hydrothermal quartz crystal growth are obtained from silica solutions charged with alkali halides and hydroxides as mineralizers. The role of these mineralizers is not only to improve the solubility of silica changing the pH or the quartz solubility according to the ionic strength of the growing bath but also to cooperate with the growing crystal by acting on its surface structures.

As a matter of fact, one can easily find a very good parametric agreement between the 2D cells of the experimentally obtained forms of quartz and the most frequent forms shown by natural trona crystals, as reported in Table 3.

The 2D parametric coincidences and sharing of PBCs between different crystal species induce a lowering of the surface free energy of both host and guest phases, favoring crystal growth and face smoothness at both atomistic and microscopic levels. The lack of isolated silanol (Si-OH) species on the surface of GC quartz, evidenced by FTIR spectroscopy (Figure 5), clearly signals a high uniformity of the surface. In fact, the lack of surface hydroxyl groups not hydrogen-bonded to neighbors (isolated) may likely be related to the large local extension of the 2D spatial order of the CG-grown quartz surface. Isolated silanols on an unaltered (e.g., not thermally dehydroxylated) crystalline surface occur preferentially on defective sites, where a limited number of nearest neighbors are available.
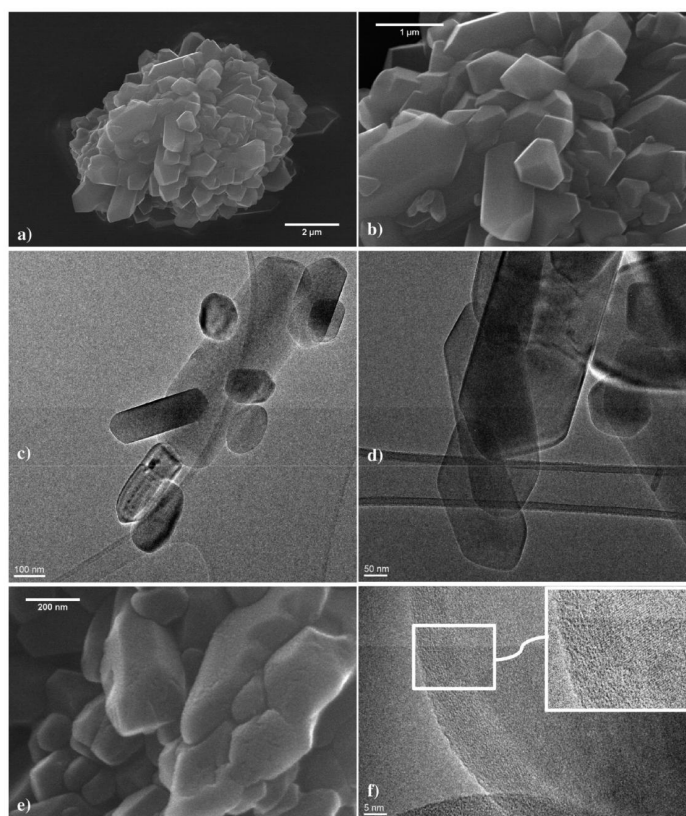
Figure 7. SEM and TEM images of NG as grown aggregates of quartz crystals. (a) spherulitic aggregate of NG-grown crystals, (b) a detail of the previous image, (c and d) TEM images of NG crystals confirming straight edges and very simple morphology, (e) NG-grown crystals show rough surfaces at SEM high magnification. (f) HR-TEM image of the outer shell with the less-ordered structure.

Table 3. Parametric Coincidences between Quartz (0100 Prism and 10$\overline{1}\overline{1}$ Rhombohedron) and Most Common Growth Forms of Trona

quartz lattice plane	trona lattice plane	parametric misfit %
01.0	001	
4x[010] = 19.6512	[100] = 20.36	3.6
2x[001] = 10.8084	3x[010] = 10.44	3.5
	100	
2x[010] = 9.8256	[001] = 10.29	4.7
2x[001] = 10.8084	3x[010] = 10.44	3.5
	010	
2x[010] = 9.8256	[011]cos β = 9.8673	0.4
4x[001] = 21.6168	[100] = 20.36	6.1
10.-1	001	
4x[010] = 19.6512	[100] = 20.36	3.6
[211] = 10.0803	3x[010] = 10.44	3.5
	100	
2x[010] = 9.8256	[001] = 10.29	4.7
[211] = 10.0803	3x[010] = 10.44	3.5
	010	
2x[010] = 9.8256	[011]cos β = 9.8673	0.4
2x[211] = 20.1606	[100] = 20.36	0.9

The hosting phases epitaxial enhancement on the growth of the GC quartz is further supported by a comparative analysis of specific surface area and particle size measurements. In fact, particle size distribution (Figure 4) indicates that CG quartz crystals are smaller than natural milled quartz. Nonetheless, the surface area is about 6 times smaller. The smoothness of CG-grown crystal faces could possibly explain the very low specific surface area (ca. 1 m^2/g) measured on this sample.

The cooperative effect between hydrated sodium carbonates and quartz is proved also by the quartz crystal cell deformation measured by XRPD and shown in Figure S1.

4.2. The NG Case. In the NG case, a slightly higher gel dilution is induced by the water content of the polymerizing agent (aqueous HNO_3). The small amount of air entrapped into the forming gel is negligible if compared with the CG, when CO_2 is forced to enter the solution until the end of gel formation. As a consequence, the bubbles entrapped in the gel become smaller. In this case, the bubbles act as nucleation centers but do not behave as cavities to obtain geode-like growth of quartz crystals.

Contrary to what was observed inside the large CO_2 bubbles, the lower density and size of bubbles in the NG system brings to a more performing gel with truly reduced convection, thus preventing local discontinuities (inside the cavities) in silica supersaturation. Because of their small size, only the outer walls

of the bubbles in NG can work as nucleation sites. No lower supersaturation volumes are present in the batch, as happens in CG inner bubbles cavities. Hence, quartz crystals form in the presence of high supersaturation that promotes more nucleation than growth. For this reason, NG-grown crystals are smaller than CG ones. This explanation is further supported by what was observed when NG is forced to become a macroporous matrix under inert N_2 bubbling. Large bubbles are formed, and the uniform arrangement of the silica reservoir falls down. The crystallization behavior becomes, in turn, similar to what was observed for CG.

Moreover, in the NG case, the rearrangement of the amorphous polymerized gel toward the ordered phase increasing the temperature seems to be the main quartz growth mechanism, not favored by the cooperative effect of a specific impurity.

In fact, when comparing the structure of the quartz stable surfaces with the surface structure of the most likely hosting phase, i.e., nitratine ($NaNO_3$), a poor parametric agreement between the two phases appears, as shown in Table 4. In this case, a cooperative mechanism on quartz crystal growth is unlikely.

Table 4. Parametric Coincidences between Quartz Prism and Rhombohedron, and Nitratine Cleavage Rhombohedron

quartz lattice plane	nitratine lattice plane	parametric misfit %
10.-1	10.4	
[100] = 4.9128	[010] = 5.070	3.2
2x[211] = 20.1606	[421] = 24.318	20.6
01.0	10.4	
[010] = 4.9128	[010] = 5.070	3.2
5x[001] = 27.021	[421] = 24.318	11.1

The rough surfaces evidenced by high-magnification SEM images (Figure 7) and the presence of a thin shell of a phase with a lower ordered lattice structure covering the NG quartz crystal evidenced by HR-TEM analysis (Figure 7f) support this hypothesis. This is a low range rearrangement effect due to the growing crystal surfaces that impose their ordering to the surrounding amorphous phase. The lower crystal cell deformation calculated from Rietveld crystal cell refinements (Figure S1) in these samples supports this hypothesis as well.

5. CONCLUSIONS

An unusual, easy to perform, and clean synthetic route to obtain a large population of quartz crystals (in the range of nano−micro size) is proposed and discussed. To keep the chemical complexity of the system as low as possible, hydrothermal growth of quartz in mild (T, p) conditions was carried out starting from silica gel polymerized using H_2CO_3 and HNO_3 (CG and NG growth gels, respectively). Quartz grows quickly at low temperature thanks to the presence of nucleation centers (bubbles) which shift nucleation from homogeneous to heterogeneous, requiring lower activation energy. Moreover, in the CG case, the presence of large bubbles acting as growth cavities with reduced matter transport, locally lowers the supersaturation, moving the process from nucleation to growth. The quality of crystals and surfaces depends on the existence of a cooperation effect between quartz and guest phases during crystal growth, as already proposed in previous works.[40,47] Guest phases (even if present in solution at a concentration lower than the saturation) act as specific surface

impurities during growth, lowering the involved surface energies.

The envisaged possibility to fine-tune some key physico-chemical features relevant to quartz toxicity makes this synthetic approach a novel and unique tool for an improved understanding of the molecular mechanisms of the detrimental effect of crystalline silica on human health. A paper that specifically addresses this issue has been submitted.[48]

ASSOCIATED CONTENT

* Supporting Information

The Supporting Information is available free of charge on the ACS Publications website at DOI: 10.1021/acs.cgd.6b00183.

Figure S1: Comparison between the cell parameters and between cell volume and crystallite size of NG and CG crystals, as calculated by Rietveld refinement (PDF)

AUTHOR INFORMATION

Corresponding Author
*E-mail: linda.pastero@unito.it.

Notes
The authors declare no competing financial interest.

REFERENCES

(1) Carretero-Genevrier, A.; Gich, M.; Picas, L.; Gazquez, J.; Drisko, G. L.; Boissiere, C.; Grosso, D.; Rodriguez-Carvajal, J.; Sanchez, C. Science 2013, 340, 827−831.

(2) Jiang, X.; Bao, L.; Cheng, Y.-S.; Dunphy, D. R.; Li, X.; Brinker, C. J. Chem. Commun. 2012, 48, 1293−1295.

(3) Brinker, C. J. J. Non-Cryst. Solids 1988, 100, 31−50.

(4) Warheit, D. B.; Webb, T. R.; Colvin, V. L.; Reed, K. L.; Sayes, C. M. Toxicol. Sci. 2007, 95, 270−280.

(5) Rimola, A.; Tosoni, S.; Sodupe, M.; Ugliengo, P. ChemPhysChem 2006, 7, 157−163.

(6) Rabolli, V.; Thomassen, L. C. J.; Princen, C.; Napierska, D.; Gonzalez, L.; Kirsch-Volders, M.; Hoet, P. H.; Huaux, F.; Kirschhock, C. E. A.; Martens, J. A.; Lison, D. Nanotoxicology 2010, 4, 307−318.

(7) Donaldson, K.; Borm, P. J. A. Ann. Occup. Hyg. 1998, 42, 287−294.

(8) Fubini, B. Ann. Occup. Hyg. 1998, 42, 521−530.

(9) Pavan, C.; Rabolli, V.; Tomatis, M.; Fubini, B.; Lison, D. Part. Fibre Toxicol. 2014, 11, 76.

(10) van Berlo, D.; Knaapen, A. M.; van Schooten, F.-J.; Schins, R. P.; Albrecht, C. Part. Fibre Toxicol. 2010, 7, 13.

(11) Mossman, B. T.; Glenn, R. E. Crit. Rev. Toxicol. 2013, 43, 632−660.

(12) Arsenic, Metals, Fibres, and Dusts: A Review of Human Carcinogens: A Review of Human Carcinogens; IARC Monographs; International Agency for Research on Cancer: Lyon, France, 2012; Vol. 100C.

(13) Monopoli, M. P.; Walczyk, D.; Campbell, A.; Elia, G.; Lynch, I.; Bombelli, F. B.; Dawson, K. A. J. Am. Chem. Soc. 2011, 133, 2525–2534.

(14) Napierska, D.; Thomassen, L. C. J.; Rabolli, V.; Lison, D.; Gonzalez, L.; Kirsch-Volders, M.; Martens, J. A.; Hoet, P. H. Small 2009, 5, 846–853.

(15) Napierska, D.; Thomassen, L. C. J.; Lison, D.; Martens, J. a; Hoet, P. H. Part. Fibre Toxicol. 2010, 7, 39.

(16) Ariano, P.; Zamburlin, P.; Gilardino, A.; Mortera, R.; Onida, B.; Tomatis, M.; Ghiazza, M.; Fubini, B.; Lovisolo, D. Small 2011, 7, 766–774.

(17) Bertone, J. F.; Cizeron, J.; Wahi, R. K.; Bosworth, J. K.; Colvin, V. L. Nano Lett. 2003, 3, 655–659.

(18) Li, L.-J.; Fang, J.-N.; Lo, H.-J.; Song, S.-R.; Chen, Y.-L.; Chen, H.-F.; Lin, I.-C. J. Chin. Chem. Soc. 2003, 50, 395–398.

(19) Zhdanov, S. P. Adv. Chem. Ser. 1971, 101, 20–43.

(20) Prieto, M.; García-Ruiz, J. M.; Amoros, J. L. J. Cryst. Growth 1981, 52, 864–867.

(21) McCauley, J. W.; Roy, R. Am. Mineral. 1974, 59, 947–963.

(22) Pastero, L.; Costa, E.; Alessandria, B.; Rubbo, M.; Aquilano, D. J.Cryst. Growth 2003, 247, 472–482.

(23) Garcia-Ruíz, J. M.; Gonzalez-Ramirez, L. A.; Gavira, J. A.; Otalora, F. Acta Crystallogr., Sect. D: Biol. Crystallogr. 2002, 58, 1638–1642.

(24) Moran, P. A. P. The Theory of Storage; Methuen: London, 1959.

(25) Cetini, G.; Ricca, F. Ric. Sci. 1960, 7, 994–1009.

(26) Kirov, G. K.; Vesselinov, I.; Cherneva, Z. Krist. Tech. 1972, 7, 497–509.

(27) Kirov, G. K. In Growth of Crystals; Chernov, A. A., Ed.; Springer: Berlin, 1984; Vol. 12, p 355.

(28) Parkhurst, D. L.; Appelo, C. A. J. In U.S. Geological Survey Techniques and Methods, Book 6; USGS: Reston, VA, 2013; p 497.

(29) Lutterotti, L.; Bortolotti, M.; Ischia, G.; Lonardelli, I.; Wenk, H.-R. Z. Kristallogr. 2007, 2007 (Suppl. 26), 125–130.

(30) Lutterotti, L. Nucl. Instrum. Methods Phys. Res., Sect. B 2010, 268, 334–340.

(31) Ghiazza, M.; Polimeni, M.; Fenoglio, I.; Gazzano, E.; Ghigo, D.; Fubini, B. Chem. Res. Toxicol. 2010, 23, 620–629.

(32) Pavan, C.; Tomatis, M.; Ghiazza, M.; Rabolli, V.; Bolis, V.; Lison, D.; Fubini, B. Chem. Res. Toxicol. 2013, 26, 1188–1198.

(33) Donaldson, K.; Stone, V.; Duffin, R.; Clouter, A.; Schins, R.; Borm, P. J. Environ. Pathol. Toxicol. Oncol. 2001, 20 (Suppl. 1), 109–118.

(34) Ghiazza, M.; Scherbart, A. M.; Fenoglio, I.; Grendene, F.; Turci, F.; Martra, G.; Albrecht, C.; Schins, R. P. F.; Fubini, B. Chem. Res. Toxicol. 2011, 24, 99–110.

(35) Peeters, P. M.; Eurlings, I. M. J.; Perkins, T. N.; Wouters, E. F.; Schins, R. P. F.; Borm, P. J. A.; Drommer, W.; Reynaert, N. L.; Albrecht, C. Part. Fibre Toxicol. 2014, 11, 58.

(36) Murashov, V. V. J. Phys. Chem. B 2005, 109, 4144–4151.

(37) Zhdanov, S. P.; Kosheleva, L. S.; Titova, T. I. Langmuir 1987, 3, 960–967.

(38) Friedel, C.; Sarrasin, E. Bull. Soc. Mineral. Fr. 1879, 4, 113–117.

(39) de Kroustchoff, M. K. C. R. Hebd. Seances Acad. Sci. 1887, 104, 602–603.

(40) Pastero, L.; Aquilano, D. Cryst. Growth Des. 2008, 8, 3451–3460.

(41) Hartman, P. Bull. Soc. Fr. Mineral. 1959, 82, 335–340.

(42) Bittarello, E.; Massaro, F. R.; Rubbo, M.; Costa, E.; Aquilano, D. Cryst. Growth Des. 2009, 9, 971–977.

(43) Jiang, X.; Jiang, Y.-B.; Brinker, C. J. Chem. Commun. (Cambridge, U. K.) 2011, 47, 7524–7526.

(44) Swinnerton, A. C.; Owen, G. E.; Corwin, J. F. Discuss. Faraday Soc. 1949, 5, 172.

(45) Wooster, N.; Wooster, W. A. Nature 1946, 157, 297.

(46) Brown, C. S.; Kell, R. C.; Thomas, L. A.; Wooster, N.; Wooster, W. A. Nature 1951, 167, 940–941.

(47) Aquilano, D.; Pastero, L. Cryst. Res. Technol. 2013, 48, 819–839.

(48) Turci, F.; et al. Part. Fiber Toxicol., submitted.

Supporting Information

Synthesis of α-Quartz with Controlled Properties for the Investigation of the Molecular Determinants in Silica Toxicology

Linda Pastero, Francesco Turci, Riccardo Leinardi, Cristina Pavan, Marco Monopoli
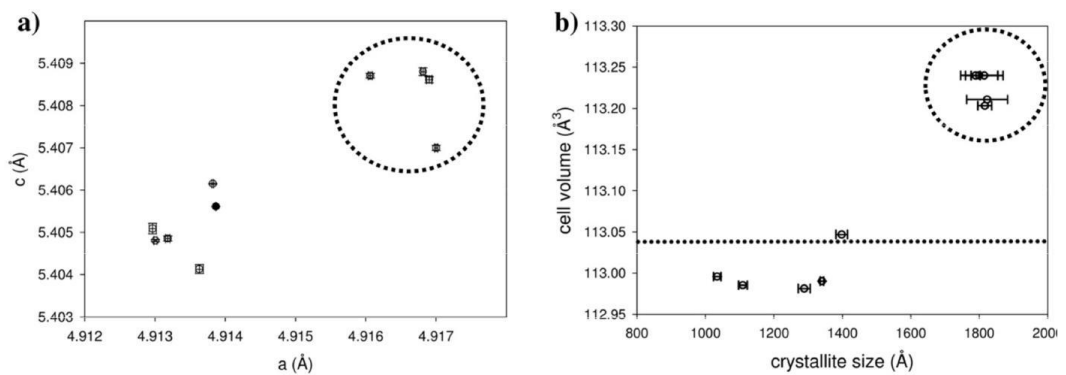

Figure S1. Comparison between the cell parameters (a), and the cell volume and crystallite size (b) of NG and CG (inside the dotted circle) crystals, as calculated by Rietveld refinement. The black point and the line represent the dimensional parameters of the SRM 1878a standard quartz sample.

R E S E A R C H

Revisiting the paradigm of silica pathogenicity with synthetic quartz crystals: the role of crystallinity and surface disorder

Francesco Turci[1,2*†], Cristina Pavan[1,2†], Riccardo Leinardi[1,2], Maura Tomatis[1,2], Linda Pastero[2,3], David Garry[4], Sergio Anguissola[4], Dominique Lison[5] and Bice Fubini[1,2]

Abstract

Background: Exposure to some - but not all - quartz particles is associated to silicosis, lung cancer and autoimmune diseases. What imparts pathogenicity to any single quartz source is however still unclear. Crystallinity and various surface features are implied in toxicity. Quartz dusts used so far in particle toxicology have been obtained by grinding rocks containing natural quartz, a process which affects crystallinity and yields dusts with variable surface states. To clarify the role of crystallinity in quartz pathogenicity we have grown intact quartz crystals in respirable size.

Methods: Quartz crystals were grown and compared with a fractured specimen obtained by grinding the largest synthetic crystals and a mineral quartz (positive control). The key physico-chemical features relevant to particle toxicity - particle size distribution, micromorphology, crystallinity, surface charge, cell-free oxidative potential - were evaluated. Membranolysis was assessed on biological and artificial membranes. Endpoints of cellular stress were evaluated on RAW 264.7 murine macrophages by High Content Analysis after ascertaining cellular uptake by bio-TEM imaging of quartz-exposed cells.

Results: Quartz crystals were grown in the submicron (n-Qz-syn) or micron (μ-Qz-syn) range by modulating the synthetic procedure. Independently from size as-grown quartz crystals with regular intact faces did not elicit cellular toxicity and lysosomal stress on RAW 264.7 macrophages, and were non-membranolytic on liposome and red blood cells. When fractured, synthetic quartz (μ-Qz-syn-f) attained particle morphology and size close to the mineral quartz dust (Qz-f, positive control) and similarly induced cellular toxicity and membranolysis. Fracturing imparted a higher heterogeneity of silanol acidic sites and radical species at the quartz surface.

Conclusions: Our data support the hypothesis that the biological activity of quartz dust is not due to crystallinity but to crystal fragmentation, when conchoidal fractures are formed. Besides radical generation, fracturing upsets the expected long-range order of non-radical surface moieties - silanols, silanolates, siloxanes - which disrupt membranes and induce cellular toxicity, both outcomes associated to the inflammatory response to quartz.

Keywords: Quartz, Silica, Toxicity, Silanols, Crystallinity, Membranolysis, Conchoidal fracture, Surface charge, Radicals

* Correspondence: francesco.turci@unito.it
[†]Equal contributors
[1]Department of Chemistry, University of Torino, Via P. Giuria 7, Turin 10125, Italy
[2]"G. Scansetti" Interdepartmental Center for Studies on Asbestos and Other Toxic Particulates, University of Torino, Via P. Giuria 7, Turin 10125, Italy Full list of author information is available at the end of the article

Turci et al. Particle and Fibre Toxicology (2016) 13:32

Page 2 of 12

Background

Excessive exposure to crystalline silica dusts is associated with silicosis, lung cancer and autoimmune diseases, and the crystalline structure has been traditionally consid-ered as a key determinant of silica pathogenicity. How-ever, not all crystalline silica dusts are pathogenic [1, 2]. A preamble in IARC monograph volume 68 recalls that carcinogenicity of crystalline silica dust does not apply to all occupational exposures examined [1].

Several amorphous silica particles have the potential to cause adverse cellular effects associated with the develop-ment of silica-related pathologies [3–14]. Vitreous silica par-ticles obtained by grinding a pure silica glass exhibited all the physico-chemical features of quartz dusts except crystal-linity [15], and the same biological reactivity as quartz in vitro [3]. Some cases of silicosis and lung cancer were also reported among workers exposed to this type of amorphous silica [16, 17]. Thus, the traditional paradigm confining ad-verse effects exclusively to crystalline silica comes under dis-cussion. Furthermore, a large amount of studies on amorphous nanosilicas have shown remarkable in vitro toxic responses [4–9], and in vivo, transient, adverse pulmonary effects [10–14]. Even for amorphous nanosilicas, toxic re-sponses markedly varied from one type to the other [11].

This variability of silica hazard stems from both the chemical nature of the dust and the multiple interactions of silica particles with biomolecules and cells within the respiratory system, each interaction being possibly mod-ulated by the different physico-chemical features of the particles [2, 18]. In spite of a large body of studies, the role of each physico-chemical property in triggering a specific biological event remains unclear, mainly because of (1) the intrinsic variability of the mineral sources of quartz investigated, and (2) the variability induced dur-ing industrial processing which largely alters many key surface features [19–23], thus making the toxicity of each silica dust quite unpredictable.

All silicas share a $[SiO_4]^{4-}$ tetrahedron as basic unit and may differ by their spatial arrangement. As a consequence, several crystalline polymorphs as well as many kinds of amorphous specimens exist [24], differing in surface chem-ical functionalities as well as in biological reactivity and pathogenicity [18, 25]. During mechanical fracturing, silicon-oxygen bonds, being covalent and slightly polar, yields both surface radicals (dangling bonds) and charges. Upon surface reconstruction with ambient water vapour, a complex array of silanol families (Si-OH) and siloxane bridges (Si-O-Si) form rings of different sizes, whose kinet-ics of formation and stability are strongly dependent upon the origin, mechanical, chemical, and thermal history of the particles.

To revisit the role of crystallinity in the pathogenicity of silica particles, we have grown and tested two preparations of quartz crystals with intact and unaltered surfaces. Both crystals were mostly in the respirable size, ranging from submicrometric (n-Qz-syn) to micrometric (μ-Qz-syn). A portion of the micrometric quartz was then mechanically fractured (μ-Qz-syn-f) to induce structural surface alter-ations, including radicals and new silanol distributions on freshly formed surfaces. A well-characterized pure quartz dust (Qz-f), obtained by grinding large quartz crystals from Madagascar and previously used in toxicity tests [3], was in-cluded in each experiment as positive control. The four quartz samples were fully characterized for morphology and crystallinity (SEM, HR-TEM, XRD), particle size distri-bution (differential centrifugal sedimentation, DCS), surface area (BET), heterogeneity of surface acidic silanols (electro-phoretic light scattering, ELS), and radical-mediated surface reactivity (spin trapping/EPR spectroscopy). We compared as-grown crystals vs fractured ones in a series of cellular and acellular assays relevant for the pathogenicity of silica particles, including i) membranolytic activity towards bio-logical (red blood cells, RBCs) and artificial (liposomes) membranes, ii) cell viability and stress-related endpoints (high content analysis, HCA) in murine macrophages, and iii) particle uptake/internalization (bio-TEM).

Results

Synthetic quartz was grown in different sizes with intact surfaces, and then fractured to obtain features similar to ground mineral quartz dust

Two synthetic quartz crystals with controlled properties were produced with a novel approach described in a paral-lel paper devoted to the mineralogical details of the crystal synthesis [26]. The technique adopted allowed modulation of crystal size, while keeping the lattice distortion to a minimum, close to the ideal structure of quartz. Size and surface area of as-grown and fractured quartz crystals employed in the study are reported in Table 1. The particle size of the two as-grown crystals was largely different and surface area varied with particle size accordingly. The scanning electron microscopy (SEM) images of the two types of synthetic crystals are reported in Fig. 1a and b. The n-Qz-syn exhibited regular shape and very fine par-ticle size (from 100 to 400 nm). Hexagonal-shaped sub-micrometric crystals were often observed for this sample. Larger crystals of μ-Qz-syn had a less regular morphology and a higher size range (up to ca. 2500 nm). Both crystals exhibited smooth and regular surfaces [26]. A representa-tive HR-TEM image of as-grown synthetic quartz crystals is reported in Fig. 1e. Single ordered lattice layers (diffrac-tion fringes) were observed to be extending over the whole crystal particle, including the regions close to the surfaces.

Mechanical fracturing of μ-Qz-syn crystals caused the formation of conchoidal fractures [27, 28] and sub-micrometric particles electrostatically stacked on larger crystals, clearly visible in the SEM image of μ-Qz-syn-f (Fig. 1c) and responsible for the significant increase in

Table 1 Size and specific surface area of the studied quartz crystals

Crystal type	Acronym	Particle diameter 10th percentile (nm)[a]	Particle diameter 50th percentile (nm)[a]	Particle diameter 90th percentile (nm)[a]	Surface area (m^2/g)[b]
Synthetic as-grown crystals in submicron size	n-Qz-syn	174	276	408	6.2
Synthetic as-grown crystals in micron size	μ-Qz-syn	405	904	2520	0.3
Fractured micron size synthetic crystals	μ-Qz-syn-f	409	914	1960	9.5
Mineral quartz dust (positive control)	Qz-f	285	704	1290	6.1

[a]Measured by Differential Centrifugal Sedimentation (DCS), see Additional file 1: Figure S1 [b]Measured by Kr-BET method
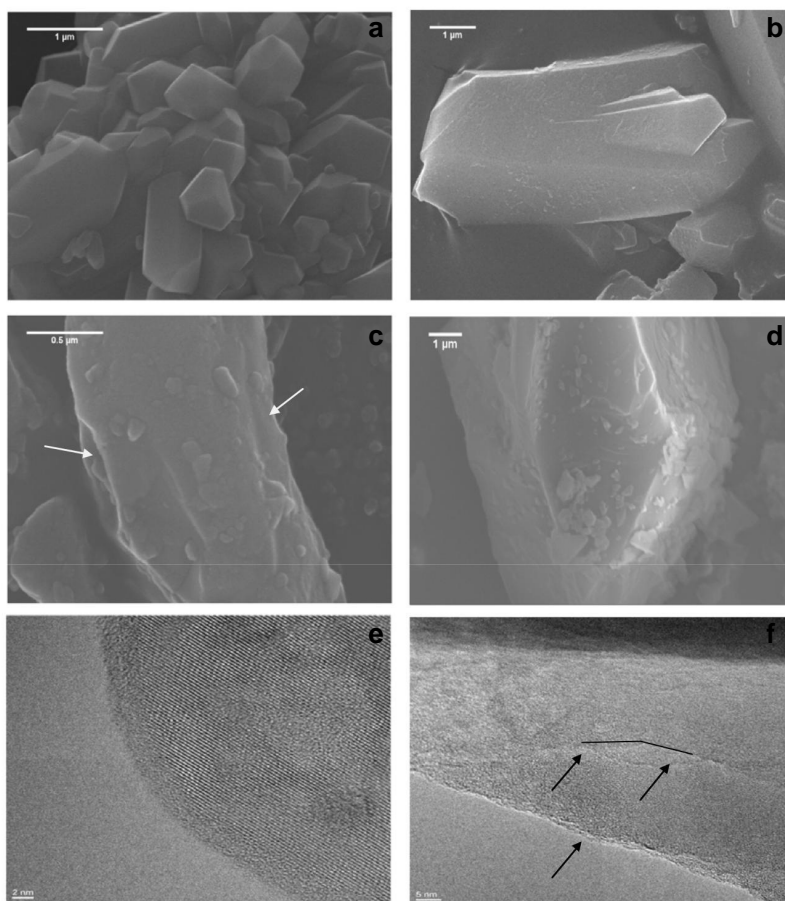
Fig. 1 FE-SEM imaging of n-Qz-syn, μ-Qz-syn, μ-Qz-syn-f, and Qz-f (a, b, c, and d, respectively) and HR-TEM imaging of as-grown (n-Qz-syn) and fractured (μ-Qz-syn-f) samples (e and f, respectively). Flat, well-formed, smooth surfaces characterized as-grown quartz (a and b), while conchoidal fractures (arrow) were visible on ground particles (c and d). Crystal structure was preserved up to the very last atomic boundary of the synthetic crystal (e), while fracturing induced partial disorganization of crystal lattice (absence of diffraction fringes) and loss of long-range ordered crystalline planes (f, arrows)

surface area (from 0.3 to 9.5 m^2/g). Similar fractures and surface area were evidenced for ground mineral quartz dust, Qz-f (Fig. 1d and Table 1). HR-TEM performed on fractured synthetic quartz (μ-Qz-syn-f) highlighted a large amount of defects and disordered structures introduced into the crystal lattice, with consequent loss of long-range crystal planes (Fig. 1f, arrows).

Contrary to fractured quartz, as-grown crystals do not reduce cell viability or induce cellular stress in RAW 264.7 macrophages

Cytotoxic profiles of the as-grown quartz crystals (n-Qz-syn, μ-Qz-syn) were examined by means of High Content Analysis (HCA) [5, 29, 30] and compared with those

of the fractured crystals (μ-Qz-syn-f) and the ground mineral quartz dust (Qz-f). RAW 264.7 macrophages were exposed for 24 h over a range of particle concentrations (1, 12, 25, 50 and 100 μg/ml). After exposure (Fig. 2) as-grown quartz crystals (n-Qz-syn and μ-Qz-syn) did not cause any alteration of the five cytotoxicity parameters assessed. In contrast, fractured synthetic quartz (μ-Qz-syn-f) elicited an increase of cell nuclear size at the highest dose (100 μg/ml) and a remarkable dose-dependent increase of lysosomal acidification. Lysosomal acidification and increase of nuclear size were also recorded in cells incubated with mineral quartz dust (Qz-f), which also reduced cell count and increased cell membrane permeability.
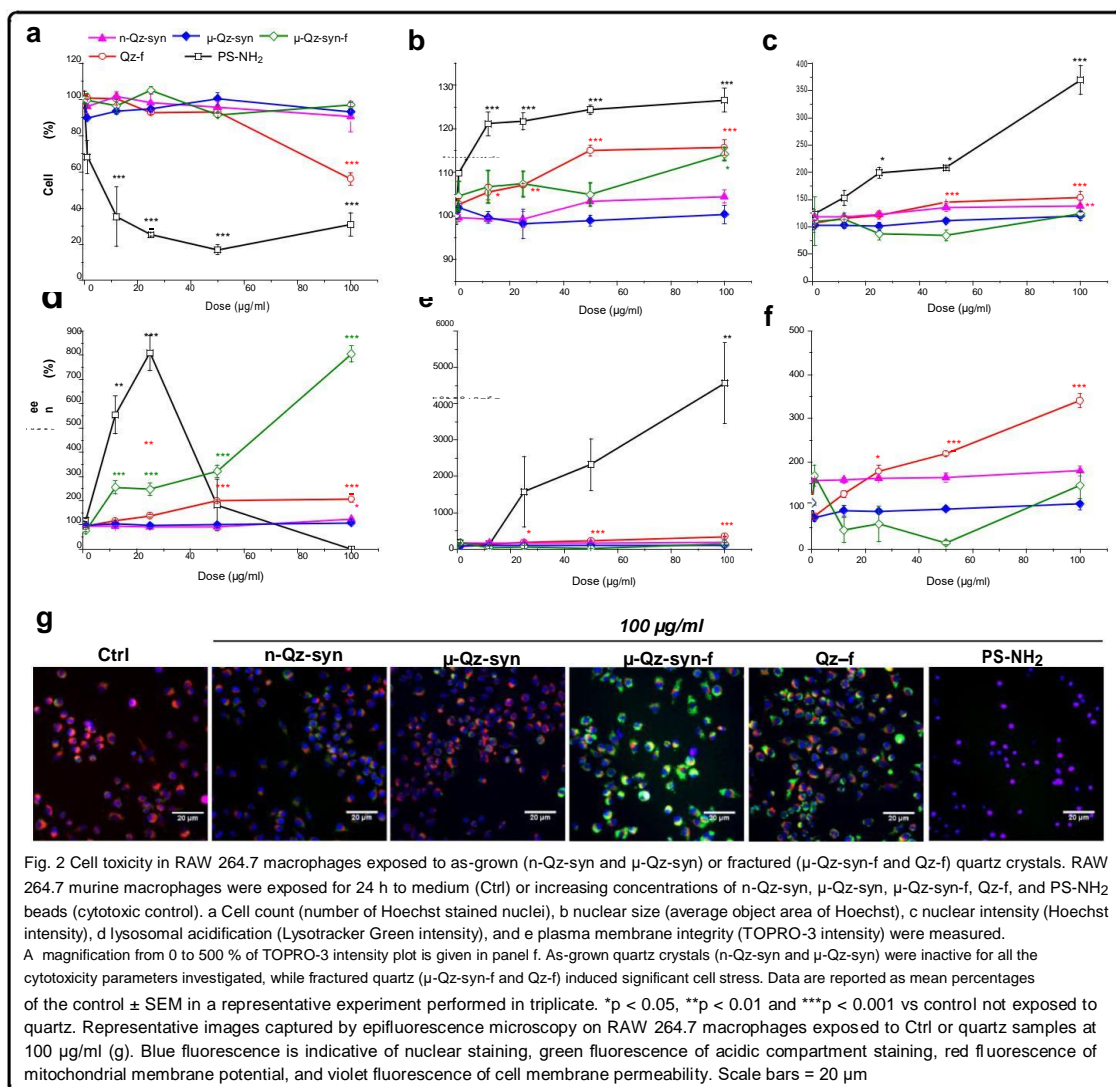

Fig. 2 Cell toxicity in RAW 264.7 macrophages exposed to as-grown (n-Qz-syn and μ-Qz-syn) or fractured (μ-Qz-syn-f and Qz-f) quartz crystals. RAW 264.7 murine macrophages were exposed for 24 h to medium (Ctrl) or increasing concentrations of n-Qz-syn, μ-Qz-syn, μ-Qz-syn-f, Qz-f, and PS-NH$_2$ beads (cytotoxic control). a Cell count (number of Hoechst stained nuclei), b nuclear size (average object area of Hoechst), c nuclear intensity (Hoechst intensity), d lysosomal acidification (Lysotracker Green intensity), and e plasma membrane integrity (TOPRO-3 intensity) were measured. A magnification from 0 to 500 % of TOPRO-3 intensity plot is given in panel f. As-grown quartz crystals (n-Qz-syn and μ-Qz-syn) were inactive for all the cytotoxicity parameters investigated, while fractured quartz (μ-Qz-syn-f and Qz-f) induced significant cell stress. Data are reported as mean percentages of the control ± SEM in a representative experiment performed in triplicate. *p < 0.05, **p < 0.01 and ***p < 0.001 vs control not exposed to quartz. Representative images captured by epifluorescence microscopy on RAW 264.7 macrophages exposed to Ctrl or quartz samples at 100 μg/ml (g). Blue fluorescence is indicative of nuclear staining, green fluorescence of acidic compartment staining, red fluorescence of mitochondrial membrane potential, and violet fluorescence of cell membrane permeability. Scale bars = 20 μm

These quantitative data are supported by imaging (Fig. 2g) of RAW 264.7 macrophages exposed to medium (Ctrl) or to 100 µg/ml of n-Qz-syn, µ-Qz-syn, µ-Qz-syn-f, Qz-f, and PS-NH$_2$ (cytotoxic control). Control cells (Ctrl) showed blue and red fluorescence reflecting nuclear staining and intact mitochondria, respectively. n-Qz-syn and µ-Qz-syn were similar to Ctrl. µ-Qz-syn-f and Qz-f induced an increase of the green staining, due to lysosomal acidification. A violet fluorescence staining due to plasma membrane permeabilization was observed for the cytotoxic control.

Bio-TEM images of RAW 264.7 macrophages incubated with quartz particles for 24 h confirmed that all samples were internalized (Additional file 1: Figure S2).

Contrary to fractured quartz, as-grown quartz crystals show a low membranolytic activity towards RBCs and small liposomes

As-grown quartz crystals (n-Qz-syn and µ-Qz-syn) incubated with purified human red blood cells (RBCs) induced only a modest hemolytic activity (Fig. 3a). On the contrary, fractured synthetic quartz (µ-Qz-syn-f) showed a strong dose-dependent hemolytic activity. The interaction of quartz with artificial, small phosphatidylcholine liposomes (hydrodynamic diameter peaks at ca. 50 and 280 nm, measured with DLS − Additional file 1: Figure S3) was assessed by a fluorescent probe leakage assay. The membranolytic activity towards liposomes (Fig. 3b) confirmed the low and the strong activity of as-grown quartz crystals and fractured ones, respectively. Consistently, the ground mineral quartz dust (Qz-f) showed a high lytic activity in both assays.

Fractured particles exhibit a less homogeneous distribution of surface silanol acidity than as-grown quartz crystals

The chemical homogeneity of the surface acidic functionalities (i.e. silanols) of the four samples was investi-gated by evaluating the variations of their ζ potential in aqueous medium as a function of pH. Surface charge is a function of the equilibrium between the protonated and dissociated silanols [31]. Silanols are Brønsted acidic sites and the equilibrium condition can be described with a "titration curve" (ζ plot) performed by acidifying the medium while the surface net charge of the sus-pended quartz is measured by ELS (Fig. 4) [32]. In alka-line conditions the vast majority of silanols on all quartz crystals were dissociated, resulting in a markedly negative surface zeta potential (ca. −65 mV). By decreasing the pH, the negative surface charge was progressively reduced and approached the point of zero charge (PZC), asymptotically. All curves exhibited a sigmoid pattern, but the slope of the two as-grown crystals (a, b) was much steeper than that of the fractured ones, both synthetic (c) and mineral (d) (see Additional file 1: Table S1), reflecting a greater heterogen-eity of silanols at the surface of fractured particles.

Surface radicals are generated after grinding synthetic as-grown quartz crystals

The surface radicals of quartz particles, generated by cleavage of the Si-O-Si bonds during grinding and subse-quent reaction with atmospheric water and O$_2$ mole-cules, have been extensively described [15, 33, 34]. The presence of surface radicals in quartz was often related
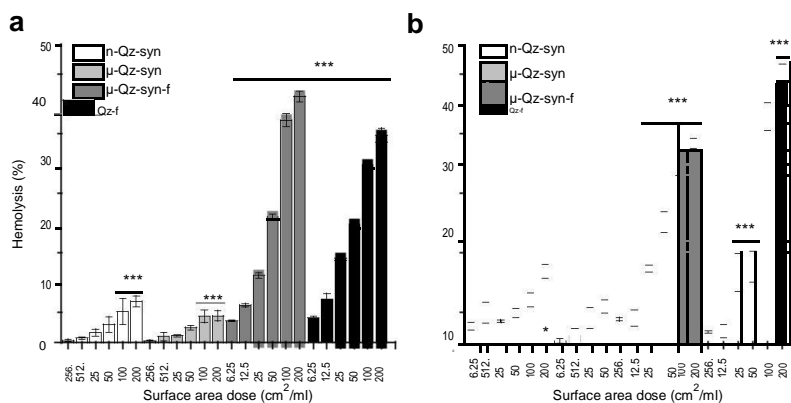
Fig. 3 Hemolysis (a) and liposome rupture (b) induced by as-grown (n-Qz-syn, µ-Qz-syn) and fractured (µ-Qz-syn-f and Qz-f) quartz crystals. Quartz was incubated at increasing concentrations with purified human red blood cells (RBCs) or phosphatidylcholine vesicles. Values are mean ± SD from at least three independent experiments. *p < 0.05, **p < 0.01 and ***p < 0.001 vs control not exposed to particles. A modest lytic effect towards RBCs and small lipid vesicles (<300 nm) was observed upon incubation with as-grown quartz crystals, while a remarkable dose-dependent lysis, up to ca. 45 %, was induced by fractured quartz

Fig. 4 Z plot (ζ potential vs pH) of as-grown n-Qz-syn (a) and μ-Qz-syn (b), and fractured μ-Qz-syn-f (c) and Qz-f (d) quartz crystals. Experimental points acquired with at least three measurements are fitted with a non-linear curve to help the reader's eye. The slope of the tangent line at the inflection point is a convenient estimate of the heterogeneity of surface silanol acidity (see Additional file 1: Table S1). The steeper the slope of the tangent line the more homogeneous the acidic nature of the silanols at the surface

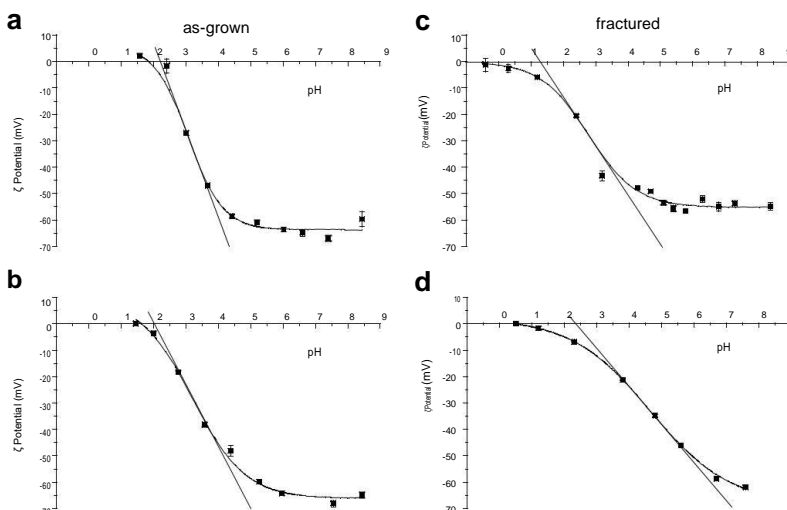to the potential to generate free radicals [35–37] hence promoting pathogenicity [38, 39]. Figure 5 reports the solid state EPR (SS-EPR) spectra of as-grown μ-Qz-syn (a) and the same crystal mechanically fractured (μ-Qz-syn-f) after 0 (b), 3 (c), and 30 days (d). Remarkably, as-grown μ-Qz-syn crystals did not show any radical specie.

Right after mechanical fracturing, SS-EPR spectrum was characterized by an intense signal at g values (defined by the resonance condition $g = h\nu_0/\mu_B B$, in which B is the resonant field and ν_0 the applied microwave frequency) of $g_{//} = 2.000$ and $g_x = 2.0017$ (μ-Qz-syn-f, spectrum b), corresponding to the parallel and x-axis component of
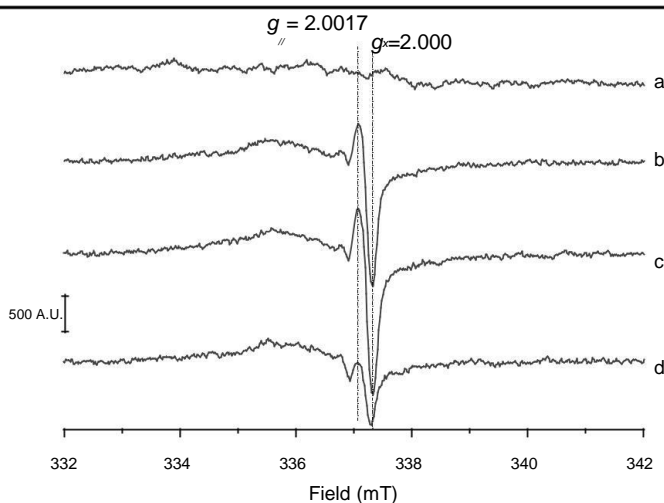
Fig. 5 Solid state EPR spectra of μ-Qz-syn crystal recorded at −196 °C: as-grown (a), as milled (b), 3 days after milling (c), and 1 month after milling (d).

The spectra were recorded with: sweep width 100 G, receiver gain 1×10^4, microwave power 0.1 mW (a very low potency at which the silyl radical is visible and not saturated, while all the other silico-oxygen radical features are hardly visible), scan time 80 s. Mechanical fracturing of as-grown μ-Qz-syn introduced radical defects (b), absent on the pristine quartz crystal (a). Two components ($g_{//}$ and g_x) of the signal relative to silyl radicals were detected. Silyl radicals were stable for three (c) and decreased 30 days after milling (d)

Turci et al. Particle and Fibre Toxicology (2016) 13:32

Page 7 of 12

the silyl radical (Si$^\bullet$), respectively [33]. The radical signal was stable up to three days (spectrum c). Other silicon and oxygen based radicals (for instance, SiO$^\bullet$, SiO$^\bullet_2$, SiO$^\bullet_3$, O$^{\bullet-}_2$) could also be detected after fracturing as revealed by the complex convoluted signal at much lower magnetic field [40]. After a longer time (30 days, spectrum d) silyl radicals decreased in intensity, probably due to surface re-construction [37]. Notably, all spectra did not exhibit paramagnetic centres arising from metal ions occluded, confirming the high purity of the crystals obtained.

Fractured, but not as-grown, quartz crystals generate carbon-centred radicals

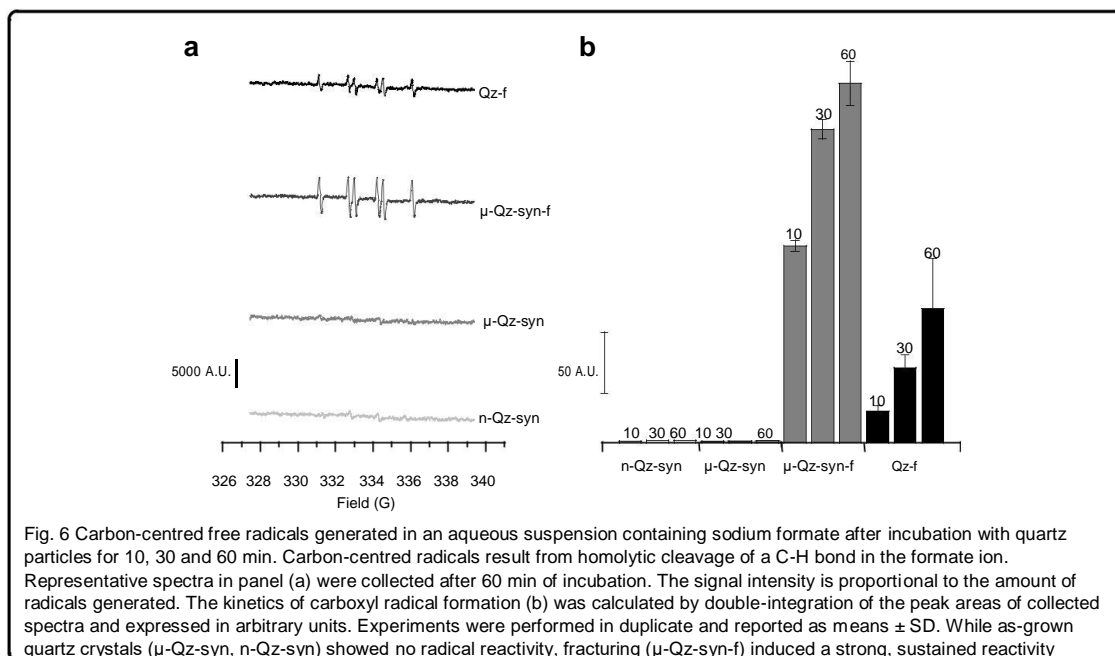All quartz samples were tested for their potential to gen-erate carbon-centred radicals after 10, 30 and 60 min of incubation with formate ion. The homolytic cleavage of the hydrogen-carbon bond in formate was followed by spin trapping technique and quantified with EPR spectroscopy, as carried out in several previous studies with quartz dusts [20, 41–43]. Representative EPR/spin trapping spectra of the [DMPO−COO]$^{\bullet-}$ adduct obtained in the presence of sodium formate at 60 min and double-integration of the reaction kinetics are reported in Fig. 6a and b, respectively. No radical was observed with as-grown quartz crystals (μ-Qz-syn, n-Qz-syn), whereas freshly fractured quartz (μ-Qz-syn-f) had a strong ability to generate carbon-centred free radicals in solution, even more than ground mineral quartz (Qz-f). The strong reactivity of fractured crystals was sus-tained over time, up to 60 min.

Discussion

This study reveals, for the first time, that disorder in the crystal lattice drives the biological reactivity of quartz, leading to a new paradigm of toxicity. Crystallinity, so far held responsible for the adverse effects of silica [1, 2], does not appear related per se to toxicity because quartz crystals grown with intact faces were inert in several cel-lular and cell-free tests relevant for the pathogenicity of inhaled silica particles.

We newly synthesized model quartz crystals to overcome the variability of mineral quartz dusts, usually obtained by grinding, that have been used in previous toxicological and mechanistic investigations. The synthetic procedure adopted in this work yielded quartz crystals with intact sur-faces, in submicron or micron size (depending on the syn-thetic environment) in the respirable dimension. Usually, in silica or silica-related specimens, the near-to-surface re-gions often appear amorphous, even in samples with good crystallinity at the core [15, 44–46]. In the present case, the surface of as-grown quartz crystals was a well-formed, or-dered crystal face. These as-grown quartz crystals were readily internalized by macrophages, but did not elicit evi-dent cytotoxic or cell-stress responses, in particular lyso-somal acidification, in HCA tests. Furthermore, they did not exhibit membranolytic activity in biological or artificial membrane models. The large differentiation in size of the two as-grown crystals led us to exclude that particle size alone could be a key parameter in eliciting the biological reactivity of quartz. This is consistent with previous

Fig. 6 Carbon-centred free radicals generated in an aqueous suspension containing sodium formate after incubation with quartz particles for 10, 30 and 60 min. Carbon-centred radicals result from homolytic cleavage of a C-H bond in the formate ion. Representative spectra in panel (a) were collected after 60 min of incubation. The signal intensity is proportional to the amount of radicals generated. The kinetics of carboxyl radical formation (b) was calculated by double-integration of the peak areas of collected spectra and expressed in arbitrary units. Experiments were performed in duplicate and reported as means ± SD. While as-grown quartz crystals (μ-Qz-syn, n-Qz-syn) showed no radical reactivity, fracturing (μ-Qz-syn-f) induced a strong, sustained reactivity

Turci et al. Particle and Fibre Toxicology (2016) 13:32

Page 8 of 12

findings, showing that the in vivo pulmonary toxicity of quartz particles correlates better with surface activity than particle size and surface area [47].

Upon fracturing, conchoidal surface fractures, characterized by a less ordered lattice structure [27, 28] and a morphology typical of ground mineral quartz, were observed. Under these experimental conditions, the dramatic increase of specific surface area (from 0.3 to 9 m^2/g, for μ-Qz-syn and μ-Qz-syn-f respectively) did not parallel the lowering in particle size. This confirms that the main modification which is induced by fracturing occurs at the surface level, determining the formation of highly irregular parti-cles with an increased specific surface area. Stable surface radicals and the ability to form carbon-centred radicals, which have an essential role in promoting the complex mechanisms of quartz pathogenicity [2, 39, 48–50], were measured. Fractured quartz crystals induced, like ground mineral quartz, strong lysosomal stress to RAW 264.7 cells, as well as RBC and liposome lytic activity.

The long-range order of surface functionalities present on as-grown crystal faces was partially lost upon grind-ing. The progressive surface reconstruction can leave hydrophilic and hydrophobic patches and disordered silanols arrays similar to the surface of some amorphous silicas [24, 51, 52] also reported as highly hemolytic [5, 53]. Fractured quartz exhibited a higher heterogeneity of the surface acidic sites (silanols) compared to the as-grown crystals (ζ plot). The steeper slopes measured for as-grown quartz indicate that silanols on intact surfaces have mostly the same acidity, while the lower slopes of fractured quartz indicate a greater silanol heterogeneity, due to a less spatially-ordered state of polar moieties, including silanols. This finding is also supported by the structural disorder of the crystalline lattice observed with HR-TEM. These ir-regular surfaces were here shown to strongly interact with membranes inducing lysis. Congruently, previous studies associated the hemolytic activity to some peculiar spatial arrangements of silanols and siloxanes [51, 53, 54].

We also evaluated the interaction between nano-sized lipid vesicles and quartz crystals through a liposome leakage assay [55]. The results of liposome lysis were similar to those obtained with RBC, even if the sizes of the membrane models largely differed (<300 nm liposome, ca. 7 μm RBC). The small dimension of liposomes allowed to probe nanometric patches on the quartz surface and to rule out the hypothesis that micrometric features on the quartz crystals (such as spikes and sharp edges) may have a role in determining the interaction between quartz and membranes.

Together, the data are consistent with the notion that most of the biological reactivity of quartz dusts is origi-nated via fragmentation, when cell membranes and tissues interact with conchoidal fractures and not with intact as-grown crystal faces. Conchoidal fracture generates surface

radicals and, cutting across several crystal planes, a disor-dered array of silanols, siloxanes and rings. Surface modifi-cations of quartz dusts which reduce silanol heterogeneity, e.g. hydration [53], surface coverage by polymers [56, 57], reaction of silanols with metal ions [56, 58–61] were shown to reduce or blunt silica toxicity, likely by avoiding the phagolysosomal rupture within macrophages and in-flammatory responses [19, 62–65].

Conclusion

As-grown synthetic quartz crystals did not show bio-logical reactivity in a series of toxicologically relevant tests, indicating that crystallinity per se does not appear as a key determinant of the pathogenic activity of silica particles. A regular distribution of the silanols at the par-ticle surface was shown to occur in synthetic as-grown quartz crystals. Fracturing led to a disorganization of these surface moieties, causing a loss of the long-range spatial order and probably creating reactive surface sila-nol patches. Biological reactivity, and possibly toxicity, appears related with disordered surface functionalities following crystal fracture.

Methods

Chemical reagents

Dulbecco's modified Eagle medium (DMEM) glutamax, fetal bovine serum (FBS) and penicillin-streptomycin were purchased from Life Technologies. NaCl 0.9 % was obtained from B. Braun Medical (Diegem, Belgium), Tri-ton X-100 from Flucka (Buchs, Switzerland). The fluor-escent dyes, Hoechst 33342, TMRM, Lysotracker green and TOPRO-3 were purchased from Life Technologies. All the reagents used for liposome synthesis (methanol, chloroform, L-α-phosphatidylcholine, and calcein) were purchased from Sigma-Aldrich (Milan, Italy). Ultrapure Milli-Q water (Millipore) was used throughout.

Synthetic and mineral quartz

Four powdered quartz samples of synthetic or mineral origin have been here investigated. As-grown quartz crystals (n-Qz-syn and μ-Qz-syn) were obtained by hydrothermal synthesis following a procedure well de-scribed in [26]. Briefly, a 25 % w/w sodium metasilicate pentahydrate solution (Na-MTS, Sigma-Aldrich) was po-lymerized using two mineral acids, i) HNO$_3$ (for n-Qz-syn), and ii) H$_2$CO$_3$ obtained by bubbling CO$_2$ into the Na-MTS solution until gel formation (for μ-Qz-syn). The gel was stabilized at pH ≈ 8. Growth runs were per-formed in PFTE liner sealed into steel autoclaves at 200 ° C and autogenic pressure for 168 h. Fractured μ-Qz-syn-f was obtained by milling 75 mg of μ-Qz-syn in a ball mill (Retsch MM200) in agate jars (27 Hz, with 2 agate spheres) for 30 min. One pure quartz dust (Qz-f) of mineral origin was prepared by grinding a very pure

Turci et al. Particle and Fibre Toxicology (2016) 13:32

Page 9 of 12

quartz crystal from Madagascar in a planetary ball mill (Retsch S100, GmbH, Haan, Germany) for 3 h (70 rpm) and then in the ball mill for 9 h (27 Hz).

Differential centrifugal sedimentation (DCS)

Particle size distribution was determined by differential centrifugal sedimentation using a CPS Disc Centrifuge DC24000 (CPS Instruments Europe) operating at $14000\times$ g with a 6–24 % sucrose gradient in phosphate buffer solution (PBS, pH 7.4). Further details on the technique adopted are reported in [66]. Each experiment has been repeated at least twice.

Surface area determination

The surface area of the quartz particles was measured using the BET method based on Kr or N_2 adsorption, as appropriate. Quartz samples have been degassed for hours prior to analysis, which was carried out at -196 ° C (ASAP 2020 Micromeritics, Norcross, USA).

Field emission scanning electron microscopy (FE-SEM)

Sample morphology was investigated by Scanning Electron Microscopy (SEM) using a Zeiss Evo50 and a Hitachi S-4300 Field Emission SEM. Quartz samples were sonicated for 30 min in ultrapure water, dropped off on conductive stubs, and coated with gold in order to prevent the electron beam from charging the sample. The operating conditions were: EHT 15 to 25 kV, WD 1 to 6 mm, probe current 100 pA.

High resolution transmission electron microscopy (HR-TEM)

To inspect the crystal lattice and the defectiveness of the quartz samples, high resolution transmission electron microscopy was carried out with a JEOL 3010-UHR, equipped with a LaB_6 filament operating at 300 kV, beam current 114 μA and with a 2 k × 2 k pixels Gatan US1000 CCD camera. Quartz samples were dispersed in ultrapure water, sonicated for 20 min and a droplet was deposited on lacey carbon Cu grids.

Cell toxicity assessment by high content analysis (HCA) on RAW 264.7 murine macrophages

High Content Analysis (HCA) for toxicological investigation [5, 30, 67] was used to screen quartz samples for cell viability and stress-related responses. The protocol refers to [29]. Briefly, RAW 264.7 murine macrophages (pur-chased from ECACC) were grown to pre-confluence at 37 ° C in a 5 % CO_2-supplemented atmosphere in DMEM glutamax supplemented with 10 % FBS, 1 % penicillin (100 U/ml) and streptomycin (100 μg/ml). 5×10^3 cells/ well were seeded in a 96-well tissue culture plate and allowed to adhere in 100 μl of DMEM glutamax supple-mented with 10 % FBS for 16–24 h (37 ° C, 5 % CO_2) be-fore particle incubation. Stock suspensions were prepared

by suspending 2 mg/ml of quartz particles in PBS and sonicated for 10 min with an ultrasonic bath (Branson, Bransonic 1510; 80 W). Particle dispersions were prepared by diluting sample stock suspensions in the culture media to $3 \times$ the final concentration required; then, 50 μl of par-ticle suspensions were distributed in cell culture plates, obtaining the final concentrations of 1, 12, 25, 50 and 100 μg/ml. A negative control (only culture medium) and a cytotoxic control (NH_2-conjugated polystyrene beads, PS-NH_2) [29] were also included. Cells were incubated with quartz particles for 24 h (37 ° C, 5 % CO_2). One hour before cell imaging, 50 μl of medium was replaced with 50 μl of a cocktail of fluorescent probes containing: Hoechst 33342 (400 nM), Lysotracker Green (200 nM), TOPRO-3 (800 nM), and TMRM (20 nM). After 1 h incu-bation (37 ° C, 5 % CO_2), cells were imaged using the Arrayscan VTI 740 (Thermo Scientific). During measure-ments standard cell conditions were maintained (37 ° C and 5 % CO_2) through the Arrayscan Live Cell Module (Thermo Scientific). Plates were then read using 20× ob-jective lens and fluorescent intensities were collected using four combinations of excitation/emission filters. Hoechst was visualized in the blue channel, Lysotracker in the green channel, TOPRO-3 and TMRM in the far-red and in the red, respectively. The utility of these dyes, their exci-tation/emission wavelengths and response profiling have been described previously [29]. For each well, ten inde-pendent fields were configured to image an average of 300 to 500 cells. Data were collected and analysed using the vHCS View software (Thermo Scientific) and the parame-ters investigated were: cell count (generated from the number of Hoechst stained nuclei), nuclear size (from the average object area of Hoechst), nuclear intensity, Lyso-tracker Green intensity and TOPRO-3 intensity. Analysis parameters were set according to manufacturer's instruc-tions and background noise was separated from fluores-cence through fixed thresholds for each parameter. A specific algorithm was written in order to extract the quantitative data from images using the Cell Health Profile bioapplication.

Hemolysis of human RBCs

RBCs were separated from fresh human blood of healthy volunteer donors not receiving any pharmacological treatment. The method for assessing the hemolytic activ-ity induced by particles refers to [63], with minor modi-fications given in [53]. Hemolytic activity was evaluated exposing RBCs to increasing concentrations of quartz particles (from 6.25 to 200 cm^2/ml) calculated on the basis of the BET surface area of each particle, as best metric for a surface-driven process. The haemoglobin re-leased and measured spectrophotometrically at 540 nm did not adsorbed on quartz samples (data not shown).

Lysis assay of artificial phosphatidylcholine unilamellar vesicles

Preparation and characterization

Calcein-loaded unilamellar vesicles were prepared by hydration of a dry lipid film and size exclusion chromatography. A dry film, obtained by the dissolution of 10 mg of phosphatidylcholine in a mixture of methanol-chloroform (1:2) followed by their removal with a rotary evaporator (Büchi Rotovapor R-200) and a stream of ni-trogen gas, was hydrated with 4 ml of a 0.01 M calcein solution in 0.01 M PBS. The pH was adjusted to 7.4 with NaOH to ensure complete solubilisation of the calcein crystals. To separate the calcein-loaded vesicles from the free calcein molecules, a gel filtration step was per-formed. Approximately, 1 ml of liposome dispersion was loaded in a column filled with 10 ml Sepharose CL-4B beads, using 0.01 M PBS as eluent. Liposome dispersion was then diluted 1:8 with PBS and stored at +4 °C. Liposome dispersion was characterized by dynamic light scattering (DLS) and ζ potential measurements (Zetasi-zer Nano–ZS, Malvern Instruments, Worcestershire, U.K.) (see Additional file 1: Figure S3). The ζ potential (at pH 7.4) was −7 ± 0.6 mV.

Leakage assay

Liposomes were incubated with increasing concentrations of quartz particles as for the hemolytic assay. Leakage of the fluorescent dye calceine (excitation and emission wavelength of 495 and 515 nm, respectively) encapsulated into liposomes was used as marker of liposome rupture.

This method refers to [55, 68], with minor modifications. Briefly, liposomes dispersed in 0.01 M PBS were distrib-uted in a 96-well plate (100 μL). A baseline fluorescence signal (intensity I_0) was recorded with an excitation wave-length of 490 nm and an emission wavelength at 520 nm. Subsequently, particles dispersed in PBS were added to the final concentrations (in quadruplicate for each con-centration) and fluorescence changes were monitored for 30 min (I_t). Finally, a 20 % solution of Triton X-100 (10 μL) was added to completely disrupt the vesicles, and the fluorescence intensity (I_{max}) of the complete release of the dye from the vesicles was determined. Percentage of the dye released from vesicles was calculated for each con-centration with the following equation (Equation 1):

$$\frac{(I_t - I_0)}{(I_{max} - I_0)} \cdot 100 \qquad (1)$$

ζ Potential

The ζ plot (ζ potential vs pH) for the four as-grown and fractured crystals was evaluated by means of electro-phoretic light scattering (ELS) (Zetasizer Nano–ZS). In this technique the velocity of a particle in an oscillating electric field, which is proportional to its ζ potential, is

measured by light scattering. The ζ potential was measured suspending quartz (0.6 mg/ml) in ultrapure water and adjusting the pH of the suspension with 0.1 M HCl or 0.1 M NaOH. A plot of ζ potential values versus pH was obtained. The set of experimental points was fitted with a sigmoid curve (Boltzmann equation) with OriginPro8.0 software suite (OriginLab Corp., Northampton, MA, USA), a simple approximation for the single-site equation model proposed by Sverjensky and Sahai [69] (Equation 2):

$$y = A_2 + \frac{A_1 - A_2}{1 + e^{(x-x_0)/dx}} \qquad (2)$$

where A_1 and A_2 are the lower and upper horizontal asymptotes respectively, x_0 the point of inflection and dx the curve rate, i.e. the change in x corresponding to the most significant change in y values.

Solid state electron paramagnetic resonance (EPR) spectroscopy

The EPR spectra of the solid quartz dusts were recorded in vacuum at −196 °C on a Bruker EMX spectrometer op-erating in the X–band mode (9.5 GHz), using a technique previously reported [33]. The spectra have been recorded with a scan range of 100 G (332–432 mT), receiver gain of 1×10^4, microwave power of 0.1 mW, modulation ampli-tude of 1 G, and scan time of 80 s. Three scans per meas-urement were performed.

Carbon-centred free radical detection

Free radical generation was monitored by EPR spectros-copy coupled with the spin trapping technique, using 5,5-dimethyl-pirroline-N-oxide (DMPO, Cayman chem-ical company, Ann Arbor, USA) as trapping agent, and following a well-established procedure [41, 70]. EPR spectra were recorded at room temperature on a Minis-cope100 X– band CW- EPR spectrometer (Magnettech, Berlin, Germany) at a microwave power level of 10 mW, scan range of 120 G, and modulation amplitude of 1 G. Each quartz sample (37.5 mg) was suspended in 125 μL of 0.15 M DMPO. The reaction was triggered by adding formate ion (125 μL of 1.0 M HCOONa solution in 0.5 M PBS, pH 7.4) as a target molecule. The kinetic of radical release was progressively measured up to 1 h on an aliquot of 50 μL of the suspension. The amount of carbon-centred radicals generated is proportional to the intensity of the EPR signal after double integration. Each measurement was repeated three times.

Statistical analysis

Statistical analysis was carried out by one-way analysis of variance (ANOVA) followed by Dunnett's or Tukey's post hoc tests, as appropriate. Differences with p value < 0.05 were considered statistically significant.

Turci et al. Particle and Fibre Toxicology (2016) 13:32

Page 11 of 12

Additional file

Additional file 1: Figure S1. Particle size distribution curves of the quartz crystals studied measured with DCS technique. Figure S2. Bio-TEM images of quartz samples internalized by RAW 264.7 murine macrophages. Figure S3.
Size characterization curve of liposome dispersion measured by DLS.
Table S1. Curve-fit parameters calculated by fitting experimental dataset (ζ potential vs pH) with a Boltzmann equation. (DOCX 952 kb)

Abbreviations
BET: Brunauer, Emmett, and Teller method; DLS: dynamic light scattering; DMEM: Dulbecco's modified Eagle medium; DMPO: 5,5-dimethyl-pirroline-N-oxide; DSC: differential centrifugal sedimentation; ECACC: European collection of authenticated cell cultures; EHT: extra high tension; ELS: electrophoretic light scattering; EPR: electron paramagnetic resonance; FBS: foetal bovine serum; FE-SEM: field emission scanning electron microscopy; HCA: high content analysis; HR-TEM: high resolution transmission electron microscopy; Na-MTS: sodium metasilicate pentahydrate; PBS: phosphate buffer solution; PS-NH$_2$: amino-conjugated polystyrene beads; RBC: red blood cell; SD: standard deviation; SEM: scanning electron microscopy; SEM: standard error of the mean; SS-EPR: solid state EPR; WD: working distance.

Authors' contributions
FT designed and carried out part of the experiments, and wrote the manuscript. CP carried out the HCA experiments under the supervision of DG and SA at UCD, Dublin, performed the hemolysis experiments under the supervision of DL at UCL, Brussels, and wrote the manuscript. RL and MT performed physico-chemical characterization and liposome lysis assay. RL and LP synthesized quartz crystals. BF supervised the whole project and wrote the manuscript. All authors read and approved the final manuscript.

Competing interests
The authors declare that they have no competing interests.

Author details
[1]Department of Chemistry, University of Torino, Via P. Giuria 7, Turin 10125, Italy. [2]"G. Scansetti" Interdepartmental Center for Studies on Asbestos and Other Toxic Particulates, University of Torino, Via P. Giuria 7, Turin 10125, Italy. [3]Department of Earth Sciences, University of Torino, Via V. Caluso 35, Turin 10125, Italy. [4]Centre for BioNano Interactions, School of Chemistry and Chemical Biology, University College Dublin, Dublin, Belfield, Ireland. [5]Louvain centre for Toxicology and Applied Pharmacology (LTAP), Université catholique de Louvain, Avenue E. Mounier 52 – bte B1.52.12, Brussels 1200, Belgium.

References
1. International Agency for Research on Cancer (IARC). Silica, Some Silicates, Coal Dust and Para-Aramid Fibrils. In: IARC Monographs on the Evaluation of Carcinogenic Risks to Humans, vol. 68. Lyon: IARC; 1997.
2. International Agency for Research on Cancer (IARC). A Review of Human Carcinogens: Arsenic, Metals, Fibres, and Dusts. In: IARC Monographs on the Evaluation of Carcinogenic Risks to Human, vol. 100C. Lyon: IARC; 2012.
3. Ghiazza M, Polimeni M, Fenoglio I, Gazzano E, Ghigo D, Fubini B. Does vitreous silica contradict the toxicity of the crystalline silica paradigm? Chem Res Toxicol. 2010;23:620–9.
4. Di Cristo L, Movia D, Bianchi MG, Allegri M, Mohamed BM, Bell AP, Moore C, Pinelli S, Rasmussen K, Riego-Sintes J, et al. Pro-inflammatory effects of pyrogenic and precipitated amorphous silica nanoparticles in innate immunity cells. Toxicol Sci. 2015;150:40–53.
5. Zhang HY, Dunphy DR, Jiang XM, Meng H, Sun BB, Tarn D, Xue M, Wang X, Lin SJ, Ji ZX, et al. Processing pathway dependence of amorphous silica nanoparticle toxicity: colloidal vs pyrolytic. J Am Chem Soc. 2012;134: 15790–804.
6. Gazzano E, Ghiazza M, Polimeni M, Bolis V, Fenoglio I, Attanasio A, Mazzucco G, Fubini B, Ghigo D. Physicochemical determinants in the cellular responses to nanostructured amorphous silicas. Toxicol Sci. 2012;128:158–70.
7. Sandberg WJ, Lag M, Holme JA, Friede B, Gualtieri M, Kruszewski M, Schwarze PE, Skuland T, Refsnes M. Comparison of non-crystalline silica nanoparticles in IL-1 beta release from macrophages. Part Fibre Toxicol. 2012;9:13.
8. Guidi P, Nigro M, Bernardeschi M, Scarcelli V, Lucchesi P, Onida B, Mortera R, Frenzilli G. Genotoxicity of amorphous silica particles with different structure and dimension in human and murine cell lines. Mutagenesis. 2013;28:171–80.
9. Napierska D, Thomassen LC, Rabolli V, Lison D, Gonzalez L, Kirsch-Volders M, Martens JA, Hoet PH. Size-dependent cytotoxicity of monodisperse silica nanoparticles in human endothelial cells. Small. 2009;5:846–53.
10. Merget R, Bauer T, Küpper HU, Philippou S, Bauer HD, Breitstadt R, Bruening T. Health hazards due to the inhalation of amorphous silica. Arch Toxicol. 2002;75:625–34.
11. Napierska D, Thomassen LCJ, Lison D, Martens JA, Hoet PH. The nanosilica hazard: another variable entity. Part Fibre Toxicol. 2010;7:32.
12. Maser E, Schulz M, Sauer UG, Wiemann M, Ma-Hock L, Wohlleben W, Hartwig A, Landsiedel R. In vitro and in vivo genotoxicity investigations of differently sized amorphous SiO$_2$ nanomaterials. Mutat Res Genet Toxicol Environ Mutagen. 2015;794:57–74.
13. Guichard Y, Maire MA, Sébillaud S, Fontana C, Langlais C, Micillino JC, Darne C, Roszak J, Stępnik M, Fessard V, et al. Genotoxicity of synthetic amorphous silica nanoparticles in rats following short-term exposure. Part 2: intratracheal instillation and intravenous injection. Environ Mol Mutagen. 2015;56:228–44.
14. Rabolli V, Badissi AA, Devosse R, Uwambayinema F, Yakoub Y, Palmai-Pallag M, Lebrun A, De Gussem V, Couillin I, Ryffel B, et al. The alarmin IL-1α is a master cytokine in acute lung inflammation induced by silica micro- and nanoparticles. Part Fibre Toxicol. 2014;11:69.
15. Fubini B. Health effects of silica. In: Legrand AP, editor. The surface properties of silicas. Chichester: Wiley; 1998. p. 415–64.
16. Sankila R, Karjalainen S, Pukkala E, Oksanen H, Hakulinen T, Teppo L, Hakama M. Cancer risk among glass factory workers: An excess of lung cancer? Br J Ind Med. 1990;47:815–8.
17. Guldner K. Development of silicosis in the ceramics and glass industry. Gefahrst Reinhalt Luft. 1999;59:189–91.
18. Fubini B. Surface chemistry and quartz hazard. Ann Occup Hyg. 1998;42:521–30.
19. Clouter A, Brown D, Hohr D, Borm P, Donaldson K. Inflammatory effects of respirable quartz collected in workplaces versus standard DQ12 quartz: particle surface correlates. Toxicol Sci. 2001;63:90–8.
20. Fubini B, Fenoglio I, Ceschino R, Ghiazza M, Martra G, Tomatis M, Borm P, Schins R, Bruch J. Relationship between the state of the surface of four commercial quartz flours and their biological activity in vitro and in vivo. Int J Hyg Envir Health. 2004;207:89–104.
21. Donaldson K, Stone V, Duffin R, Clouter A, Schins R, Borm P. The quartz hazard: effects of surface and matrix on inflammogenic activity. J Environ Pathol Toxicol Oncol. 2001;20 Suppl 1:109–18.
22. Bruch J, Rehn S, Rehn B, Borm PJA, Fubini B. Variation of biological responses to different respirable quartz flours determined by a vector model. Int J Hyg Environ Health. 2004;207:203–16.
23. Stone V, Jones R, Rollo K, Duffin R, Donaldson K, Brown DM. Effect of coal mine dust and clay extracts on the biological activity of the quartz surface. Toxicol Lett. 2004;149:255–9.
24. Rimola A, Costa D, Sodupe M, Lambert JF, Ugliengo P. Silica surface features and their role in the adsorption of biomolecules: computational modeling and experiments. Chem Rev. 2013;113:4216–313.
25. Donaldson K, Borm PJ. The quartz hazard: a variable entity. Ann Occup Hyg. 1998;42:287–94.
26. Pastero L, Turci F, Leinardi R, Pavan C, Monopoli M. Synthesis of α-quartz with controlled properties for the investigation of the molecular determinants in silica toxicology. Cryst Growth Des. 2016;16:2394–403.
27. Murashov VV, Demchuk E. A comparative study of unrelaxed surfaces on quartz and kaolinite, using the periodic density functional theory. J Phys Chem B. 2005;109:10835–41.
28. Margolis SVK, David H. Processes of formation and environmental occurrence of microfeatures on detrital quartz grains. Am J Sci. 1974;274:449–64.

Turci et al. Particle and Fibre Toxicology (2016) 13:32

Page 12 of 12

29. Anguissola S, Garry D, Salvati A, O'Brien PJ, Dawson KA. High content analysis provides mechanistic insights on the pathways of toxicity induced by amine-modified polystyrene nanoparticles. PLoS One. 2014;9:e108025.

30. Jan E, Byrne SJ, Cuddihy M, Davies AM, Volkov Y, Gun'ko YK, Kotov NA. High-content screening as a universal tool for fingerprinting of cytotoxicity of nanoparticles. ACS Nano. 2008;2:928–38.

31. Iler RK. The Surface Chemistry of Silica. In: The Chemistry of Silica: Solubility, Polymerization, Colloid and Surface Properties, and Biochemistry. New York: Wiley; 1979. p. 622–729.

32. Turci F, Ghibaudi E, Colonna M, Boscolo B, Fenoglio I, Fubini B. An integrated approach to the study of the interaction between proteins and nanoparticles. Langmuir. 2010;26:8336–46.

33. Fubini B, Giamello E, Pugliese L, Volante M. Mechanically induced defects in quartz and their impact on pathogenicity. Solid State Ionics. 1989;32–3:334–43.

34. Ratdzig VA, Bystrikov AV. ESR study of chemically active centers on the surface of quartz. Kinet Catal. 1978;19:713–9.

35. Giamello E, Fubini B, Volante M, Costa D. Surface oxygen radicals originating via redox reactions during the mechanical activation of crystalline SiO_2 in hydrogen-peroxide. Colloid Surface. 1990;45:155–65.

36. Fubini B, Giamello E, Volante M, Bolis V. Chemical functionalities at the silica surface determining its reactivity when inhaled - formation and reactivity of surface radicals. Toxicol Ind Health. 1990;6:571–98.

37. Vallyathan V, Shi XL, Dalal NS, Irr W, Castranova V. Generation of free radicals from freshly fractured silica dust. Potential role in acute silica-induced lung injury. Am Rev Respir Dis. 1988;138:1213–9.

38. Castranova V, Dalal N, Vallyathan V. Role of surface free radicals in the pathogenicity of silica. In: Castranova V, Vallyathan V, Wallace WE, editors. Silica and silica-induced lung diseases. Boca Raton: CRC Press; 1996. p. 91–105.

39. Fubini B, Hubbard A. Reactive oxygen species (ROS) and reactive nitrogen species (RNS) generation by silica in inflammation and fibrosis. Free Radical Bio Med. 2003;34:1507–16.

40. Fubini B, Bolis V, Giamello E. The surface chemistry of crushed quartz dust in relation to its pathogenicity. Inorg Chim Acta. 1987;138:193–7.

41. Fenoglio I, Martra G, Prandi L, Tomatis M, Coluccia S, Fubini B. The role of mechanochemistry in the pulmonary toxicity caused by particulate minerals. J Mater Synth Proces. 2000;8:145–53.

42. Fenoglio I, Fonsato S, Fubini B. Reaction of cysteine and glutathione (GSH) at the freshly fractured quartz surface: A possible role in silica-related diseases? Free Radical Bio Med. 2003;35:752–62.

43. Ghiazza M, Tomatis M, Doublier S, Grendene F, Gazzano E, Ghigo D, Fubini B. Carbon in intimate contact with quartz reduces the biological activity of crystalline silica dusts. Chem Res Toxicol. 2013;26:46–54.

44. Hemley RJ, Jephcoat AP, Mao HK, Ming LC, Manghnani MH. Pressure-induced amorphization of crystalline silica. Nature. 1988;334:52–4.

45. Li I, Bandara J, Shultz M. Time evolution studies of the H_2O/quartz interface using sum frequency generation, atomic force microscopy, and molecular dynamics. Langmuir. 2004;20:10474–80.

46. Jones RC, Uehara G. Amorphous coatings on mineral surfaces. Soil Sci Soc Am J. 1973;37:792–8.

47. Warheit DB, Webb TR, Colvin VL, Reed KL, Sayes CR. Pulmonary bioassay studies with nanoscale and fine-quartz particles in rats: toxicity is not dependent upon particle size but on surface characteristics. Toxicol Sci. 2007;95:270–80.

48. Øvrevik J, Refsnes M, Låg M, Holme JA, Schwarze PE. Activation of proinflammatory responses in cells of the airway mucosa by particulate matter: oxidant- and non-oxidant-mediated triggering mechanisms. Biomolecules. 2015;5:1399–440.

49. Castranova V. Signaling pathways controlling the production of inflammatory mediators in response to crystalline silica exposure: role of reactive oxygen/ nitrogen species. Free Radic Biol Med. 2004;37:916–25.

50. Albrecht C, Knaapen AM, Becker A, Höhr D, Haberzettl P, van Schooten FJ, Borm PJ, Schins RP. The crucial role of particle surface reactivity in respirable quartz-induced reactive oxygen/nitrogen species formation and APE/Ref-1 induction in rat lung. Respir Res. 2005;6:129.

51. Murashov V, Harper M, Demchuk E. Impact of silanol surface density on the toxicity of silica aerosols measured by erythrocyte haemolysis. J Occup Environ Hyg. 2006;3:718–23.

52. Fenoglio I, Fubini B, Ghibaudi EM, Turci F. Multiple aspects of the interaction of biomacromolecules with inorganic surfaces. Adv Drug Deliv Rev. 2011;63: 1186–209. doi:10.1016/j.addr.2011.08.001.

53. Pavan C, Tomatis M, Ghiazza M, Rabolli V, Bolis V, Lison D, Fubini B. In search of the chemical basis of the hemolytic potential of silicas. Chem Res Toxicol. 2013;26:1188–98.

54. Pandurangi RS, Seehra MS, Razzaboni BL, Bolsaitis P. Surface and bulk infrared modes of crystalline and amorphous silica particles: a study of the relation of surface structure to cytotoxicity of respirable silica. Environ Health Perspect. 1990;86:327–36.

55. Alkhammash HI, Li N, Berthier R, de Planque MR. Native silica nanoparticles are powerful membrane disruptors. Phys Chem Chem Phys. 2015;17:15547–60.

56. Nolan RP, Langer AM, Harington JS, Oster G, Selikoff IJ. Quartz hemolysis as related to its surface functionalities. Environ Res. 1981;26:503–20.

57. Prügger F, Mallner B, Schlipköter HW. Polyvinylpyridine N-oxide (Bay 3504, P-204, PVNO) in the treatment of human silicosis. Wien Klin Wochenschr. 1984;96:848–53.

58. Duffin R, Gilmour PS, Schins RPF, Clouter A, Guy K, Brown DM, MacNee W, Borm PJ, Donaldson K, Stone V. Aluminium lactate treatment of DQ12 quartz inhibits its ability to cause inflammation, chemokine expression, and nuclear factor-kappa B activation. Toxicol Appl Pharm. 2001;176:10–7.

59. Le Bouffant LDH, Martin JC. The terapeutic action of aluminium compounds on the development of experimental lesions produced by pure quartz or mixed dust. Inhaled Part. 1977;4:389–400.

60. Bégin R, Massé S, Sébastien P, Martel M, Bossé J, Dubois F, Geoffroy M, Labbé J. Sustained efficacy of aluminum to reduce quartz toxicity in the lung. Exp Lung Res. 1987;13:205–22.

61. Schins RP, Duffin R, Höhr D, Knaapen AM, Shi T, Weishaupt C, Stone V, Donaldson K, Borm PJ. Surface modification of quartz inhibits toxicity, particle uptake, and oxidative DNA damage in human lung epithelial cells. Chem Res Toxicol. 2002;15:1166–73.

62. Peeters PM, Eurlings IMJ, Perkins TN, Wouters EF, Schins RPF, Borm PJA, Drommer W, Reynaert NL, Albrecht C. Silica-induced NLRP3 inflammasome activation in vitro and in rat lungs. Part Fibre Toxicol. 2014;11:58.

63. Lu SL, Duffin R, Poland C, Daly P, Murphy F, Drost E, MacNee W, Stone V, Donaldson K. Efficacy of simple short-term in vitro assays for predicting the potential of metal oxide nanoparticles to cause pulmonary inflammation. Environ Health Persp. 2009;117:241–7.

64. Cho WS, Duffin R, Bradley M, Megson IL, MacNee W, Lee JK, Jeong J, Donaldson K. Predictive value of in vitro assays depends on the mechanism of toxicity of metal oxide nanoparticles. Part Fibre Toxicol. 2013;10:15.

65. Pavan C, Rabolli V, Tomatis M, Fubini B, Lison D. Why does the hemolytic activity of silica predict its pro-inflammatory activity? Part Fibre Toxicol. 2014;11:76.

66. Monopoli MP, Walczyk D, Campbell A, Elia G, Lynch I, Bombelli FB, Dawson KA. Physical-chemical aspects of protein corona: relevance to in vitro and in vivo biological impacts of nanoparticles. J Am Chem Soc. 2011;133:2525–34.

67. George S, Pokhrel S, Xia T, Gilbert B, Ji Z, Schowalter M, Rosenauer A, Damoiseaux R, Bradley KA, Mädler L, Nel AE. Use of a rapid cytotoxicity screening approach to engineer a safer zinc oxide nanoparticle through iron doping. ACS Nano. 2010;4:15–29.

68. Ladokhin AS, Wimley WC, White SH. Leakage of membrane vesicle contents: determination of mechanism using fluorescence requenching. Biophys J. 1995;69:1964–71.

69. Sverjensky DA, Sahai N. Theoretical prediction of single-site surface-protonation equilibrium constants for oxides and silicates in water. Geochim Cosmochim Acta. 1996;60:3773–97.

70. Fubini B, Mollo L, Giamello E. Free-radical generation at the solid/liquid interface in iron-containing minerals. Free Radical Res. 1995;23:593–614.

Additional file 1

The pathogenicity of silica, crystallinity and surface disorder: revisiting the paradigm with synthetic quartz crystals

Francesco Turci, Cristina Pavan, Riccardo Leinardi, Maura Tomatis, Linda Pastero, David Garry, Sergio Anguissola, Dominique Lison, Bice Fubini
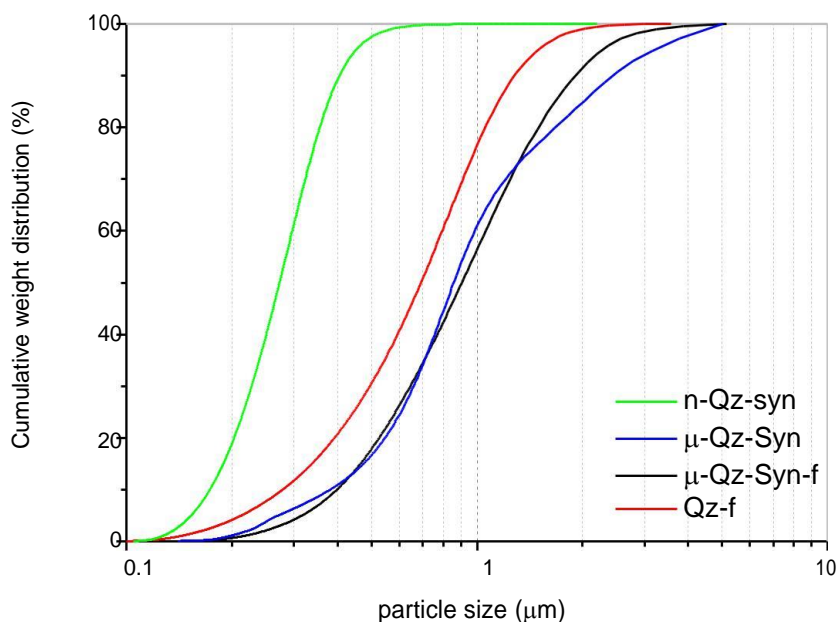
Fig. S1 Particle size cumulative distribution curves measured by DCS technique. The particle size of the two as-grown crystals was largely different, being the average particle diameter of n-Qz-syn $\ll$ μ-Qz-syn (50th percentile of the cumulative size distribution at ca. 280 nm and 900 nm, respectively). Particle size distribution of fractured quartz crystals (μ-Qz-syn-f) was similar to mineral quartz dust (Qz-f).
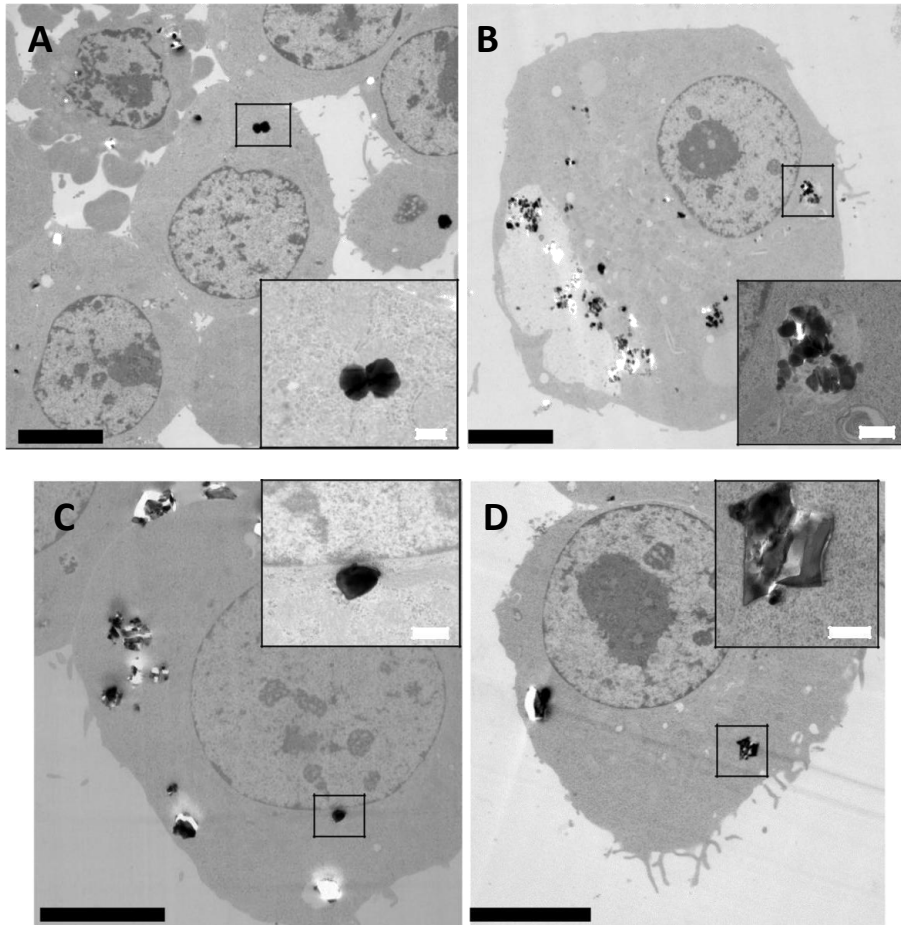
Fig. S2 Bio-TEM images of quartz samples internalized by Raw264.7 murine macrophage cell line. Cells were exposed to 100 µg/ml of as-grown (n-Qz-syn and µ-Qz-syn) and fractured (µ-Qz-syn-f and Qz-f) quartz (A, B, C, and D, respectively) for 24h and thin cross-sections of fixed cell observed at low and high (insets) magnification. Internalization was observed at all exposures investigated, with particles (aggregates and largest particles) mainly localized in lysosomal compartments. In some cases, the fusion of lysosomes in larger compartments could be observed (panel B), but without any sign of nuclear uptake of intact particles. Scale bars: 5 µm, black and 500 nm, white. TEM imaging was performed accordingly to [1].
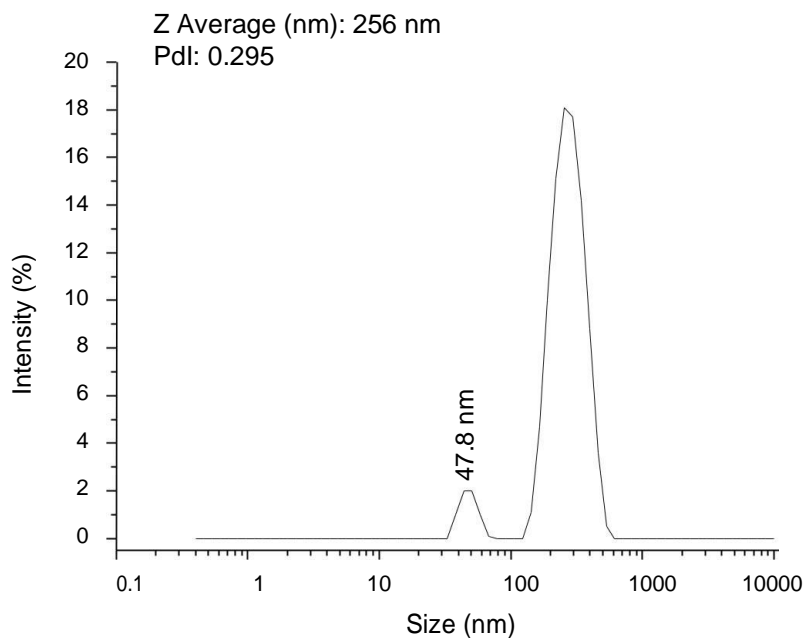
Fig. S3 Size characterization curve of liposome dispersion measured by DLS, expressed in intensity (%) *vs* size (nm). After being synthesized, liposomes were dispersed in 0.01 M phosphate-buffered saline (PBS, pH 7.4), and characterized for their hydrodynamic size through dynamic light scattering technique (DLS). The first peak (at ca. 50 nm) is representative of small unilamellar vesicles (SUVs), usually characterized by a diameter of 20 nm up to 100 nm. The second peak (at ca. 280 nm) is representative of large unilamellar vesicles (LUVs), usually ranging from 100 nm up to few micrometers. In our dispersion, LUVs ranges from 120 to 580 nm.

Table S1 Curve-fit parameters calculated by fitting experimental dataset (ζ potential *vs* pH) with a Boltzmann equation

	n-Qz-syn	μ-Qz-syn	μ-Qz-syn-f	Qz-f
Ave. pK$_a$ §	3.08 ± 0.07	3.21 ± 0.11	2.77 ± 0.11	4.65 ± 0.06
$f'(\text{pK}_a)$ †	-32.9	-23.2	-18.6	-14.4

§ the point of inflection

† the curve slope at the point of inflection

When quartz is suspended in water an equilibrium is readily established between protonated and dissociated silanols [2]:

$$\text{-SiO}^- + H_2O \rightleftharpoons \text{-SiOH} + OH^-$$
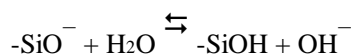
In an alkaline environment the vast majority of silanols will be dissociated with a net surface charge markedly negative (ca. -65 mV). As the pH decreases, the protonated form is favoured and the overall surface charge becomes less negative. At pH < 2, all silanols are in the protonated form and the net charge of quartz is virtually zero. This pH value corresponds to the PZC, which in quartz can reasonably considered asymptotic, since the formation of surface species $SiOH_2^+$ is not expected for silica [3].

As reported in the Methods section, the experimental ζ potential points can be fitted with a non-linear Boltzmann equation. Two parameters can be readily extrapolated, namely the point of inflection (x_0) and the curve slope at the point of inflection ($f'(x_0)$), i.e. the change in x corresponding to the most significant change in y values. Those empirical parameters may conveniently be used to describe the "average acidity" of surface silanols (*Ave.* pK$_a$ = x_0) and the intrinsic variability of acidic character showed by the families of silanols (curve slope at the point of inflection, ($f'(\text{pK}_a)$).

The steeper slope ($f'(\text{pK}_a)$) observed for n-Qz-syn and μ-Qz-syn may account for a less heterogeneous distribution of surface acidic sites (i.e. silanols) with respect to fractured quartz (μ-Qz-syn-f and Qz-f). We may infer that the slope decreases by increasing the heterogeneity of the surface acidic silanols as it occurs after fragmentation of the crystals during milling. While as-grown quartz crystals expose intact crystal planes (n-Qz-syn and μ-Qz-syn), fractured quartz (Qz-syn-f and Qz-f) is characterized by conchoidal fractures, imparting a more heterogeneous silanol composition on quartz surface. Therefore, depending on the heterogeneity of the surface acidic

silanols, the curve slope of the tangent line may vary, and it may represent an indirect measure of the surface chemical homogeneity of a quartz particle.

References

1. Lesniak A, Fenaroli F, Monopoli MP, Åberg C, Dawson KA, Salvati A: **Effects of the presence or absence of a protein corona on silica nanoparticle uptake and impact on cells.** *ACS Nano* 2012, **6:**5845-5857.

2. Iler RK: **The Surface Chemistry of Silica.** In *The Chemistry of Silica: Solubility, Polymerization, Colloid and Surface Properties, and Biochemistry.* Edited by Wiley. New York; 1979:622-729.

3. Liu X, Cheng J, Lu X, Wang R: **Surface acidity of quartz: understanding the crystallographic control.** *Phys Chem Chem Phys* 2014, **16:**26909-26916.